DTU Physics
Department of Physics

Ph.D. thesis

Exploring challenges and solutions towards polymer-based acoustofluidics

Fabian Lickert

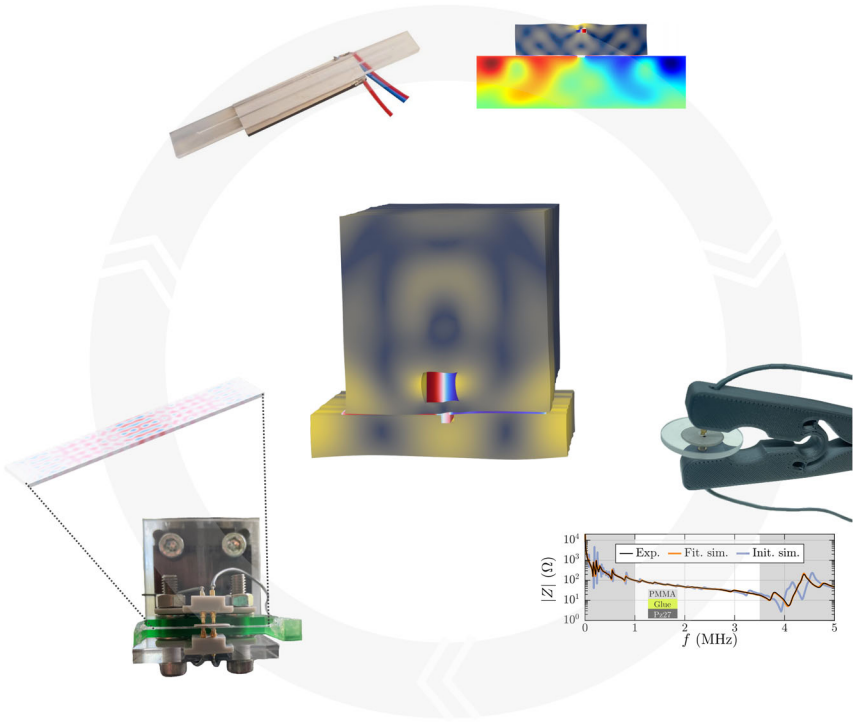

Supervisor: Henrik Bruus

Department of Physics
Technical University of Denmark

14 November 2022

Cover illustration:
This thesis follows a feedback loop between experimental validation and numerical simulations for designing and optimizing a polymer-based acoustofluidic device. An adapted form of the results from Paper I [1], Paper II [2], and Paper III [3] are arranged around this loop. The center, constituting the outcome of the feedback loop, shows the 3D simulation results of an optimized geometry for a polymer-based acoustofluidic device.

Exploring challenges and solutions towards polymer-based acoustofluidics

Typeset using LaTeX.

Department of Physics
Technical University of Denmark
DTU Physics Building 309, DK-2800 Kongens Lyngby, Denmark
http://www.fysik.dtu.dk/microfluidics

Abstract

In acoustofluidic devices, sound waves are used to enable the manipulation of small particles suspended in a fluid and the fluid itself. The resulting particle motion due to an acoustic field is called acoustophoresis. Acoustophoresis can be utilized in many biomedical applications for contact- and label-free cell handling. Being able to perform acoustophoresis in polymer-based chips is highly desirable due to the low associated fabrication cost of such chips. Polymer devices can be manufactured using injection molding for a much lower cost than conventional glass- or silicon-based devices. With this goal in mind, we explore and quantify the performance of an acoustophoresis device made from the polymer PMMA. The experimental results are compared to numerical results to establish a feedback loop between simulations and experiments. In an initial validation study, the need for more accurate and precise material parameters is identified as the bottleneck in performing reliable numerical optimization of polymer chips. Many conventional techniques that characterize the acoustic properties of a polymer are very costly and time-consuming. Furthermore, they often rely on a static or low-frequency measurement of the properties, in contrast to the required material parameters measured in the MHz region. This lack of suitable measurement methods led to the development of a novel technique labeled ultrasound electrical impedance spectroscopy (UEIS). This novel method enables to obtain material parameters for the piezoelectric transducer, the glue layer, and the polymer chip based on a simple measurement of the electrical impedance spectrum and an inverse numerical fitting approach. Different validation measurements have verified the UEIS technique to ensure the correctness of the method, as is discussed in detail within this thesis. Utilizing the UEIS technique, the properties of several materials have been measured, and the corresponding values have been used to perform numerical simulations and optimize acoustofluidic devices. We also explore some experimental challenges in this work and compare the performance of acoustofluidic devices under different electrical excitation methods. We find that constant-power excitation might be advantageous in frequency sweeps when attempting to find the most power-efficient frequency. Combining all the lessons learned on polymer-device performance, material parameter measurement using the UEIS method, and experimental considerations such as constant-power excitation, we perform optimization of an acoustophoresis device. The optimization result is a device geometry based on the polymer COC that promises to achieve more than an order of magnitude increase in the acoustophoresis performance compared to the reference geometry.

Resumé

I akustofluidiske enheder anvendes lydbølger til at manipulere små partikler, der er suspenderet i en væske, og selve væsken. Den resulterende partikelbevægelse som følge af et akustisk felt kaldes akustoforese. Akustoforese kan bruges i mange biomedicinske anvendelser til kontakt- og etiketfri cellehåndtering. Det er fordelagtigt at kunne udføre akustoforese i polymerbaserede chips grundet de lave fremstillingsomkostninger, der er forbundet med sådanne chips. Polymerenheder kan fremstilles ved hjælp af sprøjtestøbning til en meget lavere pris end konventionelle glas- eller siliciumbaserede enheder. Med dette mål for øje, undersøger og kvantificerer vi ydeevnen af en akustoforeseenhed fremstillet af polymeren PMMA. De eksperimentelle resultater sammenlignes med numeriske resultater for at etablere et feedbackloop mellem simuleringer og eksperimenter. I en indledende valideringsundersøgelse identificeres behovet for mere nøjagtige og præcise materialeparametre som er flaskehalsen for at udføre pålidelig numerisk optimering af polymerchips. Mange konventionelle teknikker til karakterisering af polymerens akustiske egenskaber er meget dyre og tidskrævende. Desuden er de ofte baseret på en statisk eller lavfrekvent måling af egenskaberne i modsætning til de nødvendige materialeparametre, der måles i MHz-området. Denne mangel på egnede målemetoder førte til udvikling af en ny teknik med betegnelsen ultralyd elektrisk impedansspektroskopi (UEIS). Denne nye metode gør det muligt at opnå materialeparametre for den piezoelektriske transducer, limlaget og polymerchippen på grundlag af en simpel måling af det elektriske impedansspektrum og en omvendt numerisk tilpasning. Forskellige valideringsmålinger har verificeret UEIS-teknikken for at sikre metodens korrekthed, hvilket diskuteres i detaljer i denne afhandling. Ved hjælp af UEIS-teknikken er egenskaberne for flere materialer blevet målt, og de tilsvarende værdier er blevet brugt til at udføre numeriske simuleringer og optimere akustofluidiske enheder. Vi undersøger også nogle eksperimentelle udfordringer i dette arbejde og sammenligner akustofluidiske enheders ydeevne under forskellige elektriske excitationsmetoder. Vi finder, at excitation med konstant effekt kan være fordelagtig i frekvenssøgninger, når vi forsøger at finde den mest energieffektive frekvens. Ved at kombinere alle de fundne erfaringer om polymerenhedens ydeevne, måling af materialeparametre ved hjælp af UEIS-metoden og eksperimentelle overvejelser, som f.eks. excitation med konstant effekt-energitilførsel, udfører vi optimering af en akustoforeseenhed. Resultatet af optimeringen er en enhedsgeometri baseret på polymeren COC, som lover at opnå en forbedring på mere end en størrelsesorden i akustoforesepræstationen sammenlignet med referencegeometrien.

Preface

This thesis is submitted in candidacy for the degree of Doctor of Philosophy (Ph.D.) from Technical University of Denmark (DTU). The work was carried out in the Department of Physics, Section of Biophysics and Fluids, in the Theoretical Microfluidics Group, during the three years from 15 November 2019 to 14 November 2022, with Professor Henrik Bruus as main supervisor and Associate Professor Per Augustsson as co-supervisor.

This Ph.D. project is part of the Eureka Eurostars-2 joint program E!113461 AcouPlast project funded by Innovation Fund Denmark, grant no. 9046-00127B, and Vinnova, Sweden's Innovation Agency, grant no. 2019-04500, with co-funding from the European Union Horizon 2020 Research and Innovation Programme. In addition, the project included an external research stay from September to December 2021 in the group of Associate Professor Jered Haun at the department of Biomedical Engineering at the University of California, Irvine. The external research stay was generously supported by the Otto Mønsteds Foundation, the Reinholdt W. Jorck og Hustrus Foundation, the William Demant Foundation, and the Niels Bohr Foundation.

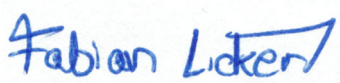

Fabian Lickert
Department of Physics
Technical University of Denmark
14 November 2022

Acknowledgement

I am grateful for the support of several people who have guided me during my thesis over the past three years. First and foremost, I would like to thank my supervisor, Professor Henrik Bruus, for introducing me to the field of acoustofluidics. Henrik taught me how to see new challenges not only with an engineer's eye but also with a physicist's eye. As a result, I learned a lot during the last few years, and I also understood how many things I do not know yet, which is not always easy to admit.

Next, I would like to thank Associate Professor Massimiliano Rossi. When I started my Ph.D. at the Theoretical Microfluidics Group in 2019, I was hired to perform numerical and experimental work. At this time, however, the acoustofluidic lab at DTU was non-existent, or rather consisted of an empty room. Therefore, over the coming years, Massi equipped the TMF laboratory with all the essential equipment to perform acoustophoresis experiments. This resulted in a great collaboration and several experiments, which were performed in the newly equipped laboratory.

A large thank you also to my current and former colleagues at the Theoretical Microfluidics Group at DTU: Jacob Søberg Bach, whose development of an effective boundary layer theory made many of my simulations only possible; André Gugele Steckel, with whom I had very fruitful discussions about electrical impedance spectroscopy; Jonas Helboe Jørgensen, who answered many of my questions about symmetry boundary conditions; William Naundrup Bodé, for the excellent collaboration on the UEIS technique and many discussions about polymer-based acoustofluidics; Bjørn G. Winckelmann, for his valuable input on many theory questions and all things radiation-force related; Søren A.S. Kuhberg, for his great commitment as the current TMF president. I would also like to thank the bachelor and master students Aslak Rønnow Franzen, Gustav Kildevang Modler, and Benjamin Tang Hallengreen for interesting discussions and their perspectives on various topics, both experimental- and theory-related. I want to highlight Gustav's support with the optimization procedure of polymer devices. His thoughts on the cost function have been very valuable to me.

Thank you also to all members of the FLUIDS section at DTU whom I had the pleasure to meet. I enjoyed our weekly section meetings, and it was great to get an overview outside my little bubble of the field of acoustofluidics. Extending my gratitude outside the hallways of building 309, I would like to thank Komeil Saeedabadi and his supervisors, Guido Tosello and Matteo Calaon, at DTU Construct for their outstanding contribution to the AcouPlast project. Especially Komeil's tireless commitment and many hours spent on injection molding and bonding need to be pointed out. Finally, extending my acknowledgment

over the Øresund to my collaborators at AcouSort and Lund University: Pelle Ohlsson, Mathias Ohlin, Per Augustsson, Wei Qiu, Ola Jakobsson, and all Ph.D. students in Per Augustsson's group. I was always greeted by a very welcoming and supportive atmosphere on my visits to LTH. I am very grateful for Mathias' expertise on the experimental side of acoustofluidics and the extensive characterization of our polymer devices. Special thanks also go to Pelle for steering the AcouPlast project through many months of COVID19-uncertainties and organizing very productive bi-weekly meetings.

Moving westward and over the Atlantic Ocean, I would like to thank Associate Professor Jered Haun, his Ph.D. students Marzieh Aliaghaei, and Jonathan Piceno for welcoming me to UC Irvine and allowing me to explore some parts of California during my Ph.D. studies.

Last but not least, I want to thank my family: My mother, Susanne, and father, Martin, for showing their care and interest in a research topic that perhaps not many people outside academia are familiar with. Thank you to my siblings, Maren, Tim, and Katrin, for enduring long discussions about my work during my visits at home. My biggest gratitude goes to my partner Julija for moving to Copenhagen with me three years ago, supporting me through all the ups and downs that come with a Ph.D. thesis, and believing in me until the end.

Contents

Publications in the PhD project

Peer-reviewed journal papers

I. F. Lickert, M. Ohlin, H. Bruus, and P. Ohlsson, *Acoustophoresis in polymer-based microfluidic devices: Modeling and experimental validation*, J. Acoust. Soc. Am. **149**, 4281-4291 (2021).
Enclosed in Chapter 5, Ref. [1].

II. W.N. Bodé, F. Lickert, P. Augustsson, and H. Bruus, *Determination of the complex-valued elastic moduli of polymers by electrical impedance spectroscopy for ultrasound applications*, **resubmitted** to Phys. Rev. Appl., 1-11 (2022).
Enclosed in Chapter 6, Ref. [2].
Remarks: This work has been performed in collaboration with fellow Ph.D. student William Naundrup Bodé with equal first-authorship.

III. F. Lickert, H. Bruus, and M. Rossi, *Constant-Power versus Constant-Voltage Actuation in Frequency Sweeps for Acoustofluidic Applications*, Micromachines **13**, 1886 1-16 (2022).
Enclosed in Chapter 7, Ref. [3].

Peer-reviewed conference contributions

1. F. Lickert, M. Ohlin, H. Bruus, and P. Ohlsson, *Modeling and experimental evaluation of a polymer-based acoustophoresis chip*, Acoustofluidics Conference, 26-27 Aug 2020, Virtual Conference, **Oral presentation**.

2. K. Saeedabadi, F. Lickert, H. Bruus, G. Tosello, and M. Calaon, *Dimensional characterization of micro-milled polymer channels for acoustic blood plasma separation*, EUSPEN's 21st International Conference & Exhibition, Copenhagen, DK, 7-10 June 2021, **Poster presentation** by K. Saeedabadi.

3. F. Lickert, M. Ohlin, H. Bruus, and P. Ohlsson, *Particle focusing in polymer-based acoustofluidic devices: An experimental and numerical study*, Acoustofluidics Conference, 26-27 August 2021, Virtual Conference, **Flash presentation**.

4. W. N. Bodé, F. Lickert, and H. Bruus, *The elastic, dielectric, and piezoelectric constants of PZT transducers for acoustofluidics determined by electrical impedance*

spectroscopy, Acoustofluidics Conference, 26-27 August 2021, Virtual Conference, **Flash presentation** by W. N. Bodé.

5. F. Lickert, M. Ohlin, H. Bruus, and P. Ohlsson, *Acoustic particle focusing in polymer microfluidic devices*, MicroTAS Conference, 10-14 October 2021, Palm Springs, CA, USA, **Poster presentation**.

6. K. Saeedabadi, F. Lickert, M. Ohlin, H. Bruus, G. Tosello, and M. Calaon, *Micro-injection moulding simulation and manufacturing of polymer chips for acoustic separation*, EUSPEN's 22nd International Conference & Exhibition, Geneva, CH, 30 May - 3 June 2022, **Poster presentation** by K. Saeedabadi.

7. F. Lickert, H. Bruus, and M. Rossi, *Constant voltage versus constant power in acoustofluidic applications*, Acoustofluidics Conference, 19-21 October 2022, Glasgow, UK, **Flash presentation**.

8. W. N. Bodé, F. Lickert, and H. Bruus, *Electrical impedance spectroscopy for acoustofluidic applications*, Acoustofluidics Conference, 19-21 October 2022, Glasgow, UK, **Oral presentation** by W. N. Bodé.

List of Figures

List of Tables

Chapter 1

Introduction

This chapter starts with a general introduction to the field of acoustofluidics before giving an overview of the start-of-the-art in polymer-based acoustofluidics. The structure of the thesis follows a feedback loop for the optimization of polymer devices based on the three papers published in the context of this work. Finally, an outline of the thesis is presented at the end of this introduction.

1.1 Introduction to acoustofluidics

Acoustofluidic devices utilize acoustic waves in order to manipulate small particles and fluids. Piezoelectric transducers are commonly used to generate the required acoustic waves with frequencies ranging from kHz [4] to GHz [5]. Depending on the fluid medium, this leads to acoustic waves with wavelengths of several micrometers to a few centimeters. For biomedical applications, channels with dimensions in the order of a few 100 µm are beneficial, where only small fluid sample volumes are required, and µm-sized particles can be easily processed. Microfluidic channels furthermore have the advantage that they can be co-integrated with various analysis steps on a single *lab-on-a-chip* platform. Such a platform is sometimes labeled a total analysis system (TAS). The combination of ultrasound acoustics with microfluidics allows shrinking the analysis systems' space requirements from meters to micrometers, turning the TAS into a micro total analysis system (µTAS).

The field of acoustofluidics already has generated a broad spectrum of applications such as mixing [6, 7], and purification [8] of fluids, as well as trapping [9, 10], and separation of particles [11–13] inside those fluids. One crucial example of particle separation is the separation of blood cells from blood plasma in whole blood. This step is a common requirement for many biomedical analysis tasks to study different biomarkers inside the blood plasma. In the conventional approach, blood plasma separation is done through blood centrifugation and requires a dedicated processing task. Alternative solutions to centrifugation are required when aiming to integrate the blood separation process into a µTAS. Acoustofluidic technologies are a promising candidate for developing point-of-care devices requiring blood plasma separation.

The two fundamental forces in the field of acoustofluidics are the acoustic radiation force and the drag force. The acoustic radiation force results from the transferred momentum of an acoustic wave scattering of a particle inside a fluid. The acoustic drag force stems from the time-averaged acoustic streaming velocity, which is caused by the viscous effects of the fluid. For larger particles of the size of red blood cells, ranging from 5 to 10 µm, the radiation force is typically the dominating force, and effects due to acoustic streaming only become important for much smaller particle radii.

Acoustofluidic systems are slowly but steadily maturing to a point where applications can enter the market [14]. The underlying theory has been developed to an extent where numerical simulations can aid the numerical optimization of devices [15, 16]. At the same time, there is rapid progress in the field of 3D printing for applications in microfluidics [17]. Digital Light Processing (DLP) 3D printers, with resolutions as low as 1 µm, open up possibilities for 3D-printed acoustofluidic devices. Techniques, such as (micro)-injection molding, promise a dramatic reduction in the fabrication cost compared to usual cleanroom processing techniques. Moreover, micro-milling machines are standard equipment found in many microfluidics laboratories that can be used for device fabrication.

The fascination with using polymers as the basis for microfluidics experiments is evident, as such polymer devices are easy to fabricate and low in cost. For point-of-care testing, cheap and, ideally, single-use devices are desirable because the risk of contamination is high when reusing acoustofluidic chips. In addition, the cost- and material effort required to perform appropriate sterilization of glass-based chips may otherwise make such testing non-viable in many environments. However, there are still some challenges to solve to make polymer chips a viable platform not only for microfluidics but also for acoustophoresis experiments.

1.2 State-of-the-art in polymer-based acoustofluidics

Depending on the fabrication technique, using polymers for acoustofluidic application allows for great flexibility in the device design, short design-to-prototype times, and low fabrication costs. Microfluidic channels that are 3D-printed or injection-molded allow a higher design complexity compared to a typical device's conventional rectangular channel cross-section. Tubing connectors can be integrated into such a polymer design, and a wide range of polymer materials are available. There, however, are a few challenges when comparing polymer-based devices with glass chips: The acoustophoresis performance is typically lower in polymer chips due to the high acoustic attenuation of polymers and low acoustic contrast between fluid and channel walls. Furthermore, many polymers are incompatible with chemicals such as ethanol, acetone, or isopropanol. Nevertheless, a few polymers have a promising outlook within the field of acoustofluidics, such as cyclic olefin copolymer (COC), showing good resistance to many of the abovementioned chemicals and with comparatively low acoustic attenuation.

In the following subsections, a look at the existing literature on polymer-based acoustofluidic devices is taken, and the different approaches to designing effective devices are compared. Several techniques for manufacturing polymer devices exist, the most prominent ones being micro-milling, 3D printing, and injection molding. While an extensive range of devices is manufactured from plastic using micro-milling or 3D printing, there is still only a small number of papers that present all-polymer devices for acoustofluidic applications. In many cases in the literature, only a tiny fraction of the acoustofluidic system consists of a polymer, or the polymer acts as the frame holding stiffer materials in place.

1.2.1 Micro-milled devices

The group of Jason Fiering at the Draper labs started to explore acoustic manipulation in thermoplastic microchannels in a paper published by Mueller *et al.* in 2013 [18]. In the years from 2017 to 2019, further articles followed, exploring the use of micromachining for acoustofluidic polymer-based devices [11, 19–21]. The presented devices consist of polystyrene (PS), selected due to a comparably low acoustic attenuation and higher acoustic impedance than many other polymers. Flow rates from 40 µL/min to 110 µL/min at a power dissipation of 1 W were reported for the single-channel devices. A multi-channel device was presented by Dubay *et al.* [21], achieving flow rates of up to 1 mL/min, albeit at a much higher power dissipation of the system with up to 18 W. The design process used by the Fiering group followed a 1D approach, taking the longitudinal speed of sound of the solid and the fluid into account. In an experimental parametric study, the best devices were identified. The authors, however, note that a better understanding of the mechanism is required, and the found resonance frequencies were quite off from the expected values used in the simplified 1D approach [18].

1.2.2 3D-printed devices

While 3D printing typically aids the design of acoustofluidic systems by either enabling the quick production of molds for PDMS devices or acting as the sample holder, there is only a limited range of fully 3D-printed, all-polymer devices used for acoustophoresis. In work by Santos *et al.* [22], a 3D-printed cylindrical device forms the side walls of a fluid channel, while the top and bottom of the channel consist of a piezoelectric transducer and a thin glass slide. This cylindrical device successfully demonstrated the trapping of polystyrene particles at voltages as low as $V_{\mathrm{pp}} = 4$ V. Cesewski *et al.* [23] present an acoustofluidic device with a fluid channel made from printed PDMS. Their approach utilizes the multi-material printing of conductive silver electrodes, epoxy, and PDMS to fabricate devices capable of acoustic particle manipulation in droplets and microchannels.

1.2.3 Multi-layer devices

Approaches, such as multi-layer devices, as presented by [12], consist of several polymer sheets that are either laminated or glued together. This technique requires only relatively low-cost equipment and is, therefore, a desirable candidate for polymer-devices fabrication. Gu *et al.* present acoustic separation at a sample throughput of 20 mL/min with

an efficiency of 89% in removing blood cells. The voltage used during that study was $V_{\mathrm{pp}} = 45$ V, however, at an unspecified power dissipation. A drawback of the foil-based approach is typically the limitation in terms of the available thicknesses of the foils. Other examples of lab-on-foil systems include an acoustofluidic micromixer and an acoustofluidic micropump presented by Lin *et al.* [24, 25].

1.2.4 Injection-molded devices

The benefits of using the process of injection molding compared to the fabrication techniques mentioned earlier are given in terms of very low sample-to-sample variability and low costs in the case of high-batch fabrication. After the high initial cost required for mold manufacturing, many samples can be produced quickly. Injection molding is, therefore, the method of choice when industrializing the acoustofluidic chips. However, the drawbacks are lower flexibility when producing different designs, as each requires a new master mold. While injection molding enables fast and low-cost production, it does not necessarily classify as a rapid-prototyping technology due to the associated time-consuming mold development. To the author's knowledge, no injection-molded acoustofluidic devices have been reported in the literature so far.

1.3 Towards improved performance of polymer devices

In order to make polymer-based devices a viable alternative to glass and silicon devices in acoustophoresis applications, a flow rate in the order of 1 L/h $\approx$ 17 mL/min is desirable. In addition, biomedical cell-separation applications, such as blood plasma separation, require short sample processing times to be a viable alternative to, e.g., centrifugation. A solid understanding of the driving mechanisms for acoustophoresis is fundamental to improving the performance of existing devices.

Moiseyenko and Bruus explored the driving mechanism of polymer-based acoustophoresis in 2019 [26] and labeled the corresponding mode *whole-system ultrasound resonances* (WSUR). Contrary to bulk acoustic wave (BAW) and surface acoustic wave (SAW) devices, the concept of WSUR extends the resonant mode of the device beyond the vibrational mode of the channel and the transducer and takes the vibrations of the polymer chip into account as well. While WSURs are not limited to exist in soft materials, such as polymers, new challenges exist in developing a functioning polymer-based acoustofluidic device. Perhaps the biggest challenge in obtaining a viable numerical prediction for the performance of such a polymer device is the lack of accurate material parameters. Our simulations require a good knowledge of the longitudinal and transverse speed of sound, attenuation, and density of the polymer used. Furthermore, resonances in polymer devices are not simply governed by the channel dimensions and the properties of the fluid. Therefore, the resonant modes of the polymer chip and the piezoelectric transducer also need to be considered.

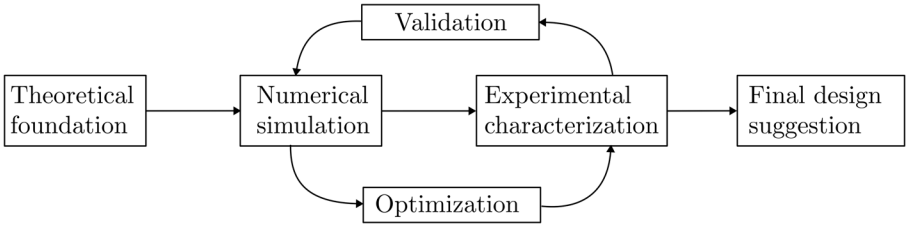

Figure 1.1: An overview of the feedback loop for the design of acoustophoresis devices is shown. After introducing the fundamental theory of acoustofluidics, numerical simulations are performed, and a device with the same parameters used in the simulation is experimentally characterized. The experimental data can then be used to validate the numerical model. The validated model allows performing device optimization to obtain the final geometry of an optimized design.

1.4 Scope of this thesis

The work has been performed as part of the Eureka Eurostars-2 joint program *AcouPlast*, a collaboration between the DTU departments DTU Physics and DTU Construct, Lund University, and the companies AcouSort AB and Ortofon A/S. Members of the AcouPlast project include Pelle Ohlsson (Senior Project Manager at AcouSort and Project Coordinator of the AcouPlast project), Mathias Ohlin (Technology Manager at AcouSort), Per Augustsson (Associate Professor at Lund University), Henrik Bruus (Professor at DTU Physics), Guido Tosello (Associate Professor at DTU Construct), Matteo Calaon (Senior researcher at DTU Construct), Komeil Saeedabadi (Ph.D. student at DTU Construct), and Bo Christian Nielsen (Project Manager at Ortofon).

The goal of the *AcouPlast* project is to accelerate the development of polymer acoustofluidics chips for blood plasma separation to enable point-of-care diagnostics. This collaboration between experts on the theoretical, numerical, and experimental background of acoustofluidics and experts on the fabrication of polymer devices has opened up the unique opportunity to perform a complete feedback loop from polymer device design, validation, and optimization to experimental characterization.

The scope of this thesis has been to establish and complete such a feedback loop leading to an improved polymer chip design. A schematic of such a feedback loop is shown in Fig. 1.1. After introducing the ground-laying theoretical concepts, a numerical model is implemented to simulate the device's performance. Afterward, the simulated device is characterized experimentally, and the numerical results are compared to the measurement results. Finally, the numerical model is refined based on the experimental findings and aids in optimizing an improved final polymer-chip design. The structure of this thesis follows this feedback loop, where each chapter relates to one step in the procedure.

In this context it has been crucial to identify and to overcome some of the challenges related to the validation of the numerical model and the optimization of polymer-based acoustofluidics. The key challenges and the contributions of this work on how to overcome

those challenges are summarized below:

(1) **Ensuring the validity of the numerical model** (Paper I [1])
The comparison of numerical and experimental results of a polymer-based acoustofluidic device acts as the baseline for further device development and improvement of a polymer chip for particle separation. The work of Paper I [1] allowed the validation of the WSUR model [26] and to identify the driving mechanism of acoustophoresis in polymer devices. In addition, the quantitative comparison between the experimental and numerical device performance helped to identify the lack of accurate and precise material parameters for polymer chips as a bottleneck of the numerical simulation.

(2) **Obtaining accurate material parameters of polymers** (Paper II [2])
In order to obtain an accurate and complete set of material properties of polymers that can be used in the numerical simulation, a new measurement technique has been co-developed with my colleague William Naundrup Bodé by extending concepts introduced in Refs. [27–31]. This approach is based on a measurement of the electrical impedance spectrum of a polymer-loaded piezoelectric transducer. The technique allows obtaining the material properties of the piezoelectric transducer, coupling layer, and polymer chip by fitting a numerically obtained impedance spectrum to the measured spectrum. The technique was named ultrasound electrical impedance spectroscopy (UEIS) and has been used to characterize several materials used throughout this thesis.

(3) **Establishing a standard for the electrical excitation method** (Paper III [3])
The lack of standardization in the field of acoustofluidics has been identified as one of the significant challenges when comparing device performance by Rufo *et al.* [14]. The electrical excitation voltage and power are crucial when comparing device performance over a wider frequency range, and monitoring those quantities during a frequency sweep is essential. The lack of standardization led to a study comparing constant-voltage and constant-power excitation, with the conclusion that keeping the power dissipation in the transducer at a constant level might be the beneficial approach in experimental studies, as well as in numerical optimization.

1.5 Structure of the thesis

This thesis is based on the results, which are presented in Paper I [1], Paper II [2], and Paper III [3]. In order to give sufficient context for the understanding of the three papers, a theory chapter summarizes the underlying theory, which has been used to implement the numerical model. Additionally, a chapter highlighting some of the experimental considerations and observations is included, before in Chapter 5, Chapter 6, and Chapter 7 the core results of this thesis are presented and put into context with the whole body of this work. Each of the scientific papers is included in the corresponding chapter. A summary of the main findings of the papers is given in the respective chapters. However, the reader of this thesis is nevertheless encouraged to read the included papers, as the

summary only restates the core findings. Finally, in Chapter 8, before concluding the thesis, the results and lessons learned from the three presented papers are connected by performing numerical optimization of a polymer-based acoustofluidic device. Below is an overview of the contents of all chapters of the thesis.

Chapter 1: Introduction — An introduction to acoustofluidics and the state-of-the-art in polymer-based acoustofluidics is given. The scope and the structure of the thesis are outlined.

Chapter 2: Theoretical foundation — A brief recapitulation of the underlying theory governing acoustofluidics, solid mechanics, and the piezoelectric coupling of mechanical and electrical fields are presented.

Chapter 3: Simulation of acoustofluidic systems — The numerical model, its implementation using the software *COMSOL Multiphysics*, and the necessary boundary conditions are detailed. The chapter concludes with an overview of different validation methods of the numerical simulations.

Chapter 4: Experimental aspects of acoustofluidic systems — A typical setup to characterize the performance of an acoustofluidic device is described in this chapter. In that scope, a few experimental considerations regarding some electrical characteristics are investigated: transducer properties, impedance matching, and split-electrode designs will be compared. Different device types, such as trapping compared to focusing chips and devices obtained following 1D-design rules, are presented.

Chapter 5: Validation study of a polymer-based acoustofluidic device — The thoughts and motivation behind Paper I [1] on the experimental and numerical validation of a polymer-based acoustofluidic chip are discussed. The concept of transverse resonances in polymer chips is explored in this context.

Chapter 6: Ultrasound electrical impedance spectroscopy — The results of Paper II [2] on the measurements of mechanical material parameters are discussed in this chapter. This paper was written in collaboration with my colleague William Naundrup Bodé with shared first-authorship and was the logical consequence of the findings in Paper I [1]. Previously the availability of material parameters and characterization methods for our numerical predictions was deemed insufficient. However, the development of an improved method, titled ultrasound electrical impedance spectroscopy (UEIS), allowed the characterization of several polymers used in a later optimization study. The UEIS technique is explained in this chapter.

Chapter 7: Constant-power versus constant-voltage excitation — The details of the study comparing different electrical excitation methods for acoustofluidic devices, constituting Paper III [3], are given. Acoustophoretic particle focusing is compared in the three cases of constant transducer voltage, constant transducer power dissipation, and

constant input voltage to the amplifier. The chapter furthermore explains the excitation method's relevance for optimizing polymer devices.

Chapter 8: Numerical optimization of polymer-based devices — In this chapter, the lessons learned from Paper I [1], Paper II [2], and Paper III [3] are combined and applied in order to obtain an improved polymer device for acoustophoresis applications. A numerical routine is presented, and the resulting dimensions and performance metrics are listed and compared to a reference geometry. This chapter contains unpublished numerical results and – given the time constraints of the Ph.D. project – still needs experimental validation. The project partners are currently fabricating the suggested device design.

Chapter 9: Conclusion and outlook — The thesis concludes with a summary and outlook on the future perspective of polymer-based acoustofluidic devices.

Chapter 2

Theoretical foundation

In this chapter, the theoretical framework will be introduced, which is necessary for the understanding of the following chapters. We typically study microfluidic channels embedded in a microfluidic chip driven by a bulk-acoustic piezoelectric transducer. The theoretical building blocks necessary to model such a system consist of

- Fluid dynamics, describing the propagation of pressure- and velocity-fields inside a microfluidic channel,
- Solid mechanics, describing the deformation of all solid materials, such as the microfluidic chip, but also the coupling layer and the mechanical deformation of the transducer,
- Piezoelectric coupling, describing how the stress and strain inside piezoelectric materials are coupled to the electric displacement field.

We will start introducing the theory relevant to acoustofluidics in the fluid domain. Then, the other system domains, namely the solid-mechanic and piezoelectric domains, will be introduced in the following sections. Finally, the chapter concludes with an overview of the necessary boundary conditions used throughout this work, and equations for the power dissipation in the different domains of the system are given.

In this chapter, we follow the theory presented in the previous work of Refs. [1, 3, 32–34] and describe the effective-boundary-layer theory derived by Bach and Bruus [35]. Thermal effects are neglected throughout this work, as the devices are kept at a constant temperature using a Peltier-element feedback loop, or the piezoelectric transducer is excited at sufficiently low powers where heating is assumed to be negligible. Therefore, all processes are assumed to be isentropic. The reader shall be referred to recent work by Karlsen *et al.* and Jørgensen *et al.* [36–39] if the impact of thermal effects is of interest.

2.1 Acoustics in fluids

We consider a compressible fluid with a local mass density $\tilde{\rho}(\boldsymbol{r}, t)$ and velocity $\tilde{\boldsymbol{v}}(\boldsymbol{r}, t)$. The tilde symbol is used to distinguish time-dependent fields $\tilde{A}(\boldsymbol{r}, t)$ from time-independent

fields $A(\boldsymbol{r})$. Explicit reference to the position and time dependence of the fields will be omitted henceforth to avoid cumbersome notation. From the fundamental conservation laws, we know that the mass $M(\Omega,t)=\int_\Omega \tilde{\rho}\,\mathrm{d}\boldsymbol{r}$ and momentum $P(\Omega,t)=\int_\Omega \tilde{\rho}\tilde{\boldsymbol{v}}\,\mathrm{d}\boldsymbol{r}$ inside an arbitrarily shaped, but fixed region Ω are conserved. These conditions lead to the continuity equation and the Navier–Stokes equation,

$$\partial_t\tilde{\rho} = -\boldsymbol{\nabla}\cdot(\tilde{\rho}\tilde{\boldsymbol{v}}), \tag{2.1}$$

$$\partial_t(\tilde{\rho}\tilde{\boldsymbol{v}}) = \boldsymbol{\nabla}\cdot\tilde{\boldsymbol{\sigma}} - \boldsymbol{\nabla}\cdot(\tilde{\rho}\tilde{\boldsymbol{v}}\tilde{\boldsymbol{v}}) + \tilde{\boldsymbol{f}}, \tag{2.2}$$

where $\tilde{\boldsymbol{\sigma}}$ is the viscous stress tensor, and the term $\boldsymbol{\nabla}\cdot\tilde{\boldsymbol{\sigma}}$ expresses forces due to pressure $\tilde{p}$, dynamic shear viscosity η_0, and bulk viscosity η_0^{b}. The second term on the right-hand side of Eq. (2.2) describes changes in the momentum due to a momentum flux. The last term $\tilde{\boldsymbol{f}}$ represents external forces, such as gravity, acting throughout the entire volume of the fluid, which will be neglected in the following analysis. The viscous stress tensor $\tilde{\boldsymbol{\sigma}}$ in the Navier–Stokes equation is given as,

$$\tilde{\boldsymbol{\sigma}} = -\tilde{p}\mathbf{I} + \eta_0\left[\boldsymbol{\nabla}\tilde{\boldsymbol{v}} + (\boldsymbol{\nabla}\tilde{\boldsymbol{v}})^{\intercal} - \frac{2}{3}(\boldsymbol{\nabla}\cdot\tilde{\boldsymbol{v}})\mathbf{I}\right] + \eta_0^{\mathrm{b}}(\boldsymbol{\nabla}\cdot\tilde{\boldsymbol{v}})\mathbf{I}, \tag{2.3}$$

with the superscript $^{\intercal}$ representing the transposed matrix and the symbol $\mathbf{I}$ denoting the unit tensor.

2.1.1 First-order pressure acoustics

In the field of acoustofluidics, it is common to describe acoustic fields $\tilde{A}_1(\boldsymbol{r},t)$, as small perturbations to a stationary ground state $A_0(\boldsymbol{r})$, such that the total field is

$$\tilde{A}(\boldsymbol{r},t) = A_0(\boldsymbol{r}) + \tilde{A}_1(\boldsymbol{r},t). \tag{2.4}$$

The following analysis assumes that the first-order fields $\tilde{A}_1(\boldsymbol{r},t)$ are time-harmonic with angular frequency ω due to a periodic actuation of the piezoelectric transducer. Their contribution to the total field can therefore be written as $\tilde{A}_1(\boldsymbol{r},t) = \mathrm{Re}\left[A_1(\boldsymbol{r})\,\mathrm{e}^{-\mathrm{i}\omega t}\right]$. Applying this formalism to the density-, pressure-, and velocity field, we obtain

$$\tilde{\rho}(\boldsymbol{r},t) = \rho_0 + \mathrm{Re}\left[\rho_1(\boldsymbol{r})\,\mathrm{e}^{-\mathrm{i}\omega t}\right], \tag{2.5a}$$

$$\tilde{p}(\boldsymbol{r},t) = p_0 + \mathrm{Re}\left[p_1(\boldsymbol{r})\,\mathrm{e}^{-\mathrm{i}\omega t}\right], \tag{2.5b}$$

$$\tilde{\boldsymbol{v}}(\boldsymbol{r},t) = \mathbf{0} + \mathrm{Re}\left[\boldsymbol{v}_1(\boldsymbol{r})\,\mathrm{e}^{-\mathrm{i}\omega t}\right], \tag{2.5c}$$

where the fluid is to be assumed at rest in the ground state and therefore $\boldsymbol{v}_0=\mathbf{0}$. Using this perturbation approach, and utilizing the relation $p_1 = c_0^2\rho_1$ for the isentropic speed of sound c_0, and the definition of the isentropic compressibility $\kappa_0^{-1} = \rho_0 c_0^2$, the first-order expressions of the continuity equation (2.1), and Navier–Stokes equation (2.2), can be obtained. Together with the assumption of time-harmonic first-order fields, allowing us to evaluate the time derivative as $\partial_t = -\mathrm{i}\omega$, and factoring out $\mathrm{e}^{-\mathrm{i}\omega t}$, this yields

$$-\mathrm{i}\omega\kappa_0 p_1 = -\boldsymbol{\nabla}\cdot\boldsymbol{v}_1, \tag{2.6a}$$

$$-\mathrm{i}\omega\rho_0\boldsymbol{v}_1 = \boldsymbol{\nabla}\cdot\boldsymbol{\sigma}_{1,\mathrm{fl}} = -\boldsymbol{\nabla}[p_1 - \beta\eta_0\boldsymbol{\nabla}\cdot\boldsymbol{v}_1] + \eta_0\nabla^2\boldsymbol{v}_1, \tag{2.6b}$$

$$\boldsymbol{\sigma}_{1,\mathrm{fl}} = -p_1\mathbf{I} + \eta_0(\beta-1)(\boldsymbol{\nabla}\cdot\boldsymbol{v}_1)\mathbf{I} + \eta_0\left[\boldsymbol{\nabla}\boldsymbol{v}_1 + (\boldsymbol{\nabla}\boldsymbol{v}_1)^{\intercal}\right], \tag{2.6c}$$

where the dimensionless viscosity ratio $\beta = \frac{\eta_0^{\mathrm{b}}}{\eta_0} + \frac{1}{3}$ has been introduced. These equations constitute what will be referred to as the *full theory*, and rewriting them to the *weak-form* allows the implementation in COMSOL, as will be described in Chapter 3.

2.1.2 Viscous boundary layer

Typically a fluid inside a microchannel will be subject to a no-slip boundary condition at the channel wall, forcing the first-order fluid velocity $\boldsymbol{v}_1$ to match the velocity of the wall. In a viscous fluid with kinematic viscosity $\nu_0 = \frac{\eta_0}{\rho_0}$ this leads to the formation of a boundary layer of thickness $\delta = \sqrt{\frac{2\nu_0}{\omega}}$. Depending on the fluid, the thickness of this layer ranges from several micrometers down to 500 nm in water at a frequency of 1 MHz. Numerical simulations of such thin boundary layers require a very fine mesh, leading to high computation times. An effective boundary layer theory can be utilized to reduce the computational demands, as developed by Bach *et al.* [35, 40]. This theory will be briefly described in the following section.

2.1.3 Helmholtz equation

Eq. (2.6) can be used to derive the Helmholtz equation for the pressure field p_1 for the implementation of an effective boundary layer as presented thoroughly in work by Bach and Bruus [35, 40]. A Helmholtz decomposition allows separating the velocity field $\boldsymbol{v}_1$ into a bulk part $\boldsymbol{v}_1^d$ and a boundary-layer part $\boldsymbol{v}_1^\delta$ that only enters the problem through an effective boundary condition on p_1. The damped Helmholtz equation for the first-order pressure field p_1 is then given as

$$\nabla^2 p_1 = -k_{\mathrm{c}}^2 p_1 = -k_0^2 \left(1 + \mathrm{i}\frac{\Gamma_0}{2}\right)^2 p_1, \quad \text{with} \quad \Gamma_0 = (\beta+1)\eta_0\omega\kappa_0, \tag{2.7}$$

where k_{c} is the compressional wavenumber, $k_0 = \frac{\omega}{c_0}$, and Γ_0 is the damping coefficient. The bulk velocity $\boldsymbol{v}_1^d$ can be expressed as a gradient of the pressure p_1, which yields

$$\boldsymbol{v}_1^d = -\mathrm{i}\,\frac{1 - \mathrm{i}\Gamma_0}{\omega\rho_0}\,\boldsymbol{\nabla} p_1. \tag{2.8}$$

The beauty of splitting up the velocity fields into a long-range bulk-velocity field $\boldsymbol{v}_1^d$ and a short-range boundary-layer velocity $\boldsymbol{v}_1^\delta$ is that it allows one to absorb the effects of the boundary layer fields into an effective boundary condition for the pressure field p_1. The boundary layer velocity $\boldsymbol{v}_1^\delta$, which is confined to the thin boundary layer, therefore does not need to be computed numerically. However, the analysis by Bach and Bruus is limited to weekly curved and thin boundary layers with $k_0\delta \ll 1$, where $\boldsymbol{v}_1^\delta$ can be determined analytically. The boundary condition for p_1 is described in Section 2.4.1.

2.1.4 Acoustic energy density, radiation force and drag force

Acoustic energy density

The acoustic energy density of an acoustic field is a standard measure of the acoustophoresis performance of a given device. It is composed of the kinetic energy density E_{kin} and the potential energy density E_{pot}. By calculating the time-average $\langle q \rangle = \frac{1}{T}\int_0^T q(t)\,\mathrm{d}t$ over one oscillation period T of the sum of the kinetic and the potential energy density, we obtain an expression for the time-averaged acoustic energy density

$$E_{\text{ac}} = \frac{1}{4}\rho_0 \left|\boldsymbol{v}_1\right|^2 + \frac{1}{4}\kappa_0 \left|p_1\right|^2. \tag{2.9}$$

Frequencies f_{res}, which yield a particularly high acoustic energy density, are called resonance frequencies. Such resonances in the acoustic energy density E_{ac} can be described by a Lorentzian of the form

$$E_{\text{ac}}(f) = \frac{(\frac{1}{2}\Gamma_0)^2 E_0}{(\frac{f}{f_{\text{res}}} - 1)^2 + (\frac{1}{2}\Gamma_0)^2}, \tag{2.10}$$

where E_0 is the maximum acoustic energy density at resonance. The quality factor $Q = 1/\Gamma_0$ is a measure of the damping of the system and is typically formally defined by the ratio of the energy stored in the system and the energy dissipated per oscillation cycle $1/f$.

Acoustic radiation force

The acoustic radiation force results from the scattering of acoustic waves on particles suspended in a fluid and is the primary mechanism of acoustophoresis. Settnes *et al.* [41] derived a general expression for the acoustic radiation force for particles of radius a inside a viscous fluid, neglecting thermal effects and the influence of micro-streaming,

$$\boldsymbol{F}^{\text{rad}} = -\pi a^3 \left[\frac{2\kappa_0}{3}\,\mathrm{Re}\left[f_0^* p_1 \nabla p_1\right] - \rho_0\,\mathrm{Re}\left[f_1^* \boldsymbol{v}_1^* \cdot \nabla \boldsymbol{v}_1\right]\right]. \tag{2.11}$$

For particles that are small compared to the acoustic wavelength λ, but much larger than the viscous boundary layer ($\delta \ll a \ll \lambda$), the scattering coefficients are given as derived by Gorkov in 1962 [42],

$$f_0 = 1 - \frac{\kappa_{\text{p}}}{\kappa_0}, \tag{2.12a}$$

$$f_1 = \frac{\rho_{\text{p}} - \rho_0}{\rho_{\text{p}} + \frac{1}{2}\rho_0}. \tag{2.12b}$$

Here κ_{p} and ρ_{p} describe the particles' compressibility and density, respectively. If the pressure field p_1 resembles a standing wave, then the acoustic radiation force can be

expressed by the gradient of the so-called Gorkov potential U^{rad} as,

$$\boldsymbol{F}^{\mathrm{rad}} = -\boldsymbol{\nabla} U^{\mathrm{rad}}, \tag{2.13a}$$

$$U^{\mathrm{rad}} = \frac{4\pi}{3} a^3 \left(f_0 \, \frac{1}{4} \kappa_0 |p_1|^2 - f_1 \, \frac{3}{8} \rho_0 |\boldsymbol{v}_1|^2 \right). \tag{2.13b}$$

Acoustic drag force

The acoustic drag force, resulting from the frictional Stokes' drag on a particle moving in a viscous liquid, is given by the expression

$$\boldsymbol{F}^{\mathrm{drag}} = 6\pi\eta_0 a(\boldsymbol{v}_2 - \boldsymbol{v}_{\mathrm{p}}), \tag{2.14}$$

where $\boldsymbol{v}_2$ is the acoustic streaming velocity and $\boldsymbol{v}_{\mathrm{p}}$ is the velocity of the particle. We can see from Eq. (2.13) that the acoustic radiation force scales with the particle radius cubed (a^3), while the drag force generated by acoustic streaming phenomena only scales linearly with a. For particles with $a \gg 1$ µm, typically, the radiation force is the dominating force, and the drag force due to $\boldsymbol{v}_2$ can be neglected for the fluids and channel cross-sections studied within this work. As we work with particles of the size of red blood cells with $a \approx 5$ µm, we neglect the streaming-generated acoustic drag force throughout this thesis.

2.1.5 Acoustophoresis of microparticles

A particle inside an acoustically-excited fluid is subject to several forces, leading to the force balance

$$\boldsymbol{F} = \boldsymbol{F}^{\mathrm{rad}} + \boldsymbol{F}^{\mathrm{drag}} + \boldsymbol{F}^{\mathrm{buoy}} + \boldsymbol{F}^{\mathrm{grav}}, \tag{2.15}$$

where the buoyancy of the particle is described by $\boldsymbol{F}^{\mathrm{buoy}} = -\frac{4}{3}\pi a^3 \boldsymbol{g}\rho_0$ and forces due to gravity acting on the particle are given by $\boldsymbol{F}^{\mathrm{grav}} = \frac{4}{3}\pi a^3 \boldsymbol{g}\rho_{\mathrm{p}}$. Neglecting acoustic streaming, $\boldsymbol{v}_2 \approx 0$, we obtain the following expression for the acceleration of a particle with mass m_{p} and volume V_{p}

$$\left(m_{\mathrm{p}} + \frac{1}{2}\rho_0 V_{\mathrm{p}} \right) \frac{\partial \boldsymbol{v}_{\mathrm{p}}}{\partial t} + 6\pi\eta_0 a \boldsymbol{v}_{\mathrm{p}} = \boldsymbol{F}^{\mathrm{rad}} + V_{\mathrm{p}} \boldsymbol{g}(\rho_{\mathrm{p}} - \rho_0). \tag{2.16}$$

The term $\frac{1}{2}\rho_0 V_{\mathrm{p}}$ on the left-hand side of Eq. (2.16) is the virtual mass, which describes the effect of inertia added to the system resulting from the required displacement of fluid around a moving particle [43]. Under the assumption of negligible inertia ($\frac{\partial \boldsymbol{v}_{\mathrm{p}}}{\partial t} \approx 0$) and through the use of a density-matched fluid with $\rho_{\mathrm{p}} - \rho_0 \approx 0$ this expression simplifies furthermore and we can directly obtain the particle velocity through the radiation force by,

$$\boldsymbol{v}_{\mathrm{p}} = \frac{\boldsymbol{F}^{\mathrm{rad}}}{6\pi\eta_0 a}. \tag{2.17}$$

In a 1D-approximation the focusing time for a particle of radius a, placed in a standing half-wave with $k = \frac{2\pi}{\lambda} = \frac{\pi}{w_{\mathrm{ch}}}$ and moving from $\frac{w_{\mathrm{ch}}}{8}$ to $\frac{3}{8}\frac{w_{\mathrm{ch}}}{8}$ is given as [44]

$$t_{\mathrm{foc}} \approx \frac{3}{2\Phi} \frac{{w_{\mathrm{ch}}}^2}{\pi^2 a^2} \frac{\eta_0}{E_{\mathrm{ac}}}. \tag{2.18}$$

2.1.6 Acoustic impedance

The acoustic impedance describes the resistance of an acoustic medium towards sound propagation. The characteristic acoustic impedance Z_m is defined by the speed of sound c_m and the density ρ_m of the medium m as

$$Z_\mathrm{m} = \rho_\mathrm{m} c_\mathrm{m}. \tag{2.19}$$

2.2 Acoustics in linear elastic media

An equation for the displacement $\boldsymbol{u}$ of solids with density ρ_sl, subject to a stress $\boldsymbol{\sigma}_\mathrm{sl}$, can be derived in analogy to the Navier-Stokes equation, Eq. (2.2), from the conservation of momentum. Assuming low strain $\boldsymbol{s} = \frac{1}{2}\left[(\boldsymbol{\nabla u} + (\boldsymbol{\nabla u})^\mathsf{T})\right]$ in the solid, and time-harmonic behavior, this results in Cauchy's momentum equation,

$$-\omega^2 \rho_\mathrm{sl}\, \boldsymbol{u} = \boldsymbol{\nabla} \cdot \boldsymbol{\sigma}_\mathrm{sl}. \tag{2.20}$$

In order to relate the stress tensor $\boldsymbol{\sigma}_\mathrm{sl}$ to the displacement $\boldsymbol{u}$, we can use the following stress-strain relation, which relates the stress tensor $\boldsymbol{\sigma}_\mathrm{sl}$ linearly to the mechanical strain tensor $\boldsymbol{s}$ via the stiffness tensor $\boldsymbol{C}$,

$$\boldsymbol{\sigma}_\mathrm{sl} = \boldsymbol{C} : \boldsymbol{s}. \tag{2.21}$$

In this formulation, $\boldsymbol{\sigma}_\mathrm{sl}$ and $\boldsymbol{s}$ are second-order tensors with nine components each, and $\boldsymbol{C}$ is a fourth-order tensor with 81 components. Utilizing the symmetry of the stress and strain tensor allows the use of the Voigt notation to write both $\boldsymbol{\sigma}_\mathrm{sl}$ and $\boldsymbol{s}$ as a 1×6 vector, and $\boldsymbol{C}$ as a 6×6 matrix. For isotropic materials, $\boldsymbol{C}$ is a sparse matrix with only three different components C_{11}, C_{12}, and C_{44}. The stress-strain relation in Voigt notation for isotropic solids is

$$\begin{pmatrix} \sigma_{xx} \\ \sigma_{yy} \\ \sigma_{zz} \\ \hline \sigma_{yz} \\ \sigma_{xz} \\ \sigma_{xy} \end{pmatrix} = \left(\begin{array}{ccc|ccc} C_{11} & C_{12} & C_{12} & 0 & 0 & 0 \\ C_{12} & C_{11} & C_{12} & 0 & 0 & 0 \\ C_{12} & C_{12} & C_{11} & 0 & 0 & 0 \\ \hline 0 & 0 & 0 & C_{44} & 0 & 0 \\ 0 & 0 & 0 & 0 & C_{44} & 0 \\ 0 & 0 & 0 & 0 & 0 & C_{44} \end{array}\right) \begin{pmatrix} \partial_x u_x \\ \partial_y u_y \\ \partial_z u_z \\ \hline \partial_y u_z + \partial_z u_y \\ \partial_x u_z + \partial_z u_x \\ \partial_x u_y + \partial_y u_x \end{pmatrix}. \tag{2.22}$$

The components of the stiffness tensor $\boldsymbol{C}$ are complex-valued with $C_{ik} = C'_{ik} + \mathrm{i}C''_{ik}$ to express the attenuation of the acoustic motion in solids through the imaginary parts C''_{ik}. For isotropic solids, the relationship $C_{12} = C_{11} - 2C_{44}$ holds, which leaves the two unknown coefficients C_{11} and C_{44}.

2.2.1 Relationship between the elastic moduli

The real parts C'_{11} and C'_{44} of the stiffness tensor components can be related to a range of other quantities commonly used to describe the properties of an elastic solid. The relations

for the Young's modulus E, the Poisson's ratio ν, the longitudinal speed of sound c_{lo}, and the transverse speed of sound c_{tr} are given by the expressions

$$C'_{11} = \rho_{\mathrm{sl}} c_{\mathrm{lo}}^2 = \frac{E(1-\nu)}{(1+\nu)(1-2\nu)}, \tag{2.23a}$$

$$C'_{44} = \rho_{\mathrm{sl}} c_{\mathrm{tr}}^2 = \frac{E}{2(1+\nu)}. \tag{2.23b}$$

We can also compute the Young's modulus E, and the Poisson's ratio ν from the coefficients C'_{11} and C'_{44} by

$$E = \frac{C'_{44}(3C'_{11} - 4C_{44'})}{C'_{11} - C'_{44}}, \tag{2.24a}$$

$$\nu = \frac{C'_{11} - 2C'_{44}}{2C'_{11} - 2C'_{44}}. \tag{2.24b}$$

2.2.2 Solid energy density

The time-averaged acoustic energy density in the solids is given by the sum of the kinetic and elastic energy densities,

$$E_{\mathrm{sl}} = \frac{1}{4}\rho_{\mathrm{sl}}\omega^2|\boldsymbol{u}|^2 + \frac{1}{4}\,\mathrm{Re}\left[(\boldsymbol{\nabla u} + (\boldsymbol{\nabla u})^{\intercal}) : \boldsymbol{\sigma}_{\mathrm{sl}}\right]. \tag{2.25}$$

2.3 Acoustics in piezoelectric ceramics

Gauss' law governs the electric potential φ inside a piezoelectric solid for a linear, homogeneous dielectric without free surface charges

$$\boldsymbol{\nabla} \cdot \boldsymbol{D} = 0, \tag{2.26}$$

where $\boldsymbol{D}$ is the electric displacement field. Cauchy's momentum equation (2.20) also holds for piezoelectric materials, but here the stress tensor $\boldsymbol{\sigma}_{\mathrm{pzt}}$ depends on the strain $\boldsymbol{s}$ and the electric field $\boldsymbol{E} = -\boldsymbol{\nabla}\varphi$. Likewise, the electric displacement field $\boldsymbol{D}$ depends on both $\boldsymbol{s}$ and $\boldsymbol{E}$. Those relations can be expressed by the equations

$$\boldsymbol{\sigma}_{\mathrm{pzt}} = \boldsymbol{C} : \boldsymbol{s} - \boldsymbol{e}^T \cdot \boldsymbol{E}, \tag{2.27a}$$

$$\boldsymbol{D} = \boldsymbol{e} : \boldsymbol{s} + \boldsymbol{\varepsilon} \cdot \boldsymbol{E}, \tag{2.27b}$$

where $\boldsymbol{e}$ is the piezoelectric coupling tensor, and $\boldsymbol{\varepsilon}$ is the permittivity tensor. The above expressions can be written in matrix form using the Voigt notation for a piezoelectric

material in the ∞mm-symmetry class as [45],

$$\left(\begin{array}{c} \sigma_{xx} \\ \sigma_{yy} \\ \sigma_{zz} \\ \hline \sigma_{yz} \\ \sigma_{xz} \\ \sigma_{xy} \\ \hline D_x \\ D_y \\ D_z \end{array}\right) = \left(\begin{array}{ccc|ccc|ccc} C_{11} & C_{12} & C_{13} & 0 & 0 & 0 & 0 & 0 & -e_{31} \\ C_{12} & C_{11} & C_{13} & 0 & 0 & 0 & 0 & 0 & -e_{31} \\ C_{13} & C_{13} & C_{33} & 0 & 0 & 0 & 0 & 0 & -e_{33} \\ \hline 0 & 0 & 0 & C_{44} & 0 & 0 & 0 & -e_{15} & 0 \\ 0 & 0 & 0 & 0 & C_{44} & 0 & -e_{15} & 0 & 0 \\ 0 & 0 & 0 & 0 & 0 & C_{66} & 0 & 0 & 0 \\ \hline 0 & 0 & 0 & 0 & e_{15} & 0 & \varepsilon_{11} & 0 & 0 \\ 0 & 0 & 0 & e_{15} & 0 & 0 & 0 & \varepsilon_{11} & 0 \\ e_{31} & e_{31} & e_{33} & 0 & 0 & 0 & 0 & 0 & \varepsilon_{33} \end{array}\right) \left(\begin{array}{c} \partial_x u_x \\ \partial_y u_y \\ \partial_z u_z \\ \hline \partial_y u_z + \partial_z u_y \\ \partial_x u_z + \partial_z u_x \\ \partial_x u_y + \partial_y u_x \\ \hline -\partial_x \varphi \\ -\partial_y \varphi \\ -\partial_z \varphi \end{array}\right). \tag{2.28}$$

In this symmetry class the relationship $C_{66} = \frac{1}{2}(C_{11} - C_{12})$ reduces the required number of material parameters to five complex-valued $C_{ik} = C'_{ik} + \mathrm{i}C''_{ik}$ coefficients, three real-valued $e_{ik} = e'_{ik}$ coefficients, and two complex-valued $\varepsilon_{ik} = \varepsilon'_{ik} + \mathrm{i}\varepsilon''_{ik}$ coefficients.

2.3.1 Electrical impedance

The electrical impedance Z, analogous to the acoustic impedance defined in Eq. (2.19), describes the opposition of a medium towards an alternating electrical current. The electrical impedance is a complex-valued quantity and defined as the ratio of the voltage potential difference φ_{diff} and the electrical current I. The current I can be derived by the surface integral of the normal component of the polarization current density $\boldsymbol{J}_{\mathrm{P}} = -\mathrm{i}\omega\,(\boldsymbol{D} - \epsilon_0 \boldsymbol{E})$ over the surface $\partial\Omega$ of the electrode,

$$Z = \frac{\varphi_{\mathrm{diff}}}{I}, \tag{2.29}$$

$$I = \int_{\partial\Omega} \boldsymbol{n} \cdot \boldsymbol{J}_{\mathrm{P}}\, \mathrm{d}a = -\mathrm{i}\omega \int_{\partial\Omega} \boldsymbol{n} \cdot (\boldsymbol{D} - \epsilon_0 \boldsymbol{E})\, \mathrm{d}a. \tag{2.30}$$

For a PZT transducer with a single top electrode and a grounded bottom electrode, the potential φ_{diff} equals the voltage amplitude of the driving signal, $\varphi_{\mathrm{diff}} = \varphi_0 - 0$ V. In the case of anti-symmetric actuation with a split top electrode, we define φ_{diff} as the potential difference between each of the split electrodes, so that $\varphi_{\mathrm{diff}} = \varphi_+ - \varphi_-$.

2.3.2 Electrical input power

The time-averaged electrical input power P_{input}, which is applied to the PZT transducer, is given in terms of the potential difference φ_{diff} between the electrodes and the electrical current I,

$$P_{\mathrm{input}} = \frac{1}{2} \operatorname{Re}\left[\varphi_{\mathrm{diff}}\, I^{\star}\right] = \frac{1}{2} \left|\varphi_{\mathrm{diff}}\right| \left|I\right| \cos(\theta), \quad \text{with} \quad \theta = \arg(Z). \tag{2.31}$$

The angle θ describes the phase of the electrical impedance Z, and the factor $\cos(\theta)$ is sometimes referred to as the power factor.

2.4 Boundary conditions

2.4.1 Boundary conditions at the fluid–solid interface

Full theory

In the full theory formulation for the first-order fields, the boundary conditions at the fluid–solid interface for the first-order fluid velocity $\boldsymbol{v}_1$ and solid stress tensor $\boldsymbol{\sigma}_{\mathrm{sl}}$ are

$$\boldsymbol{v}_1 = \boldsymbol{v}_{\mathrm{sl}}, \tag{2.32a}$$

$$\boldsymbol{\sigma}_{\mathrm{sl}} \cdot \boldsymbol{n} = \boldsymbol{\sigma}_{1,\mathrm{fl}} \cdot \boldsymbol{n}. \tag{2.32b}$$

These conditions express that the first-order fluid velocity needs to match the wall velocity $\boldsymbol{v}_{\mathrm{sl}} = -\mathrm{i}\omega\boldsymbol{u}$ at the interface between fluid and solid. Furthermore, we ensure continuity of the normal component of the stress tensor $\boldsymbol{\sigma}_{\mathrm{sl}}$ and the normal component of the fluid stress tensor $\boldsymbol{\sigma}_{1,\mathrm{fl}}$ across the boundary.

Effective theory

The boundary conditions for the pressure p_1 and the solid stress tensor $\boldsymbol{\sigma}_{\mathrm{sl}}$ in the effective formulation, with a normal vector $\boldsymbol{n}$ pointing outwards from the fluid domain, are derived by Bach and Bruus in Ref. [35] and given by

$$\boldsymbol{\nabla} p_1 \cdot \boldsymbol{n} = \frac{\mathrm{i}\omega\rho_0}{1-\mathrm{i}\Gamma}\left(\boldsymbol{v}_{\mathrm{sl}} \cdot \boldsymbol{n} - \frac{\mathrm{i}}{k_{\mathrm{s}}}\boldsymbol{\nabla}_{\!||} \cdot \boldsymbol{v}_{\mathrm{sl},||}\right) - \frac{\mathrm{i}}{k_{\mathrm{s}}}\left(k_{\mathrm{c}}^2 p_1 + (\boldsymbol{n}\cdot\boldsymbol{\nabla})^2\, p_1\right), \tag{2.33a}$$

$$\boldsymbol{\sigma}_{\mathrm{sl}} \cdot \boldsymbol{n} = -p_1\boldsymbol{n} + \mathrm{i}k_{\mathrm{s}}\eta_0\left(\boldsymbol{v}_{\mathrm{sl}} - \boldsymbol{v}_1^d\right), \tag{2.33b}$$

with the complex-valued shear-wavenumber $k_{\mathrm{s}} = \frac{1+\mathrm{i}}{\delta}$, and where $\parallel$ denotes tangential components. These boundary conditions take the thin viscous boundary layer in the fluid domain into account analytically and do not require any explicit reference to the velocity field $\boldsymbol{v}_1^{\delta} = \boldsymbol{v}_{\mathrm{sl}} - \boldsymbol{v}_1^d$ inside the viscous boundary layer. For the implementation of the effective theory, only the boundary conditions for p_1 and $\boldsymbol{\sigma}_{\mathrm{sl}}$ are necessary, as the fluid velocity $\boldsymbol{v}_1$ is determined by p_1 through Eq. (2.8).

2.4.2 Boundary conditions at the PZT and solid interfaces

In the piezoelectric domain, we need to define the voltage amplitude, which is applied to the system's electrodes. Furthermore, we assume that the normal component of the displacement field $\boldsymbol{D}$, the solid stress tensor $\boldsymbol{\sigma}_{\mathrm{sl}}$, and the piezoelectric stress tensor $\boldsymbol{\sigma}_{\mathrm{pzt}}$ are zero at the surfaces facing the surrounding air. The corresponding boundary conditions are

$$\text{PZT domain} \leftarrow \text{ground electrode:} \qquad \varphi = 0, \tag{2.34a}$$

$$\text{PZT domain} \leftarrow \text{phase electrode:} \qquad \varphi = \varphi_0, \tag{2.34b}$$

$$\text{PZT domain} \leftarrow \text{air:} \qquad \boldsymbol{n}\cdot\boldsymbol{\sigma}_{\mathrm{pzt}} = \boldsymbol{0} \quad \text{and} \quad \boldsymbol{n}\cdot\boldsymbol{D} = 0, \tag{2.34c}$$

$$\text{Solid domain} \leftarrow \text{air:} \qquad \boldsymbol{n}\cdot\boldsymbol{\sigma}_{\mathrm{sl}} = \boldsymbol{0}. \tag{2.34d}$$

2.4.3 Symmetry boundary conditions

Symmetric boundaries

If the pressure field and the electrical potential are symmetric in a given plane, we can impose the following boundary conditions to reduce the dimensions of the geometry,

$$\boldsymbol{u}_{\perp} = 0, \tag{2.35a}$$
$$(\boldsymbol{\sigma}_{\mathrm{sl}} \cdot \boldsymbol{n})_{\parallel} = 0, \tag{2.35b}$$
$$(\boldsymbol{\sigma}_{\mathrm{pzt}} \cdot \boldsymbol{n})_{\parallel} = 0, \tag{2.35c}$$
$$\boldsymbol{n} \cdot \boldsymbol{\nabla} p_1 = 0, \tag{2.35d}$$
$$\boldsymbol{n} \cdot \boldsymbol{\nabla} \varphi = 0. \tag{2.35e}$$

In this formulation, $\perp$ describes components normal to the symmetry plane, and $\parallel$ describes components tangential to the symmetry plane. These boundary conditions ensure that the components of the displacement $\boldsymbol{u}$, the flux $\boldsymbol{\nabla} p_1$, and $\boldsymbol{\nabla} \varphi$, which are normal to the symmetry plane, as well as the tangential component of $\boldsymbol{\sigma}_{\mathrm{sl}} \cdot \boldsymbol{n}$ and $\boldsymbol{\sigma}_{\mathrm{pzt}} \cdot \boldsymbol{n}$ are set to zero.

Anti-symmetric boundaries

For an anti-symmetric surface, the tangential components of the displacement $\boldsymbol{u}$ need to be set to zero. The same is required for the value of the pressure field p_1 and the electric potential φ at this surface. Furthermore, the normal components $\boldsymbol{\sigma}_{\mathrm{sl}} \cdot \boldsymbol{n}$ and $\boldsymbol{\sigma}_{\mathrm{pzt}} \cdot \boldsymbol{n}$ need to be zero. The corresponding boundary conditions are

$$\boldsymbol{u}_{\parallel} = 0, \tag{2.36a}$$
$$(\boldsymbol{\sigma}_{\mathrm{sl}} \cdot \boldsymbol{n})_{\perp} = 0, \tag{2.36b}$$
$$(\boldsymbol{\sigma}_{\mathrm{pzt}} \cdot \boldsymbol{n})_{\perp} = 0, \tag{2.36c}$$
$$p_1 = 0, \tag{2.36d}$$
$$\varphi = 0. \tag{2.36e}$$

2.5 Dissipated power in different domains

The computation of the dissipated power in different domains of the modeled system allows for an interesting overview. It enables us to compare how much of the applied electrical power is dissipated in the individual domains. In the following chapter, in Section 3.3.3, a numerical study of the dissipated power is presented, and this section, therefore, introduces the required equations. We can compute the time-averaged dissipated power P_d in a domain Ω from the divergence of the time-averaged Poynting vector $\langle \boldsymbol{\Sigma} \rangle$ as,

$$P_\mathrm{d} = -\int_\Omega \mathrm{Re}\left\{ \boldsymbol{\nabla} \cdot \langle \boldsymbol{\Sigma} \rangle \right\} \mathrm{d}V = \int_\Omega p_\mathrm{d} \, \mathrm{d}V, \tag{2.37}$$

where $p_\mathrm{d} = -\mathrm{Re}\left\{ \boldsymbol{\nabla} \cdot \langle \boldsymbol{\Sigma} \rangle \right\}$ is the power dissipation density. [46]

2.5.1 Losses in piezoelectric materials

The time-averaged generalized Poynting vector in piezoelectric materials is defined as,

$$\left\langle \boldsymbol{\Sigma}_\mathrm{pzt} \right\rangle = \frac{1}{2} \mathrm{Re}\left\{ \boldsymbol{E} \times \boldsymbol{H}^\star - \boldsymbol{\sigma}_\mathrm{pzt} \cdot \boldsymbol{v}_\mathrm{pzt}^\star \right\}, \tag{2.38}$$

where $\boldsymbol{H}^\star$ is the complex-conjugate of the magnetic field $\boldsymbol{H}$, and $\boldsymbol{v}_\mathrm{pzt}^\star = \mathrm{i}\omega \boldsymbol{u}^\star$ describes the complex-conjugated velocity of the piezoelectric transducer [46]. By utilizing Maxwell's equations in a non-magnetic material, the power dissipation density p_pzt in a piezoelectric material can be written as

$$p_\mathrm{pzt} = -\mathrm{Re}\left\{ \boldsymbol{\nabla} \cdot \left\langle \boldsymbol{\Sigma}_\mathrm{pzt} \right\rangle \right\} = -\frac{1}{2}\omega \ \mathrm{Im}\left\{ \boldsymbol{E} \cdot \boldsymbol{D}^\star + \boldsymbol{\sigma}_\mathrm{pzt} : \boldsymbol{s}^\star \right\}. \tag{2.39}$$

2.5.2 Losses in solid materials

The losses in the solid domain can be obtained in analogy to the previous case of piezoelectric materials, but neglecting the contributions from the electric field. The power dissipation density for a solid is given as,

$$p_\mathrm{sl} = -\frac{1}{2}\omega \ \mathrm{Im}\left\{ \boldsymbol{\sigma}_\mathrm{sl} : \boldsymbol{s}^\star \right\}. \tag{2.40}$$

2.5.3 Losses in fluids

The losses in the fluid domain can be derived from the time-averaged Poynting vector

$$\langle \boldsymbol{\Sigma}_\mathrm{fl} \rangle = \frac{1}{2} \ \mathrm{Re}\left\{ -\boldsymbol{\sigma}_{1,\mathrm{fl}} \cdot \boldsymbol{v}_1^\star \right\}. \tag{2.41}$$

The density of the time-averaged dissipated power can then be calculated as

$$p_\mathrm{fl} = -\mathrm{Re}\left\{ \boldsymbol{\nabla} \cdot \langle \boldsymbol{\Sigma}_\mathrm{fl} \rangle \right\} = \frac{1}{2} \ \mathrm{Re}\left\{ \boldsymbol{\sigma}_{1,\mathrm{fl}} : \boldsymbol{\nabla} \boldsymbol{v}_1^\star \right\}.$$

Chapter 3

Simulation of acoustofluidic systems

3.1 Numerical methods

In order to predict and optimize the behavior of acoustofluidic devices, we are interested in obtaining a solution for the acoustic pressure p_1, the fluid velocity $\boldsymbol{v}_1$, the solid displacement $\boldsymbol{u}$, the electric potential φ, and all quantities that can be derived from those fields. The corresponding governing equations, however, can only be solved numerically. We utilize the finite-element method (FEM) in this work to obtain approximate solutions for these fields. In this chapter, a brief overview of FEM will be given, and the implementation of the governing equations using the software `COMSOL Multiphysics` will be described. In Section 3.3, different methods to ensure the validity of the numerical model will be discussed. The theory presented in this chapter is based on Refs. [47, 48].

3.1.1 Finite element modeling

All partial differential equations (PDEs) used throughout this thesis can be described by a flux $\boldsymbol{J}$ resulting from a force F, generally called *strong-form* representation, of the form

$$\boldsymbol{\nabla} \cdot \boldsymbol{J} - F = 0. \tag{3.1}$$

The finite element method aims to approximate the complex-valued, time-independent solution $a_{\text{exact}}(\boldsymbol{r})$, which fulfills Eq. (3.1). In order to solve such equations numerically, we need to discretize the domain into small finite elements on which the equation is being solved. Typically only an approximate solution $a(\boldsymbol{r}) \approx a_{\text{exact}}(\boldsymbol{r})$ can be found, which is subject to an error $e(\boldsymbol{r})$,

$$\boldsymbol{\nabla} \cdot \boldsymbol{J}[a(\boldsymbol{r})] - F[a(\boldsymbol{r})] = e(\boldsymbol{r}). \tag{3.2}$$

Such an approximate solution $a(\boldsymbol{r})$ is obtained by the introduction of so-called test functions $\hat{a}_n$, that are defined on each node point n of a mesh consisting of N node points in total, as visualized in Fig. 3.1(a). At each node point a weight w_n is calculated in order

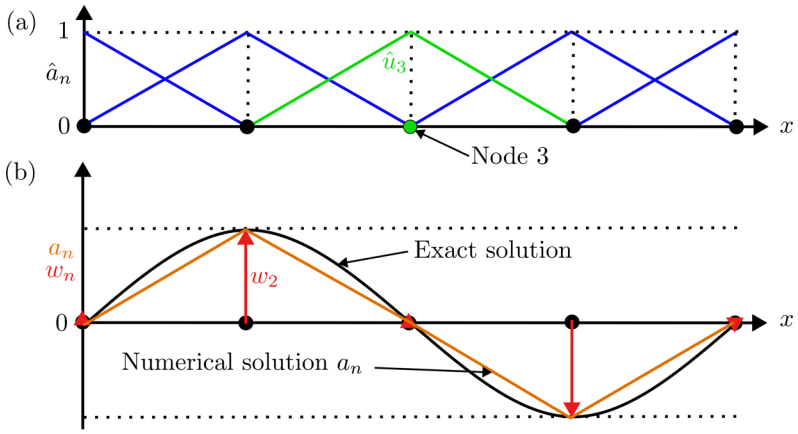

Figure 3.1: (a) 1D mesh consisting of five nodes and four mesh elements. For each node n a linear Lagrangian test function $\hat{a}_n$ is drawn, which equals one at the node's location and is zero at all other nodes. (b) The exact solution a_{exact} is shown in black, and the numerical values $a_n = w_n \hat{a}_n$ and their corresponding weights w_n are shown in orange and red, respectively.

to locally approximate the solution as,

$$a(\boldsymbol{r}) \approx \sum_{n=1}^{N} w_n \hat{a}_n(\boldsymbol{r}). \tag{3.3}$$

For $a(\boldsymbol{r})$ to be a viable solution of Eq. (3.1), the error $e(\boldsymbol{r})$ has to be as small as possible. To ensure that $e(\boldsymbol{r})$ is minimal, it is helpful to implement the *weak-form* representation of Eq. (3.1),

$$\int_{\Omega} \hat{a}_m(\boldsymbol{r}) \left\{ \boldsymbol{\nabla} \cdot \boldsymbol{J}[a(\boldsymbol{r})] - F[a(\boldsymbol{r})] \right\} \mathrm{d}V = 0, \tag{3.4}$$

which corresponds to the expression $\int_{\Omega} \hat{a}_m(\boldsymbol{r})\, e(\boldsymbol{r})\, \mathrm{d}V = 0$, which is enforcing the error to be minimal in each mesh point. A visualization of a 1D mesh including linear test functions $\hat{a}_n$ and weights w_n is shown in Fig. 3.1. If we assume, that both the flux $\boldsymbol{J}$ and the force F depend linearly on the field $a(\boldsymbol{r})$, such that $\boldsymbol{J}[a(\boldsymbol{r})] = \sum_n w_n \boldsymbol{J}[\hat{a}_n]$ and $F[a(\boldsymbol{r})] = \sum_n w_n F[\hat{a}_n]$, we can express Eq. (3.4) as a system of equations in matrix representation as,

$$\sum_{n=1}^{N} K_{mn} w_n = 0, \quad \text{with} \quad K_{mn} = \int_{\Omega} \hat{a}_m(\boldsymbol{r}) \left\{ \boldsymbol{\nabla} \cdot \boldsymbol{J}[\hat{a}_n(\boldsymbol{r})] - F[\hat{a}_n(\boldsymbol{r})] \right\} \mathrm{d}V \tag{3.5}$$

In order to find the required weights w_n necessary to compute the solution $a(\boldsymbol{r})$, finite element software typically solves such a system via the usual matrix operations based on the known matrix K_{mn}. This process is eased by the fact that K_{mn} typically is a sparse

matrix since the m test functions $\hat{a}_m$ are only nonzero close to a given mesh element n. Nevertheless, solving numerical problems in 3D results in large meshes with thousands of mesh nodes and, therefore, large matrices that need to be solved.

3.1.2 Boundary conditions

In order to obtain meaningful results, FEM requires the specification of boundary conditions to solve a given differential equation. The two most common boundary conditions that we encounter in our numerical model are

- Dirichlet boundary conditions, forcing the field value at the boundary to a specified value $D(\boldsymbol{r})$,
- Neumann boundary conditions, defining the flux $N(\boldsymbol{r}) = \boldsymbol{n} \cdot \boldsymbol{J}$ normal to the boundary, with normal vector $\boldsymbol{n}$.

Dirichlet boundary conditions are implemented by defining the weights $w_n = D(\boldsymbol{r}_n)$ at the boundary, where the field value $D(\boldsymbol{r})$ is known. The implementation of Neumann boundary conditions becomes straightforward if we rewrite K_{mn} in Eq. (3.5) using Gauss' theorem as,

$$K_{mn} = \oint_{\partial\Omega} [\hat{a}_m \, \boldsymbol{n} \cdot \boldsymbol{J}[\hat{a}_n(\boldsymbol{r})]] \, \mathrm{d}A - \int_{\Omega} \boldsymbol{\nabla} \hat{a}_m \cdot \boldsymbol{J}[\hat{a}_n(\boldsymbol{r})] + \hat{a}_m F[\hat{a}_n(\boldsymbol{r})] \, \mathrm{d}V = 0. \tag{3.6}$$

In this representation, it can be seen that the Neumann boundary condition $N(\boldsymbol{r}) = \boldsymbol{n} \cdot \boldsymbol{J}$ can be directly included in the surface-integral formulation.

3.2 Implementation

For the numerical simulations, the weak-form interface *"Weak Form PDE"* of the FEM-solver `COMSOL Multiphysics` [49] is used to implement the governing equations. These numerical simulations allow us to obtain solutions for the potential φ in the piezoelectric transducer, the displacement $\boldsymbol{u}$ in all solids, and the acoustic pressure field p_1 in the microfluidic channel.

In the simulations presented in Chapter 5 and Chapter 8, a thin liquid coupling layer between the piezoelectric transducer and the microfluidic chip is used. For a coupling medium such as glycerol, the boundary layer thickness is $\delta = 17$ µm at 1 MHz and, therefore, similar to the thickness of a typical coupling layer with $h_{\mathrm{cpl}} \approx 20$ µm. In such cases, the effective boundary layer theory developed by Bach and Bruus [35] cannot be utilized, and the full theory for the pressure p_1 and velocity field $\boldsymbol{v}_1$, described in Section 2.1.1, is implemented for the coupling layer. The effective boundary layer theory, described in Section 2.1.3, together with the boundary conditions listed in Section 2.4.1, is implemented to solve the fields inside the typically water-based microfluidic channel.

3.2.1 Fluid domain

Full theory

The full theory is implemented as a weak-form PDE solving Eq. (2.6b) for the velocity field $\boldsymbol{v}_1$, described by a flux $\boldsymbol{J}(\boldsymbol{v}_1)$ and force $\boldsymbol{F}(\boldsymbol{v}_1)$,

$$\boldsymbol{J} = \boldsymbol{\sigma}_{1,\mathrm{fl}}, \tag{3.7a}$$
$$\boldsymbol{F} = -\mathrm{i}\omega\rho_0\boldsymbol{v}_1, \tag{3.7b}$$

with $\boldsymbol{\sigma}_{1,\mathrm{fl}}$ as defined in Eq. (2.6c). The pressure field p_1 is added as a weak contribution via Eq. (2.6a), using p_1 as an auxiliary dependent variable. The boundary condition on the velocity $\boldsymbol{v}_1$ is simply a Dirichlet condition, implementing the no-slip velocity by setting $\boldsymbol{v}_1 = \mathrm{i}\omega\boldsymbol{u}_{\mathrm{sl}}$. The stress on the surrounding walls is implemented as a weak contribution, requiring $\boldsymbol{\sigma}_{\mathrm{sl}} \cdot \boldsymbol{n} = \boldsymbol{\sigma}_{1,\mathrm{fl}} \cdot \boldsymbol{n}$.

Effective boundary layer theory

The effective boundary layer theory described in Section 2.4.1 is implemented as a weak-form PDE solving for the pressure field p_1 with a flux $\boldsymbol{J}(p_1)$ and force $F(p_1)$,

$$\boldsymbol{J} = \boldsymbol{\nabla} p_1, \tag{3.8a}$$
$$F = -k_c^2 p_1. \tag{3.8b}$$

The velocity field $\boldsymbol{v}_1$ does not need to be implemented as a weak-form PDE and can be calculated from the pressure field p_1 via Eq. (2.8). The boundary condition for the pressure can be implemented as a weak contribution, given by Eq. (2.33a).

3.2.2 Solid domain

In order to implement Cauchy's momentum equation, see. Eq. (2.20), we are solving for the displacement field $\boldsymbol{u}$ using a flux $\boldsymbol{J}(\boldsymbol{u})$ and a force $\boldsymbol{F}(\boldsymbol{u})$,

$$\boldsymbol{J} = \boldsymbol{\sigma}_{\mathrm{sl}}, \tag{3.9a}$$
$$\boldsymbol{F} = -\omega^2\rho_{\mathrm{sl}}\boldsymbol{u}. \tag{3.9b}$$

The boundary condition for the stress $\boldsymbol{\sigma}_{\mathrm{sl}}$ on the walls surrounding the fluid channel can be implemented as a weak contribution, given by Eq. (2.33b).

3.2.3 Piezoelectric domain

For the piezoelectric transducer, we are interested in the electric potential φ, the displacement field $\boldsymbol{u}$, and how the two fields interact. We, therefore, implement two PDEs: Gauss' law with a flux $\boldsymbol{J}(\varphi)$, as well as the stress-strain relation for the transducer with $\boldsymbol{J}(\boldsymbol{u})$ and $\boldsymbol{F}(\boldsymbol{u})$. The stress-strain formulation for piezoelectric transducers is similar to Eq. (3.9), with the difference that the flux equals the stress tensor of a piezoelectric material, which

includes the coupling coefficients between the electrical and mechanical field, $\boldsymbol{J} = \boldsymbol{\sigma}_{\text{pzt}}$. The formulation for the generalized flux and force for Gauss' law is

$$\boldsymbol{J} = \boldsymbol{D}, \tag{3.10a}$$

$$F = 0. \tag{3.10b}$$

3.3 Model validation

Several tests have been performed throughout the Ph.D. project to verify the validity of the numerical model. One of the most important tests is verifying if the mesh, which has been used for a numerical study, yields solutions converging toward the true solution. Further verification tests include comparing full simulations and simulations utilizing symmetry planes. In this section, we gain some additional insight into the consistency of the numerical model by comparing the dissipated power in the different sub-domains of the system with the input power and comparing the results of 2D and 3D simulations. The validation of the model by experiment will be the content of Chapter 5. The 2D and 3D models studied in this section are visualized in Fig. 3.2 and consist of a PZT transducer, a thin coupling layer, a fluid channel, and a polymer chip.

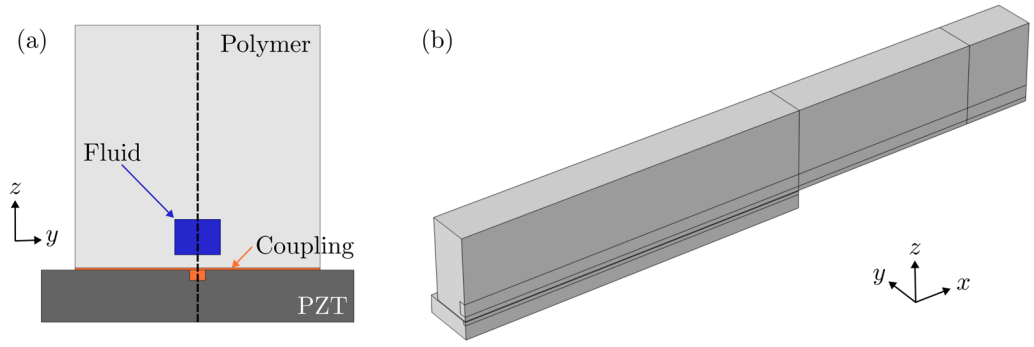

Figure 3.2: (a) Overview of the 2D model, consisting of the fluid channel (blue), polymer chip (light gray), coupling layer (orange), and PZT transducer (dark gray). A dotted line indicates the symmetry line in the vertical z-direction. (b) A quarter of the entire 3D model is shown, where symmetry conditions at the yz- and xz-plane have been used.

3.3.1 Mesh convergence

To evaluate if a chosen mesh is fine enough to resolve the correct solution, we perform mesh-convergence testing as the initial step when setting up a new numerical model. The maximum element size in a mesh is usually defined as,

$$h_{\text{max}} = \frac{\lambda}{s}, \tag{3.11}$$

where $\lambda = c/f_{\text{mesh}}$ is the wavelength at frequency f_{mesh} in a given domain. The speed of sound c equals c_0 in the fluid domain, while the transverse speed of sound c_{tr} is used in

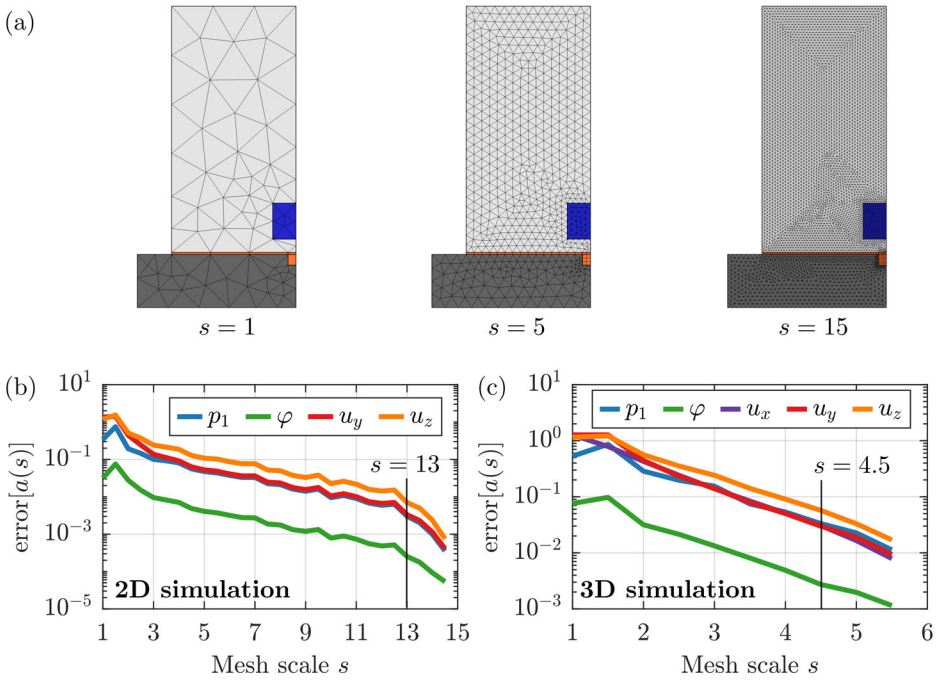

Figure 3.3: (a) Overview of the 2D mesh at different mesh scale values $s = 1$, 5 and 15. (b) Mesh convergence plot for a 2D simulation showing the mesh convergence, defined by error$[a(s)]$, of the pressure field p_1, electrical potential φ and displacement u_y and u_z versus the scaling parameter s. (c) Mesh convergence plot for a 3D simulation showing error$[a(s)]$ versus the scaling parameter s.

the solid domain to define the mesh. Mesh convergence testing is performed by gradually increasing the mesh resolution s to the highest possible value, $s_{\max}$, which can still be computed on a workstation. We consider the solution to a given field $a(\boldsymbol{r}, s)$ at position $\boldsymbol{r}$ to be a function of the mesh scaling parameter s and denote the error between the solution $a(\boldsymbol{r}, s_{\max})$ using the highest possible mesh scaling parameter $s_{\max}$ as,

$$\text{error}[a(s)] = \sqrt{\frac{\int_\Omega |a(\boldsymbol{r}, s) - a(\boldsymbol{r}, s_{\max})|^2 \, \mathrm{d}V}{\int_\Omega |a(\boldsymbol{r}, s_{\max})|^2 \, \mathrm{d}V}}. \tag{3.12}$$

Fig. 3.3(a) visualizes the 2D mesh at different scaling parameters s. In Fig. 3.3(b,c), we compare the results of such a mesh convergence test for a 2D and a 3D model. While we typically aim for convergence error below 1% in our 2D simulations, which is achieved for $s = 13$ in the example shown in Fig. 3.3(b), reaching a high convergence in a 3D simulation requires a large amount of *random access memory* due to the many degrees of freedom. We, therefore, reach convergence in the order of 5% in our 3D simulations, seen for $s = 4.5$ in Fig. 3.3(c).

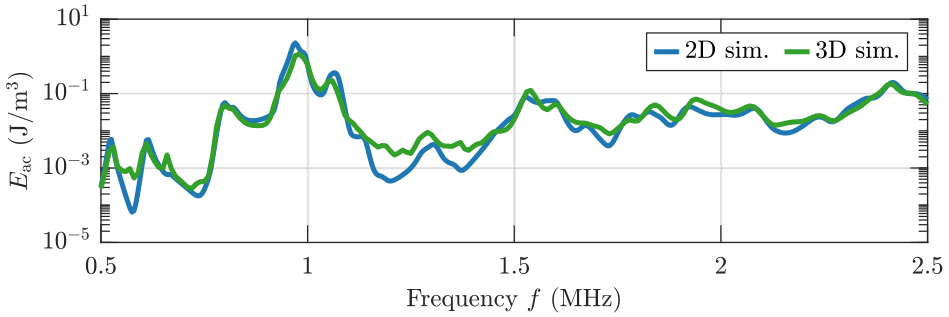

Figure 3.4: Comparison of the simulated acoustic energy density E_{ac} inside the fluid channel of a COC-based device, coupled to a Pz27 transducer. Frequencies f in the range from 0.5 to 2.5 MHz were simulated using an anti-symmetric actuation voltage with an amplitude of $\varphi_0 = 1$ V. In the 2D simulation, the highest acoustic energy density is found at $f = 0.97$ MHz with $E_{ac}^{2D} = 2.3\ \mathrm{J\,m^{-3}}$. In the 3D simulation, the acoustic energy density is highest at $f = 0.98$ MHz with $E_{ac}^{3D} = 1.2\ \mathrm{J\,m^{-3}}$.

3.3.2 2D and 3D comparison

Due to time and computation constraints, many simulations are performed in 2D, and only final validation is performed using 3D simulations. Especially when performing parametric sweeping over a wide frequency range or numerical optimization, using 3D simulations is too time-consuming. Many of our typical systems, however, utilize 2D-like actuation. In Fig. 3.4, the results obtained from a 2D-cross-section are compared with the simulation results of a full 3D simulation. The simulation is based on the system shown in Fig. 3.2 and is similar to the one that will be studied in Chapter 8. The device consists of a 3-mm-wide, 0.5-mm-high Pz27 transducer, a 20-µm-thin solid coupling layer, and a 2.4-mm-wide, 2.3-mm-high COC chip. The frequency sweep in 2D and 3D is performed with a constant voltage amplitude of $\varphi_0 = 1$ V from 0.5 to 2.5 MHz in steps of 5 kHz. The simulation shows a good agreement between the 2D and the 3D results. While the amplitudes differ by an order of magnitude at some frequencies, the resonance frequencies between the two simulations match well.

3.3.3 Dissipated power in different domains

A further way of validating if the numerical model is self-consistent is by comparing the dissipated power in the different domains of the acoustofluidic device and comparing those with the total power delivered to the system. The sum of the electrical and mechanical power dissipation in the transducer P_{pzt}, the mechanical power dissipation in the solid P_{solid}, and the power dissipation in the fluid P_{fluid} has to match the input power P_{input} delivered to the piezoelectric transducer,

$$P_{input} \approx P_{tot} = P_{pzt} + P_{sl} + P_{fl}. \tag{3.13}$$

In Fig. 3.5, we compare the power loss in the case of a polymer-based system and a glass-based system. Over the studied frequency range from 0.5 to 2.5 MHz, we find

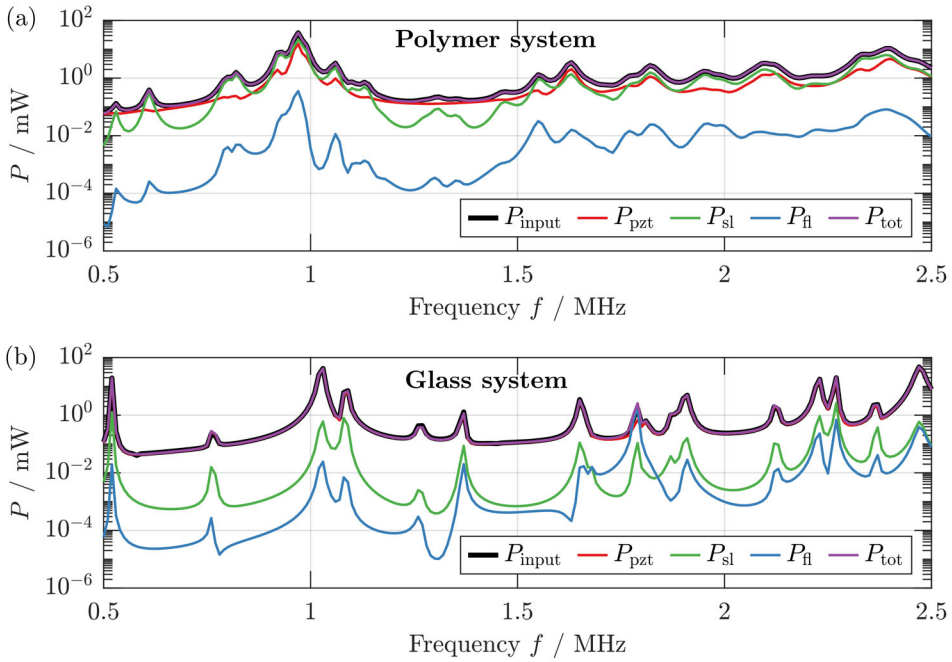

Figure 3.5: The time-averaged dissipated power in the solid (P_{sl}), fluid (P_{fl}) and piezoelectric domain (P_{pzt}) is shown versus frequency f in the range from 0.5 to 2.5 MHz. The values are compared with the input power P_{input} and the total power P_{tot} for (a) a system with a polymer chip made from COC and (b) a glass-based system using the material parameters for borosilicate glass.

the total power dissipation to match the input power, $P_{\mathrm{input}} \approx P_{\mathrm{tot}}$. While in a glass-based device, most losses occur in the piezoelectric transducer, the situation is different for polymer-based systems. Due to polymers' high acoustic attenuation, the polymer's mechanical power dissipation (green curve) is almost as high and sometimes higher than the transducer's power dissipation (red curve), as seen in Fig. 3.5(a). In both systems, the power dissipation in the fluid makes up only a tiny fraction of the total power P_{tot}.

3.4 Material parameters

In order to perform numerical simulations of the pressure field p_1, the displacement field $\boldsymbol{u}$, and the electric potential φ, several material parameters are required. A list of all material parameters used throughout this thesis can be found in the appendix in Chapter A. The material parameters are categorized in two sections: Parameters obtained from literature are listed in Section A.1. Parameters measured using the UEIS technique are listed in Section A.2.

Chapter 4

Experimental aspects of acoustofluidic systems

To further validate the numerical model as part of the feedback loop, experimental characterization of the performance of acoustofluidic devices is crucial. This chapter aims to establish the experimental foundation for the work performed in Paper I [1], Paper II [2], and Paper III [3], which will be presented in the subsequent chapters. In this chapter, the terminology and different concepts relevant to acoustofluidic experiments will be introduced. Furthermore, the fabrication procedure of polymer devices and different characterization methods shall be established in the following.

4.1 Fabrication of polymer-based devices

This thesis aims to close the feedback loop and move from numerical simulations to fabricating polymer-based acoustofluidic devices. In this context, it is imperative to consider the details of the fabrication process in the device design. This work is part of the AcouPlast project, where we are lucky to collaborate with experts on injection molding from the department DTU Construct.

In contrast to some glass-based acoustofluidic devices, the fabrication of injection-molded polymer chips typically involves an additional process step consisting of bonding a thin polymer foil, which seals the channel. The fabrication procedure starts with selecting a suitable polymer. Afterward, the injection molding, bonding of the thin polymer foil, and acoustic coupling to a piezoelectric transducer can commence.

In my work, I have been partially involved in selecting a suitable polymer and in different experiments on polymer-polymer bonding to seal the microfluidic channel. The injection molding and bonding of polymer chips are performed by Komeil Saeedabadi (DTU Construct). The following overview presents a short introduction to the injection-molding process, which is relevant for understanding some of the fabrication constraints imposed on the optimization procedure performed in Chapter 8.

Table 4.1: Comparison between different properties of the polymers COC, PC, PMMA, PS, and PDMS. Here, different symbols are used to express good (+), neutral (0), and unfavourable properties (−).

	COC	PC	PMMA	PS	PDMS
Injection molding [50]	0	+	+	0	−
Bonding [51, 52]	0	+	+	+	+
Transparency [53]	+	0	+	+	+
Mechanical stability [53]	+	+	0	+	−
Chemical resistance [53]	+	−	−	0	0

4.1.1 Material requirements

The list of polymers relevant for acoustofluidic applications includes cyclic olefin copolymer (COC), polycarbonate (PC), polymethyl methacrylate (PMMA), and polystyrene (PS). The properties for these polymer and their suitability for biomedical applications are given in Table 4.1. The polymer polydimethylsiloxane (PDMS) is furthermore included in the comparison table, because it is commonly used in acoustofluidics due to its compatibility with conventional cleanroom fabrication techniques, albeit not suitable for injection-molding. Optical transparency is initially required to verify the performance of the device. At a later stage this property however is not strictly required anymore. The polymers COC, PC, PMMA and PS are all available in medical grades, ensuring biocompatibility of the polymer devices. Of the listed polymers, COC and PMMA have been selected for injection-molding trials. COC has been chosen as a promising candidate for acoustofluidic devices due to its good mechanical stability and chemical resistance. A disadvantage of COC, however, is difficulties in the injection-molding- and bonding process. PMMA, on the other hand, is a material commonly used for injection molding and with established bonding techniques. At the same time, the poor chemical resistance towards acetone and ethanol is a weak point of the material for use in biomedical applications.

4.1.2 Injection molding

Injection molding of thermoplastic polymers is performed by heating pellets of the desired polymer well above their glass transition temperature and injecting them into a mold. Several process parameters can have an impact on the quality of the injection-molded sample:

- Melt temperature,
- Mold temperature,
- Packing pressure,
- Injection speed.

The melt temperature defines the temperature that polymer pellets are heated to before being injected through the barrel. This process takes place at a defined injection speed into

the mold while keeping the mold at a constant temperature. Once the mold is filled, the so-called packing pressure is applied to the molten polymer until it has solidified. Volumetric shrinkage, difficulties in the demolding process, and insufficient mold filling are among the problems if incorrect process parameters are chosen. In addition, enclosed structures cannot be fabricated when using injection molding as the fabrication technique. The device, therefore, needs to be assembled from two parts to obtain an enclosed microfluidic channel. Alternatively, as intended in this work, the channel can be sealed off using a thin sheet of polymer-foil using polymer-polymer bonding. [50]

4.1.3 Polymer-polymer bonding

Various approaches for polymer-polymer bonding exist, such as plasma-activated bonding, thermally-, chemically-, or pressure-assisted bonding, ultrasonic welding, and ultraviolet-light (UV) assisted bonding techniques. For the PMMA and COC samples considered in this work, a combination of UV-bonding and pressure-assisted bonding is used by the collaborators at DTU Construct. UV exposure to the polymer surfaces leads to photo-oxidation, causing the breaking of polymer chains. Bringing such two surfaces into contact while applying sufficiently high pressure and heating the polymers to temperatures slightly below their glass transition temperature enables a good chemical bond between the two polymers.

4.1.4 Coupling layers

Once the polymer-based chip has been molded and bonded, it needs to be mechanically coupled to a piezoelectric transducer. Such coupling can be achieved through a thin layer of glycerol or an adhesive, which permanently connects the transducer and chip. For example, in work presented in Paper I [1], a glycerol coupling layer has been used to allow reversible coupling. Another advantage of glycerol from a numerical point of view is the fact that the acoustic properties of glycerol are reasonably well-known. In contrast, the mechanical properties of cured adhesive layers are only sparsely reported in the literature.

4.2 Overview of acoustofluidic design configurations

Acoustofluidic devices and their corresponding designs can be categorized by their means of actuation into either bulk acoustic wave (BAW) devices or surface acoustic wave (SAW) devices. In this thesis, only BAW devices are considered, and such devices can be further sub-categorized broadly into particle trapping and particle separation devices that are briefly introduced below. [14, 54, 55]

4.2.1 Devices for particle trapping

Particle trapping devices are typically built using a bulk piezoelectric transducer, with a length that is much smaller than the length of the microfluidic chip. Often glass capillary tubes are used, and a spatially-localized acoustic half-wave in the vertical direction leads to localized *trapping* of seed particles. [55]

Figure 4.1: (a) Standing-pressure $\lambda/4$-mode in a microfluidic channel with particles being pushed to the top of the channel (green arrow). (b) $\lambda/2$-mode with particle focusing at the channel center.

4.2.2 Devices for particle separation

As opposed to trapping devices, particle separation devices usually utilize longer piezoelectric transducers to ensure a homogeneous acoustic field across a large area of the microfluidic chip. In order to perform particle separation, desired particles need to be focused in a pressure node inside the microchannel. To ensure sufficient focusing even at high flow rates, long straight channels with sufficiently strong acoustic fields help to achieve good results. Often a transverse acoustic field, which is perpendicular to the direction of actuation, is used in such devices, and either standing-pressure $\lambda/2$- or $\lambda/4$-waves are used, as shown in Fig. 4.1.

Quarter-wave designs

A standing quarter-wave inside a microfluidic channel with a pressure node at one of the channel walls will lead to particle focusing at the respective wall. In 1D-like systems, where the channel comprises a significant fraction of the system, such devices are often developed based on one-dimensional design rules. For example, Gu *et al.* [12] presented a high throughput device for platelet separation in 2019, using a standing quarter-wave in a polymer device. The device was optimized for a frequency of 610 kHz and consisted of a piezoelectric transducer and two PMMA layers separated by a divider. The top PMMA layer was designed to match a thickness of $\lambda/2$, while the channel and the bottom layer match a wavelength of $\lambda/4$.

Half-wave designs

A standing pressure half-wave inside a hard-walled microfluidic channel will cause particles to focus in the center of such a channel. Typically these configurations utilize a channel width matching half the acoustic wavelength at a given frequency to yield a pressure node in the channel center. Half-wave designs have been utilized for the devices presented in Paper I [1] and Paper III [3]. However, for polymer-based acoustofluidic devices with a complex resonance structure and mechanically-soft walls, the observed resonance frequencies typically do not translate to a standing half-wave in the channel. Therefore, the conventional design rules can be misleading for polymer chips, and a complete simulation taking all the components of the whole system is needed. Modified design rules, however, can act as an initial guess for optimizing the device geometry for good acoustophoretic performance, as shall be discussed further in Chapter 5 and Chapter 8.

4.3 Device characterization

The work performed for Paper I [1], Paper II [2], and Paper III [3] heavily relied on experimental input. The AcouPlast project enabled a great collaboration with AcouSort and the Department of Biomedical Engineering at Lund University. The thorough acoustofluidic measurements of the polymer device presented in Paper I [1] have been performed by Mathias Ohlin in the laboratories in Lund. The electrical impedance measurements and further validation measurements required for Paper II [2] have been performed in collaboration with my colleague William Naundrup Bodé. Finally, the experimental work for Paper III [3] has been performed by me and was supported by Massimiliano Rossi. The following sections will give a short overview of the required equipment and measurement techniques used throughout this thesis.

4.3.1 Overview of a typical acoustofluidic platform

A typical acoustofluidic platform consists of a frequency generator, power amplifier, microscope, camera, and the acoustofluidic device, including a piezoelectric transducer. In

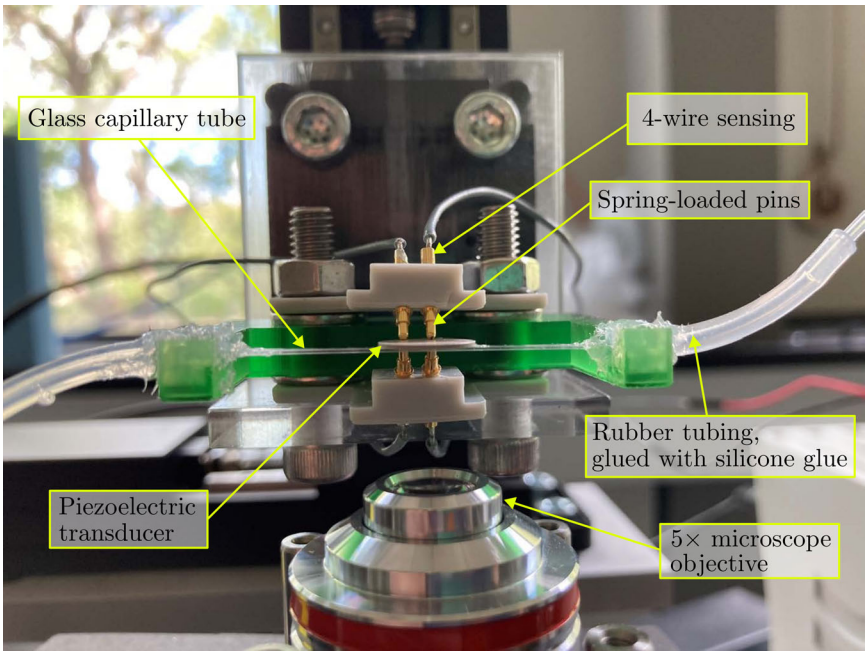

Figure 4.2: Overview of the experimental setup used in Paper III [3] to study acoustophoresis in a glass-capillary tube. The essential equipment of the experimental platform was acquired and assembled by Associate Professor Massimiliano Rossi. The measurement automation, voltage- and power control, and device assembly were performed as part of this thesis. The setup includes a self-developed 4-wire sensing configuration consisting of four spring-loaded pins that directly measure the true voltage amplitude at the transducer.

order to ensure perfect agreement between numerical simulations and experimental data, any external influence on the acoustic fields should be minimized. Thermoelectric cooling is suggested to minimize the influence of heating of the transducer for applications requiring high electrical power. Furthermore, a good knowledge of the actuation voltage and frequency is required. Therefore, in collaboration with Associate Professor Massimiliano Rossi, an experimental setup was developed for the work of Paper III [3] that aims to achieve the closest possible match to the numerical system configuration. Massimiliano Rossi acquired and assembled all the equipment for the basic acoustophoresis system. The automation- and control software and the 4-wire sensing configuration were developed as part of this Ph.D. project. The resulting experimental setup is shown in Fig. 4.2. The use of spring-loaded pins and a four-wire sensing approach allows for the determination of the driving voltage of the piezoelectric transducer while minimizing the mechanical clamping of the acoustofluidic device. Furthermore, the mechanical clamping of the glass-capillary tube is kept minimal by using silicone glue at both ends of the capillary.

The acoustic focusing time t_{foc}, energy density E_{ac} or particle velocities v_{p} are typically studied by switching on the acoustic fields and recording the response of fluorescent microparticles suspended in a fluid inside the channel. The use of a neutrally-buoyant solution helps prevent sedimentation of the particles. Therefore, the framerate of the recording camera needs to be high enough to resolve the particle motion, or the actuation voltage needs to be adjusted to reduce focusing times. When driving piezoelectric transducers at high voltages, the resulting high power dissipation requires sufficient cooling to neglect thermal effects, leading to changes in the acoustic properties of the materials.

If the acoustics are kept on while particles are flowing through the channel, measurements can yield additional insights into achievable flow rates Q_{max} while maintaining particle focusing. Data analysis methods to obtain the desired performance metrics are discussed in the following section.

4.3.2 Determination of particle focusing metrics

Rapid light-intensity method by Barnkob *et al.*

Barnkob *et al.* [44] presented a technique using the light intensity across the channel over a series of frames to obtain the acoustic energy density E_{ac}. By summing the pixel intensities in a given area of the channel and fitting a polynomial with E_{ac} as the free fitting parameter, reasonable estimates of the energy density can be obtained. This approach assumes that particles in the channel follow a known trajectory when subject to a standing half-wave pressure field. This technique has been utilized in Paper I [1] to determine the acoustic energy density over a wide frequency range.

Focusability metric

A different metric introduced in Paper I [1] is the focusability $\mathcal{F}$, which was inspired by the *FocuScan* method used by Vitali *et al.* [56]. The value $\mathcal{F}$ describes the number of particles focused within 10% of the center of a channel of width w_{ch}. Similar to the light-intensity method, the intensity distribution $I(y)$ across the channel (in y-direction) is used

to compute the focusability $\mathcal{F}$,

$$\mathcal{F} = \frac{\int_{-1/2w_{\mathrm{foc}}}^{1/2w_{\mathrm{foc}}} I(y)\,\mathrm{d}y}{\int_{-1/2w_{\mathrm{ch}}}^{1/2w_{\mathrm{ch}}} I(y)\,\mathrm{d}y}. \tag{4.1}$$

Here, a width $w_{\mathrm{foc}} = \frac{1}{10} w_{\mathrm{ch}}$ for the focus band is assumed, with the center of the channel located at $y = 0$. An advantage of the focusability metric is that it yields an easy-to-interpret value, which can easily be obtained experimentally, and allows for a good comparison between experiment and simulation.

General defocusing particle tracking

The general defocusing particle tracking technique (GDPT), developed by Barnkob and Rossi [57, 58], utilizes cross-correlation of a set of calibration images in order to obtain x-, y- and z-coordinates of particles in a given channel region across the recorded frames. The particle's depth position results from the defocusing pattern change. By nearest-neighbor-tracking, it allows for obtaining the trajectories of individual particles. Those trajectories can be used to obtain information about the strength of the acoustic field, the acoustic energy density, and average particle velocities, as done in work presented in Paper III [3]. The advantage of the average particle velocity over the acoustic energy density or focusing times is that no assumptions about the underlying acoustic fields need to be made.

4.3.3 Electrical impedance measurements

Measurements of the electric impedance spectrum $Z(f)$ allow further insights into ideal driving frequencies and can be used to determine material parameters of the system, as will be discussed in Chapter 6. In that context, it is crucial to perform calibration measurements using an open-circuit, short-circuit, and known-resistor configuration to obtain correct impedance measurements. These calibration measurements ensure that parasitic components in the wiring do not distort the impedance measurement.

Impedance measurement of split-electrode devices

The impedance of piezoelectric transducers with a split top electrode can be measured by applying a driving voltage to one of the two split electrodes. The other split electrode is grounded, and the bottom electrode is left electrically floating. In physical terms, a floating electrode means that the tangential components of the electrical field equal zero, $\boldsymbol{E}_{||} = 0$, while in practical terms, the electrode is left unconnected. Such a measurement approach ensures comparability with our numerical model. As can be seen from Fig. 4.3, such a configuration is equal to the usual split-electrode actuation, where the two top electrodes are actuated with a signal that is 180° out of phase between the left and right electrode, while the bottom electrode is grounded. If we add a potential of 0.5 V to the entire field in Fig. 4.3(a), we obtain the field shown in Fig. 4.3(b). The two fields, therefore, only differ by a constant offset, while the simulated impedance is identical for the two configurations, as shown in Fig. 4.3(c).

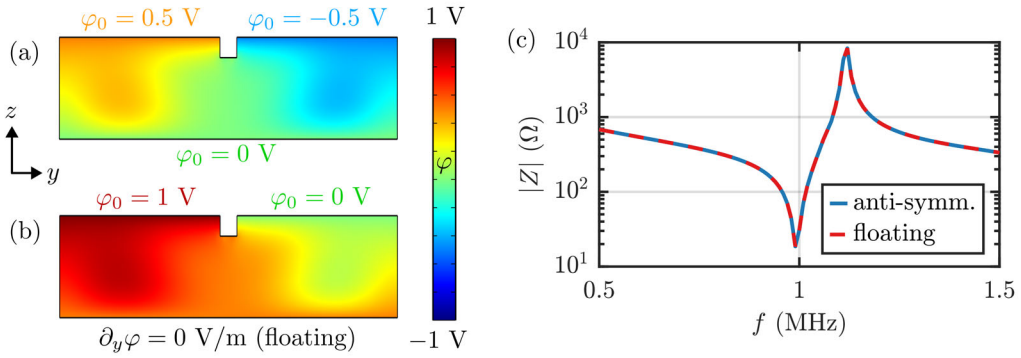

Figure 4.3: (a) Simulated electrical potential φ in the configuration with an anti-symmetric potential applied to the two split top electrodes. (b) Configuration with a floating bottom electrode. In this case, the observed potential resembles the potential of the previous case with a constant offset of 0.5 V. (c) The simulated electrical impedance $|Z|$ versus frequency f is shown for the anti-symmetric and the floating electrode configuration, with identical impedance in both cases.

4.4 Device actuation using piezoelectric transducers

In order to focus particles in the center of a microfluidic channel, a pressure field resembling a standing half-wave needs to be created. Typically acoustofluidic devices either focus particles in the transverse direction or vertically compared to the device actuation. In the following, we will mainly consider transverse focusing, as it is easier to observe experimentally and is better suitable for polymer-based devices due to the fabrication constraints imposed by injection molding.

4.4.1 Actuation methods

Different ways of actuating the microfluidic chip exist to achieve a transverse, anti-symmetric pressure field. If the device is actuated from the bottom, the symmetry needs to be broken to create an anti-symmetric pressure wave around the channel center. The three most common actuation principles are schematically shown in Fig. 4.4. We distinguish between anti-symmetric actuation [26, 59], off-centered actuation [16, 59, 60], and side-wall actuation [61] and their advantages will be discussed in the following paragraphs.

Anti-symmetric actuation using split electrodes

In work by Moiseyenko *et al.* [26], the concept of whole-system resonances (WSUR) was explored, and actuation with two piezoelectric transducers driven in anti-phase was proposed. Such actuation theoretically allows for perfect symmetry-breaking and is ideal for achieving transverse particle focusing. However, a disadvantage of anti-symmetric actuation is that two driving signals are required that must be out of phase by 180°. Furthermore, the electrode of the transducer needs to be separated perfectly in the center to achieve perfect symmetric breaking, which is an additional experimental challenge.

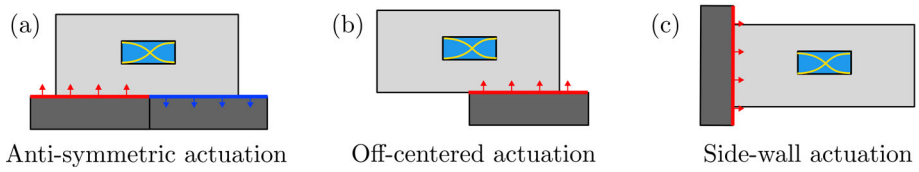

Figure 4.4: Schematic overview of different ways of actuating an acoustofluidic device. (a) Anti-symmetric actuation, (b) off-centered actuation, and (c) side-wall actuation.

Off-centered actuation

Another way of breaking the symmetry in the actuation of a microfluidic chip is to place the chip asymmetrically onto the transducer. Alternatively, the channel can be positioned off the center axis inside the chip, leading to symmetry breaking. A study of such symmetry-breaking has been performed by Tahmasebipour *et al.* [59]. This work found that in asymmetrical glass devices under symmetric actuation, resonances with higher amplitudes than in the geometrically-symmetric case can be obtained. A combination of asymmetric geometry and anti-symmetric transducers produced the strongest half-wave resonances according to numerical simulations of silicon and glass devices performed by Tahmasebipour *et al.*

Side-wall actuation

Qiu *et al.* [61] showed that using side-wall actuation for glass chips can increase the acoustic energy density by up to four times compared to actuation from the bottom. In their numerical model, however, they observe the highest pressure amplitudes for the case of anti-symmetric bottom actuation. Experimentally, side-wall actuation using a piezoelectric transducer that is not much wider than the thickness of the glass capillary can induce symmetry breaking and yield acoustic energy densities that are much higher than when utilizing symmetric actuation from the bottom.

Actuation in this thesis

In this thesis, particularly in Chapter 5 and Chapter 8, mainly anti-symmetric actuation from the bottom of the chip has been considered. Actuation from the bottom is beneficial due to practical considerations, such as mounting the chip to the transducer via a glycerol coupling layer. While the resulting pressure fields under side-wall actuation are naturally asymmetric, they might not necessarily be anti-symmetric in polymer-based devices. However, if anti-symmetry in the pressure field can be achieved, side-wall actuation presents a viable alternative. A possible solution to achieve anti-symmetry using side-wall actuation is using two transducers, one on each side of the chip. However, this solution comes with similar drawbacks as the technique of anti-symmetric actuation from the bottom.

4.4.2 Acoustic and electrical impedance matching

Another technique for improving the performance of an acoustophoresis device is to ensure impedance matching, both electrically as well as acoustically. If the impedance Z_1 of the first medium and Z_2 of the second medium differ, this will lead to reflection of the electric (or acoustic) wave with reflection coefficient r, defined as [55]

$$r = \frac{Z_2 - Z_1}{Z_1 + Z_2}. \tag{4.2}$$

In order to maximize the transmitted energy from medium 1 to medium 2, a matching layer can be introduced. This matching can be done both for the electrical circuit and through an acoustic layer in the mechanical domain. [55]

4.4.3 Non-linear effects due to voltage and aging

Non-linearity with increased voltage

Our numerical model assumes that the piezoelectric transducer's impedance spectrum $Z(f)$ will remain the same, regardless of the actuation voltage applied to the transducer.

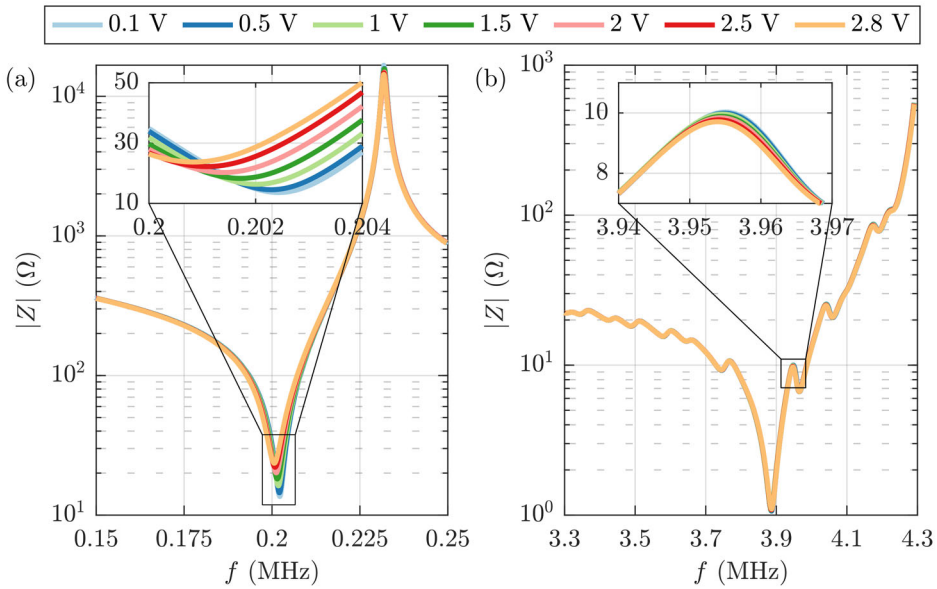

Figure 4.5: Measured impedance $|Z|$ versus frequency f of a Pz27 transducer at different voltages. (a) The impedance is shown for frequencies ranging from 0.15 to 0.25 MHz. A zoom-in of the impedance minimum close to 200 kHz shows a slight downward shift of the resonance by $\Delta f \approx 2$ kHz when increasing the actuation voltage from 0.1 V_{pp} to 2.8 V_{pp}. (b) The impedance spectrum is shown from 3.3 to 4.3 MHz, with a zoom-in of a local minimum close to 4 MHz. In the zoom-in, a small downward-shift of the impedance by $\Delta f \approx 2$ kHz is observed, when increasing the actuation voltage from 0.1 V_{pp} to 2.8 V_{pp}.

This assumption, however, might not always be justified, as work by Ural *et al.* and Liu *et al.* shows [62, 63]. Non-linear effects can cause a shifting of the impedance spectrum, hysteresis effects, and "jumping phenomena," describing a sudden in- or decrease in the impedance spectrum, depending on how and which actuation voltage is applied. Non-linear effects of piezoelectrics transducers are grouped into dielectric and mechanical nonlinearities. Dielectric nonlinearity dominates in the case of high electric field strengths and far from the transducer resonance frequency. On the other hand, mechanical nonlinearities are expected to be dominant when driving transducers at resonance [63].

For this reason, the impact of the actuation voltage on the impedance spectrum of a Pz27 transducer was investigated. The transducer, with a diameter of 10 mm, and a thickness of 0.5 mm, has a nominal resonance frequency of 4 MHz. The results of this measurement are shown in Fig. 4.5, separated into two frequency ranges. Fig. 4.5(a) shows the impedance spectrum from 150 to 250 kHz. An approximately 2 kHz shift of the impedance minimum close to 200 kHz is observed when increasing the actuation voltage from 0.1 V_{pp} to 2.8 V_{pp}. This shift relates to a 1% change in resonance frequency. At the same time, the value in the minimal impedance increases by 10 Ω from 14 Ω to 24 Ω with increasing voltage. In Fig. 4.5(b), the frequency region from 3.3 to 4.3 MHz, around the nominal 4 MHz resonance frequency of the transducer, is shown. Again, we find an approximately 2 kHz downward shift of the impedance when increasing the peak-to-peak voltage by 2.7 V. This presents a shift by 0.05% relative to the resonance frequency. The impedance in the zoomed-in area changes by $\Delta|Z| = -0.25$ Ω when the voltage is increased. For the main thickness resonance at $f = 3.9$ MHz, a minor 0.04 Ω change in the absolute impedance was found. Therefore, it is assumed that these effects can be neglected in our numerical model for moderate voltages and frequencies in the MHz range.

Aging effects

The measured impedance spectrum $Z(f)$ of a transducer-glue-chip system is subject to various aging effects. The impedance spectrum of a chip-loaded Pz27 transducer was

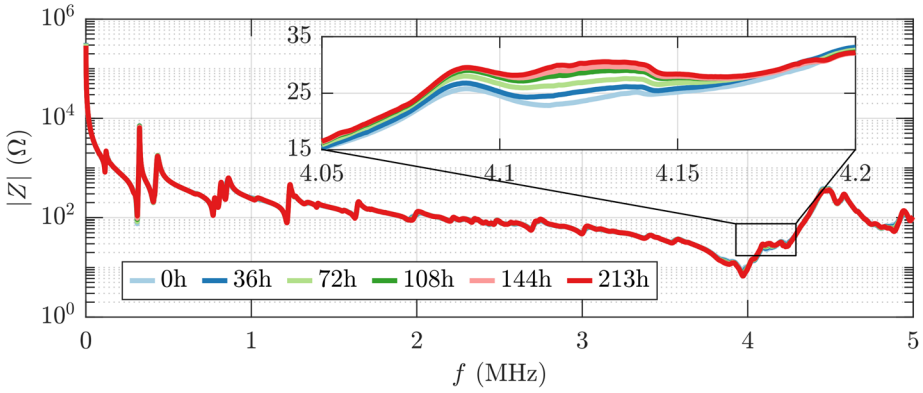

Figure 4.6: Measured electrical impedance $|Z|$ versus frequency f of a transducer-glue-chip system at different measurement intervals from $t = 0$ h to 213 h.

recorded in defined time intervals for 213 hours to characterize this effect. The results of this measurement are shown in Fig. 4.6. Here a change in the electrical impedance of approximately 10 Ω is observed for 213 hours. The cause of this aging phenomenon is unknown. However, the most likely cause is the stiffening of the glue layer, which leads to lower system damping. Another possible cause for the observed increase in the impedance is the oxidation of the electrodes of the piezoelectric transducer.

Chapter 5

Validation study of a polymer-based acoustofluidic device

5.1 Motivation

Polymer-based acoustofluidic devices open up many possibilities in the field of point-of-care diagnostics by enabling the fabrication of devices outside the cleanroom environment leading to a decreased cost per chip. However, polymer-based devices for acoustic particle separation are still largely unexplored. So far, the analysis of such polymer devices has been mainly limited to experimental studies [11, 12, 18–22, 24]. However, the whole-system ultrasound resonance (WSUR) model developed by Moiseyenko and Bruus [26] in 2019 introduced a paradigm shift in the understanding of resonance modes observed in polymer chips. This chapter aims to extend our understanding of the underlying mechanism of acoustophoresis in polymer chips by comparing experimental and numerical results.

The work of Paper I [1], presented in this chapter, acts as the cornerstone of the feedback loop to allow subsequent optimization of polymer-based devices. In order to develop high-performance acoustophoresis devices made from polymers, it needs to be validated that our numerical model can correctly predict the experimental performance of the device. In this chapter, an acoustofluidic device milled from the polymer PMMA, using a design following conventional glass chips but utilizing anti-symmetric actuation as proposed in Refs. [26], is presented. Experimental results of the devices' ability to focus 5 µm-diameter polystyrene particles are compared with numerical results. Furthermore, the focusability $\mathcal{F}(f)$ is introduced as a metric to compare device performance across frequencies f between experiment and simulation.

To extend beyond the work of Paper I [1], a 1D model of transverse resonances of polymer chips perpendicular to the actuation direction is discussed at the end of this chapter. While the resonance modes of polymer devices are typically too complex to utilize such 1D models, they can aid numerical optimization by providing the dimensions of an initial geometry.

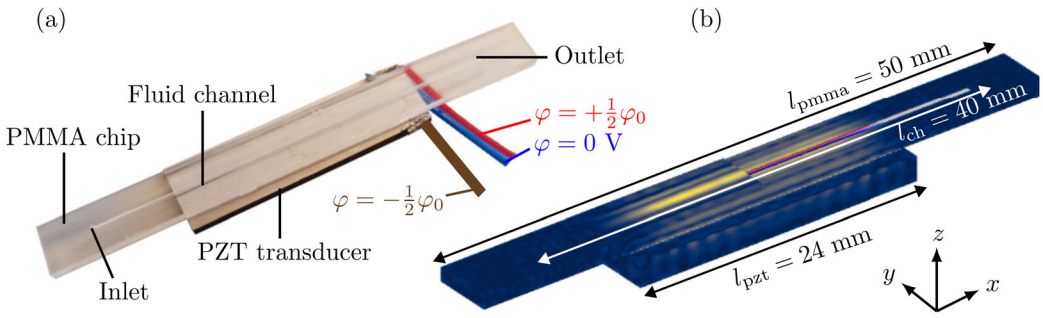

Figure 5.1: (a) Image of the polymer-based acoustofluidic device consisting of piezoelectric transducer and PMMA-based microfluidic chip. An anti-symmetric electrical potential $\pm\frac{\varphi_0}{2}$ was applied to the split top electrodes to achieve anti-symmetric actuation. (b) Numerical results of the displacement field of the whole chip at the system resonance frequency $f = 1.17$ MHz with displacement magnitude u ranging from 0 nm (dark blue) to 50 nm (yellow). The pressure field in the channel $p_{1,\mathrm{fl}}$ ranges from -600 kPa (blue) to 600 kPa (red). In the microfluidic channel, a pressure wave resembling a half-wave is observed at this frequency. Figure adapted from [1].

5.2 Summary of the results from Paper I

Fig. 5.1(a) shows an overview of the polymer-based chip, which is studied in Paper I [1]. The microfluidic chip consists of micro-milled PMMA, and it is coupled to a piezoelectric Pz26 transducer via a thin glycerol-based coupling layer. A slight groove separates the top electrode of the transducer to allow anti-symmetric actuation with a constant voltage amplitude $\frac{\varphi_0}{2} = 15$ V across the frequency range from 0.5 to 2.5 MHz. Numerical simulations of a quarter of the actual geometry were performed, and symmetry boundary conditions were utilized to obtain the results for the whole device, as shown in Fig. 5.1(b).

In the acoustic focusing experiments that were performed by Mathias Ohlin (AcouSort), a strong resonance at a frequency of 1.14 MHz was observed with an acoustic energy density of 13 J m^{-3} in the fluid channel. The electrical input power has not been monitored during the measurement, but based on the applied actuation voltage and the measured admittance, the power dissipation of the system is estimated to approximately 200 mW at this resonance frequency. Flow rates of up to 10 µL/min have been achieved experimentally while maintaining focusing of 5 µm-diameter polystyrene particles in the PMMA device.

In the numerically simulated fields, shown in Fig. 5.2(a), the driving mechanism for this resonance is identified: a resonance of the polymer chip leads to an anti-symmetric "squeezing" motion caused by the motion of the channel walls. This finding confirms previous observations [18, 26], that the optimal driving frequency of polymer-based devices is often far from the theoretical half-wave resonance frequency at $f_{\lambda/2} = \frac{c_0}{2w_{\mathrm{ch}}} \approx 2$ MHz, for a 375 µm-wide channel containing water.

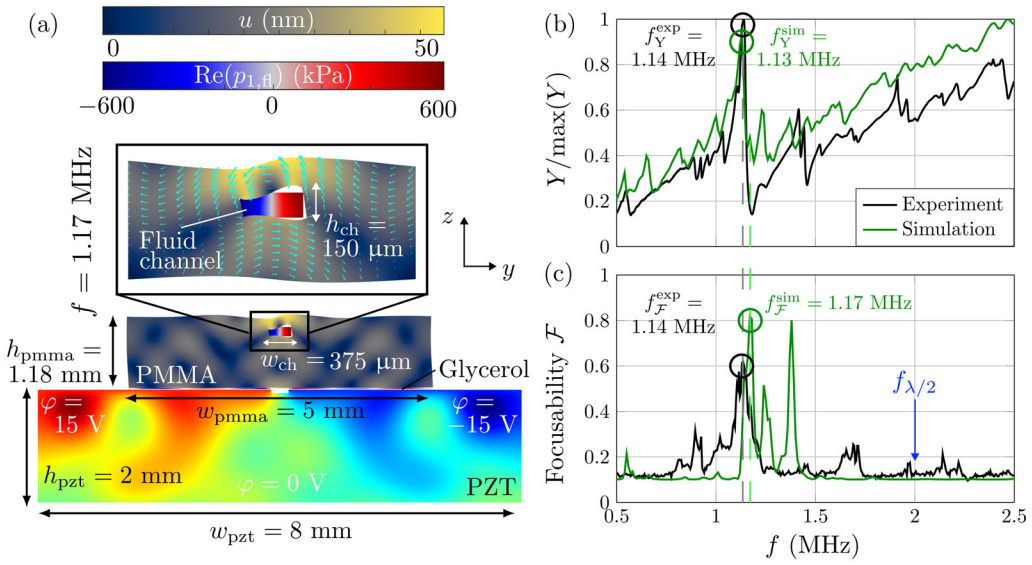

Figure 5.2: Overview of the numerical and experimental results of Paper I, adapted from [1] (a) 2D cross-section of the simulated pressure field $p_{1,\mathrm{fl}}$, displacement field u in the polymer chip, and electric potential φ in the transducer, at $f = 1.17$ MHz. Furthermore, a close-up view of the channel and the surrounding solid is provided, where the displacement has been scaled up by a factor of 1000. (b) Comparison of the experimentally measured (black) and simulated (green) admittance spectrum $Y/\max Y$. (c) Comparison of the measured and calculated focusability $\mathcal{F}$, where a blue arrow highlights the non-existent half-wave frequency $f_{\lambda/2}$.

One measure to compare the numerical and experimental results across the frequency range lies in the electrical impedance or admittance spectrum $Y(f) = 1/|Z(f)|$, as shown in Fig. 5.2(b). Using manufacturer-provided material parameters for Pz26, we find a good agreement in the frequency of the admittance maximum between simulation and experiment, which differ by only 1 kHz.

Next, to quantify the focusing performance both experimentally and numerically, the so-called focusability $\mathcal{F}$ is introduced. This quantity describes the relative fraction of particles focused in the center of the channel, as described earlier in Section 4.3.2. The experimentally-observed resonance frequency in the focusability spectrum, shown in Fig. 5.2(c), deviates by only 2.6% from the numerically simulated resonance found at 1.17 MHz. Taking a closer look at the focusability spectrum, we note that some resonances found in the simulation are not observed in the experiment and vice versa. Some of the numerically found resonances result from the assumed perfect anti-symmetry in the model. Other deviations are believed to stem from the poor knowledge of some of the required material parameters of the system, such as the complex-valued stiffness component C_{44}, relating to the transverse speed of sound and attenuation in PMMA.

A further observation that can be drawn from Fig. 5.2(b) and (c) is that in the experi-

ment, the frequency of the admittance maximum and the focusability maximum coincide. As will be discussed later in Chapter 7, in the case of constant voltage actuation, the power dissipation of the piezoelectric transducer is typically highest at this frequency. Therefore the most energy is supplied to the system at this frequency. In our numerical model, we, however, find a mismatch between the admittance maximum and focusability maximum by about 4 kHz. The best focusability coincides with a small local maximum in the admittance spectrum. This mismatch might be due to the neglection of the vertical radiation force F_z^{rad} when calculating the numerical focusability $\mathcal{F}$. Utilizing particle tracking, as done in Chapter 7, might therefore be beneficial for the computation of the focusability.

5.3 Transverse resonances in polymer devices

In Paper I [1], transverse resonances, perpendicular to the actuation direction of the chip, are observed in the microfluidic channel and the polymer chip. These resonances include longitudinal standing waves in the width of the polymer chip, which lead to a side wall motion that causes a standing pressure wave in the fluid channel. However, the frequency where these standing pressure waves occur does not match the frequency $f_{\lambda/2}$, which would be expected for such a transverse standing half-wave in a hard-walled device. Good focusing was observed at around 1.14 MHz, rather than the 2 MHz hard-wall frequency, resulting from the channel width of 375 µm. Instead of a transverse standing half-wave, typically in polymer devices, wavelengths closer to a quarter of the acoustic wavelength λ_0 are observed in the fluid channel at resonance [11, 18–20].

Polymers typically have an acoustic impedance Z_{polymer} in the order of 1–3 MRayl, while the acoustic impedance of glass or silicon is almost an order of magnitude larger.

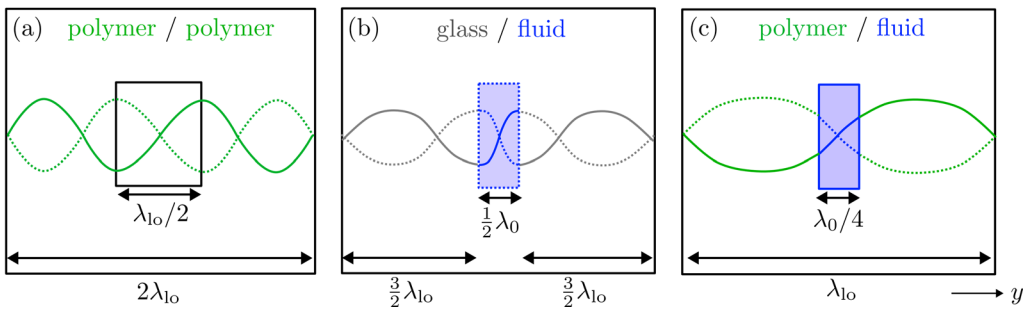

Figure 5.3: Schematic illustration of a 1D model of standing waves for different material combinations. λ_{lo} is the longitudinal wavelength in the solid material, and λ_0 is the wavelength of the fluid. (a) Standing waves in a polymer chip with a polymer-filled channel. (b) Waves in a glass chip containing a fluid channel. In this case, the hard-wall boundary condition $\boldsymbol{n} \cdot \boldsymbol{\nabla} p_1 = 0$ at the channel walls is fulfilled, and a standing half-wave in the fluid channel is observed. (c) In the case of a polymer/fluid interface, the hard-wall boundary condition is not justified anymore. In the illustrated case, a longitudinal standing wave λ_{lo} across the whole width of the polymer chip is seen. In this configuration, the fluid channel supports a quarter wave $\lambda_0/4$ to match the stress at the solid boundaries.

The hard-wall approximation ($\boldsymbol{n} \cdot \boldsymbol{\nabla} p_1 = 0$) with a resulting standing wave confined between the side walls of a microfluidic channel, therefore, is not accurate for polymer devices. Polymer-based devices characteristically show a low reflection coefficient $r \approx 0.3$ for an acoustic wave traveling from the fluid to the polymer due to the similar acoustic impedance of Z_{polymer} and Z_{water} for water. Therefore, the polymer chip's eigenmode has a substantial impact on the observed channel resonance, as explained by the WSUR model [26]. A simple 1D model illustrates the standing waves in the horizontal direction of a microfluidic device for different material combinations in Fig. 5.3.

In Fig. 5.3(a), a polymer chip with a hypothetical polymer-filled channel is shown. In such a system, the formation of standing waves in the stress σ_{yy} in the horizontal y-direction is expected. Fig. 5.3(b) shows a transverse resonator, if actuated vertically from the bottom, with a glass chip and a fluid channel. Typically, standing half-waves in the channel are observed in such a glass system. A large difference in the acoustic impedance between glass and water causes the condition $\partial_y p_1 = 0$ at the boundaries to be fulfilled. For good performance, 1D design rules suggest side wall thicknesses of $(2n+1)\,\frac{\lambda_{\text{lo}}}{4}$ for $n \in \mathbb{N}$, based on the longitudinal wavelength λ_{lo} in the chip material [55]. In contrast, Fig. 5.3(c) visualizes a simplified 1D model of standing waves in a polymer system with a fluid channel. Due to the similar acoustic impedance between water and many polymers, the standing wave inside the fluid channel is no longer confined to the channel boundaries and extends into the fluid domain. In such a system, the WSUR is the governing driving mechanism of acoustophoresis in the channel. Therefore, the width of the chip and the channel must be matched to the acoustic properties of the respective material. A good starting point for numerical optimization is a chip width of λ_{lo} and a channel width of $\lambda_0/4$, as visualized in Fig. 5.3(c).

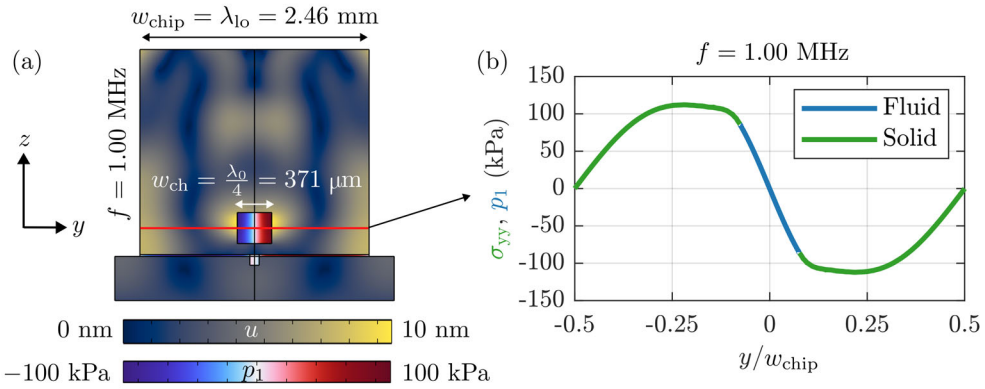

Figure 5.4: (a) The 2D simulation results of a polymer chip at a frequency of $f = 1$ MHz, a voltage amplitude of $\varphi_0 = 1\ V$, and an input power of $P_{\text{input}} = 13$ mW are shown. The chip is made from COC, has a width of 2.46 mm, and contains a 371 µm-wide channel. The displacement magnitude u and the pressure field p_1 are shown. (b) The horizontal stress component σ_{yy} (green) and the pressure p_1 (blue) along a 1D cutline (red) through the device are shown. A standing wave is observed along the y-direction of the chip.

It is, however, essential to note that this 1D model neglects shear waves with the speed of sound c_{tr}, and numerical simulations in 2D and 3D are required for an accurate description of the underlying resonances. Moreover, if the channel is placed close to the lid, as seen in Fig. 5.2, the lid's motion can impact the channel resonance. Nevertheless, geometries with an almost 1D behavior with dominating lateral displacement of the left and right channel walls exist and can yield strong acoustophoresis responses. An example of such a system is shown in Fig. 5.4. Here a polymer chip made of COC, with a chip width of $w_{\mathrm{chip}} = 2.46$ mm, matching the longitudinal wavelength λ_{lo} of COC at $f = 1$ MHz, has been simulated. The width of the channel in this system is set to $w_{\mathrm{ch}} = 371$ µm. This width relates to a quarter wavelength of water at a frequency of 1 MHz. A strong acoustophoretic response is observed in this system, with a standing wave of the stress component σ_{yy} in the horizontal y-direction of the chip, shown in Fig. 5.4(b). This numerically observed transverse resonance matches the ideal case sketched in Fig. 5.3(c) closely, and this mode forms the basis of the optimization procedure that will be described in Chapter 8.

5.4 Concluding remarks

In this chapter, the validity and the limitations of our numerical model were presented. The numerical model enables valuable insights into the mechanisms of acoustophoresis in polymer devices and extends the concept of whole-system ultrasound resonances [26].

The work presented in this chapter enables us to solve some of the confusion in the existing literature [18] on polymer-based acoustofluidics about the prediction of observed resonance frequencies. Half-wave resonances in the microfluidic channel, as such, do not exist in polymer chips due to the low acoustic impedance of polymers. Instead, the vibrational mode of the entire polymer chip needs to be considered to predict the device's resonance frequency. Typically these eigenmodes have complex displacement patterns, and their prediction requires numerical simulations and precise and accurate knowledge of the polymer material parameters. However, device geometries, with a narrow chip width in the order of the longitudinal wavelength λ_{lo} of the polymer, can result in transverse modes that match 1D predictions well. The geometry shown in Fig. 5.4(a) can be used as a starting point for further numerical optimization, as will be demonstrated in Chapter 8.

The lack of sufficiently accurate and precise material parameters for polymers has been identified as one of the main contributors to deviations between the numerical and the experimental results. In the next chapter, an easy-to-execute and low-cost technique for determining the elastic moduli of different polymer chips will be presented to solve this problem.

5.5 Paper I: J. Acoust. Soc. Am. 149, 4281-4291 (2021)

Acoustophoresis in polymer-based microfluidic devices: Modeling and experimental validation

DOI: 10.1121/10.0005113

Authors: F. Lickert, M. Ohlin, H. Bruus, and P. Ohlsson.
Journal: J. Acoust. Soc. Am. **149**, 4281-4291 (2021)

JASA ARTICLE

Acoustophoresis in polymer-based microfluidic devices: Modeling and experimental validation[a)]

Fabian Lickert,[1,b)] Mathias Ohlin,[2,c)] Henrik Bruus,[1,d)] and Pelle Ohlsson[2,e)]
[1]*Department of Physics, Technical University of Denmark, DTU Physics Building 309, DK-2800 Kongens Lyngby, Denmark*
[2]*AcouSort AB, Medicon Village, S-223 81 Lund, Sweden*

ABSTRACT:
A finite-element model is presented for numerical simulation in three dimensions of acoustophoresis of suspended microparticles in a microchannel embedded in a polymer chip and driven by an attached piezoelectric transducer at MHz frequencies. In accordance with the recently introduced principle of whole-system ultrasound resonances, an optimal resonance mode is identified that is related to an acoustic resonance of the combined transducer-chip-channel system and not to the conventional pressure half-wave resonance of the microchannel. The acoustophoretic action in the microchannel is of comparable quality and strength to conventional silicon-glass or pure glass devices. The numerical predictions are validated by acoustic focusing experiments on 5-μm-diameter polystyrene particles suspended inside a microchannel, which was milled into a polymethylmethacrylate chip. The system was driven anti-symmetrically by a piezoelectric transducer, driven by a 30-V peak-to-peak alternating voltage in the range from 0.5 to 2.5 MHz, leading to acoustic energy densities of 13 J/m^3 and particle focusing times of 6.6 s.
https://doi.org/10.1121/10.0005113
(Received 29 January 2021; revised 8 May 2021; accepted 10 May 2021; published online 16 June 2021)
[Editor: James Friend] Pages: 4281–4291

I. INTRODUCTION

Polymer-based microfluidic chips offer a multitude of advantages compared to traditional glass-based devices. A big advantage of polymers is the ease of volume fabrication and the low cost per chip using well-established manufacturing processes such as micro-injection molding or hot embossing. Further processing, such as the creation of channel structures through micro-milling as well as polymer-polymer bonding, can be performed to complete the design. Those processes also bring great flexibility in terms of materials. Thermosoftening plastics such as polycarbonate (PC) or cyclic olefin copolymer (COC), as well as polymethylmethacrylate (PMMA) or polystyrene (PS), are widely seen in the context of microfluidics. The price per polymer chip falls more than an order of magnitude below the typical cost of glass-based devices. This offers a solution to establish acoustophoresis devices also outside academia for use in medical devices. In applications outside the research environment, the need for single use devices is rising. Applications such as blood-plasma separation in a point-of-care environment require clean and unused fluidic chips to avoid cross-contamination. Furthermore, lab-on-a-chip systems are becoming well-established solutions. For acoustophoresis to play a role in those systems, compatibility with existing polymer-based microfluidic platforms is a requirement.

While polymers are already broadly used in many areas of microfluidics,[1] there have been only a few research groups working with polymers in the field of acoustofluidics. Published work on polymer-based acoustofluidic devices, made of either PMMA or PS, includes separation of bacteria and blood cells,[2,3] platelet separation,[4] and purification of lymphocytes[5,6] as well as particle flow-through separation[7,8] and focusing.[9] A common problem of single channel devices, however, is the low throughput compared to similar glass or silicon devices. This may be caused by the fact that they typically are designed for an acoustic resonance between the channel walls as is the case for glass- or silicon-based devices. This assumption is not necessarily true for polymer-based devices where the difference in the acoustic impedance between the chip material and liquid, causing the acoustic reflection, may be much lower. An indication of this is the sometimes surprising optimal operation frequency.[10]

Moiseyenko and Bruus recently introduced the principle of whole-system ultrasound resonances (WSURs)[9] and contrasted it with the conventional use of bulk acoustic waves (BAWs) and surface acoustic waves (SAWs) in acoustophoresis devices. According to the WSUR principle, the optimal conditions for achieving acoustophoresis in polymer devices are obtained by considering the dimensions of the whole system and the corresponding whole-system resonances instead of attempting to base the acoustophoresis on local standing wave resonances excited locally inside the liquid of the microchannels. We base our analysis of acoustophoresis in polymer chips on the WSUR principle.

[a)]This paper is part of a special issue on Theory and Applications of Acoustofluidics.
[b)]ORCID: 0000-0001-7729-5976.
[c)]ORCID: 0000-0002-7023-4772.
[d)]Electronic mail: bruus@fysik.dtu.dk, ORCID: 0000-0001-5827-2939.
[e)]ORCID: 0000-0003-4038-1605.

In this paper, we present a finite-element model for three-dimensional (3D) numerical simulations of polymer-based acoustofluidic devices and validate it experimentally. As a proof of concept, we model acoustophoresis of suspended microparticles in a specific microchannel embedded in a PMMA polymer chip and driven by an attached piezoelectric transducer at MHz frequencies. We validate the model experimentally and use it to explore some of the obstacles for efficient polymer-based acoustophoresis and to design an operational device. Our results show that the usual design rules of conventional glass-based devices do not apply for polymer-based chips. This especially holds true when comparing channel resonances in hard-walled glass devices with the WSUR modes found in polymer-based devices with acoustic impedances close to that of water.

In Sec. II, we introduce the geometry, the materials, and the design of the polymer-based acoustofluidic device. In Sec. III, we present the basic theory, including governing equations and boundary conditions, and its implementation in the numerical 3D finite-element model. We show the resulting fields of the chip at resonance in Sec. IV and define a metric for the efficiency of the acoustophoretic particle focusing as a function of frequency. The experimental setup and the fabricated polymer chip are described in Sec. V A, and in Sec. V B, we summarize our experimental findings on the focusing ability of the chip as a function of frequency. Finally, in Sec. VI, we conclude with a discussion of the presented results.

II. THE DEVICE

The design of our acoustofluidic device is following the design of typical glass-based BAW devices with a long straight channel used for acoustic particle separation.[11–13] As listed in Table I, the channel is rectangular with height $h_{\mathrm{ch}} = 150\,\mu$m and width $w_{\mathrm{ch}} = 375\,\mu$m, which in a hard-wall channel would sustain a horizontal pressure half-wave at 2 MHz. In a polymer device governed by WSUR modes, a much different resonance frequency is found. The device consists of a polymer chip made from PMMA, containing a microfluidic channel. Actuation is performed using a piezoelectric lead-zirconate-titanate (PZT) transducer. The PZT transducer and the PMMA chip are coupled through a 20-μm-thin layer of glycerol [99% volume-per-volume (v/v) glycerol, 1% (v/v) water], a well-proven method that allows for long-time operation and access to simple exchange of chip and transducer.[14–16] Since the temperature of the device is kept constant in the experiments by using a Peltier-element feedback loop, we neglect thermal effects in the numerical modeling.

TABLE I. The length (l), width (w), and height (h) of the chip (pmma), the channel (ch), the piezoelectric transducer (pzt), the groove (grv), and the glycerol coupling layer (glc).

Symbol	Value	Symbol	Value
l_{pmma}	50 mm	l_{ch}	40 mm
w_{pmma}	5 mm	w_{ch}	375 μm
h_{pmma}	1.18 mm	h_{ch}	150 μm
l_{pzt}	24 mm	w_{grv}	300 μm
w_{pzt}	8 mm	h_{grv}	65 μm
h_{pzt}	2 mm	h_{cpl}	20 μm

A sketch of the acoustofluidic device used in the modeling and experiments is shown in Fig. 1 and supplemented by Table I. For simplicity, the shown inlets and outlets were omitted in the modeling. To ensure an optimal anti-symmetric motion in the yz-plane, the top electrode of the transducer is split in two halves by cutting a small groove using a dicing saw along the x-direction and driven by respective alternating (AC) voltages with a 180° phase difference similar to the work reported in the literature.[9,17,18]

III. THEORY

A. Governing equations

In our simulations, we follow closely the theory presented by Skov *et al.*,[19] including the effective boundary layer theory by Bach and Bruus.[20] We consider a time-harmonic electric potential $\tilde{\varphi}(\boldsymbol{r}, t)$, which excites the piezoelectric transducer and induces a displacement field $\tilde{\boldsymbol{u}}(\boldsymbol{r}, t)$

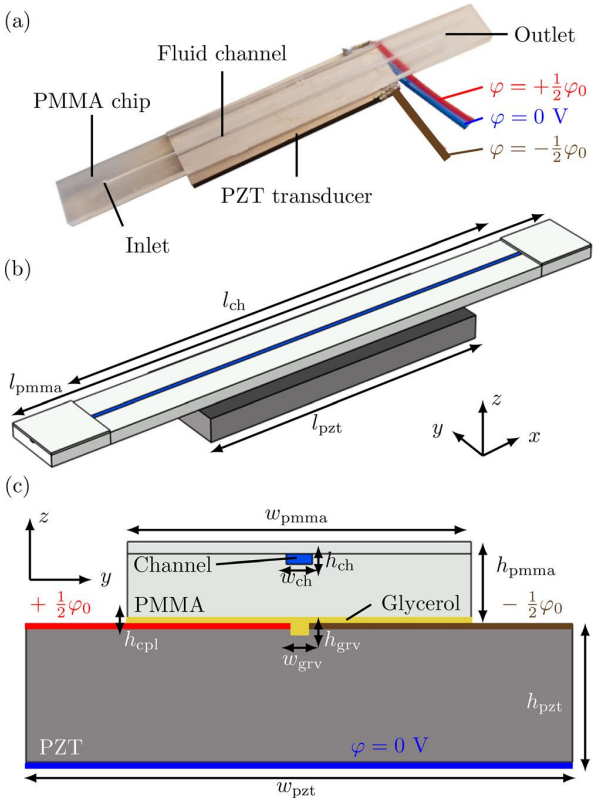

FIG. 1. (Color online) (a) A photograph of the acoustofluidic device, consisting of PMMA chip with a straight microfluidic channel, a piezoelectric transducer and a coupling layer made from glycerol. (b) Sketch of the 3D model, where the PMMA lid above the channel is removed to show the microchannel (blue) along the x axis. (c) Cross section of the 3D model in the vertical yz-plane. The coupling layer is visualized in yellow.

https://doi.org/10.1121/10.0005113

in the solids as well as an acoustic pressure $\tilde{p}_1(\boldsymbol{r},t)$ in the fluid channel and in the coupling layer,

$$\tilde{\varphi}(\boldsymbol{r},t) = \varphi(\boldsymbol{r})\,\mathrm{e}^{-\mathrm{i}\omega t}, \tag{1a}$$

$$\tilde{\boldsymbol{u}}(\boldsymbol{r},t) = \boldsymbol{u}(\boldsymbol{r})\,\mathrm{e}^{-\mathrm{i}\omega t}, \tag{1b}$$

$$\tilde{p}_1(\boldsymbol{r},t) = p_1(\boldsymbol{r})\,\mathrm{e}^{-\mathrm{i}\omega t}, \tag{1c}$$

with the angular frequency $\omega = 2\pi f$. The time-harmonic phase factor $\mathrm{e}^{-\mathrm{i}\omega t}$ cancels out in the following linear governing equations. From first-order perturbation theory, it follows that the acoustic pressure $p_{1,\mathrm{fl}}$ in the fluid channel is governed by the Helmholtz equation with damping coefficient Γ_{fl},

$$\nabla^2 p_{1,\mathrm{fl}} = -\frac{\omega^2}{c_{\mathrm{fl}}^2}(1+\mathrm{i}\Gamma_{\mathrm{fl}})\,p_{1,\mathrm{fl}},$$
$$\text{with } \Gamma_{\mathrm{fl}} = \left(\frac{4}{3}\eta_{\mathrm{fl}} + \eta_{\mathrm{fl}}^{\mathrm{b}}\right)\omega\kappa_{\mathrm{fl}}, \tag{2}$$

where c_{fl} is the speed of sound, ρ_{fl} is the density, $\kappa_{\mathrm{fl}} = (\rho_{\mathrm{fl}}c_{\mathrm{fl}}^2)^{-1}$ is the isentropic compressibility, and η_{fl} and $\eta_{\mathrm{fl}}^{\mathrm{b}}$ are the dynamic and bulk viscosity of the fluid, respectively. The acoustic velocity $\boldsymbol{v}_{1,\mathrm{fl}}$ of the fluid inside the channel can be expressed as a gradient of the pressure $p_{1,\mathrm{fl}}$ as

$$\boldsymbol{v}_{1,\mathrm{fl}} = -\mathrm{i}\,\frac{1-\mathrm{i}\Gamma_{\mathrm{fl}}}{\omega\rho_{\mathrm{fl}}}\,\nabla p_{1,\mathrm{fl}}. \tag{3}$$

In the thin glycerol coupling layer, we cannot apply the effective boundary layer theory for the acoustic pressure $p_{1,\mathrm{cpl}}$ and velocity $\boldsymbol{v}_{1,\mathrm{cpl}}$.[20] So here, we implement the full set of governing equations,

$$\nabla\cdot\boldsymbol{v}_{1,\mathrm{cpl}} = \mathrm{i}\omega\kappa_{\mathrm{cpl}}p_{1,\mathrm{cpl}}, \tag{4a}$$

$$\nabla\cdot\boldsymbol{\sigma}_{\mathrm{cpl}} = -\mathrm{i}\omega\rho_{\mathrm{cpl}}\,\boldsymbol{v}_{1,\mathrm{cpl}}, \tag{4b}$$

$$\boldsymbol{\sigma}_{\mathrm{cpl}} = \eta_{\mathrm{cpl}}\left[\nabla\boldsymbol{v}_{1,\mathrm{cpl}} + (\nabla\boldsymbol{v}_{1,\mathrm{cpl}})^{\top}\right] + \left(\eta_{\mathrm{cpl}}^{\mathrm{b}} - \frac{2}{3}\eta_{\mathrm{cpl}}\right)(\nabla\cdot\boldsymbol{v}_{1,\mathrm{cpl}})\mathbf{I} - p_{1,\mathrm{cpl}}\,\mathbf{I}. \tag{4c}$$

Here, $\boldsymbol{\sigma}_{\mathrm{cpl}}$ is the viscous stress tensor, $\mathbf{I}$ is the identity tensor, $()^{\top}$ is the transpose, ρ_{cpl} is the density, κ_{cpl} is the isentropic compressibility, and η_{cpl} and $\eta_{\mathrm{cpl}}^{\mathrm{b}}$ are the dynamic and bulk viscosity of the coupling layer, respectively.

The equation of motion for the displacement field $\boldsymbol{u}$ of an elastic solid with density ρ_{sl} is Cauchy's equation

$$-\omega^2\rho_{\mathrm{sl}}\,\boldsymbol{u} = \nabla\cdot\boldsymbol{\sigma}_{\mathrm{sl}}, \tag{5}$$

where $\boldsymbol{\sigma}_{\mathrm{sl}}$ is the stress tensor. The components σ_{ik} of the stress tensor are related by the stiffness tensor $\boldsymbol{C}$ to the strain tensor $\frac{1}{2}(\partial_i u_k + \partial_k u_i)$ and, for a linear isotropic elastic material, are written in the Voigt notation as

$$\begin{pmatrix}\sigma_{xx}\\ \sigma_{yy}\\ \sigma_{zz}\\ \hline \sigma_{yz}\\ \sigma_{xz}\\ \sigma_{xy}\end{pmatrix} = \left(\begin{array}{ccc|ccc} C_{11} & C_{12} & C_{12} & 0 & 0 & 0\\ C_{12} & C_{11} & C_{12} & 0 & 0 & 0\\ C_{12} & C_{12} & C_{11} & 0 & 0 & 0\\ \hline 0 & 0 & 0 & C_{44} & 0 & 0\\ 0 & 0 & 0 & 0 & C_{44} & 0\\ 0 & 0 & 0 & 0 & 0 & C_{44}\end{array}\right)\begin{pmatrix}\partial_x u_x\\ \partial_y u_y\\ \partial_z u_z\\ \hline \partial_y u_z + \partial_z u_y\\ \partial_x u_z + \partial_z u_x\\ \partial_x u_y + \partial_y u_x\end{pmatrix}. \tag{6}$$

Due to symmetry, the remaining three components of the stress are obtained by the relation $\sigma_{ik} = \sigma_{ki}$. The components $C_{ik} = C'_{ik} + \mathrm{i}C''_{ik}$ of the stiffness tensor $\boldsymbol{C}$ are complex-valued to describe the weakly attenuated acoustics in the solid.

The electrical potential φ inside the PZT transducer is governed by Gauss's law for a linear, homogeneous dielectric with a zero density of free charges,

$$\nabla\cdot\boldsymbol{D} = \nabla\cdot(-\boldsymbol{\varepsilon}\cdot\nabla\varphi) = 0, \tag{7}$$

where $\boldsymbol{D}$ is the electric displacement field and $\boldsymbol{\varepsilon}$ the dielectric tensor. Furthermore, in PZT, the complete linear electromechanical coupling relating the stress and the electric displacement to the strain and the electric field is given by the Voigt notation as

$$\begin{pmatrix}\sigma_{xx}\\ \sigma_{yy}\\ \sigma_{zz}\\ \hline \sigma_{yz}\\ \sigma_{xz}\\ \sigma_{xy}\\ \hline D_x\\ D_y\\ D_z\end{pmatrix} = \left(\begin{array}{ccc|ccc|ccc} C_{11} & C_{12} & C_{13} & 0 & 0 & 0 & 0 & 0 & -e_{31}\\ C_{12} & C_{11} & C_{13} & 0 & 0 & 0 & 0 & 0 & -e_{31}\\ C_{13} & C_{13} & C_{33} & 0 & 0 & 0 & 0 & 0 & -e_{33}\\ \hline 0 & 0 & 0 & C_{44} & 0 & 0 & 0 & -e_{15} & 0\\ 0 & 0 & 0 & 0 & C_{44} & 0 & -e_{15} & 0 & 0\\ 0 & 0 & 0 & 0 & 0 & C_{66} & 0 & 0 & 0\\ \hline 0 & 0 & 0 & 0 & e_{15} & 0 & \varepsilon_{11} & 0 & 0\\ 0 & 0 & 0 & e_{15} & 0 & 0 & 0 & \varepsilon_{11} & 0\\ e_{31} & e_{31} & e_{33} & 0 & 0 & 0 & 0 & 0 & \varepsilon_{33}\end{array}\right)\begin{pmatrix}\partial_x u_x\\ \partial_y u_y\\ \partial_z u_z\\ \hline \partial_y u_z + \partial_z u_y\\ \partial_x u_z + \partial_z u_x\\ \partial_x u_y + \partial_y u_x\\ \hline -\partial_x\varphi\\ -\partial_y\varphi\\ -\partial_z\varphi\end{pmatrix}. \tag{8}$$

As before, the remaining three components of the stress tensor are given by the symmetry relation $\sigma_{ik} = \sigma_{ki}$.

B. Boundary conditions between liquid, solid, and PZT

In the following, we state the boundary conditions of the fields on all boundaries and interfaces of the model. On the surfaces facing the surrounding air, we assume zero stress on the PMMA and the PZT as well as zero free surface charge density on the PZT. On the surfaces with electrodes, the PZT has a specified AC-voltage amplitude. On the internal surfaces between PMMA and PZT, the stress and displacement are continuous, and likewise on the fluid-solid interface, but here they are in the form of the effective boundary conditions derived by Bach and Bruus.[20] These effective boundary conditions include the viscous boundary layer analytically, and thus we avoid resolving these very shallow boundary layers numerically. The effective boundary conditions include the velocity $\boldsymbol{v}_{\mathrm{sl}} = -\mathrm{i}\omega\boldsymbol{u}$ of the solid (sl) and the complex-valued shear-wave number $k_{\mathrm{s}} = (1+\mathrm{i})\,\delta_{\mathrm{fl}}^{-1}$ of the fluid (fl), where $\delta_{\mathrm{fl}} = \sqrt{2\eta_{\mathrm{fl}}/(\rho_{\mathrm{fl}}\omega)} \approx 0.5\,\mu\mathrm{m}$ is the thickness of the boundary layer. In the coupling layer of height $h_{\mathrm{cpl}} = 20\,\mu\mathrm{m}$, the boundary layer thickness, $\delta_{\mathrm{cpl}} = 12\,\mu\mathrm{m}$, is nearly the same, so the effective boundary conditions do not apply. We therefore implement the full continuous conditions for stress and velocity at the interface of the solid (sl) and the coupling layer (cpl),

$$\text{PZT bottom}: \quad \varphi = 0, \tag{9a}$$

$$\text{PZT top}: \quad \varphi = \pm\frac{1}{2}\varphi_0, \tag{9b}$$

$$\text{PZT}-\text{air}: \quad \boldsymbol{D}\cdot\boldsymbol{n} = 0, \tag{9c}$$

$$\text{sl}-\text{air}: \quad \boldsymbol{\sigma}_{\mathrm{sl}}\cdot\boldsymbol{n} = \boldsymbol{0}, \tag{9d}$$

$$\text{sl}-\text{fl}: \quad \boldsymbol{\sigma}_{\mathrm{sl}}\cdot\boldsymbol{n} = -p_{1,\mathrm{fl}}\,\boldsymbol{n} + \mathrm{i}k_{\mathrm{s}}\eta_{\mathrm{fl}}(\boldsymbol{v}_{\mathrm{sl}} - \boldsymbol{v}_{1,\mathrm{fl}}), \tag{9e}$$

$$\text{fl}-\text{sl}: \quad \boldsymbol{v}_{1,\mathrm{fl}}\cdot\boldsymbol{n} = \boldsymbol{v}_{\mathrm{sl}}\cdot\boldsymbol{n} + \frac{\mathrm{i}}{k_{\mathrm{s}}}\nabla_{\parallel}\cdot(\boldsymbol{v}_{\mathrm{sl}} - \boldsymbol{v}_{1,\mathrm{fl}})_{\parallel}, \tag{9f}$$

$$\text{cpl}-\text{sl}: \quad \boldsymbol{v}_{1,\mathrm{cpl}} = \boldsymbol{v}_{\mathrm{sl}} \tag{9g}$$

$$\text{sl}-\text{cpl}: \quad \boldsymbol{\sigma}_{\mathrm{sl}}\cdot\boldsymbol{n} = \boldsymbol{\sigma}_{\mathrm{cpl}}\cdot\boldsymbol{n}. \tag{9h}$$

We use the symmetry at the yz- and xz-planes to reduce the model to quarter size in the domain $x > 0$ and $y > 0$, allowing for finer meshing and/or faster computations. We apply symmetric boundary conditions at the yz-plane $x = 0$ and anti-symmetry at the xz-plane $y = 0$,

$$\text{Symmetry at } x = 0:$$

$$u_x = 0, \quad \sigma_{yx,\mathrm{sl}} = \sigma_{zx,\mathrm{sl}} = 0, \tag{10a}$$

$$v_{x,\mathrm{cpl}} = 0, \quad \sigma_{yx,\mathrm{cpl}} = \sigma_{zx,\mathrm{cpl}} = 0, \tag{10b}$$

$$\partial_x p_{1,\mathrm{fl}} = 0, \quad \partial_x\varphi = 0. \tag{10c}$$

$$\text{Anti-symmetry at } y = 0:$$

$$\sigma_{yy,\mathrm{sl}} = 0, \quad u_x = u_z = 0, \tag{10d}$$

$$\sigma_{yy,\mathrm{cpl}} = 0, \quad v_{x,\mathrm{cpl}} = v_{z,\mathrm{cpl}} = 0, \tag{10e}$$

$$p_{1,\mathrm{fl}} = 0, \quad \varphi = 0. \tag{10f}$$

C. Acoustic energy density and radiation force

The space- and time-averaged acoustic energy density $E_{\mathrm{ac}}^{\mathrm{fl}}$ in a fluid in a specified volume V_{fl} is given as the sum of the time-averaged kinetic and compressional energy,

$$E_{\mathrm{ac}}^{\mathrm{fl}} = \frac{1}{V_{\mathrm{fl}}}\int_{V_{\mathrm{fl}}}\left[\frac{1}{4}\rho_{\mathrm{fl}}|\boldsymbol{v}_{1,\mathrm{fl}}|^2 + \frac{1}{4}\kappa_{\mathrm{fl}}|p_{1,\mathrm{fl}}|^2\right]\mathrm{d}V. \tag{11}$$

The acoustic radiation force $\boldsymbol{F}^{\mathrm{rad}}$ acting on particles in the fluid is minus the gradient of the potential U^{rad}, specified for particles with radius a, density ρ_{ps}, and compressibility κ_{ps}, suspended in a fluid with density ρ_{fl} and compressibility κ_{fl},[21]

$$\boldsymbol{F}^{\mathrm{rad}} = -\nabla U^{\mathrm{rad}}, \tag{12a}$$

$$U^{\mathrm{rad}} = \pi a^3\left(\frac{1}{3}f_0\,\kappa_{\mathrm{fl}}|p_{1,\mathrm{fl}}|^2 - \frac{1}{2}f_1\,\rho_{\mathrm{fl}}|\boldsymbol{v}_{1,\mathrm{fl}}|^2\right), \tag{12b}$$

$$f_0 = 1 - \frac{\kappa_{\mathrm{ps}}}{\kappa_{\mathrm{fl}}}, \quad f_1 = \frac{2(\rho_{\mathrm{ps}} - \rho_{\mathrm{fl}})}{2\rho_{\mathrm{ps}} + \rho_{\mathrm{fl}}}, \tag{12c}$$

where f_0 and f_1 are the so-called acoustic monopole and dipole scattering coefficients, respectively.

D. Electrical impedance and admittance

The electrical impedance $Z = \varphi_0/I$ and admittance $Y = I/\varphi_0$ of the device are defined by the potential difference φ_0 between the two split top electrodes of the PZT [Eq. (9b)] and the electrical current I through one of these electrodes. Denoting the surface of the positive split electrode as $\partial\Omega_+$, we use the surface integral of the current density $\boldsymbol{J}$ to obtain $I = \int_{\partial\Omega_+}\boldsymbol{n}\cdot\boldsymbol{J}\,\mathrm{d}a = -\mathrm{i}\omega\int_{\Omega_+}\boldsymbol{n}\cdot(\boldsymbol{D} + \epsilon_0\nabla\varphi)\,\mathrm{d}a$,[22]

$$\begin{aligned} Y = \frac{1}{Z} = \frac{I}{\varphi_0} &= \frac{1}{\varphi_0}\int_{\partial\Omega_+}\boldsymbol{J}\cdot\boldsymbol{n}\,\mathrm{d}a \\ &= \frac{-\mathrm{i}\omega}{\varphi_0}\int_{\partial\Omega_+}[e_{31}(\partial_x u_x + \partial_y u_y) + e_{33}\partial_z u_z \\ &\quad + (\varepsilon_0 - \varepsilon_{33})\partial_z\varphi]\mathrm{d}a. \end{aligned} \tag{13}$$

E. Material properties

The values of the material parameters are taken from the literature to match the validation experiments we have carried out. We study a suspension of 4.8-μm-diameter PS particles at a temperature of $T = 20\,^{\circ}\mathrm{C}$. To obtain neutral buoyancy, the liquid in the microchannel is chosen to be water mixed with a volume fraction of 16% iodixanol. The polymer is PMMA, the transducer is PZT, and the coupling

https://doi.org/10.1121/10.0005113

layer is glycerol. All parameter values used in the simulation are listed in Table II.

IV. RESULTS OF 3D SIMULATIONS

The simulations were implemented in the finite-element software COMSOL Multiphysics 5.5.[37] We closely follow the implementation of the numerical model given by Skov *et al.*,[19] where further details on the implementation are given. Using the symmetry conditions presented above, we solved a quarter of the actual 3D geometry and subsequently obtained the full solutions by mirroring the results along the *xz*- and *yz*-planes. The obtained fields are the potential φ in the PZT, the displacement $\boldsymbol{u}$ in all solid materials, and the acoustic pressure fields $p_{1,\mathrm{fl}}$ and $p_{1,\mathrm{cpl}}$ in the fluid and the coupling layer, respectively. In our time-harmonic simulations, we study the frequency range between 0.5 and 2.5 MHz, around the nominal 1-MHz resonance of the PZT transducer. The simulations were performed on the DTU high-performance cluster computer using shared-memory parallelism with a total of 16 cores and 160 gigabytes of random access memory. The meshing was done with a maximum element size of $h_{\mathrm{fl}}^{\max} = 70\,\mu$m in the fluid channel, $h_{\mathrm{pzt}}^{\max} = 280\,\mu$m in the PZT, and $h_{\mathrm{pmma}}^{\max} = 200\,\mu$m in the PMMA and vertically resolving the boundary layer in the coupling layer with five elements. The final mesh consists of about 100 000 mesh elements, corresponding to approximately 1.8×10^6 degrees of freedom. The computation time per frequency was about 20 min. We have performed a standard mesh-convergence study to ensure that our meshing is adequate.[19,38]

TABLE II. List of parameters at 20 °C used in the numerical simulation. Channel fluid [84% (v/v) water, 16% (v/v) iodixanol], 4.8-μm-diameter PS particles, glycerol solution [99% (v/v) glycerol, 1% (v/v) water], PMMA, and PZT. For PMMA $C_{12} = C_{11} - 2C_{44}$. For PZT $C_{12} = C_{11} - 2C_{66}$. ε_0 is the vacuum permittivity.

Parameter	Symbol	Value	Unit
Water-iodixanol mixture (Refs. 23 and 24)			
Mass density	ρ_{fl}	1050	kg m^{-3}
Speed of sound	c_{fl}	1482.3	m s^{-1}
Compressibility	κ_{fl}	433.4	TPa^{-1}
Dynamic viscosity	η_{fl}	1.474	mPa s
Bulk viscosity	$\eta_{\mathrm{fl}}^{\mathrm{b}}$	1.966	mPa s
PS (Ref. 25)			
Mass density	ρ_{ps}	1050	kg m^{-3}
Compressibility	κ_{ps}	238	TPa^{-1}
Monopole coefficient	f_0	0.479	—
Dipole coefficient	f_1	0	—
Glycerol (Refs. 26–28)			
Mass density	ρ_{cpl}	1260.4	kg m^{-3}
Speed of sound	c_{cpl}	1922.8	m s^{-1}
Compressibility	κ_{cpl}	214.6	TPa^{-1}
Dynamic viscosity	η_{cpl}	1.137	Pa s
Bulk viscosity	$\eta_{\mathrm{cpl}}^{\mathrm{b}}$	0.790	Pa s
PMMA (Refs. 29–36)			
Mass density	ρ_{sl}	1186	kg m^{-3}
Elastic modulus	C_{11}	8.934 − i0.100	GPa
Elastic modulus	C_{44}	2.323 − i0.029	GPa
PZT (Refs. 17, 19, and 36)			
Mass density	ρ_{sl}	7700	kg m^{-3}
Elastic modulus	C_{11}	168 − i3.36	GPa
Elastic modulus	C_{12}	110 − i2.20	GPa
Elastic modulus	C_{13}	99.9 − i2.00	GPa
Elastic modulus	C_{33}	123 − i2.46	GPa
Elastic modulus	C_{44}	30.1 − i0.60	GPa
Coupling constant	e_{15}	9.86 − i0.20	C m^{-2}
Coupling constant	e_{31}	−2.8 + i0.06	C m^{-2}
Coupling constant	e_{33}	14.7 − i0.29	C m^{-2}
Electric permittivity	ε_{11}	$828\epsilon_0\,(1 - \mathrm{i}0.02)$	—
Electric permittivity	ε_{33}	$700\epsilon_0\,(1 - \mathrm{i}0.02)$	—

A. Electric admittance and acoustic energy density

The response of a piezoelectric transducer is usually studied by measuring the electrical impedance Z and finding its characteristic resonance and anti-resonance frequencies. The latter correspond to minima in the electrical impedance spectrum or maxima in the admittance spectrum $Y = 1/Z$ and are associated with maxima in the displacement of the transducer.[39] The simulated electrical admittance spectrum is shown in Fig. 2(a). The simulations show a maximum of the admittance at a frequency $f_{\mathrm{pzt}} = 1.13$ MHz, close to the 1-MHz resonance frequency specified by the manufacturer of the PZT transducer. This fair agreement is obtained despite our use of a split top electrode driven with an antisymmetric voltage actuation, in contrast to the usual symmetrically driven full-top electrode mode.

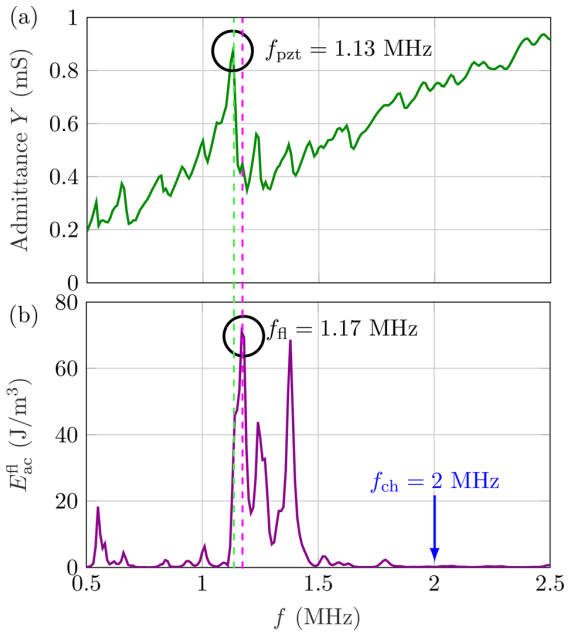

FIG. 2. (Color online) Simulation results in the frequency range 0.5–2.5 MHz. (a) The electrical admittance Y of the mounted PZT transducer with a maximum at $f_{\mathrm{pzt}} = 1.13$ MHz. (b) The acoustic energy density $E_{\mathrm{ac}}^{\mathrm{fl}}$ in the channel with a maximum $E_{\mathrm{ac}}^{\mathrm{fl}} = 71\,\mathrm{J\,m^{-3}}$ at $f_{\mathrm{fl}} = 1.17$ MHz, far below the hard-wall resonance $f_{\mathrm{ch}} = 2$ MHz (blue).

In Fig. 2(b) is shown the simulated acoustic energy density E_{ac}^{fl} of the part of the fluid channel that is located directly above the PZT transducer. We find the maximum value to be $E_{ac}^{fl} = 71\,\mathrm{J\,m^{-3}}$ at $f_{fl} = 1.17\,\mathrm{MHz}$, which is close to, but 0.04 MHz higher than, the resonance frequency f_{pzt} found in the admittance spectrum.

As mentioned in Sec. II, had the microchannel of width $w_{ch} = 375\,\mu\mathrm{m}$ had hard walls, it would have sustained an acoustic half-wave resonance at $f_{ch} = 2\,\mathrm{MHz}$. In contrast, the simulations with PMMA walls show a strong acoustic resonance at $f_{fl} = 1.17\,\mathrm{MHz}$, much lower than f_{ch}, but near the resonance frequency $f_{pzt} = 1.13\,\mathrm{MHz}$ of the PZT transducer. As the resonance f_{fl} matches neither f_{ch} nor f_{pzt}, it is clearly a whole-system resonance.[9] This conclusion is supported by a closer inspection of the simulated fields at f_{fl} shown in Fig. 3 and in the corresponding videos in the supplementary material.[40]

Analyzing the displacement field $\boldsymbol{u}$, we note that the strongest displacement amplitude is obtained in the part of the PMMA located above the PZT [see Fig. 3(d)]. In particular, the highest displacement is found in the region above the fluid channel, which we will refer to as the channel lid in the following. We further note that the acoustic pressure forms a perfect standing anti-symmetric wave (albeit not a half-wave) with a vertical pressure nodal plane along the channel center in the region above the transducer. The amplitude of the pressure in the center of the fluid channel amounts to $p_{1,fl} = 755\,\mathrm{kPa}$. This pressure amplitude decreases along the x-direction, toward both ends of the polymer chip. Finally, we observe a horizontal pressure wave in the glycerol coupling layer with an amplitude of about $p_{1,cpl} = 491\,\mathrm{kPa}$.

The cross section of the acoustofluidic device, shown in Figs. 3(c) and 3(d), reveals an anti-symmetric motion of the sidewalls in the horizontal y-direction. The channel lid is performing a standing half-wave-like motion, perfectly in phase with the oscillation of the standing pressure wave inside the channel. An analysis of varying geometries of the polymer chip dimensions gave rise to the hypothesis that it is the motion of the sidewalls that is driving the channel resonance. To obtain a strong resonance, it is furthermore important to match the sidewall motion with the motion of the channel lid. Simulations so far have shown ideal results for inward motion of the sidewall, coupled with outward motion of the channel lid in one side of the channel. The width w_{ch} of the fluid channel and the thickness of the lid appear to set the frequency of the anti-symmetric standing wave in the lid, and by matching this frequency with that of the anti-symmetric sidewall resonance, high acoustic pressure amplitudes and gradients are produced in the channel. This whole-system resonance is governed by the dimensions of the entire geometry of the chip and is difficult to predict analytically.

B. Acoustophoretic focusability

To predict the acoustic focusing abilities of the device numerically, we compute the fraction of suspended particles

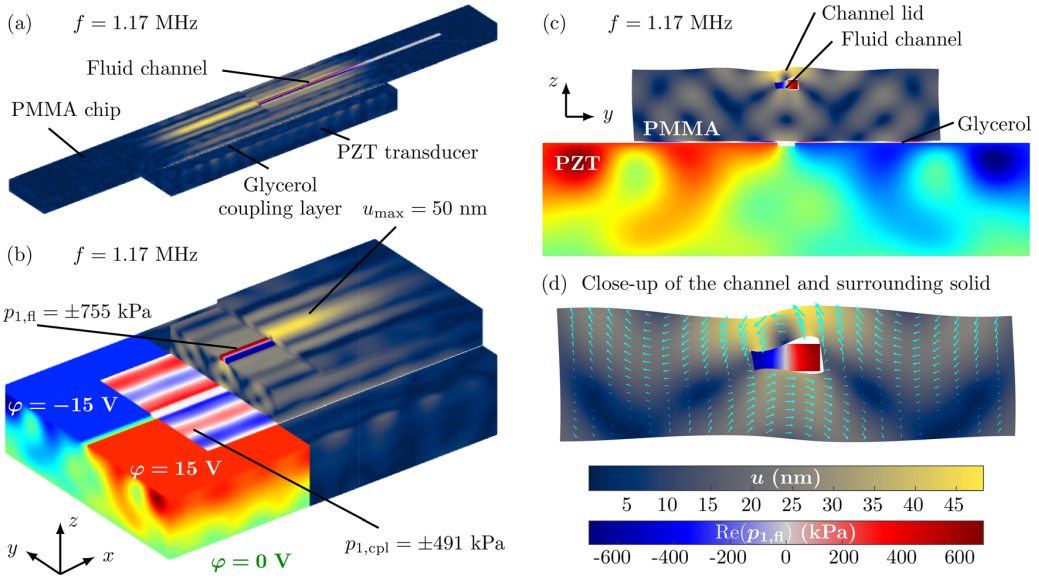

FIG. 3. (Color online) Numerical results of the 3D model, evaluated at a frequency of $f = f_{fl} = 1.17\,\mathrm{MHz}$ and after mirroring the quarter-geometry results in the yz- and xz-symmetry planes back into the full geometry. (a) Color plot of the displacement magnitude u from 0 (dark blue) to 50 nm (yellow) and of the real part of the acoustic pressure p_1 in the fluid and in the coupling layer from minimum (blue) to maximum (red). (b) Cut-view of the simulated device showing color plots of the fields in the interior parts of the model, including the anti-symmetrically actuated electric potential φ in the PZT from -15 V (blue) to 15 V (red) and showing the different amplitudes of $p_{1,fl}$ and $p_{1,cpl}$. (c) Cross-section of the device in the yz-plane, which emphasizes the motion of the channel lid and the acoustic pressure inside the glycerol coupling layer. (d) Close-up view of the fluid channel and the adjacent lid. The displacement $\boldsymbol{u}$ (cyan vectors) has been scaled with a factor of 1000 to make the lid movement more visible. See the supplementary material for animations of the four views of the resonance mode (Ref. 40).

https://doi.org/10.1121/10.0005113

focused in the center region of the channel at different focusing times t as a function of frequency. We assume transverse acoustic focusing in the node of a half-wave pressure with the simulated amplitude, neglect acoustic streaming, and consider the case of a neutrally buoyant solution. In this case, the horizontal trajectory $y(y_0, t)$ of a particle at time t, starting at position y_0, is known analytically. Shifting the coordinate system so that the pressure node is at $y = \frac{1}{2}w_{\mathrm{ch}}$ and the channel lies at $0 < y < w_{\mathrm{ch}}$, we find that[41]

$$y(y_0, t) = \frac{w_{\mathrm{ch}}}{\pi} \arctan\left[\tan\left(\pi \frac{y_0}{w_{\mathrm{ch}}}\right) \exp\left(\frac{t}{t^*}\right)\right], \tag{14a}$$

$$t^* = \frac{3\eta_{\mathrm{fl}} w_{\mathrm{ch}}^2}{4\pi^2 \Phi a^2} \frac{1}{E_{\mathrm{ac}}^{\mathrm{fl}}}, \text{ with } \Phi = \frac{1}{3}f_0 + \frac{1}{2}f_1, \tag{14b}$$

where Φ is the acoustic contrast factor and t^* is the characteristic focusing time. Using this expression, we then calculate the fraction of particles that are focused in a band of width w_{foc} around the nodal plane:

(1) Compute $E_{\mathrm{ac}}^{\mathrm{fl}}$ from the numerical simulation and select the focusing band width w_{foc} and time t_{foc}.
(2) For a large number N of uniformly distributed initial positions y_0 for $0 < y_0 < \frac{1}{2}w_{\mathrm{ch}}$, compute the final positions $y_{\mathrm{foc}} = y(y_0, t_{\mathrm{foc}})$ using Eq. (14).
(3) Count the number N_{foc} of particles inside the focusing band: $y_{\mathrm{foc}} > \frac{1}{2}(w_{\mathrm{ch}} - w_{\mathrm{foc}})$.

The simulated focusability $\mathcal{F}_{\mathrm{sim}}$ is then defined by

$$\mathcal{F}_{\mathrm{sim}} = \frac{N_{\mathrm{foc}}}{N}. \tag{15}$$

In our simulations, we chose $N = 10^5$ initial positions y_0 and a focusing bandwidth $w_{\mathrm{foc}} = \frac{1}{10}w_{\mathrm{ch}}$. We choose the focusing time to be the time it takes a given set flow rate Q_{flow} to sweep half the active volume $V_{\mathrm{fl}} = l_{\mathrm{pzt}} w_{\mathrm{ch}} h_{\mathrm{ch}}$ above the PZT transducer, $t_{\mathrm{foc}} = \frac{1}{2}(V_{\mathrm{fl}}/Q_{\mathrm{flow}}) = l_{\mathrm{pzt}} w_{\mathrm{ch}} h_{\mathrm{ch}}/2Q_{\mathrm{flow}}$, which sets an upper limit to achieve good microparticle focusing in the center of the device for the given geometry. The resulting focusability $\mathcal{F}_{\mathrm{sim}}$ is plotted versus frequency in Fig. 4(a) for the three flow rates $Q_{\mathrm{flow}} = 10$, 50, and 100 μl/min, corresponding to the focusing times $t_{\mathrm{foc}} = 4.0$, 0.8, and 0.4 s. The model predicts the best focusing of the device at the frequency $f_1 = 1.17$ MHz, identical to the frequency f_{fl} of Fig. 2(b) with the maximum acoustic energy density in the fluid channel. The acoustic pressure $p_{1,\mathrm{fl}}$ and the acoustic radiation force $\boldsymbol{F}^{\mathrm{rad}}$ at this frequency are shown in Fig. 4(b). Clearly, the simulated pressure is an antisymmetric standing pressure wave, for which the acoustic radiation force points toward the pressure node in the center of the channel, causing focusing in the center of the channel of suspended particles. Based on our simulations of the radiation force $\boldsymbol{F}^{\mathrm{rad}} = (F_y^{\mathrm{rad}}, F_z^{\mathrm{rad}})$, we compute the figure of merit,[9] $R = \int_{V_{\mathrm{fl}}} -\mathrm{sign}(y) F_y^{\mathrm{rad}}\, \mathrm{d}V / \int_{V_{\mathrm{fl}}} |F_z^{\mathrm{rad}}|\, \mathrm{d}V = 3.9$, which reveals that on average the horizontal focusing force F_y^{rad} is about 4 times larger than vertical force F_z^{rad} at the frequency

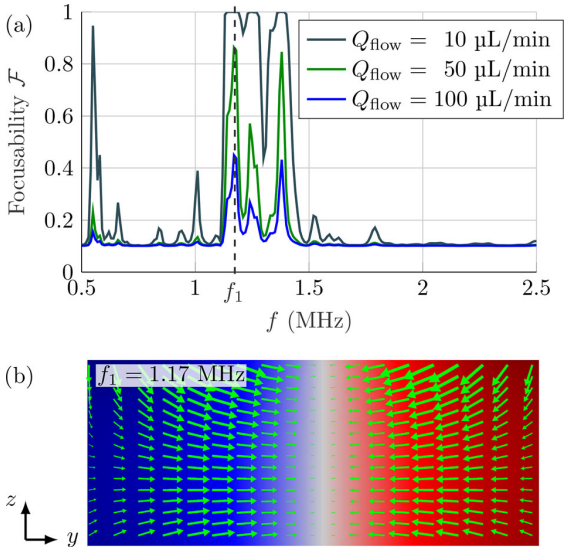

FIG. 4. (Color online) Simulation results. (a) Plot of the focusability $\mathcal{F}_{\mathrm{sim}}$ versus frequency with a focusing bandwidth $w_{\mathrm{foc}} = \frac{1}{10}w_{\mathrm{ch}}$ and for the listed three flow rates Q_{flow}. (b) Color plot in the vertical channel cross section of the acoustic pressure $p_{1,\mathrm{fl}}$ from −755 (blue) to +755 kPa (red) and the acoustic radiation force $\boldsymbol{F}^{\mathrm{rad}}$ (green vectors) with a magnitude up to 5.5 pN for suspended 4.8-μm-diameter PS particles.

$f_1 = 1.17$ MHz, as can be seen qualitatively from the $\boldsymbol{F}^{\mathrm{rad}}$ vectors (green) in Fig. 4(b). We therefore concentrate on the focusing in the y-direction toward the pressure node in this work.

V. EXPERIMENTAL SETUP AND RESULTS

A. Setup and procedure

The first step in the characterization of the acoustofluidic device was the measurement of the electrical admittance. The admittance spectrum $Y(f)$ between the two halves of the split top electrodes is measured using a Digilent (Pullman, WA) Analog Discovery 2 oscilloscope, applying the driving voltage to one of the top electrodes, grounding the other top electrode, and leaving the bottom electrode electrically floating. This is equivalent to adding a constant potential $+\frac{1}{2}\varphi_0$ to the simulated voltage configuration shown in Fig. 1(c). Observed differences between measured and simulated results for Y might be caused by a temperature sensor that is mounted on one side of the piezoelectric transducer but not included in the simulations. The piezoelectric transducer is coupled through a thin glycerol layer [99% (v/v) glycerol, 1% (v/v) water] to the microfluidic polymer chip. The thickness of this coupling layer was measured using a feeler gauge to be approximately 20 μm thick. For more information about the role of coupling layers, see Refs. 14–16 and 36.

In the following measurement, a frequency sweep at a fixed voltage amplitude of V = 15 V from 0.5 to 2.5 MHz was performed to analyze the experimental focusability of a neutrally buoyant suspension of 4.8-μm-diameter

fluorescent PS particles in a water-iodixanol mixture [84% (v/v) water, 16% (v/v) iodixanol]. The solution was pumped through the acoustofluidic device with a flow rate of 10 μl/min delivered by a syringe pump. Bright-field images were taken in steps of 5 kHz with a Hamamatsu (Hamamatsu City, Japan) Orca Flash 4.0 camera with 50 ms exposure time. At each frequency, the channel was flushed by briefly increasing the flow rate to 1800 μl/min for 0.1 s, followed by a waiting time of 45 s to stabilize the flow at a flow rate of 10 μl/min. Afterward, a series of ten images were taken with the piezoelectric transducer switched on and another ten images with the transducer switched off. The temperature during the experiment was kept constant at $T = 20\,^{\circ}\mathrm{C}$ using a Peltier element. From the obtained images, an average intensity profile $I_{\mathrm{exp}}(y)$ across the channel was calculated at each frequency. The experimental focusability $\mathcal{F}_{\mathrm{exp}}$ was then obtained from the integral of the intensity curve around the channel center divided by the integral across the entire channel, in analogy with $\mathcal{F}_{\mathrm{sim}}$ in Eq. (15),

$$\mathcal{F}_{\mathrm{exp}} = \frac{\int_{-1/2w_{\mathrm{foc}}}^{1/2w_{\mathrm{foc}}} I_{\mathrm{exp}}(y)\,\mathrm{d}y}{\int_{-1/2w_{\mathrm{ch}}}^{1/2w_{\mathrm{ch}}} I_{\mathrm{exp}}(y)\,\mathrm{d}y}. \tag{16}$$

Here, we used $w_{\mathrm{foc}} = \frac{1}{10}\,w_{\mathrm{ch}}$ and thus determined the focusability into a band having the width of 10% of the channel width w_{ch}. In the experiments, we observed that at some frequencies there was a small offset from the channel center to the pressure node where the particles got focused. To facilitate the processing of the data in those cases where an intensity offset was observed, we integrated the intensity curve symmetrically around the point y_{max} of maximum intensity, thereby changing the limits of the integral in the numerator to $y_{\mathrm{max}} \pm \frac{1}{2}w_{\mathrm{foc}}$.

In the final experiment, we measured the acoustic energy density $E_{\mathrm{ac}}^{\mathrm{fl}}$ using the same setup as described above: the neutrally buoyant solution, consisting of 84% (v/v) water, 16% (v/v) iodixanol, and fluorescent 4.8-μm-diameter PS beads is pumped through the microfluidic polymer chip at 10 μl/min. The same anti-symmetric actuation voltage with an amplitude of $\varphi_0 = \pm 15$ V was used, while the device temperature was kept constant at $T = 20\,^{\circ}\mathrm{C}$. However, unlike in the previous experiment, only selected frequencies, where some focusing had previously been observed, were studied in this experiment. A series of 600 images was recorded in time steps of $\Delta t = 20$ ms, while the fluid flow was stopped. This was done to extract the acoustic energy density $E_{\mathrm{ac}}^{\mathrm{fl}}$ around the main resonance frequency from the image series using the light-intensity method presented by Barnkob *et al.*[41]

B. Experimental results for the electrical admittance, particle focusability, and acoustic energy density

We measured the electrical admittance Y as described in Sec. V A for a 1-MHz PZT transducer, after cutting a groove in the top electrode for anti-symmetric actuation. The admittance was measured while leaving the bottom electrode at a floating potential. The transducer was characterized while coupled to the microfluidic polymer chip. The measured electrical admittance Y and the corresponding acoustic energy density $E_{\mathrm{ac}}^{\mathrm{fl}}$ measured at selected frequencies in the range from 0.5 to 2.5 MHz are shown in Fig. 5.

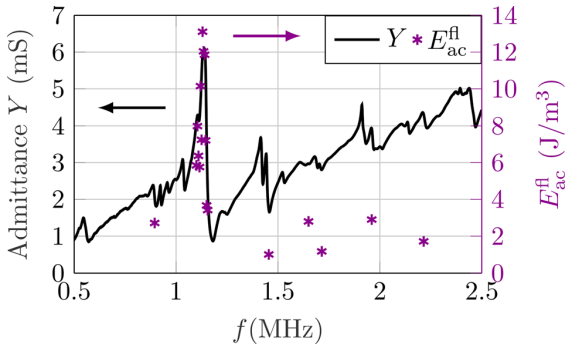

FIG. 5. (Color online) The measured admittance spectrum Y (black) from 0.5 to 2.5 MHz using a floating bottom electrode and the corresponding acoustic energy density $E_{\mathrm{ac}}^{\mathrm{fl}}$ (deep purple) obtained by the light-intensity method (Ref. 41) on a series of images recorded under stop-flow condition at selected frequencies showing good particle focusing. The resonance peak in the admittance is located at $f_Y = 1.14$ MHz, closely coinciding with the frequency $f_{\mathrm{ac}} = 1.13$ MHz, where the energy density attains its maximum value $E_{\mathrm{ac}}^{\mathrm{fl}} = 13\,\mathrm{J\,m^{-3}}$.

The admittance measurement exhibits a strong resonance peak at the frequency $f_Y = 1.14$ MHz. Deviations from the nominal 1-MHz resonance are due to the groove cut into the transducer, the anti-symmetric actuation, and the load of the chip. Furthermore, we find that the maximum $E_{\mathrm{ac}}^{\mathrm{fl}} = 13\,\mathrm{J\,m^{-3}}$ of the acoustic energy density is located close to this maximum of the measured admittance, in good agreement with what is reported in literature for typical glass-based devices.[39] This value of $E_{\mathrm{ac}}^{\mathrm{fl}}$ corresponds to a focusing time of about $t_{\mathrm{foc}} = 6.6$ s in the channel.

The results of the measurement of the particle focusability $\mathcal{F}_{\mathrm{exp}}$ during continuous flow operation from 0.5 to 2.5 MHz are shown in Fig. 6(a). The frequency with the best focusing is $f_{\mathrm{foc}} = 1.13$ MHz, where about 60% of the particles are located within the center 10% of the channel width. Images of the particles inside the channel at this frequency are shown in Figs. 6(b) and 6(c) for the ultrasound switched off and on, respectively. See the supplementary material for a video showing particle focusing.[40]

C. Comparison with simulation results

The simulated values for the three key responses, the admittance Y, the focusability $\mathcal{F}$, and the acoustic energy density E_{ac}, agree fairly well with the experimental values. As shown in Fig. 7(a), the experimental and simulated admittance show the same behavior, and the frequencies of their respective maxima coincide within 0.9%, $f_Y^{\mathrm{exp}} = 1.14$ MHz and $f_Y^{\mathrm{sim}} = 1.13$ MHz.

When comparing the measured maximum value $E_{\mathrm{ac}}^{\mathrm{exp}} = 13\,\mathrm{J\,m^{-3}}$ of the acoustic energy density with the highest

https://doi.org/10.1121/10.0005113

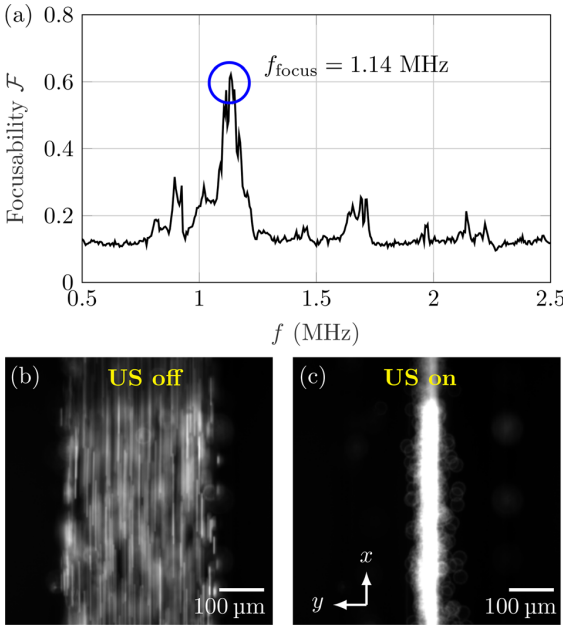

FIG. 6. (Color online) (a) The experimental focusability $\mathcal{F}_{\text{exp}}$ versus frequency [see Eq. (16)], with a maximum 0.6 at $f_{\text{foc}} = 1.14$ MHz. (b) Image of the particles in the channel with ultrasound (US) switched off. (c) Image of the particles in the channel with US switched on at the maximum $f_{\text{foc}} = 1.14$ MHz. See the supplementary material for a video showing particle focusing (Ref. 40).

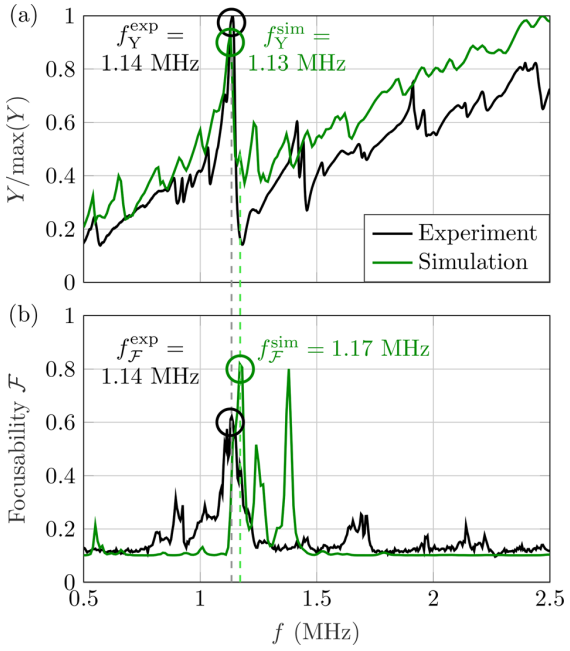

FIG. 7. (Color online) Top-view comparison between measured and simulated responses versus frequency from 0.5 to 2.5 MHz. (a) The measured (black) and simulated (green) electrical admittance Y showing closely coinciding main resonances at $f_Y^{\text{exp}} = 1.14$ MHz and $f_Y^{\text{sim}} = 1.13$ MHz, respectively. (b) The experimental $\mathcal{F}_{\text{exp}}$ (black) and simulated $\mathcal{F}_{\text{sim}}$ (green) focusability, after calibrating the simulation to match the measured maximum of the acoustic energy density. Both focusabilities $\mathcal{F}$ show a maximum in the range from 0.6 to 0.8 and a small 2.6% deviation between the frequencies $f_{\mathcal{F}}^{\text{exp}} = 1.14$ MHz and $f_{\mathcal{F}}^{\text{sim}} = 1.17$ MHz of the respective maxima.

value $E_{\text{ac}}^{\text{sim}} = 71\,\text{J m}^{-3}$ computed in the simulation, we note that the simulation result is about 5.5 times higher than the experimental value. This difference most likely results from neglecting parts of the real system in our idealized simulation, such as the tubing, the mounting stage, and the inlet and the outlets, all which cause a reduction of the total energy of the real system. We furthermore observe another peak in the simulated acoustic energy density close to the frequency 1.4 MHz, which has not been observed experimentally. This likely stems from a small offset in the y-direction between the microfluidic channel and the piezoelectric transducer. This offset could not be implemented in the three-dimensional model, as it is breaking the symmetries utilized in the model. Simulations performed in two dimensions, however, have shown this peak to decrease drastically with small variations of the chip offset in y-direction, while the main peak at $f_{\mathcal{F}}^{\text{sim}} = 1.17$ MHz stays largely unaffected by this offset.

To compare the simulated and the experimental focusability, we use the standard procedure of calibrating the actuation voltage φ_0 in the simulation to ensure that $E_{\text{ac}}^{\text{exp}} = E_{\text{ac}}^{\text{sim}}$.[13] Using this calibrated actuation voltage, we recalculate the focusability with a flow rate $Q_{\text{flow}} = 10\,\mu\text{L/min}$ according to Eq. (15) and compare the resulting $\mathcal{F}_{\text{sim}}$ with $\mathcal{F}_{\text{exp}}$ plotted versus frequency in Fig. 7(b). We observe an upward frequency shift in the maximum of the simulated focusability curve, here by 2.6%. Both curves show a similar maximum focusability, namely $\mathcal{F}_{\text{sim}} = 0.82$ for the simulation and $\mathcal{F}_{\text{exp}} = 0.62$ in the experiment. These numbers suggest good focusing of about 60%–80% of the particles. This value can be increased by lowering the flow rate or increasing the voltage amplitude on the transducer. We furthermore note that the highest measured focusability coincides with the global maximum in the measured admittance spectrum, as indicated by the gray-dashed line in Fig. 7. The simulated maximum in the focusability, however, relates to a small local maximum in the simulated admittance curve, approximately 40 kHz above the main admittance resonance $f_Y^{\text{sim}} = 1.13$ MHz. This is indicated by the green-dashed line in Fig. 7. A maximum in the admittance spectrum typically relates to a maximum in the displacement of the piezoelectric transducer, which is driving the whole-system resonance. The small 2.6% deviation between the frequencies $f_{\mathcal{F}}^{\text{exp}}$ and $f_{\mathcal{F}}^{\text{sim}}$ of the focusability maximum likely stems from the idealized assumptions made for Eq. (14), such as using a perfect horizontal standing half-wave and neglecting the vertical component of the acoustic radiation force. Figure 4(b) and the figure of merit $R = 3.9$ computed in Sec. IV B show the limitations of this assumption.

VI. CONCLUDING DISCUSSION

We have presented a numerical model for 3D simulations of an acoustofluidic polymer device for particle

focusing, and we have validated it experimentally. Our 3D simulations predict good acoustic focusing at a frequency of $f_{sim} = 1.17$ MHz, far below the half-wave resonance frequency $f_{ch} = 2$ MHz corresponding to a rigid hard-wall channel. Furthermore, we observe in our simulations that the resonance in the fluid channel is created through the motion of the sidewalls in phase with a standing wave motion of the channel lid. It is this whole-system resonance creating the standing pressure half-wave that in turn leads to good focusing at the specified frequency.

In Fig. 7(a), we find a good qualitative agreement between the simulated and measured electrical admittance spectrum of the device. Quantitatively, only a minor 0.9% shift in the two spectra was observed. More relevant for applications is the characterization of the ability of the polymer device to focus particles by acoustophoresis. To this end, we have introduced the focusability $\mathcal{F}$, which can be obtained both by simulation, $\mathcal{F}_{sim}$ in Eq. (15), and by experiments, $\mathcal{F}_{exp}$ in Eq. (16), thus enabling a good method to compare the two. The focusability $\mathcal{F}$ is the fraction of the incoming suspended particles, which are focused in the channel center for given focusing times or flow rates, enabling an estimate of the highest achievable flow rates to still maintain reasonable focusing at a selected frequency. Whereas in Fig. 7(b), we observe a small offset of 2.6% between the measured and simulated focusability, $\mathcal{F}_{exp}$ and $\mathcal{F}_{sim}$ exhibit the same focusing behavior and yield a similar maximum value of $\mathcal{F} = 0.6$–0.8, meaning that 60%–80% of the particles inside the channel are focused in the center 10% of the channel width.

By studying the electrical admittance, we find both in our simulation and in our experiment that the frequency of the admittance maximum closely coincides with the frequency of the focusability maximum. Both the resonance of the piezoelectric transducer and the whole-system resonance are governed by the dimensions of the transducer itself and the whole acoustofluidic device, respectively. Whereas the resonance frequency of the piezoelectric transducer is tunable through the height of the transducer, precisely predicting and manipulating the frequency of the WSUR is a more challenging task and requires numerical simulations. Matching this WSUR with the intrinsic resonance frequency of the transducer, however, would be ideal.

Another approach is to numerically find a design yielding a WSUR at the admittance resonance frequency of the selected piezoelectric transducer. The estimate that can be made based on numerical simulations, however, is only as good as the accuracy of the underlying material parameters. Whereas the mechanical and acoustic properties of glass and silicon are well studied and well reported in literature, it is a challenging task to obtain reliable material parameters for different polymer grades. This especially holds true for data on the transverse speed of sound and attenuation, which are required to compute the complex-valued stiffness coefficient C_{44}.

Further studies and measurements beyond the presented proof-of-concept example of the precise properties of the materials in use will increase the accuracy of our simulation model. Currently, we are working on characterizing various polymers for their applicability as base material in acoustofluidic devices. To fully model the experimental device, fluid connectors and tubing, as well as the clamping of the device in the used measurement setup, need to be considered. With our simulation model, however, we obtained a reliable technique to make predictions on the applicability of polymer-based devices for particle focusing applications.

The existing model can be used for further optimizations of the design, to yield higher acoustic energy densities and therefore in turn enable flow rates higher than the reported $Q_{flow} = 10\,\mu l/min$. Scaling up the flow rate by 1 or 2 orders of magnitude seems possible and would make polymer-based acoustofluidic devices competitive with other particle focusing and separation solutions.

ACKNOWLEDGMENTS

This work is part of the Eureka Eurostars-2 joint programme E!113461 AcouPlast project funded by Innovation Fund Denmark, Grant No. 9046-00127B, and Vinnova, Sweden's Innovation Agency, Grant No. 2019–04500, with co-funding from the European Union Horizon 2020 Research and Innovation Programme.

[1]E. K. Sackmann, A. L. Fulton, and D. J. Beebe, "The present and future role of microfluidics in biomedical research," Nature **507**(7491), 181–189 (2014).
[2]R. Silva, P. Dow, R. Dubay, C. Lissandrello, J. Holder, D. Densmore, and J. Fiering, "Rapid prototyping and parametric optimization of plastic acoustofluidic devices for blood-bacteria separation," Biomed. Microdev. **19**(3), 70 (2017).
[3]P. Dow, K. Kotz, S. Gruszka, J. Holder, and J. Fiering, "Acoustic separation in plastic microfluidics for rapid detection of bacteria in blood using engineered bacteriophage," Lab Chip **18**(6), 923–932 (2018).
[4]Y. Gu, C. Chen, Z. Wang, P.-H. Huang, H. Fu, L. Wang, M. Wu, Y. Chen, T. Gao, J. Gong, J. Kwun, G. M. Arepally, and T. J. Huang, "Plastic-based acoustofluidic devices for high-throughput, biocompatible platelet separation," Lab Chip **19**, 394–402 (2019).
[5]C. Lissandrello, R. Dubay, K. T. Kotz, and J. Fiering, "Purification of lymphocytes by acoustic separation in plastic microchannels," SLAS Technol. **23**(4), 352–363 (2018).
[6]R. Dubay, C. Lissandrello, P. Swierk, N. Moore, D. Doty, and J. Fiering, "Scalable high-throughput acoustophoresis in arrayed plastic microchannels," Biomicrofluidics **13**(3), 034105 (2019).
[7]I. González, M. Tijero, A. Martin, V. Acosta, J. Berganzo, A. Castillejo, M. M. Bouali, and J. L. Soto, "Optimizing polymer lab-on-chip platforms for ultrasonic manipulation: Influence of the substrate," Micromachines **6**(5), 574–591 (2015).
[8]C. Yang, Z. Li, P. Li, W. Shao, P. Bai, and, and Y. Cui, "Acoustic particle sorting by integrated micromachined ultrasound transducers on polymer-based microchips," in *Proceedings of the 2017 IEEE International Ultrasonics Symposium (IUS)*, Washington, DC (September 6–9, 2017).
[9]R. P. Moiseyenko and H. Bruus, "Whole-system ultrasound resonances as the basis for acoustophoresis in all-polymer microfluidic devices," Phys. Rev. Appl. **11**, 014014 (2019).
[10]A. Mueller, A. Lever, T. V. Nguyen, J. Comolli, and J. Fiering, "Continuous acoustic separation in a thermoplastic microchannel," J. Micromech. Microeng. **23**(12), 125006 (2013).
[11]R. Barnkob, P. Augustsson, T. Laurell, and H. Bruus, "Measuring the local pressure amplitude in microchannel acoustophoresis," Lab Chip **10**(5), 563–570 (2010).
[12]P. Augustsson, R. Barnkob, S. T. Wereley, H. Bruus, and T. Laurell, "Automated and temperature-controlled micro-PIV measurements

enabling long-term-stable microchannel acoustophoresis characterization," Lab Chip **11**(24), 4152–4164 (2011).
[13]P. B. Muller, M. Rossi, A. G. Marín, R. Barnkob, P. Augustsson, T. Laurell, C. J. Kähler, and H. Bruus, "Ultrasound-induced acoustophoretic motion of microparticles in three dimensions," Phys. Rev. E **88**(2), 023006 (2013).
[14]B. Hammarström, M. Evander, H. Barbeau, M. Bruzelius, J. Larsson, T. Laurell, and J. Nilsson, "Non-contact acoustic cell trapping in disposable glass capillaries," Lab Chip **10**(17), 2251–2257 (2010).
[15]A. Lenshof, M. Evander, T. Laurell, and J. Nilsson, "Acoustofluidics 5: Building microfluidic acoustic resonators," Lab Chip **12**, 684–695 (2012).
[16]W. N. Bodé and H. Bruus, "Numerical study of the coupling layer between transducer and chip in acoustofluidic devices," J. Acoust. Soc. Am. **149**(5), 3096–3105 (2021).
[17]W. N. Bodé, L. Jiang, T. Laurell, and H. Bruus, "Microparticle acoustophoresis in aluminum-based acoustofluidic devices with PDMS covers," Micromachines **11**(3), 292 (2020).
[18]A. Tahmasebipour, L. Friedrich, M. Begley, H. Bruus, and C. Meinhart, "Toward optimal acoustophoretic microparticle manipulation by exploiting asymmetry," J. Acoust. Soc. Am. **148**(1), 359–373 (2020).
[19]N. R. Skov, J. S. Bach, B. G. Winckelmann, and H. Bruus, "3D modeling of acoustofluidics in a liquid-filled cavity including streaming, viscous boundary layers, surrounding solids, and a piezoelectric transducer," AIMS Math. **4**, 99–111 (2019).
[20]J. S. Bach and H. Bruus, "Theory of pressure acoustics with viscous boundary layers and streaming in curved elastic cavities," J. Acoust. Soc. Am. **144**, 766–784 (2018).
[21]M. Settnes and H. Bruus, "Forces acting on a small particle in an acoustical field in a viscous fluid," Phys. Rev. E **85**, 016327 (2012).
[22]N. R. Skov, P. Sehgal, B. J. Kirby, and H. Bruus, "Three-dimensional numerical modeling of surface-acoustic-wave devices: Acoustophoresis of micro- and nanoparticles including streaming," Phys. Rev. Appl. **12**, 044028 (2019).
[23]P. B. Muller and H. Bruus, "Numerical study of thermoviscous effects in ultrasound-induced acoustic streaming in microchannels," Phys. Rev. E **90**(4), 043016 (2014).
[24]J. T. Karlsen, P. Augustsson, and H. Bruus, "Acoustic force density acting on inhomogeneous fluids in acoustic fields," Phys. Rev. Lett. **117**, 114504 (2016).
[25]J. T. Karlsen and H. Bruus, "Forces acting on a small particle in an acoustical field in a thermoviscous fluid," Phys. Rev. E **92**, 043010 (2015).
[26]W. Slie, A. Donfor, Jr., and T. Litovitz, "Ultrasonic shear and longitudinal measurements in aqueous glycerol," J. Chem. Phys. **44**(10), 3712–3718 (1966).
[27]L. Negadi, B. Feddal-Benabed, I. Bahadur, J. Saab, M. Zaoui-Djelloul-Daouadji, D. Ramjugernath, and A. Negadi, "Effect of temperature on density, sound velocity, and their derived properties for the binary systems glycerol with water or alcohols," J. Chem. Thermodyn. **109**, 124–136 (2017).
[28]N.-S. Cheng, "Formula for the viscosity of a glycerol-water mixture," Ind. Eng. Chem. Res. **47**(9), 3285–3288 (2008).
[29]B. Hartmann and J. Jarzynski, "Polymer sound speeds and elastic constants," Naval Ordnance Laboratory Report NOLTR 72-269, US Naval Ordnance Laboratory, White Oak, MD, 1972.
[30]D. Christman, "Dynamic properties of poly(methylmethacrylate) (PMMA) (Plexiglas)," Report No. DNA 2810F, MSL-71-24, General Motors Technical Center, Warren, MI, 1972.
[31]H. Sutherland and R. Lingle, "Acoustic characterization of polymethyl methacrylate and three epoxy formulations," J. Appl. Phys. **43**(10), 4022–4026 (1972).
[32]H. Sutherland, "Acoustical determination of shear relaxation functions for polymethyl methacrylate and Epon 828-Z," J. Appl. Phys. **49**(7), 3941–3945 (1978).
[33]J. Carlson, J. van Deventer, A. Scolan, and, and C. Carlander, "Frequency and temperature dependence of acoustic properties of polymers used in pulse-echo systems," in *Proceedings of the IEEE Symposium on Ultrasonics, 2003*, Honolulu, HI (October 5–8, 2003), Vol. 1, pp. 885–888.
[34]A. Simon, G. Lefebvre, T. Valier-Brasier, and R. Wunenburger, "Viscoelastic shear modulus measurement of thin materials by interferometry at ultrasonic frequencies," J. Acoust. Soc. Am. **146**(5), 3131–3140 (2019).
[35]H. T. Tran, T. Manh, T. F. Johansen, and L. Hoff, "Temperature effects on ultrasonic phase velocity and attenuation in Eccosorb and PMMA," in *Proceedings of the 2016 IEEE International Ultrasonics Symposium (IUS)*, Tours, France (September 18–21, 2016), pp. 1–4.
[36]P. Hahn and J. Dual, "A numerically efficient damping model for acoustic resonances in microfluidic cavities," Phys. Fluids **27**, 062005 (2015).
[37]COMSOL Multiphysics 5.5 (2019), http://www.comsol.com (Last viewed 7 May 2021).
[38]P. B. Muller, R. Barnkob, M. J. H. Jensen, and H. Bruus, "A numerical study of microparticle acoustophoresis driven by acoustic radiation forces and streaming-induced drag forces," Lab Chip **12**, 4617–4627 (2012).
[39]M. Bora and M. Shusteff, "Efficient coupling of acoustic modes in microfluidic channel devices," Lab Chip **15**(15), 3192–3202 (2015).
[40]See supplementary material at https://www.scitation.org/doi/suppl/10.1121/10.0005113 for four animations of the simulated 1.17-MHz mode shown in Fig. 3 and one video of the experimental particle focusing corresponding to Fig. 6.
[41]R. Barnkob, I. Iranmanesh, M. Wiklund, and H. Bruus, "Measuring acoustic energy density in microchannel acoustophoresis using a simple and rapid light-intensity method," Lab Chip **12**, 2337–2344 (2012).

Chapter 6

Ultrasound electrical impedance spectroscopy

6.1 Motivation

Our numerical model requires the precise knowledge of several material parameters:

- Four parameters for the liquid: the density ρ_0, the speed of sound c_0, the dynamic viscosity η_0, and bulk viscosity η_0^{b},
- Five parameters for isotropic solids: the density ρ_{sl}, as well as the stiffness components C'_{11}, C''_{11}, C'_{44}, C''_{44},
- 18 stiffness components of the piezoelectric material: the density ρ_{pzt}, five complex-valued stiffness components C_{ik}, three real-valued coupling components e_{ik}, and two complex-valued permittivity parameters ε_{ik}.

Material parameters for pure water and various mixing ratios of pure water with the density-gradient medium iodixanol are well known in literature [69, 70]. However, this leaves us with missing material parameters for the piezoelectric transducer and the polymer chip. The results of the previous chapter indicate that large uncertainties in the existing parameters for PZT and various polymers cause deviations between numerical and experimental results.

Alternative measurement techniques to obtain the required material parameters exist, but they possess different limitations, especially regarding the field of acoustofluidics, which will be further discussed at the end of this chapter. Numerical simulations of acoustofluidic devices require accurate material parameters measured at MHZ frequencies. Therefore, this chapter proposes an easy-to-execute and low-cost method to obtain these missing parameters. The method is based on measuring an electrical impedance spectrum of a piezoelectric transducer mechanically loaded with a polymer ring. The piezoelectric transducer's stiffness components, coupling components, and permittivity parameters are obtained in the initial step. This fitting of the transducer parameters is performed based

on an inverse method using the measured and simulated impedance spectrum, inspired by the approach presented in Refs. [27, 29, 30, 85]. Using the acquired transducer properties, in a consecutive step, the impedance spectrum of a polymer-loaded piezoelectric transducer is used to obtain the four elastic moduli of the polymer disk. The technique is labeled ultrasound electrical impedance spectroscopy (UEIS) and was co-developed with my colleague William Naundrup Bodé. The novelty of the UEIS technique stems from the combined determination of transducer properties and the properties of the polymer load. The method extends the approach of Ref. [31] into an automated two-step procedure, taking a wide frequency range from 500 Hz to 5 MHz into account and enabling simple, cheap, and reliable determination of the elastic moduli of polymers and other solids.

6.2 Summary of the results from Paper II

6.2.1 Overview of the system

The technique of obtaining the elastic moduli of a polymer sample requires a disk-shaped piezoelectric transducer and a ring-shaped polymer sample. The procedure is based on an inverse method, where numerical simulations are used to fit a simulated impedance spectrum to the measured spectrum. Using an axisymmetric geometry allows us to reduce the simulation to the 2D domain and speed up the computations. An overview of the transducer-glue-polymer system is shown in Fig. 6.1(a). Fig. 6.1(b) shows a cross-section in the r-z-plane of the device, including the mesh implemented in COMSOL. A polymer ring is glued to a piezoelectric transducer via a thin glue layer. The polymer sample is ring-shaped to allow electrical contact via spring-loaded pins to the bottom and top electrode of the transducer disk, as shown in Fig. 6.1(c,d). The measurement setup merely consists of a sample holder, impedance analyzer, and laptop computer. The elastic stiffness components of the glue layer need to be obtained before the final polymer parameters can be determined.

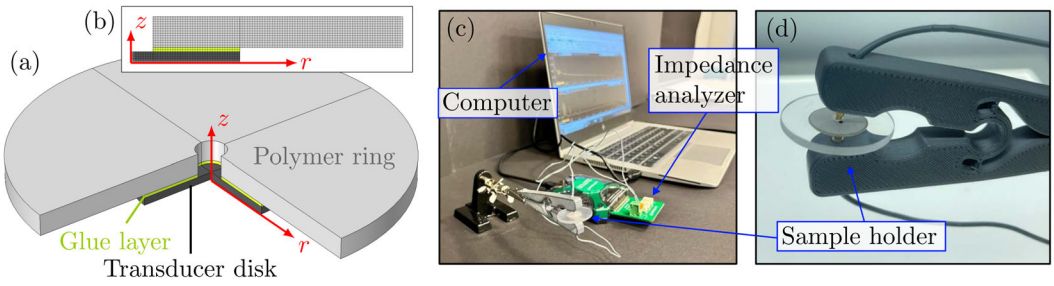

Figure 6.1: (a) Overview of the transducer-glue-polymer system. (b) The cross-section in the r-z-plane of the system is shown, including the mesh used for the numerical simulations. (c) The measurement setup consists of the sample holder, impedance analyzer, and laptop computer. (d) Image of the custom-built sample holder using spring-loaded pins on both sides of the piezoelectric transducer. The figure has been adapted from [2].

6.2.2 Details on the fitting procedure

The procedure of the UEIS technique starts with the measurement of the electrical impedance spectrum $Z_{\mathrm{exp}}(f)$ of the unloaded Pz27 disk. The impedance $Z_{\mathrm{sim}}(f)$ is then simulated in COMSOL, and the cost function

$$\mathcal{C} = \sqrt{\sum_j \left[\log_{10}\left(|Z_{\mathrm{exp}}(f_j)|\right) - \log_{10}\left(|Z_{\mathrm{sim}}(f_j)|\right)\right]^2} \tag{6.1}$$

is gradually minimized by fitting the unknown piezoelectric parameters p_i^{pz27}. This cost function uses the logarithm because the impedance varies by orders of magnitude across the frequency spectrum. The piezoelectric parameters are grouped by their sensitivity in the order from highest to lowest and fitting is performed for frequencies f_j in the range from 500 Hz to 5 MHz in increments of 10 kHz in three sub-steps:

1. Fit of the high sensitivity parameters C'_{11}, C'_{12}, C'_{13}, C'_{33}, ε'_{33}, and e'_{33}
2. Fit of the medium sensitivity parameters C'_{44}, e'_{31}, e'_{15}, C''_{11}, and C''_{33}
3. Fit of the low sensitivity parameters ε'_{11}, C''_{12}, C''_{13}, C''_{44}, ε''_{11}, and ε''_{33}

Once the cost function $\mathcal{C}$ converges with relative changes below 1%, the final piezoelectric material parameters are obtained. The fitting routine continues with the four elastic moduli of the polymer ring, which is loaded on the transducer. For this step, the electrical impedance spectrum $Z_{\mathrm{exp}}(f)$ of the polymer-loaded Pz27 disk needs to be measured. Then, the measured impedance spectrum of the loaded transducer disk is used to obtain the final parameters p_i^{polymer} in two steps:

1. As an initial step, fitting of the four parameters C'_{11}, C'_{44}, C''_{11}, and C''_{44} of the polymer is performed in the region from 500 Hz to 1 MHz to obtain improved initial values.
2. In the final step, fitting of C'_{11}, C'_{44}, C''_{11}, and C''_{44} is performed in the frequency range from 500 Hz to 1 MHz and from 3.5 MHz to 5 MHz.

In some cases, the initial guess of the polymer parameters is too far from the final parameters p_i^{polymer} to achieve good fitting in a single step. Therefore, a two-step procedure for fitting the polymer parameters is used to ensure full convergence of $\mathcal{C}$. The fitting routine utilizes the MATLAB-toolbox `fminsearchbnd` [86] to minimize the cost function $\mathcal{C}$. The function `fminsearchbnd` is a gradient-free optimization algorithm based on the Nelder-Mead method [87] and has been chosen based on the robustness and efficiency of the algorithm.

To further ensure that the correct elastic moduli of the polymer sample have been found, validation measurements were performed using the ultrasound-through-transmission (UTT) technique. A scan of the surface displacement using laser-Doppler-vibrometry (LDV) allowed for further confirmation of the results. An overview of alternative measurement techniques to obtain the elastic moduli is given in Section 6.3, among them the UTT technique, which has been used for validation. The material parameters for the glue layer are obtained similarly to the polymer ring in a previous intermediate step.

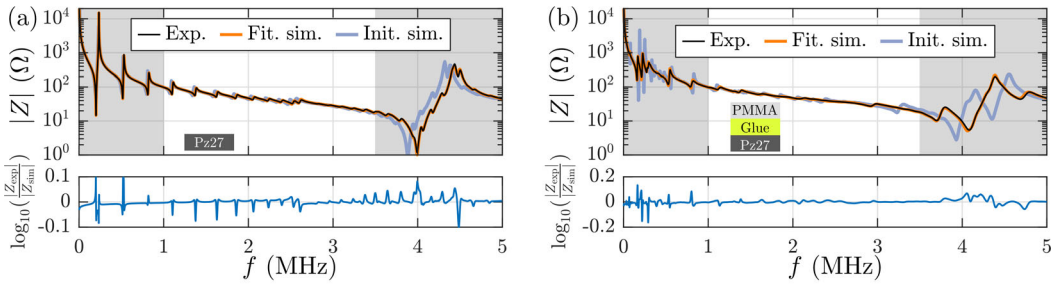

Figure 6.2: The electrical impedance spectrum versus frequency f is shown in the range from 500 Hz to 5 MHz. Experimental results (black curve) are compared with the initial simulation results (blue) and the fitted simulation results (orange). In the bottom the deviation $\log_{10}\left(\frac{|Z_{\text{exp}}|}{|Z_{\text{sim}}|}\right)$ between experimental and simulated impedance spectrum is shown. The figure has been adapted from [2]. (a) Results of the impedance spectrum of the unloaded Pz27 transducer. (b) Results for the combined Pz27-glue-PMMA system.

6.2.3 Results of the fitting procedure

The results of the fitting procedure for a Pz27 transducer loaded with a thin glue layer and the polymer PMMA are shown in Fig. 6.2. Pz27 has been selected due to its comparatively low quality factor, and lower batch-to-batch variations compared to other piezoelectric materials, such as Pz26 [88]. In Fig. 6.2(a), the experimentally obtained impedance spectrum $|Z(f)|$, as well as the initial and final fitted simulation results for the impedance spectrum of an unloaded Pz27 transducer, are compared. We find a good agreement between the measured and final simulated spectrum and a significant improvement compared to the initial simulation results shown by the blue curve. Fig. 6.2(b) shows the UEIS results for the polymer-loaded Pz27 transducer. The polymer load has significantly damped the impedance spectrum, and a good agreement between the measured and the final simulation of the impedance spectrum is seen. At some frequencies deviations in the logarithmic difference $\log_{10}\left(\frac{|Z_{\text{exp}}|}{|Z_{\text{sim}}|}\right)$ of almost 20% are observed. These deviations, however, stem from minor frequency shifts between the simulated and measured resonance frequencies, while the measured details of the spectrum are captured well by the final simulation. The UEIS method has been validated by UTT and LDV measurements to ensure that accurate material parameters have been obtained, as highlighted in detail in the Supplemental Material of Paper II [2].

6.3 Alternative techniques to measure elastic moduli

Alternative techniques to measure the elastic moduli of a material are grouped into static and dynamic techniques. Static techniques, such as tensile modulus testing, rely on the mechanical deformation of a material sample and allow us to determine the Young's modulus E of the sample under static conditions. On the contrary, dynamic techniques can determine a full set of elastic moduli, including the shear modulus G as well as the attenuation-

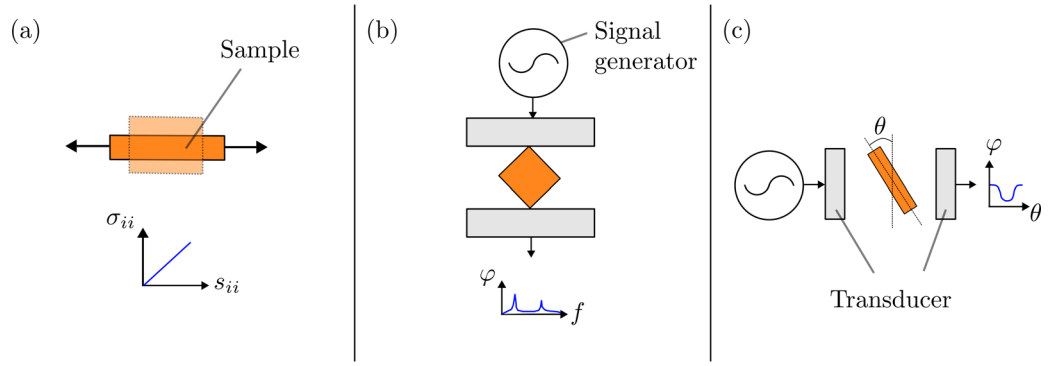

Figure 6.3: Different measurement techniques to determine elastic moduli are illustrated: (a) A sketch of the tensile testing method, where the stress-strain curve (σ_{ii} versus s_{ii}) is used to determine the Young's modulus E of the material sample (orange). (b) Resonant ultrasound spectroscopy utilizes a driving and a receiving transducer (light gray). The voltage spectrum at the receiving transducer is recorded, which is used to determine the material properties. (c) The ultrasound-through-transmission (UTT) technique uses a sending and a receiving transducer. An acoustic pulse is sent through a material sample at various rotation angles θ. The material properties of the sample can be calculated from the received signal amplitude at different angles.

related imaginary components. Three different techniques are illustrated in Fig. 6.3 and will be briefly introduced in the following. [89]

6.3.1 Tensile modulus testing

Tensile modulus measurements, schematically visualized in Fig. 6.3(a), are based on recordings of the stress σ_{ii} versus strain s_{ii} curve of a material. For example, the Young's modulus E is determined as the slope $E = \frac{\sigma_{ii}}{s_{ii}}$ of this curve in the linear regime for low stresses. Unfortunately, static techniques do not allow determining the imaginary parts of the stiffness components related to attenuation.

6.3.2 Resonant ultrasound spectroscopy

Dynamic techniques, on the contrary, allow us to determine both longitudinal and shear properties and the imaginary-valued elastic moduli. Dynamic techniques typically rely on the study of resonance frequencies of the material sample, such as torsional or longitudinal mode vibrations. Measurement techniques include resonant ultrasound spectroscopy (RUS), which is shown in Fig. 6.3(b), and the impact excitation technique. The RUS technique utilizes a signal generator and a pair of piezoelectric transducers. The material sample is clamped on two points between the two transducers, where the first transducer vibrates at a known frequency. The resonance frequencies of the material sample can be obtained from the acquired voltage signal φ versus frequency f at the second transducer. The required material parameters can be found by the numerical fitting of selected resonance frequencies for a given sample dimension and density.

6.3.3 Ultrasound-through-transmission technique

The UTT technique is based on the transmission of ultrasound waves through a material sample at various angles of incidence θ. An exemplary setup is drawn in Fig. 6.3(c). A transmitting transducer sends an acoustic pulse through the sample at a known angle θ. The speed of sound in the material can be computed from the time-of-flight delay between sending and receiving of the acoustic pulse. Furthermore, the difference in amplitude between the sent and received signal allows us to obtain the acoustic attenuation in the material. At normal incidence $\theta = 0$, only longitudinal waves are transmitted through the sample, while above the critical angle θ_{crit}, only shear waves are transmitted in the sample. The study of different incidence angles allows us to obtain both longitudinal and transverse material properties relating to the complete set of elastic moduli.

6.3.4 Advantages of the UEIS technique over conventional methods

Compared to the traditional techniques of obtaining elastic moduli, such as tensile modulus testing, RUS, and UTT, which have been briefly explained in Section 6.3, UEIS has a list of advantages:

- The technique enables easy-to-execute and low-cost measurements of the complex-valued elastic moduli using a simple experimental setup.
- The measurement occurs at frequencies f in the typical range of acoustophoresis experiments from 500 Hz to 5 MHz, where the entire spectrum is taken into account for the fitting.
- The technique is suitable for polymers with high acoustic attenuation.

In particular, compared to RUS, UEIS has the advantage that the full impedance spectrum over a wide frequency range is considered. RUS, on the contrary, utilizes only a few selected resonance frequencies of the polymer sample to compute the elastic moduli. Especially regarding numerical simulations of acoustofluidic devices, UEIS ensures that the numerical model closely matches the experimental findings in the studied frequency range from 500 Hz to 5 MHz, by providing nearly *in-situ* parameters.

6.4 Material properties for several studied materials

The UEIS technique has been utilized to determine the elastic moduli of several injection-molded polymers fabricated and provided by Ph.D. student Komeil Saeedabadi (DTU Construct). The obtained stiffness components of all materials characterized for this thesis are listed in the appendix in Section A.2. It was furthermore observed that even for the same type of polymer, such as the PMMA grades LG IG 840 and Diakon TD525, large differences in the elastic properties between the different material grades can exist. Therefore, to accurately describe the resonance modes of a polymer device, an *in-situ* measurement of the material properties using UEIS is highly beneficial.

In addition, the UEIS method can be used to determine the elastic moduli C_{ik} as a function of the different injection-molding parameters. In a proof-of-concept study, the impact of the injection speed on the polymer material parameters has been analyzed using UEIS. The injection speed describes how fast the polymer melt is injected into the mold. Mehat *et al.* [90] and Ozcelik *et al.* [91] have already shown that injection-molding process parameters can significantly impact the elastic properties of polymers. The observed change in the material parameters is particularly relevant for polymer-based acoustofluidics, where injection molding is one of the most promising fabrication techniques for high-volume production.

Fig. 6.4 shows the changes of the four elastic moduli of PMMA (LG IG 840) when increasing the injection speed from 16 mm/s to 40 mm/s. While the changes in the real parts C_{11}' and C_{44}' are only in the order of 1–2%, changes of up to 25% are found for the imaginary parts, C_{11}'' and C_{44}''. This effect can also be used as an advantage when injection-molding acoustofluidic devices if the attenuation of the polymer can be minimized using the ideal injection-molding process parameters. Nevertheless, special care must be taken when designing polymer-based devices because the fabrication can impact the elastic moduli. These results highlight the potential of the UEIS method, but more rigorous experiments are needed to reach firm conclusions.

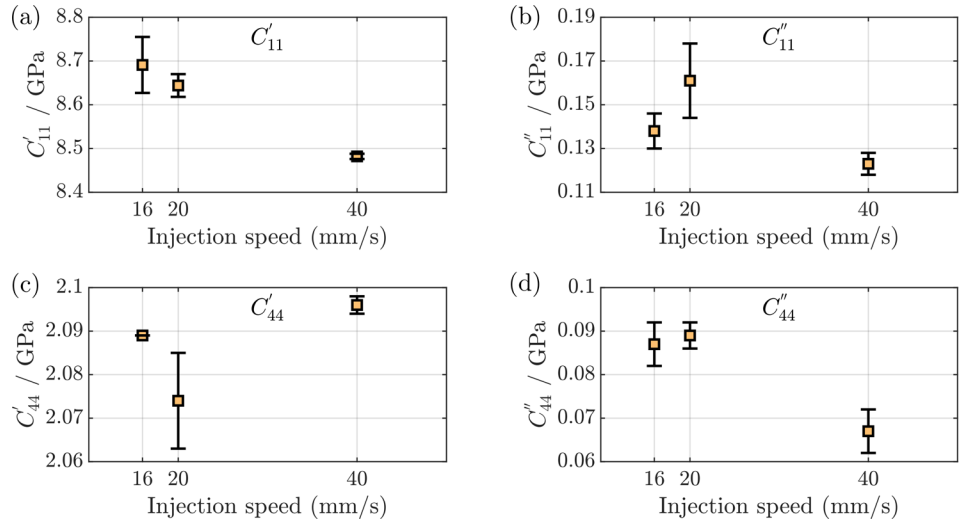

Figure 6.4: Changes in the four elastic moduli of the polymer PMMA (LG IG 840) with different injection speeds are shown. The mean of $N = 3$ measurements at the respective injection speed is indicated by a yellow square for C_{11}' (a), C_{11}'' (b), C_{44}' (c), and C_{44}'' (d). The error bars denote the standard error of the mean. Ph.D. student Komeil Saeedabadi kindly provided the polymer samples used in this study. The injection molding has been performed by the AcouPlast project partners at DTU Construct.

6.5 Concluding remarks

A new measurement technique has been developed to obtain the elastic material properties of isotropic polymer samples. The technique requires minimal experimental effort: the impedance spectrum of a piezoelectric disk is measured in the first step. Afterward, the whole stack consisting of the transducer disk, glue layer, and polymer ring must be assembled, and all dimensions must be measured. A final measurement of the electrical impedance spectrum of the polymer-loaded transducer concludes the experimental requirements. Afterward, the two measured impedance spectra and the dimensions are input into the automated fitting routine, and the final elastic material parameters are obtained within a few hours. This technique is advantageous compared to conventional methods because it allows nearly *in-situ* characterization of the material properties, as the stiffness components are obtained at a frequency range commonly used in acoustofluidics. UEIS has been employed to characterize several different polymers, with the resulting values listed in the appendix in Section A.2. Furthermore, a proof-of-concept study has evaluated the impact of changes in the injection-molding process parameters on the elastic moduli of polymers. Since the elastic moduli depend on the polymer grade and the manufacturing process, measurements of the material properties after injection molding are essential when performing numerical simulations.

6.6 Paper II: Phys. Rev. Appl., resubmitted, 1-11 (2022)

Determination of the complex-valued elastic moduli of polymers by electrical impedance spectroscopy for ultrasound applications

Authors: W.N. Bodé, F. Lickert, P. Augustsson, and H. Bruus.
Journal: Resubmitted to Phys. Rev. Appl., 1-11 (2022)
ArXiv preprint: arxiv.org/abs/2204.06464

Remarks: This work has been performed in collaboration with fellow Ph.D. student William Naundrup Bodé with equal first-authorship.

Determination of the complex-valued elastic moduli of polymers by electrical impedance spectroscopy for ultrasound applications

William N. Bodé,[1,*] Fabian Lickert,[1,†] Per Augustsson,[2,‡] and Henrik Bruus[1,§]

[1] *Department of Physics, Technical University of Denmark, DTU Physics Building 309, DK-2800 Kongens Lyngby, Denmark*

[2] *Department of Biomedical Engineering, Lund University, Ole Römers väg 3, 22363 Lund, Sweden*

(Dated: 30 September 2022)

A method is presented for the determination of complex-valued compression and shear elastic moduli of polymers for ultrasound applications. The resulting values, which are scarcely reported in the literature, are found with uncertainties typically around 1% (real part) and 6% (imaginary part). The method involves a setup consisting of a cm-radius, mm-thick polymer ring glued concentrically to a disk-shaped piezoelectric transducer. The ultrasound electrical impedance spectrum of the transducer is computed numerically and fitted to measured values as an inverse problem in a wide frequency range, typically from 500 Hz to 5 MHz, both on and off resonance. The method was validated experimentally by ultrasonic through-transmission around 1.9 MHz. The method is low cost, not limited to specific geometries and crystal symmetries, and, given the developed software, easy to execute. The method has no obvious frequency limitations before severe attenuation sets in above 100 MHz.

I. INTRODUCTION

Numerical simulations play an important role when optimizing and predicting piezoelectric device performance in applications including ultrasonic cleaning [1], energy harvesting [2], inkjet printing [3], and acoustofluidics [4, 5]. To perform precise, accurate, and predictive simulations, well-characterized material parameters such as the complex-valued elastic moduli are required. Whereas material databases exist [6], and manufactures may provide some of the required parameters, it is often not sufficient when attempting to perform reliable simulations and predictions. Polymers are in this regard a particularly challenging class of materials, since the elastic moduli of a given polymer may depend on unspecified parameters such as the distribution of polymer chain lengths and fabrication processes.

There exist a range of techniques to characterize an unknown material or substance mechanically. Dynamic techniques such as resonant ultrasound spectroscopy [7], transmission techniques [8, 9], impulse excitation [10], laser vibrometry and triangulation [11, 12], as well as static techniques, such as four-point bending, are widely used in various industries [13]. Those methods however often rely on a few mechanical eigenmodes or resonance frequencies of the material under study, a broad frequency spectrum due to a narrow pulse in the time domain, or even static or low-frequency measurements. Applications requiring actuation frequencies in the MHz-range however require material properties that were measured in similar frequency intervals for an accurate description of the system.

In this work we aim to extend the field of ultrasound spectroscopy [12, 14] by utilizing an electrical impedance spectrum spanning a frequency range of several MHz to obtain a full set of complex-valued elastic moduli of polymers. With this technique, labeled ultrasound electrical impedance spectroscopy (UEIS), a piezoelectric disk, driving vibrations in an attached polymer ring, is used to characterize the complex-valued elastic compressional and shear moduli of the polymer ring. Similar techniques have been used in the past to fit piezoelectric material parameters by an inverse problem and numerical optimization procedures on a free oscillating piezoelectric transducer [8, 12, 14–18]. Here, the same principles are used to fit elastic material parameters. From the UEIS spectrum of a mass-loaded transducer, an inverse problem is constructed to deduce the elastic moduli of the mass load. The method is similar to those of Refs. [12, 19, 20], but by including an automated whole-spectrum fit and complex parameter values, it extends the previous method as suggested in the conclusion of Ref. [20]. Instead of a thin-film transducer and manual fitting of few selected resonance peaks in the impedance spectrum, the UEIS method makes use of several hundred impedance values measured on a mechanically-loaded bulk transducer in the frequency range from 500 Hz to 5 MHz, to extract both real and imaginary parts of the complex-valued elastic moduli, and not just the real parts obtained in Ref. [20]. The UEIS technique enables low-cost and in-situ measurements of elastic moduli over a wide frequency range from low kHz to several MHz. It is easy to execute, requiring only a disk-shaped piezoelectric transducer, a ring of the unknown polymer sample, an impedance analyzer, and the developed fitting software.

The paper is organized as follows. In Section II a brief overview of the relevant theory is given, before in Section III the experimental and numerical methodology of the UEIS technique is described in detail for polymer,

* winabo@dtu.dk; Equal share first-author

† fabianl@dtu.dk; Equal share first-author

‡ per.augustsson@bme.lth.se

§ bruus@fysik.dtu.dk

glue, and transducer. In Section IV we provide validation data based on ultrasonic-through-transmission (UTT) measurements, before we in Section V present the main results of the UEIS method in terms of the complex-valued electromechanical parameters of the unloaded piezoelectric transducer and the complex-valued elastic moduli of the UV-cured glue and the polymer ring. We conclude in Section VI.

II. THEORETICAL BACKGROUND

We follow Ref. [21] and describe isotropic polymers using the standard linear theory of elastic solids in the Voigt notation, in terms of the displacement vector $\boldsymbol{u}$ of a given material point away from its equilibrium position, and the 1×6 strain $\boldsymbol{s}$ and stress $\boldsymbol{\sigma}$ column vectors with the 6×1 transposed row vectors $\boldsymbol{s}^{\mathsf{T}} = (\partial_x u_x, \partial_y u_y, \partial_z u_z, \partial_y u_z + \partial_z u_y, \partial_x u_z + \partial_z u_x, \partial_x u_y + \partial_y u_x)$ and $\boldsymbol{\sigma}^{\mathsf{T}} = (\sigma_{xx}, \sigma_{yy}, \sigma_{zz}, \sigma_{yz}, \sigma_{xz}, \sigma_{xy})$, respectively. Representing the elastic moduli C_{ik} by the tensor $\boldsymbol{C}$, the constitutive equation for an elastic solid in the ∞mm-symmetry class is [22],

$$\boldsymbol{\sigma} = \boldsymbol{C} \cdot \boldsymbol{s}, \tag{1a}$$

$$\boldsymbol{C} = \begin{pmatrix} C_{11} & C_{12} & C_{13} & 0 & 0 & 0 \\ C_{12} & C_{11} & C_{13} & 0 & 0 & 0 \\ C_{13} & C_{13} & C_{33} & 0 & 0 & 0 \\ 0 & 0 & 0 & C_{44} & 0 & 0 \\ 0 & 0 & 0 & 0 & C_{44} & 0 \\ 0 & 0 & 0 & 0 & 0 & C_{66} \end{pmatrix}. \tag{1b}$$

For an isotropic polymer $C_{33} = C_{11}$, $C_{66} = C_{44}$, and $C_{13} = C_{12} = C_{11} - 2C_{44}$, so here, $\boldsymbol{C}$ is given only by the two complex-valued elastic moduli C_{11} and C_{44}, each with a real and imaginary part, $C_{ik} = C'_{ik} + \mathrm{i}C''_{ik}$, relating to the propagation and attenuation of sound waves, respectively. Many amorphous polymers, such as the injection-molded PMMA in this work, are isotropic, but if not, such as semi-crystalline polymers [23], a $\boldsymbol{C}$ tensor with the appropriate lower symmetry must be used. Since only positive power dissipation is allowed, the elastic moduli are restricted by the constraint that the matrix $\mathrm{Im}(-\boldsymbol{C})$ must be positive definite [24].

We also model the piezoelectric lead-zirconate-titanate (PZT) transducer in the ∞mm-symmetry class [22], again following the notation of Ref. [21]. Here, $\boldsymbol{u}$, $\boldsymbol{S}$, $\boldsymbol{\sigma}$, and $\boldsymbol{C}$ are supplemented by the electric potential φ, the electric field $\boldsymbol{E} = -\boldsymbol{\nabla}\varphi$, the dielectric tensor $\boldsymbol{\varepsilon}$, the electric displacement field $\boldsymbol{D} = \boldsymbol{\varepsilon} \cdot \boldsymbol{E}$, and the piezoelectric 3×6 coupling tensor $\boldsymbol{e}$. The constitutive equation becomes,

$$\begin{pmatrix} \boldsymbol{\sigma} \\ \boldsymbol{D} \end{pmatrix} = \begin{pmatrix} \boldsymbol{C} & -\boldsymbol{e}^{\mathsf{T}} \\ \boldsymbol{e} & \boldsymbol{\varepsilon} \end{pmatrix} \begin{pmatrix} \boldsymbol{S} \\ \boldsymbol{E} \end{pmatrix} = \boldsymbol{M} \cdot \begin{pmatrix} \boldsymbol{S} \\ \boldsymbol{E} \end{pmatrix} \tag{2a}$$

$$\boldsymbol{e} = \begin{pmatrix} 0 & 0 & 0 & 0 & e_{15} & 0 \\ 0 & 0 & 0 & e_{15} & 0 & 0 \\ e_{31} & e_{31} & e_{33} & 0 & 0 & 0 \end{pmatrix}, \quad \boldsymbol{\varepsilon} = \begin{pmatrix} \varepsilon_{11} & 0 & 0 \\ 0 & \varepsilon_{11} & 0 \\ 0 & 0 & \varepsilon_{33} \end{pmatrix}. \tag{2b}$$

In the ∞mm-symmetry class, $C_{66} = \frac{1}{2}(C_{11} - C_{12})$, so the coupling tensor $\boldsymbol{M}$ is given by the five complex-valued elastic moduli C_{11}, C_{12}, C_{13}, C_{33}, and C_{44}, with $C_{ik} = C'_{ik} + \mathrm{i}C''_{ik}$, the two complex-valued dielectric constants ε_{11} and ε_{33} with $\varepsilon_{ik} = \varepsilon'_{ik} + \mathrm{i}\varepsilon''_{ik}$, and the three real-valued piezo-coupling constants e_{31}, e_{33}, and e_{15} with $e_{ik} = e'_{ik} + 0\mathrm{i}$. Since only positive power dissipation is allowed, the coupling constants are restricted by the following constraint on the matrix $\boldsymbol{K}$ [24],

$$\boldsymbol{K} = \mathrm{Im}\begin{pmatrix} -\boldsymbol{C} & \boldsymbol{e}^{\mathsf{T}} \\ \boldsymbol{e} & \boldsymbol{\varepsilon} \end{pmatrix} \text{ must be positive definite.} \tag{3}$$

We limit our analysis of the linear system to the time-harmonic response for a given angular frequency $\omega = 2\pi f$, where f is the excitation frequency of the system. Thus, any physical field $F_{\mathrm{phys}}(\boldsymbol{r}, t)$ is given by a complex-valued amplitude $F(\boldsymbol{r})$ as $F_{\mathrm{phys}}(\boldsymbol{r}, t) = \mathrm{Re}\left[F(\boldsymbol{r})\, \mathrm{e}^{-\mathrm{i}\omega t}\right]$, and we need only to compute $F(\boldsymbol{r})$. In our model of a polymer sample mounted on a PZT transducer having a bottom and top electrode, the system is excited by the excitation voltage $\varphi_{\mathrm{top}}^{\mathrm{phys}} = \mathrm{Re}\left[\varphi_{\mathrm{top}}\, \mathrm{e}^{-\mathrm{i}\omega t}\right]$ as follows,

$$\varphi_{\mathrm{bot}} = 0 \text{ V} \quad \text{and} \quad \varphi_{\mathrm{top}} = 1 \text{ V}. \tag{4}$$

By introducing the density ρ as an additional material parameter, the governing equations for the time-harmonic displacement field $\boldsymbol{u}$ in the polymer and in the PZT and for the quasi-electrostatic potential φ in the non-magnetic PZT without free charges, become

$$\boldsymbol{\nabla} \cdot \boldsymbol{\sigma} = -\rho\omega^2 \boldsymbol{u} \quad \text{and} \quad \boldsymbol{\nabla} \cdot \boldsymbol{D} = 0. \tag{5}$$

We neglect the effect of gravity in this formulation, as it only leads to a minor deformation of the geometry. The stress- and charge-free boundary conditions are imposed on free surfaces

$$\boldsymbol{\sigma} \cdot \boldsymbol{n} = \boldsymbol{0} \quad \text{and} \quad \boldsymbol{n} \cdot \boldsymbol{D} = 0. \tag{6}$$

The current density $\boldsymbol{J}$ in the PZT transducer is given by the polarization $\boldsymbol{P}$ as

$$\boldsymbol{J} = \partial_t \boldsymbol{P} = -\mathrm{i}\omega(\boldsymbol{D} - \varepsilon_0 \boldsymbol{E}). \tag{7}$$

Consequently, the electrical impedance Z central to the UEIS method can be computed via the flux integral of $\boldsymbol{J}$ through the surface $\partial\Omega_{\mathrm{top}}$ with surface normal $\boldsymbol{n}$ as,

$$Z = \frac{\varphi_{\mathrm{top}} - \varphi_{\mathrm{bot}}}{I}, \quad \text{with} \quad I = \int_{\partial\Omega_{\mathrm{top}}} \boldsymbol{n} \cdot \boldsymbol{J}\, \mathrm{d}A. \tag{8}$$

III. METHODOLOGY

The ultimate goal is to develop and test a method for determination of the complex-valued elastic moduli of polymers. However, to achieve an accuracy level of about 1-5%, we need also to determine the mechanical and electromechanical parameters of the piezoelectric transducer as well as the elastic moduli of the glue used to mount the polymer sample on the transducer.

A. Experimental procedure

Measurements of the electrical impedance spectrum $Z_{\mathrm{exp}}(f)$ were performed using a Vector Network Analyzer Bode 100 (OMICRON electronics GmbH, Klaus, Austria) in a linear interval with 10.000 steps between 500 Hz and 5 MHz, each frequency sweep taking less than 4 minutes. In a first step, the electrical impedance of an unloaded Pz27 disk (Meggitt A/S, Kvistgaard, Denmark) was characterized. The top and bottom electrode of the piezoelectric disk were contacted through spring-loaded pins in a custom-made sample holder, minimizing the contact force and area to a point in the center of the disk. In the following step, using a thin layer of the UV-curable glue NOA 86H (Norland Products, Jamesburg (NJ), USA), a polymer ring of known dimensions was glued on top of a Pz27 disk. This ring was made from either the NOA 86H glue itself or from polymethyl methacrylate (PMMA Diakon TD525, Lucite International, Rotterdam, Netherlands). We aimed at making the glue layer as thin (15-25 µm) and uniform as possible to reduce its influence on the combined system, as studied by Bodé *et al.* [25]. This was achieved by gently squeezing the system for a few seconds after assembly, just before curing the glue by UV illumination. The glue was cured at a UV-intensity of 15 mW/cm^2 at 365 nm for 167 s to achieve strong bonding between the transducer disk and the polymer ring. The glue NOA 86H was selected after performing experiments with several different adhesives, as it enables good adhesion between the PZT and the polymer and allows for good acoustic coupling due to acrylic-like properties in the cured state with an attenuation comparable to that found for the polymer ring. After curing, the electrical impedance of the polymer-loaded transducer was measured. The small hole of the polymer ring allows contacting the transducer disk using the above-mentioned spring-loaded pins. The average of three impedance measurements, taking less than 12 minutes to obtain, was used both for the unloaded and loaded case.

The diameter and thickness of the polymer ring and the Pz27 disk were measured before assembling the system using an electronic micrometer with an accuracy of ±4 µm. The glue-layer thickness was obtained as the measured total thickness of the assembled system minus the sum of the individual thicknesses of the Pz27 disk and the polymer ring. The impedance measurements were performed at 24 °C using a combination of two different nominal transducer dimensions (diameter 6.35 mm and 10 mm, thickness 0.5 mm) and two different nominal polymer ring dimensions (diameter 20 mm and 25 mm, thickness 1.4 mm), yielding four transducer-polymer systems with the dimensions listed in Tables I and II.

TABLE I. Measured thickness (TH) and outer diameter (OD) of the Pz27 disks (named Pz27-TH-OD). Measured TH, OD, and inner diameter (ID) of the rings made by the glue NOA 86H (named NOA86H-TH-OD) and of the polymer PMMA (named PMMA-TH-OD). Letters A, B, C are used as labels for samples with the same nominal dimensions. The precision is given as the standard deviation from six measurements.

Sample	TH (mm)	OD (mm)	ID (mm)
Pz27-0.5-6.35-A	0.510(1)	6.594(5)	–
Pz27-0.5-6.35-B	0.502(1)	6.587(2)	–
Pz27-0.5-10-A	0.500(1)	10.037(7)	–
Pz27-0.5-10-B	0.492(2)	10.039(3)	–
Pz27-0.5-10-C	0.505(2)	10.039(5)	–
NOA86H-1.4-20	1.5(2)	19.22(6)	1.90(2)
PMMA-1.4-20-A	1.428(2)	19.981(5)	1.98(1)
PMMA-1.4-20-B	1.440(4)	20.017(8)	1.94(1)
PMMA-1.4-25-A	1.427(5)	24.98(1)	1.92(1)
PMMA-1.4-25-B	1.437(5)	24.94(1)	1.94(2)

TABLE II. The measured glue-layer thickness of the five studied PMMA-ring-on-Pz27-disk configurations.

Pz27 disk	Polymer ring	Glue layer
Pz27-0.5-6.35-A	PMMA-1.4-20-A	15 µm
Pz27-0.5-6.35-B	PMMA-1.4-25-A	24 µm
Pz27-0.5-10-A	PMMA-1.4-25-B	21 µm
Pz27-0.5-10-B	PMMA-1.4-20-B	12 µm
Pz27-0.5-10-C	NOA86H-1.4-20	15 µm

B. Numerical model

The weak formulation of the finite element method (FEM) is used to implement the governing equations in the software COMSOL Multiphysics [26] to simulate the electrical impedance spectrum $Z_{\mathrm{sim}}(f)$ unloaded or loaded PZT transducer. In particular, we use the *weak form PDE* interface as described in our previous work [5, 21, 25]. The simulations are computed on a workstation with a 12-core, 3.5-GHz central processing unit and 128 GB random access memory. Third-order Lagrange polynomials are used as test functions for both $\boldsymbol{u}$ and φ. The model consists of three domains: a piezoelectric disk, a glue layer, and a polymer ring. Given the cylindrical geometry of the assembled stack and the axisymmetric structure of the coupling tensors $\boldsymbol{C}$ and $\boldsymbol{M}$ in Eqs. (1b) and (2a), the system can be reduced to an axisymmetric model as shown in Ref. [27] and illustrated in Fig. 1. This axisymmetrization reduces the computational time substantially. A suitable mesh element size is found by the mesh convergence study presented in Sec. S1 of the Supplemental Material [28], where in addition in Sec. S2, a COMSOL sample script is presented.

Using the "`LiveLink for MATLAB`"-interface provided by COMSOL, the MATLAB optimization procedures `fminsearchbnd` and `patternsearch` are used to fit the material parameters such that $Z_{\mathrm{sim}}(f)$ is as close to $Z_{\mathrm{exp}}(f)$ as possible. The `fminsearchbnd` algo-

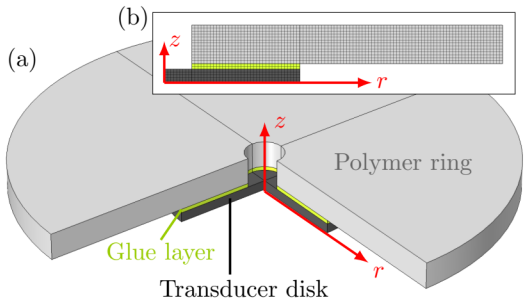

FIG. 1. (a) A 3D sketch of the system consisting of a polymer ring (light gray) glued (green) to a transducer disk (dark gray) whit a quarter cut away for visibility. (b) The inset shows the 2D axisymmetric domain in the r-z plane used for numerical simulations. The structured mesh is the one used at 5 MHz.

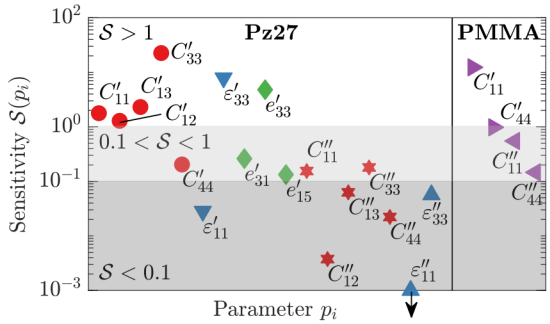

FIG. 2. The relative cost function sensitivity $\mathcal{S}(p_i)$ for the 17 piezoelectric material parameters p_i obtained as an average from four Pz27 disks in the frequency interval 500 Hz−5 MHz is shown in the left side of the figure. $\mathcal{S}(p_i)$ for the four PMMA parameters, calculated from the average of four Pz27–PMMA–systems, are shown on the right. Corresponding real and imaginary parts are visualized in the same color, and the regions of high ($\mathcal{S}(p_i) > 1$), medium ($0.1 < \mathcal{S}(p_i) < 1$) and low ($\mathcal{S}(p_i) < 0.1$) sensitivity are highlighted by gray shadows. The sensitivity of the parameter ε''_{11} is close to zero, as indicated by a black arrow.

rithm [30] allows a bounded search in parameter space. The `patternsearch` algorithm (part of the `Global Optimization Toolbox`) makes twice as many function evaluations, but it covers a larger region in parameter space and is better to locate the global minimum for poor initial values. Both algorithms use a gradient-free direct search and are therefore well suited for non-smooth numerical optimization procedures. The algorithms require three inputs: (i) initial values, (ii) upper and lower bounds, and (iii) a cost function to minimize. Based on the measured and simulated electrical impedance values $Z_{\mathrm{exp}}(f_i)$ and $Z_{\mathrm{sim}}(f_i)$ obtained at ~ 500 frequencies f_i, we define the cost function $\mathcal{C}$ as

$$\mathcal{C} = \sqrt{\sum_i \left[\log_{10}\left(|Z_{\mathrm{exp}}(f_i)|\right) - \log_{10}\left(|Z_{\mathrm{sim}}(f_i)|\right)\right]^2}. \quad (9)$$

Here, we use the logarithm, because $Z(f_i)$, having many peaks, varies by orders of magnitude as a function of f_i.

C. Sensitivity analysis

To enhance the performance of our fitting procedure, we group the parameters into sets of similar sensitivity based on the following sensitivity analysis of the cost function $\mathcal{C}$ on each of the sixteen material parameters $(p_1, p_2, \ldots p_{16})^{\mathrm{pz27}} = (C'_{11},\ C'_{12},\ C'_{13},\ C'_{33},\ C'_{44},\ \varepsilon'_{11},\ \varepsilon'_{33},\ e'_{31},\ e'_{33},\ e'_{15},\ C''_{11},\ C''_{12},\ C''_{13},\ C''_{33},\ C''_{44},\ \varepsilon''_{33})$ for the Pz27 disk and on the four polymer parameters $(p_1, \ldots p_4)^{\mathrm{polym}} = (C'_{11},\ C'_{44},\ C''_{11},\ C''_{44})$. The sensitivity analysis is performed in the frequency range from 500 Hz to 5 MHz, with the initial value p_i^0 taken from literature for a given parameter p_i, and therefore the individual sensitivity values represent averages over the entire frequency range. A more detailed study of the frequency dependency of the sensitivity is shown in Sec. S2 of the Supplemental Material [28]. We use a discrete approximation of the relative sensitivity $\mathcal{S}(p_i) = p_i \partial_{p_i} \mathcal{C}(p_i)$ of $\mathcal{C}(p_i)$ based on a ±10% variation of p_i around p_i^0, while keeping the remaining parameters fixed at p_j^0,

$$\mathcal{S}(p_i) = \frac{\mathcal{C}(1.1p_i) - \mathcal{C}(0.9p_i)}{1.1 - 0.9}, \quad p_j = p_j^0 \text{ for } j \neq i. \quad (10)$$

The obtained sensitivities $\mathcal{S}$ for the p_i^{pz27} and p_i^{pmma} parameters for Pz27 and PMMA, respectively, are shown in Fig. 2. The Pz27 parameters are classified in three groups of high $\mathcal{S}(p_i) > 1$, medium $0.1 < \mathcal{S}(p_i) < 1$, and low $\mathcal{S}(p_i) < 0.1$ sensitivity, respectively, and as described in the following section, a robust fitting is obtained by fitting the parameters group by group sequentially in descending order from high to low sensitivity. Since all four PMMA parameters have a medium-to-high sensitivity we fit them simultaneously in a single, undivided group.

D. The UEIS fitting procedure

The first step in the UEIS fitting procedure is to measure and simulate the electrical impedance $Z_{\mathrm{exp}}(f)$ and $Z_{\mathrm{sim}}(f)$, respectively, of an unloaded Pz27 transducer disk and then following Refs. [16–18] to fit the sixteen Pz27 parameters p_i^{pz27} in the form of an inverse problem by minimizing the cost function $\mathcal{C}$. In the second step, a characterized Pz27 disk is loaded by gluing on a given polymer ring using the UV-curable glue NOA 86H. To characterize the glue, the first studied polymer ring is made by the glue itself, and $Z(f)$ is used to similarly fit the four glue parameters p_i^{glue}. Subsequently, using the characterized glue, a PMMA ring is glued to a characterized Pz27 disk, and $Z(f)$ is used to similarly fit the four PMMA parameters p_i^{pmma}. See the flow chart in Fig. 3.

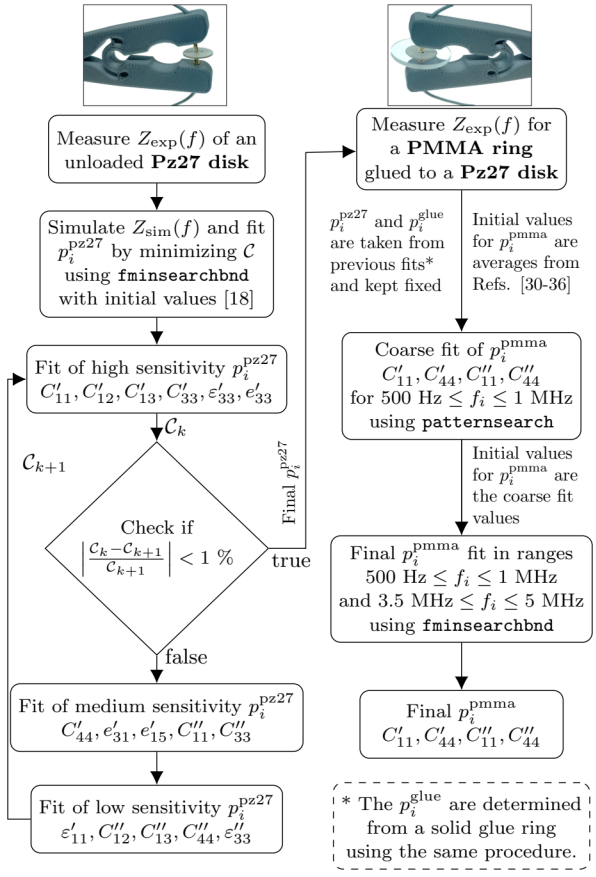

FIG. 3. A flow chart of the steps in the fitting procedure to obtain complex-valued elastic moduli for a polymer sample. First, the electrical impedance spectrum $Z_{\mathrm{exp}}(f)$ of a Pz27 transducer disk is measured in the range 500 Hz $< f_i <$ 5 MHz. Then, the Pz27 parameters p_i^{pz27} are fitted in the same frequency range with increments of $\Delta f = 10$ kHz based on their sensitivities in descending order, with initial values from Ref. [18]. Next step is the measurement of $Z_{\mathrm{exp}}(f)$ for the PMMA ring glued to the Pz27 disk in the range 500 Hz $< f_i <$ 5 MHz. Then, coarse fitting of the p_i^{pmma} is performed in the range 500 Hz $< f_i <$ 1 MHz with $\Delta f = 2$ kHz stepping, taking the initial values to be the average values of Refs. [31–37]. Lastly, a final fitting of p_i^{pmma} is done in the the range 3.5 MHz $< f_i <$ 5 MHz combined with previous range using steps of $\Delta f = 10$ kHz. A MATLAB-COMSOL sample script for the PMMA fitting procedure is presented in Sec. S2 of the Supplemental Material [28].

For the unloaded Pz27 disk, the initial values of p_i^{pz27} are taken from Ref. [18], and the kth iteration in the fit is divided into four sub-steps: (1) Fit the six parameters C'_{11}, C'_{12}, C'_{13}, C'_{33}, ε'_{33}, and e'_{33} of highest sensitivity $\mathcal{S} > 1$ using the `fminsearchbnd` algorithm in the range 500 Hz $< f_i <$ 5 MHz in increments of 10 kHz with the bounds set to ± 30 %, while keeping the remaining eleven parameters fixed. (2) Check whether the cost function $\mathcal{C}_k$ of iteration k deviates less than 1 % relative to $\mathcal{C}_{k-1}$ (the fit is converged and p_i^{pz27} have been determined) or not (the fitting continues). (3) Similarly, fit the five parameters C'_{44}, e'_{31}, e'_{15}, C''_{11}, and C''_{33} of medium sensitivity $0.1 < \mathcal{S} < 1$. (4) Likewise, fit the last six parameters ε'_{11}, C''_{12}, C''_{13}, C''_{44}, ε''_{11}, and ε''_{33} of low sensitivity $\mathcal{S} < 1$ and move on to iteration $k+1$. If during the fit a value of p_i^{pz27} is within 5 % of the pre-defined bound, the latter is changed by 50 %. Furthermore, for each evaluation of the cost function $\mathcal{C}$, it is checked if $\boldsymbol{K}$ in Eq. (3) is positive definite, and if not we set $\mathcal{C} = \infty$.

For the glue ring, the initial values of the four parameters p_i^{glue} are $C_{11}^{\mathrm{glue}} = (4.7 - 0.47\mathrm{i})$ GPa and $C_{44}^{\mathrm{glue}} = (0.9 - 0.09\mathrm{i})$ GPa inferred from Young's modulus of Ref. [38], the assumed value 0.38 of Poisson's ratio, and $C''_{ik} = 0.1C'_{ik}$. Moreover, the density of the glue ring is measured. The fitting is divided into two substeps to increase robustness and speed: (1) A coarse fit of the four parameters C'_{11}, C'_{44}, C''_{11}, and C''_{44} using the `patternsearch` algorithm in the limited range 500 Hz $< f_i <$ 1 MHz in increments of 2 kHz with the bounds set to be ± 40 % covering the typically observed range for polymers [9, 35]. (2) A final fit of C'_{11}, C'_{44}, C''_{11}, and C''_{44} using the `fminsearchbnd` algorithm in the combined ranges of 500 Hz $< f_i <$ 1 MHz and 3.5 MHz $< f_i <$ 5 MHz in increments of 2 kHz and 10 kHz, respectively, with the bounds set to ± 40 %, and with the coarse-fit values used as initial values. If during the fit a value of p_i^{glue} is within 5 % of the pre-defined bound, the bound is changed by 5 %, see the Supplemental Material [28]. Furthermore, for each evaluation of the cost function $\mathcal{C}$, it is checked if $\mathrm{Im}(-\boldsymbol{C})$ is positive definite, and if not we set $\mathcal{C} = \infty$.

For the PMMA ring, the initial values of p_i^{pmma} are taken to be the average of the values reported in Refs. [31–37]. This average is used due to the lack of parameter values provided by the manufacturer of our selected PMMA polymer. Since this PMMA consists of a toughened acrylic compound, we expect that it deviates from standard PMMA grades. Therefore we chose to use the average literature values only as initial values in our fitting routine, and we refrain from comparing them with the resulting UEIS values. Otherwise, the fitting procedure for the PMMA ring is the same as the one for the glue ring.

Note that for the selected materials in the studied frequency range from 500 Hz to 5 MHz, and measured with relative accuracies from 1% to 5%, the experimental results in Sections IV and V show that it is adequate to assume frequency-independent parameters p_i^{pz27}, p_i^{glue} and p_i^{pmma}. See further discussion in Section V C.

IV. ULTRASONIC-THROUGH-TRANSMISSION (UTT) VALIDATION DATA

For the polymer PMMA, we have carried out ultrasonic-through-transmission (UTT) measurements

[8, 37] to acquire data for experimental validation of the UEIS method. In UTT, a pulse, with center frequency f_c and width Δf in the frequency domain and width Δt in the time domain, is transmitted through a polymer slab of thickness d with its surface normal $\boldsymbol{n}$ tilted an angle θ_i relative to the incident pulse and emerged in water having the sound speed c_0. We have used $f_c = 1.90$ MHz, $\Delta f \approx 1$ MHz, and $\Delta t \approx 2$ µs. The UTT-method relies on the fact that at normal incidence only longitudinal waves are transmitted, whereas above a critical tilt angle $\theta_{\rm crit} = \sin^{-1}(c_0/c_{\rm lo})$ only transverse waves are transmitted in samples with $c_{\rm lo} > c_0$. The longitudinal and transverse speed of sound, $c_{\rm lo}$ and $c_{\rm tr}$, and the corresponding attenuation coefficients, $\alpha_{\rm lo}$ and $\alpha_{\rm tr}$, of the slab can be determined based on the difference $\Delta\tau$ of arrival times, with and without the slab placed in the water,

$$c_{\rm lo} = \left[1 + \frac{c_0}{d}\,\Delta\tau\right]^{-1} c_0, \tag{11a}$$

$$c_{\rm tr} = \left[\sin^2\theta_i + \left(\frac{c_0}{d}\,\Delta\tau + \cos\theta_i\right)^2\right]^{-\frac{1}{2}} c_0, \tag{11b}$$

$$\alpha_{\rm lo} = \alpha_0 + \frac{1}{d}\ln\left[\frac{T_{\rm lo}A_0}{A_{\rm lo}}\right], \tag{11c}$$

$$\alpha_{\rm tr} = \alpha_0\cos(\theta_s - \theta_i) + \frac{1}{d}\ln\left[\frac{T_{\rm tr}A_0}{A_{\rm lo}}\right]\cos\theta_s. \tag{11d}$$

Here, $T_{\rm lo}$ and $T_{\rm tr}$ are the longitudinal and transverse transmission coefficients, θ_s is the refractive angle of the shear wave, A_0 is the amplitude of the direct signal, and $A_{\rm lo}$ and $A_{\rm tr}$ are the longitudinal and transverse amplitudes of the transmitted signal after passing through the sample. Using the parameter values of water listed in Ref. [39], the attenuation coefficient α_0 of water is,

$$\begin{aligned}\alpha_0(T,f) &= 2\pi^2\left[\frac{4}{3}\eta_0(T) + \eta^{\rm b}(T)\right]\frac{f^2}{\rho_0 c_0^3}\\ &\approx \left[1 - 0.0249\frac{T - 25\ ^\circ\text{C}}{1\ ^\circ\text{C}}\right]\frac{0.0217 f^2}{1\ \text{MHz}^2}\frac{\text{Np}}{\text{m}}.\end{aligned} \tag{12}$$

As we do not control the room temperature in our UEIS measurements, but simply monitor it with a 1 ℃ uncertainty, we have used the UTT experiments to determine the temperature dependence of the elastic moduli of our PMMA sample. To this end, the UTT tank was filled with warm water at temperature $T = 31$ ℃. Then over a period of 6 hours, as the water steadily cooled to $T = 23$ ℃, the elastic moduli were measured at regular intervals, corresponding to steps in temperature of about −0.5 ℃. As shown in Sec. S4 of the Supplementary Material [28], the resulting longitudinal and transverse speed of sound ($c_{\rm lo}$ and $c_{\rm tr}$) and attenuation coefficients ($\alpha_{\rm lo}$ and $\alpha_{\rm tr}$) of PMMA at the frequency $f_c = 1.90$ MHz are found to depend linearly on temperature T (in ℃) as,

$$c_{\rm lo}^{1.90\ \text{MHz}}(T) = \left[-11(2)\,\frac{T}{1\ ^\circ\text{C}} + 2743(46)\right]\frac{\text{m}}{\text{s}}, \tag{13a}$$

$$c_{\rm tr}^{1.90\ \text{MHz}}(T) = \left[-4.5(4)\,\frac{T}{1\ ^\circ\text{C}} + 1267(9)\right]\frac{\text{m}}{\text{s}}, \tag{13b}$$

$$\alpha_{\rm lo}^{1.90\ \text{MHz}}(T) = \left[1.7(4)\,\frac{T}{1\ ^\circ\text{C}} + 25(10)\right]\frac{\text{Np}}{\text{m}}, \tag{13c}$$

$$\alpha_{\rm tr}^{1.90\ \text{MHz}}(T) = \left[7(2)\,\frac{T}{1\ ^\circ\text{C}} + 146(43)\right]\frac{\text{Np}}{\text{m}}. \tag{13d}$$

Here, the digits in the parentheses indicate 1σ uncertainties computed from on the sum-of-square differences between measured data and regression-line fits.

V. RESULTS OF THE UEIS METHOD

A. UEIS-fitted material parameters for Pz27

First, we determine the sixteen material parameters $p_i^{\rm pz27}$ for the four unloaded Pz27 disks with nominal outer diameters 6.35 mm and 10.0 mm and the measured dimensions listed in Table I. Using the UEIS method described in Section III involving the measured and fitted impedance spectra $Z_{\rm exp}(f)$ and $Z_{\rm sim}(f)$, we obtain the resulting parameters listed in Tables III and IV. In Table III we compare the real part of the obtained UEIS parameters to those provided in the literature (lit, [18]) and by the manufacturer (manf, [40]). The relative difference $\Delta_{\rm UEIS}^{\rm lit}$ between UEIS and literature values is in the range ∼2-8 %, whereas $\Delta_{\rm UEIS}^{\rm manf}$ is higher, typically in the range ∼5-40 %. The deviations are overall significant compared to the relative standard deviation $\hat{\sigma}_{\rm UEIS} \lesssim 2$ % of the mean of the UEIS values.

Similarly, in Table IV we compare the imaginary parts of the obtained UEIS parameters to those provided in the literature (lit, [18]). Note that ε''_{11} is set to zero due to its low value and sensitivity, and that $e''_{mj} = 0$ by assumption. In general, the imaginary parts are more difficult to measure than the real parts, which is reflected in the high values of $\hat{\sigma}_{\rm UEIS}$ ($\lesssim$10 %), $\Delta_{\rm UEIS}^{\rm lit}$ (∼5-50 %), but still with significant deviation between UEIS values and the values provided in the literature and by the manufacturer. The errors on the imaginary parts are about one order of magnitude larger than the errors on the real parts. This is in line with the previously found lower sensitivities of the former compared to the higher sensitivities of the latter shown in Fig. 2. Relative deviations of the initial values from the fitted values range from as little as 1.4 % for C''_{13} and up to 50 % for C''_{12} and above 200 % for ε''_{33}. Despite those deviations from the initial values, we find good convergence on the cost function and an excellent agreement between the measured and fitted impedance spectrum for the Pz27 disk. The uniqueness of the sixteen material parameters $p_i^{\rm pz27}$ is not guaranteed, but the simulated impedance spectrum fits the measured one, and thus they provide an adequate

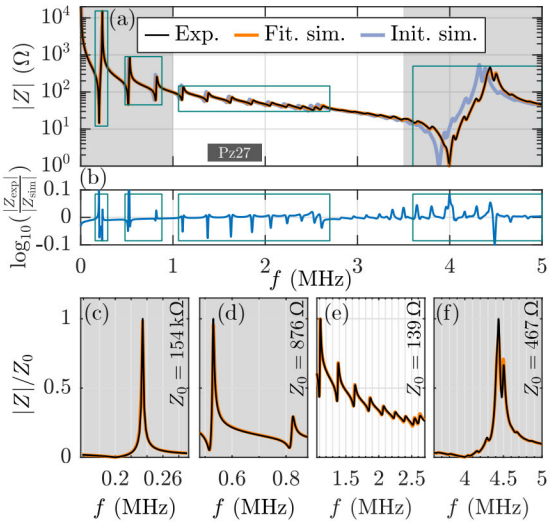

FIG. 4. (a) Semilog plot of the measured (black) and simulated UEIS $|Z(f)|$ of an unloaded Pz27-0.5-10 disk. In the simulations are used the UEIS-fitted (orange) and initial literature (blue) Pz27 parameters listed in Tables III and IV. The gray region indicates the frequency range used in the fitting. (b) The logarithmic difference $\Delta_{\rm sim}^{\rm exp} = \log_{10}(|Z_{\rm exp}|/|Z_{\rm sim}|)$ between measured and simulated impedance spectrum. (c)-(f) Zoom-in on different regions showing the measured and simulated spectrum on a linear and re-normalized scale. Each region is indicated by a frame in both (a) and (b).

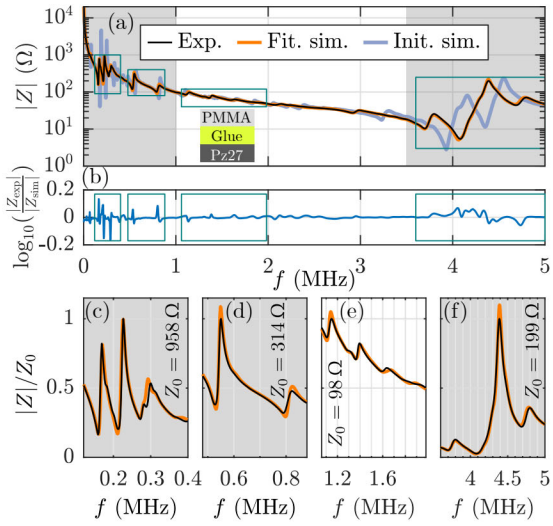

FIG. 5. (a) Semilog plot of the measured (black) and simulated UEIS $|Z(f)|$ of a PMMA-1.4-25 ring glued to a Pz27-0.5-10 disk by a 21-µm-thick layer of NOA 86H glue. The UEIS-fitted simulation (orange) is computed using the UEIS parameter values listed in Tables III, IV, V, and VI. The initial-value simulation is shown in blue. The gray regions indicate the frequency ranges used in the fitting. (b) The logarithmic difference $\Delta_{\rm sim}^{\rm exp} = \log_{10}(|Z_{\rm exp}|/|Z_{\rm sim}|)$ between measured and simulated impedance spectrum. (c)-(f) Zoom-in on different regions showing the measured and simulated spectrum on a linear and re-normalized scale. Each region is indicated by a frame in both (a) and (b).

estimate for the subsequent determination of the polymer parameters $p_i^{\rm pmma}$. In Fig. 4, an example is shown of the measured UEIS spectrum and the resulting simulated UEIS spectrum for a Pz27 disk of diameter 10 mm and thickness 0.5 mm.

B. UEIS-fitted material parameters for glue

The parameters $p_i^{\rm glue}$ of the used UV-cured NOA 86H glue were determined by the UEIS method as described in Section III D using a UV-cured glue ring glued to a Pz27 disk with the dimensions listed in Tables I and II. The resulting values for C_{11} and C_{44} are presented in Table V together with the corresponding values for the sound speeds $c_{\rm lo}$ and $c_{\rm tr}$, the attenuation coefficients $\alpha_{\rm lo}$ and $\alpha_{\rm tr}$, as well as Young's modulus E and Poisson's ratio ν. The expressions for these additional parameters, valid for any isotropic elastic material, are obtained by assuming frequency-independent moduli C_{11} and C_{44} in the limit of weak attenuation, $|C_{11}''| \ll C_{11}'$ and $|C_{44}''| \ll C_{44}'$, and by introducing the complex-valued wavenumbers $k_{\rm lo} = \omega/c_{\rm lo} + {\rm i}\alpha_{\rm lo}$ and $k_{\rm tr} = \omega/c_{\rm tr} + {\rm i}\alpha_{\rm tr}$,

$$c_{\rm lo} = \sqrt{\frac{C_{11}'}{\rho}}, \qquad \alpha_{\rm lo}(f) = \pi\sqrt{\frac{\rho}{(C_{11}')^3}}|C_{11}''|\, f, \tag{14a}$$

$$c_{\rm tr} = \sqrt{\frac{C_{44}'}{\rho}}, \qquad \alpha_{\rm tr}(f) = \pi\sqrt{\frac{\rho}{(C_{44}')^3}}|C_{44}''|\, f, \tag{14b}$$

$$\nu = \frac{\frac{1}{2}C_{11}' - C_{44}'}{C_{11}' - C_{44}'} \qquad E = \frac{3C_{11}' - 4C_{44}'}{C_{11}' - C_{44}'}\, C_{44}'. \tag{14c}$$

C. UEIS-fitted material parameters for PMMA

With the characterization of the Pz27 transducer disk and the glue completed, we move on to the determination of the complex-valued elastic moduli C_{11} and C_{44} for PMMA, which in principle could have been any other elastic polymer. We studied four PMMA polymer rings with the dimensions listed in Table I, all around 1.4 mm thick and with diameters of 20 or 25 mm, and glued to Pz27 disks with the dimensions listed in Table II.

The resulting UEIS-fitted parameters C_{11}', C_{44}', C_{11}'', and C_{44}'' at 24 °C for the PMMA are listed in Table VI together with the corresponding values obtained by the UTT technique. The relative standard deviation $\hat{\sigma}_{\rm UEIS}$ on the real parts is low (∼0.5 %), and an order of magnitude higher on the imaginary parts (3-6 %). We find good agreement between the UEIS and the UTT values, in all cases with relative deviations $\Delta_{\rm UEIS}^{\rm UTT} < 3\hat{\sigma}_{\rm UEIS}$. In

TABLE III. The real part (single prime) of the material parameters p_i^{pz27} of the four Pz27 disks of Table I obtained by the UEIS method with initial values from the literature [18]. The digits in brackets denote one standard deviation, $\hat{\sigma}_{\mathrm{UEIS}}$ is the relative standard deviation of the UEIS mean, and $\Delta^{\mathrm{lit}}_{\mathrm{UEIS}}$ and $\Delta^{\mathrm{manf}}_{\mathrm{UEIS}}$ is the relative deviation from UEIS of the values given by Ref. [18] (lit) and by the manufacturer (manf) [40], respectively. The density of Pz27 was measured to be $\rho_{\mathrm{pz27}} = 7.7(1)$ g/cm^3.

Pz27 disk	C'_{11} (GPa)	C'_{12} (GPa)	C'_{13} (GPa)	C'_{33} (GPa)	C'_{44} (GPa)	ε'_{11} (ε_0)	ε'_{33} (ε_0)	e'_{31} (C/m^2)	e'_{33} (C/m^2)	e'_{15} (C/m^2)
Pz27-0.5-6.35 (A)	127	80.1	82.3	121	20.3	963	780	−5.3	16.4	11.8
Pz27-0.5-6.35 (B)	126	78.8	81.4	122	20.7	957	753	−5.2	15.9	11.0
Pz27-0.5-10 (A)	123	75.6	77.3	117	20.8	993	839	−5.0	16.4	10.8
Pz27-0.5-10 (B)	121	74.7	76.5	117	21.3	1015	842	−5.1	16.4	10.4
Mean of UEIS	124(3)	77(3)	80(3)	119(3)	20.8(4)	982(27)	804(44)	−5.2(1)	16.3(3)	11.0(6)
Literature [18]	117.64	73.66	73.46	110.17	20.41	959.10	816.61	−5.19	16.06	11.59
Manufacturer [40]	147(4)	105(3)	94(2)	113(3)	23.0(6)	1130(113)	914(91)	−3.1(2)	16.0(8)	11.6(6)
$\hat{\sigma}_{\mathrm{UEIS}}$(%)	1.1	1.7	1.8	1.1	1.0	1.4	2.8	−1.5	0.8	2.6
$\Delta^{\mathrm{lit}}_{\mathrm{UEIS}}$(%)	−5.2	−4.7	−7.5	−7.6	−1.8	−2.3	1.6	0.6	−1.3	5.5
$\Delta^{\mathrm{manf}}_{\mathrm{UEIS}}$(%)	18	36	18	−5.2	11	15	14	−40	−1.7	5.5

TABLE IV. The imaginary part (double prime) of the material parameters p_i^{pz27} of the four Pz27 disks of Table I obtained by the UEIS method with initial values from the literature [18] and the parameters ε''_{11}, e''_{31}, e''_{33}, and e''_{15} set to zero by assumption. The digits in brackets denote one standard deviation, $\hat{\sigma}_{\mathrm{UEIS}}$ is the relative standard deviation of the UEIS mean, and $\Delta^{\mathrm{lit}}_{\mathrm{UEIS}}$ is the relative deviation from UEIS of the values of Ref. [18] (lit).

Pz27 disk	C''_{11} (MPa)	C''_{12} (MPa)	C''_{13} (MPa)	C''_{33} (MPa)	C''_{44} (MPa)	ε''_{11} (ε_0)	ε''_{33} (ε_0)	e''_{31} (C/m^2)	e''_{33} (C/m^2)	e''_{15} (C/m^2)
Pz27-0.5-6.35 (A)	−709	370	121	−280	−582	0	3.9	0	0	0
Pz27-0.5-6.35 (B)	−628	442	122	−377	−596	0	2.5	0	0	0
Pz27-0.5-10 (A)	−558	448	112	−518	−488	0	0.0	0	0	0
Pz27-0.5-10 (B)	−510	510	90.7	−538	−486	0	6.3	0	0	0
Mean of UEIS	−601(87)	442(57)	112(15)	−428(122)	−538(59)	0	3(3)	0	0	0
Literature [18]	−460	220	110	−400	−400	–	10.72	–	–	–
$\hat{\sigma}_{\mathrm{UEIS}}$(%)	−7.2	6.4	6.6	−14	−5.5	–	41	–	–	–
$\Delta^{\mathrm{lit}}_{\mathrm{UEIS}}$(%)	−23	−50	−1.4	−6.6	−26	–	235	–	–	–

terms of the derived sound speeds, c_{lo} and c_{tr}, and the derived Young's modulus E and Poisson's ratio ν, the relative deviation of UTT values from UEIS values is around 0.5 %. For the longitudinal and transverse attenuation α_{lo} and α_{tr} coefficients, the relative deviations of UTT values relative to UEIS values are higher, around 7-15 %.

Again, likely due to the lower sensitivity of the C''_{11} and C''_{44} coefficients, it proves more difficult to obtain the imaginary parts of the elastic moduli than the real parts. Deviations of the UTT values from the UEIS values, may in part be explained by the fact that the

TABLE V. The material parameters at 24 °C of the UV-cured NOA 86H glue determined by the UEIS method. The density of the glue was measured to be $\rho = 1.3(2) \times 10^3$ kg m^{-3}, and the attenuation coefficients are for the center frequency $f_c = 1.90$ MHz of the UTT method described in Section IV.

Parameter	Parameter	Parameter
$C'_{11} = 4.65$ GPa	$c_{\mathrm{lo}} = 1891$ m/s	$E = 3.20$ GPa
$C'_{44} = 1.21$ GPa	$c_{\mathrm{tr}} = 965$ m/s	$\nu = 0.32$
$C''_{11} = -0.51$ GPa	$\alpha_{\mathrm{lo}}(f_c) = 346$ Np/m	
$C''_{44} = -0.12$ GPa	$\alpha_{\mathrm{tr}}(f_c) = 613$ Np/m	

TABLE VI. The UEIS-fitted and UTT-measured elastic moduli for PMMA at 24 °C with a measured density $\rho = 1162(4)$ kg/m^3, and α_{lo} and α_{tr} evaluated at 1.90 MHz. For UEIS, $\hat{\sigma}_{\mathrm{UEIS}}$ is the relative standard deviation of the UEIS mean. For UTT, the errors are based on 1σ-prediction intervals around linear regression fits. $\Delta^{\mathrm{UTT}}_{\mathrm{UEIS}}$ is the deviation of the UTT values relative to the UEIS values.

Param.	Unit	UEIS	$\hat{\sigma}_{\mathrm{UEIS}}$ (%)	UTT	$\Delta^{\mathrm{UTT}}_{\mathrm{UEIS}}$ (%)
C'_{11}	GPa	7.18(4)	0.6	7.1(1)	−1.1
C''_{11}	GPa	−0.183(5)	2.9	−0.19(1)	3.8
C'_{44}	GPa	1.553(8)	0.5	1.56(1)	0.5
C''_{44}	GPa	−0.111(7)	6.3	−0.098(6)	−11.7
c_{lo}	m/s	2486(8)	0.3	2469(19)	−0.7
c_{tr}	m/s	1156(4)	0.3	1160(4)	0.3
α_{lo}	Np/m	61(2)	3.2	66(4)	8.2
α_{tr}	Np/m	370(24)	6.4	322(18)	−13.0
E	GPa	4.23(2)	0.5	4.25(3)	0.5
ν	–	0.362(1)	0.4	0.358(3)	−1.1

UTT technique uses a frequency pulse with a width of 1 MHz around the center frequency 1.90 MHz, whereas UEIS is based on an entire frequency spectrum from 500 Hz to 5 MHz using a single frequency at a time. However, whereas different models exist, which assume a frequency-dependence of the elastic moduli of PMMA [12], similar to the frequency dependencies measured in PDMS [9], we do find it sufficient in the UEIS method to neglect the frequency-dependence of the complex-valued elastic moduli of PMMA.

In Fig. 5 is shown an example of the measured and the simulated UEIS spectra for a PMMA ring glued to a Pz27 disk. We find a good agreement between the measured and the fitted simulated UEIS spectrum, and it can also be seen, how even smaller features of the experimental impedance curve are captured in the simulated frequency spectrum. Relative deviations $\Delta_{\mathrm{sim}}^{\mathrm{exp}} = \log_{10} \frac{|Z_{\mathrm{exp}}|}{|Z_{\mathrm{sim}}|}$ up to 20 % are found in regions near resonance peaks. However, zoom-ins there show how a frequency-shift of a few percent can lead to high deviations $\Delta_{\mathrm{sim}}^{\mathrm{exp}}$, while still maintaining good agreement between measurement and simulation. For example, shifting a Lorentzian peak with a Q-value of $Q = 250$ by 1% of its resonance frequency, results in a relative deviation $\sim 10\%$.

We furthermore studied the impact of small deviations in the thickness and elastic moduli of the glue on the obtained coefficients for the polymer ring. A change of the Young's modulus E_{glue} by ± 1 % leads to changes in the real-valued coefficients C'_{11} and C'_{44} by less than 0.05 %, while the C''_{11} and C''_{44} coefficients change by 0.4 % and 0.6 % respectively. In a separate numerical study, when changing the thickness of the glue layer from 12 µm to 8 µm, a relative deviation of 33.3 %, we observe a decrease in the real-valued coefficients C'_{11} and C'_{44} by 0.8 % and 0.2 % respectively. The relative changes for the imaginary-valued coefficients C''_{11} and C''_{44} are slightly higher by +2.4 % and −1.3 %, respectively, but still much lower when compared to the relative change in thickness and well in line with the identified uncertainties of the parameters listed in Table VI.

As a further validation of the UEIS method, we use the UEIS-fitted values p_i^{pmma} to simulate selected resonance modes in the PMMA ring. Subsequently, as shown in Sec. S5 in the Supplemental Material [28], we have successfully compared these predicted modes with direct measurements of the corresponding modes obtained by using a single-point laser-Doppler vibrometer system VibroFlex Connect (Polytec, Waldbronn, Germany).

VI. CONCLUSION

We have developed a method based on measured and simulated ultrasound electrical impedance spectroscopy (UEIS) able to determine the frequency-independent complex-valued elastic moduli of polymers. The method is a two-step procedure: Firstly, the material parameters of the used, unloaded piezoelectric transducer disk are fitted by an inverse problem, matching the measured and simulated electrical impedance spectrum. Secondly, a polymer ring is glued onto the transducer, and the same technique is used to fit the complex-valued elastic moduli of the polymer. To evaluate its reproducibility, the method was applied on four different system geometries involving the polymer PMMA, achieving a relative error below 0.5 % for Young's modulus and Poisson's ratio, and below 7 % for the attenuation coefficients. The method was validated experimentally within the 3σ-level using ultrasonic through-transmission on PMMA samples.

It is noteworthy that the model assumption of frequency-independent elastic moduli C_{ik} leads to simulated UEIS spectra $Z_{\mathrm{sim}}(f)$ that predicts the measured UEIS spectra $Z_{\mathrm{exp}}(f)$ so well in the entire frequency range from 500 Hz to 5 MHz as shown in Figs. 4 and 5 for Pz27 and PMMA, as well as for the UV-curable glue NOA 86H (not shown). This frequency independence leads to the linear frequency dependence of the attenuation coefficients α_{lo} and α_{tr} exhibited in Eq. (14), a linearity which can be contrasted with the f^2-dependence of α_0 in Newtonian fluids, Eq. (12), and the non-integer powers observed in typically softer materials, such as the $f^{1.456}$-dependence of α_{lo} and the $f^{0.924}$-dependence of α_{tr} observed in the rubber PDMS [9]. It is straightforward to include such frequency-dependency of the elastic moduli in the UEIS model, should materials with that property be studied. One simply modify the respective moduli and coupling coefficients in the constitutive equations (1) and (2) at the cost of extending the list of parameters p_i with the necessary parameters needed to describe the frequency dependency. For the relatively stiff polymer PMMA, the elastic modulus tensor $\boldsymbol{C}$ can be taken as frequency independent, whereas modeling softer, rubber-like materials, the frequency dependency of $\boldsymbol{C}$ must be taken into account [41].

The UEIS technique extends the existing field of resonance ultrasound spectroscopy by making use of the electrical impedance spectrum over a wide frequency range of several MHz involving both on-resonance and off-resonance frequencies, it has no obvious frequency limitations before severe attenuation sets in above 100 MHz, and it contains information of all relevant parameters of the piezoelectric transducer disk, the glue layer, the polymer ring, and the geometry of the assembled stack. Experimentally, the technique is low-cost, easy-to-use, simple, and well-suited for materials used in ultrasound applications. The recording of a given impedance spectrum takes less than 4 minutes. Afterwards, within about 1 minute, the impedance spectrum can be loaded into our MATLAB script, and the automated UEIS fitting procedure is executed. After a run time of about 10 hours, the resulting UEIS-fitted impedance spectrum and the parameter values p_i^{pz27}, p_i^{glue}, or p_i^{pmma} are delivered by the software.

The UEIS technique is not limited to the chosen examples of Pz27, glue, and PMMA, but it can in principle be

used on other classes of elastic materials including rubbers, glasses, and metals. We believe that the presented UEIS technique will become a valuable and easy-to-use tool in the ultrasound application fields mentioned in the introduction, by providing well-determined parameter values for the materials used, namely the relevant complex-valued elastic moduli at the relevant ultrasound frequencies.

VII. ACKNOWLEDGMENTS

We would like to thank Ola Jakobsson (Lund University) for setting up and introducing us to the laser-Doppler vibrometer system, Axel Tojo (Lund University) for his help with the UTT setup, Komeil Saeedabadi and Erik Hansen (DTU) for providing and cutting the polymer rings, and Erling Ringgaard (Meggitt) for useful discussions and for providing the Pz27 samples. This work is part of the Eureka Eurostars-2 E!113461 AcouPlast project funded by Innovation Fund Denmark, grant no. 9046-00127B, and Vinnova, Sweden's Innovation Agency, grant no. 2019-04500. Finally, the work was supported by Independent Research Fund Denmark, Technology and Production Sciences, grant no. 8022-00285B and the Swedish Foundation for Strategic Research, grant no. FFL18-0122.

[1] N. Bretz, J. Strobel, M. Kaltenbacher, and R. Lerch, Numerical simulation of ultrasonic waves in cavitating fluids with special consideration of ultrasonic cleaning, in *IEEE Int. Ultrason. Symp.* (2005) pp. 703–706.

[2] M. T. Todaro, F. Guido, V. Mastronardi, D. Desmaele, G. Epifani, L. Algieri, and M. De Vittorio, Piezoelectric MEMS vibrational energy harvesters: Advances and outlook, Microelectron. Eng. **183**, 23 (2017).

[3] M. Singh, H. M. Haverinen, P. Dhagat, and G. E. Jabbour, Inkjet printing-process and its applications, Adv. Mater. **22**, 673 (2010).

[4] W. N. Bodé, L. Jiang, T. Laurell, and H. Bruus, Microparticle acoustophoresis in aluminum-based acoustofluidic devices with PDMS covers, Micromachines **11**, 292 (2020).

[5] F. Lickert, M. Ohlin, H. Bruus, and P. Ohlsson, Acoustophoresis in polymer-based microfluidic devices: Modeling and experimental validation, J. Acoust. Soc. Am. **149**, 4281 (2021).

[6] MatWeb, LLC, http://www.matweb.com/ (2022).

[7] A. Migliori, J. Sarrao, W. M. Visscher, T. Bell, M. Lei, Z. Fisk, and R. Leisure, Resonant ultrasound spectroscopic techniques for measurement of the elastic moduli of solids, Physica B **183**, 1 (1993).

[8] H. Wang, W. Jiang, and W. Cao, Characterization of lead zirconate titanate piezoceramic using high frequency ultrasonic spectroscopy, J. Appl. Phys. **85**, 8083 (1999).

[9] G. Xu, Z. Ni, X. Chen, J. Tu, X. Guo, H. Bruus, and D. Zhang, Acoustic Characterization of Polydimethylsiloxane for Microscale Acoustofluidics, Phys. Rev. Applied **13**, 054069 (2020).

[10] G. Roebben, B. Bollen, A. Brebels, J. Van Humbeeck, and O. Van der Biest, Impulse excitation apparatus to measure resonant frequencies, elastic moduli, and internal friction at room and high temperature, Rev. Sci. Instrum. **68**, 4511 (1997).

[11] R. Willis, L. Wu, and Y. Berthelot, Determination of the complex young and shear dynamic moduli of viscoelastic materials, J. Acoust. Soc. Am. **109**, 611 (2001).

[12] J. Ilg, S. J. Rupitsch, A. Sutor, and R. Lerch, Determination of Dynamic Material Properties of Silicone Rubber Using One-Point Measurements and Finite Element Simulations, IEEE T. Instrum. Meas. **61**, 3031 (2012).

[13] M. Radovic, E. Lara-Curzio, and L. Riester, Comparison of different experimental techniques for determination of elastic properties of solids, Mat Sci Eng A-Struct **368**, 56 (2004).

[14] S. J. Rupitsch and R. Lerch, Inverse Method to estimate material parameters for piezoceramic disc actuators, Appl. Phys. A **97**, 735 (2009).

[15] J. Plesek, R. Kolman, and M. Landa, Using finite element method for the determination of elastic moduli by resonant ultrasound spectroscopy, J. Acoust. Soc. Am. **116**, 282 (2004).

[16] N. Pérez, M. A. B. Andrade, F. Buiochi, and J. C. Adamowski, Identification of elastic, dielectric, and piezoelectric constants in piezoceramic disks, IEEE Trans. Ultrason. Ferroelec. Freq. Contr. **57**, 2772 (2010).

[17] N. Pérez, R. Carbonari, M. Andrade, F. Buiochi, and J. Adamowski, A FEM-based method to determine the complex material properties of piezoelectric disks, Ultrasonics **54**, 1631 (2014).

[18] C. Y. Kiyono, N. Perez, and E. C. N. Silva, Determination of full piezoelectric complex parameters using gradient-based optimization algorithm, Smart Mater. Struct. **25**, 025019 (2016).

[19] J. Maynard, Resonant Ultrasound Spectroscopy, Physics Today **49**, 26 (1996).

[20] A. G. Steckel, H. Bruus, P. Muralt, and R. Matloub, Fabrication, characterization, and simulation of glass devices with AlN thin-film transducers for excitation of ultrasound resonances, Phys. Rev. Applied **16**, 014014, 1 (2021).

[21] N. R. Skov, J. S. Bach, B. G. Winckelmann, and H. Bruus, 3D modeling of acoustofluidics in a liquid-filled cavity including streaming, viscous boundary layers, surrounding solids, and a piezoelectric transducer, AIMS Mathematics **4**, 99 (2019).

[22] T. Ikeda, *Fundamentals of Piezoelectricity* (Oxford University Press, London, UK, 1996).

[23] G. H. Michler and W. Lebek, *Electron microscopy of polymers* (Wiley, Hoboken (NJ), 2016) pp. 277–293.

[24] R. Holland, Representation of Dielectric, Elastic, and Piezoelectric Losses by Complex Coefficients, IEEE T. Son. Ultrason **14**, 18 (1967).

[25] W. N. Bodé and H. Bruus, Numerical study of the coupling layer between transducer and chip in acoustofluidic

devices, J. Acoust. Soc. Am. **149**, 3096 (2021).
[26] COMSOL Multiphysics 5.5 (2019), http://www.comsol.com.
[27] A. G. Steckel and H. Bruus, Numerical study of acoustic cell trapping above elastic membrane disks driven in higher-harmonic modes by thin-film transducers with patterned electrodes, Phys. Rev. E **submitted**, 14 pages (2021), https://arxiv.org/abs/2112.12567.
[28] See Supplemental Material at [URL] for details on the mesh convergence analysis, a study on the sensitivity versus elastic moduli and frequency range, sample MATLAB and COMSOL scripts for the UEIS fitting procedure, the corresponding data for the impedance spectra, and the validation of the UEIS method by UTT and laser-Doppler vibrometry, which includes Refs. [16, 29].
[29] W. D. Callister Jr, *Materials Science and Engineering: An Introduction*, seventh ed. (John Wiley & Sons, York, PA, 2007) p. 975.
[30] John D'Errico, Matlab file exchange (2012), https://www.mathworks.com/matlabcentral/fileexchange/8277-fminsearchbnd-fminsearchcon, access 30 Sep 2022.
[31] B. Hartmann and J. Jarzynski, Polymer sound speeds and elastic constants, Naval Ordnance Laboratory **Report NOLTR 72-269**, 1 (1972).
[32] D. Christman, Dynamic properties of poly (methylmethacrylate) (PMMA) (plexiglas), General Motors Technical Center, Warren (MI), USA **Report No. DNA 2810F, MSL-71-24, 1**, 1 (1972).
[33] H. Sutherland and R. Lingle, Acoustic characterization of polymethyl methacrylate and 3 epoxy formulations, J. Appl. Phys. **43**, 4022 (1972).
[34] H. Sutherland, Acoustical determination of shear relaxation functions for polymethyl methacrylate and Epon 828-Z, J. Appl. Phys. **49**, 3941 (1978).
[35] J. E. Carlson, J. van Deventer, and A. S. C. Carlander, Frequency and temperature dependence of acoustic properties of polymers used in pulse-echo systems, IEEE Ultrasonics Symposium , 885 (2003).
[36] A. Simon, G. Lefebvre, T. Valier-Brasier, and R. Wunenburger, Viscoelastic shear modulus measurement of thin materials by interferometry at ultrasonic frequencies, J. Acoust. Soc. Am. **146**, 3131 (2019).
[37] H. T. Tran, T. Manh, T. F. Johansen, and L. Hoff, Temperature effects on ultrasonic phase velocity and attenuation in Eccosorb and PMMA, in *2016 IEEE International Ultrasonics Symposium (IUS)* (2016) pp. 1–4.
[38] *Norland Optical Adhesive 86H*, Norland Products Inc., Jamesburg, NJ 08831, USA, https://www.norlandprod.com/adhesives/NOA86H.html, accessed 30 Sep 2022.
[39] P. B. Muller and H. Bruus, Numerical study of thermoviscous effects in ultrasound-induced acoustic streaming in microchannels, Phys. Rev. E **90**, 043016 (2014).
[40] *Ferroperm matrix data*, Meggitt A/S, Porthusvej 4, DK-3490 Kvistgaard, Denmark, https://www.meggittferroperm.com/materials/, accessed 30 Sep 2022.
[41] T. Pritz, Frequency dependences of complex moduli and complex poisson's ratio of real solid materials, J. Sound Vib. **214**, 83 (1998).

Supplementary material: Determination of complex-valued elastic moduli of polymers by electrical impedance spectroscopy for ultrasound applications

William N. Bodé,[1,*] Fabian Lickert,[1,†] Per Augustsson,[2,‡] and Henrik Bruus[1,§]

[1] *Department of Physics, Technical University of Denmark, DTU Physics Building 309, DK-2800 Kongens Lyngby, Denmark*

[2] *Department of Biomedical Engineering, Lund University, Ole Römers väg 3, 22363 Lund, Sweden*

(Dated: 30 September 2022)

Supplementary material for details on the mesh convergence analysis, a study on the sensitivity versus elastic moduli and frequency range, sample MATLAB and COMSOL scripts for the UEIS fitting procedure, the corresponding data for the impedance spectra, and the validation of the UEIS method by UTT and laser-Doppler vibrometry.

S1. MESH CONVERGENCE

Third-order Lagrange polynomials are used as test functions for both $\boldsymbol{u}$ and φ. The model consists of three domains: a piezoelectric transducer disk, a glue layer, and a polymer ring. For each domain Ω_k, the maximum mesh element size is given as $h_{\max}^{(k)} = c_{\mathrm{tr}}^{(k)}/(sf)$, where s is a dimensionless mesh-size parameter, and f is the frequency. A mesh convergence is performed at $f = 5$ MHz by sweeping in s and computing the error $\mathrm{err}(g)$ defined by the L_2-norm for the solution $g(\boldsymbol{r})$,

$$\mathrm{err}(g) = \sqrt{\frac{\int_{\Omega_k} |g - g_0|^2 \,\mathrm{d}a}{\int_{\Omega_k} |g_0|^2 \,\mathrm{d}a}}, \tag{1}$$

where g_0 refers to the solution with the best resolved mesh obtained by the given computational resources. Results of the mesh convergence are shown in Fig. S1, where the numerical error is seen to be below 1 % and exponentially decaying for $s > 2.2$.

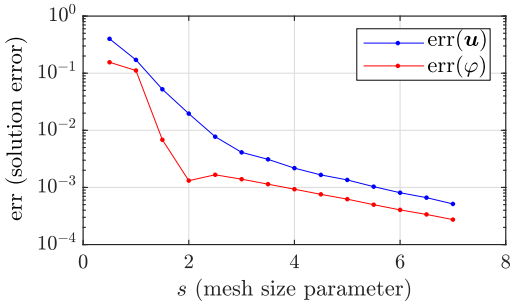

FIG. S1. Mesh convergence analysis presented as a semilog plot of the errors $\mathrm{err}(\boldsymbol{u})$ (blue) and $\mathrm{err}(\varphi)$ (red) versus the mesh size parameter s.

S2. SENSITIVITY OF $Z(f)$ VERSUS THE ELASTIC MODULI AND FREQUENCY RANGE

In Eqs. (9) and (10) of Sec. III-C in the main paper, we defined the sensitivity of the UEIS method as the logarithmic derivative $\mathcal{S}(p_i) = p_i \partial_{p_i} \mathcal{C}(p_i)$ of the cost function $\mathcal{C}$ with respect to the material parameters p_i, where $\mathcal{C}$ involves the difference between the measured and the simulated impedance spectrum $Z(f)$ averaged over the entire frequency range. Here, following the procedure in a similar study of the material parameters of a PZT transducer by Pérez *et al.* [1], we study the dependency on the elastic moduli of $Z(f)$ in two frequency ranges, the low-frequency range 0.5 - 1000 kHz and the high frequency range 3.5 - 5.0 MHz.

In Fig. S2, the changes of $Z(f)$ of a PMMA-loaded Pz27 transducer disk are observed, as the normalized elastic moduli $\tilde{C}_{ik} = C_{ik}/C_{ik}^{\mathrm{ueis}}$ of the PMMA ring are changed by from 0.80 to 1.20 in steps of 0.01, where C_{ik}^{ueis} are the values determined by the UEIS method, see Table VI. It is seen that the spectrum $Z(f)$ is nearly independent of $\tilde{C}'_{11}$ in the low frequency range (vertical ridges in the $\tilde{C}'_{11}$-f plane), and that it has a high sensitivity in the 3.5-5.0-MHz high frequency range (angled

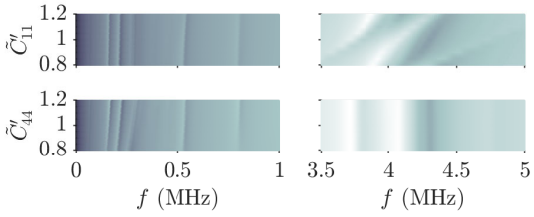

FIG. S2. Surface plot from 7 Ω (bright) to 128 kΩ (dark), using a logarithmic color scale, of the simulated electrical impedance spectrum $|Z(f)|$ of a Pz27-0.5-10 disk loaded by an on-glued PMMA-1.4-25 ring as a function of the frequency f and of the normalized real-part elastic moduli of PMMA, $\tilde{C}'_{11} = C'_{11}/C'^{\mathrm{ueis}}_{11}$ and $\tilde{C}'_{44} = C'_{44}/C'^{\mathrm{ueis}}_{44}$. Here $C'^{\mathrm{ueis}}_{11} = 7.18$ GPa and $C'^{\mathrm{ueis}}_{11} = 1.553$ GPa are the values determined by the UEIS method, see Table VI.

* winabo@dtu.dk; Equal share first-author

† fabianl@dtu.dk; Equal share first-author

‡ per.augustsson@bme.lth.se

§ bruus@fysik.dtu.dk

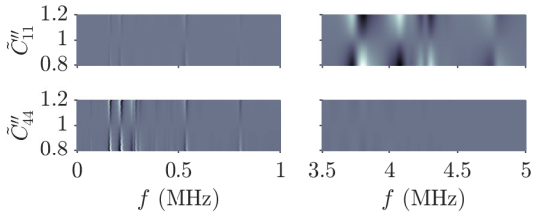

FIG. S3. Surface plot from 0.63 (bright) to 1.58 (dark), using a logarithmic color scale, of the simulated normalized electrical impedance spectrum $|Z(f)|/|Z_1(f)|$ of a Pz27-0.5-10 disk loaded by an on-glued PMMA-1.4-25 ring as a function of the frequency f and of the normalized imaginary-part elastic moduli of PMMA, $\tilde{C}''_{11} = C''_{11}/C''^{\text{ueis}}_{11}$ and $\tilde{C}''_{44} = C''_{44}/C''^{\text{ueis}}_{44}$. Here, $|Z_1(f)|$ is the reference spectrum calculated at $\tilde{C}''_{11} = \tilde{C}''_{44} = 1$, and $C''^{\text{ueis}}_{11} = -0.183$ GPa and $C''^{\text{ueis}}_{44} = -0.111$ GPa are the values determined by the UEIS method, see Table VI.

ridges in the $\tilde{C}'_{11}$-f plane). In contrast, $Z(f)$ has a small sensitivity to $\tilde{C}'_{44}$ in the low frequency range and is almost insensitive to $\tilde{C}'_{44}$ in the high frequency range. Similarly, Fig. S3 shows that $Z(f)$ is insensitive to $\tilde{C}''_{11}$ in the low frequency range, but sensitive in the high frequency range (large amplitude variations for fixed frequency). Conversely, $Z(f)$ is sensitive to $\tilde{C}''_{44}$ in the low frequency range and insensitive in the high frequency range.

S3. MATLAB AND COMSOL SCRIPTS FOR UEIS-FITTING OF PMMA PARAMETERS

In the Supplemental Material, we have included the sample files listed in Table S1. Using these files, the reader can redo the UEIS fitting procedure, described in Section V of the main paper, for the polymer PMMA based on the measured UEIS spectrum of a PMMA ring glued to a Pz27 transducer disk. The main MATLAB script `UEIS_polymer_script.m` is opened using the "`LiveLink for MATLAB`"-interface provided by COMSOL Multiphysics. It loads the COMSOL 6.0 script `UEIS_polymer_comsol_model.mph` together with the data points of the measured impedance spectrum `experiment_loaded.txt` of the PMMA-ring-glued-on-Pz27-disk system. It also calls the function `UEIS_fit_function.m`, which computes and minimizes the cost function $\mathcal{C}$ defined in Eq. (9) in the main paper, and which calls `Holland_check_elastic_iso.m` and `Holland_check_pzt_infmm.m` to check if $\text{Im}(-\boldsymbol{C})$ and $\boldsymbol{K}$ are positive definite. The main script requires the following user-input parameters: initial values and bounds for the polymer ring, the Pz27 parameters p_i^{pz27}, the glue-layer parameters p_i^{glue}, and the dimensions of the disk, the ring, and the glue layer.

Regarding the UEIS fitting, the path in parameter space during the fitting procedure of the complex-valued elastic moduli of PMMA is illustrated in Fig. S4. The path consists of (1) the initial values, (2) the results from the coarse fit using `patternsearch`, and (3) the final set of fitted PMMA parameters using `fminsearchbnd`, as illustrated in the flowchart of Fig. 3 in the main paper. The initial values are indicated by a single circle with a dot in the center, whereas the final fitted parameters are represented by a colored, star-shaped marker.

TABLE S1. List of the files provided in the Supplemental Material for redoing the UEIS fitting of the elastic moduli C_{11} and C_{44} of PMMA and for plotting $Z_{\text{exp}}(f)$ and $Z_{\text{sim}}(f)$ described in Section S3, as well as the animated gif files of the laser-Doppler vibrometer measurements presented in Section S6.

File name	File contents
`UEIS_polymer_script.m`	UEIS MATLAB script
`UEIS_polymer_comsol_model.mph`	UEIS COMSOL script
`UEIS_fit_function.m`	Support MATLAB script
`Holland_check_elastic_iso.m`	Support MATLAB script
`Holland_check_pzt_infmm.m`	Support MATLAB script
`experiment_unloaded.txt`	Data for $Z_{\text{exp}}(f)$, Fig. 4
`simulated_fit_unloaded.txt`	Data for $Z_{\text{sim}}(f)$, Fig. 4
`experiment_loaded.txt`	Data for $Z_{\text{exp}}(f)$, Fig. 5
`simulated_fit_loaded.txt`	Data for $Z_{\text{sim}}(f)$, Fig. 5
`Animation_Fig_S7.gif`	Animation of Fig. S7
`Animation_Fig_S8a.gif`	Animation of Fig. S8(a)
`Animation_Fig_S8b.gif`	Animation of Fig. S8(b)
`Animation_Fig_S8c.gif`	Animation of Fig. S8(c)
`Animation_Fig_S8d.gif`	Animation of Fig. S8(d)

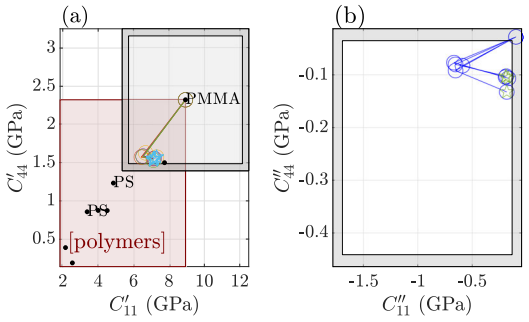

FIG. S4. The path in parameter space during the fitting procedure of the complex-valued elastic moduli $C_{11} = C'_{11} + \text{i}C''_{11}$ and $C_{44} = C'_{44} + \text{i}C''_{44}$, for four different Pz27-PMMA systems. (a) The path for the real parts C'_{44} and C'_{11}. The light-red shaded region indicates typical polymer values [2], PMMA and polystyrene (PS) are annotated. (b) The path of the imaginary parts C''_{44} and C''_{11}. The gray frame indicates the region in parameter space, where the fitting procedure will expand the upper and lower bounds used in the last step.

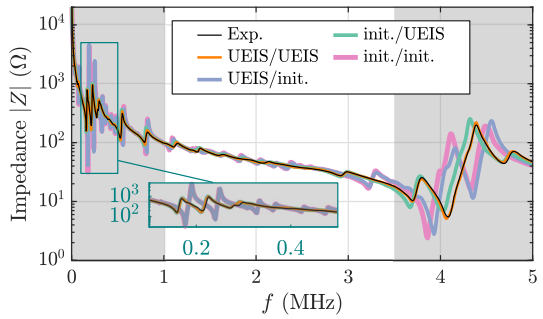

FIG. S5. The measured (Exp) and four simulated electrical impedance spectra $|Z(f)|$ for a PMMA-1.4-25 ring glued onto a Pz27-0.5-10 transducer disk. The four simulations labeled '(Pz27 parameters)/(PMMA parameters)' uses either the initial or the UEIS values as parameter values, for the Pz27 and the PMMA, respectively.

S4. SIMULATED ELECTRICAL IMPEDANCE FOR DIFFERENT MATERIAL PARAMETERS

In Fig. S5 is shown a comparison between a measured impedance spectrum and four simulated electrical impedance spectra using the four cases of material parameters obtained by combining either the initial values (init) or the final UEIS values (UEIS) of the Pz27 transducer disk with either the initial values (init) or the final UEIS values (UEIS) of the PMMA ring. Referring to Pz27 first and PMMA second, the four simulated spectra are labeled 'UEIS/UEIS', 'init/UEIS', 'UEIS/init', and 'init/init'. Clearly, 'UEIS/UEIS' fits the experimental curve best, and 'init/UEIS' comes close. Thus the final PMMA values are not so sensitive to the Pz27 values.

S5. VALIDATION DATA BY ULTRASOUND-TROUGH-TRANSMISSION

An ultrasonic-through-transmission (UTT) technique was used to validate the material parameters determined by the UEIS method. The UTT data is presented in Fig. S6, showing the temperature dependency of the longitudinal and transverse speed of sound (c_{lo} and c_{tr}) and the attenuation coefficients (α_{lo} and α_{tr}) for PMMA. The material parameters were measured at regular time intervals while the water cooled down from 31 ℃ to 23 ℃. Linear regression (LR) was performed based on the measured data points and a 1σ prediction interval (PI) as well as $\pm 1\sigma$ error bars were calculated based on the sum-of-square difference between regression line fit and the measured data points. The final UTT values of the elastic moduli C_{11} and C_{44} of PMMA are obtained by inserting the obtained UTT values for c_{lo}, c_{tr}, α_{lo}, and α_{tr} into expression (14), and they are listed in Table VI.

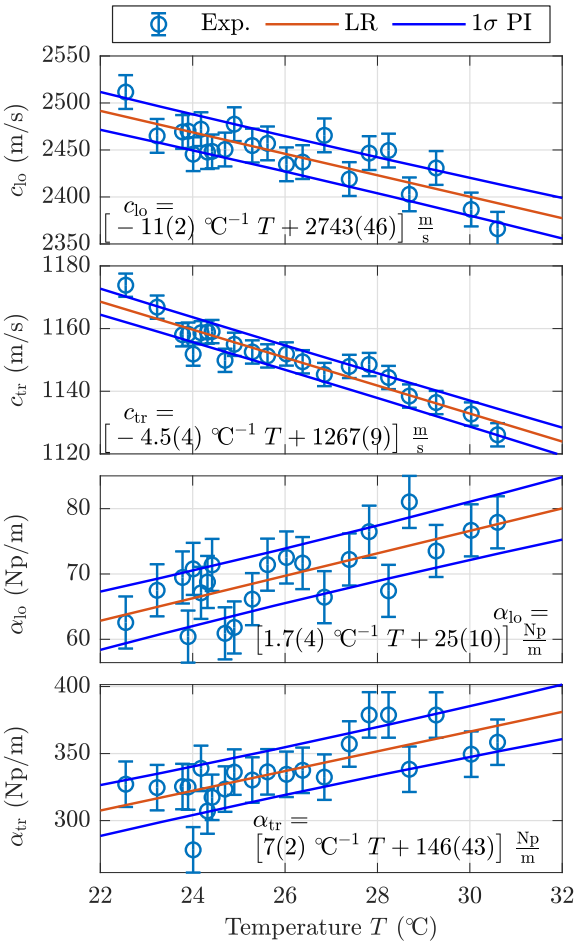

FIG. S6. Validation data obtained for a PMMA slab in water cooling steadily from 31 ℃ to 23 ℃ over a period of 6 hours using UTT measurements with a pulse of center frequency $f_c = 1.90$ MHz and width $\Delta f \approx 1$ MHz. The longitudinal and transverse sound speed (c_{lo} and c_{tr}) and the attenuation coefficients (α_{lo} and α_{tr}) of the PMMA are plotted versus temperature T. Linear regression (LR) and 1σ-prediction intervals (PI) are represented by red and blue lines, respectively. Error bars indicate the $\pm 1\sigma$ uncertainty based on the sum-of-square differences between measured data and the LR.

S6. VALIDATION DATA BY LASER-DOPPLER VIBROMETRY

Using a single-point laser-Doppler vibrometer system VibroFlex Connect (Polytec, Waldbronn, Germany), the normal displacement u_z was measured on the top-surface of an unloaded Pz27 transducer disk or of a PMMA ring glued to a Pz27 disk held in the point-contact sample holder shown in Fig. 2 of the main paper and brought into a resonance mode by applying a peak-to-peak voltage of $V_{\mathrm{pp}} = 2$ V. The PMMA surface was sputtered with a thin gold layer (approximately 14 nm thick) to increase the signal strength of the reflected signal.

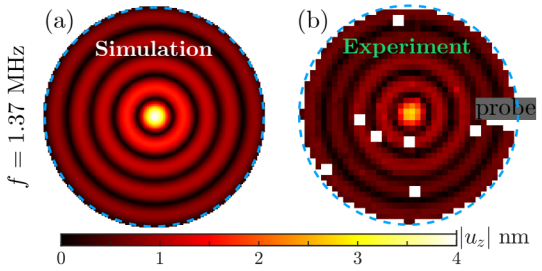

FIG. S7. (a) Simulated and (b) measured normal displacement amplitude $|u_z|$ of an unloaded Pz27-0.5-10 transducer disk (blue dashed line) driven by a 2-V peak-to-peak AC voltage at the resonance frequency $f_{\text{res}} = 1.37$ MHz.

TABLE S2. Details of the vibrometer measurements including resonance frequency f_{res}, stepping size, and data acquisition time t_{acq} for each measured resonance mode.

System	Pz27	Pz27+PMMA	Pz27+PMMA
f_{res} (MHz)	0.058	0.164	1.370
x-y step size (mm)	1	0.5	0.25
t_{acq} (min)	23	81	110

The vibrometer measurements were limited by the stepping-motor range (x from 0 to 100 mm and y from 0 to 12 mm). The step-size and the data acquisition time can be found in Table S2 for each experiment. Note that there are no free parameters in the simulation, since the geometry, the material parameters, and the amplitude and frequency of the excitation voltage are all known.

Figs. S7 and S8, and the corresponding animations of the time-dependent displacement field listed in Table S1, show a comparison between the measured and the no-free-parameter-simulated normal displacement amplitude at the selected resonances. The good qualitative and quantitative agreement in the three cases Figs. S7, S8(b), and S8(d) provide an experimental validation of the UEIS method supplementing the UTT validation. Note in Fig. S8 the improved agreement between simulation and experiment, when the actual off-center position $\Delta = 0.4$ mm of the Pz27 disk relative to the PMMA ring is taken into account in the simulation.

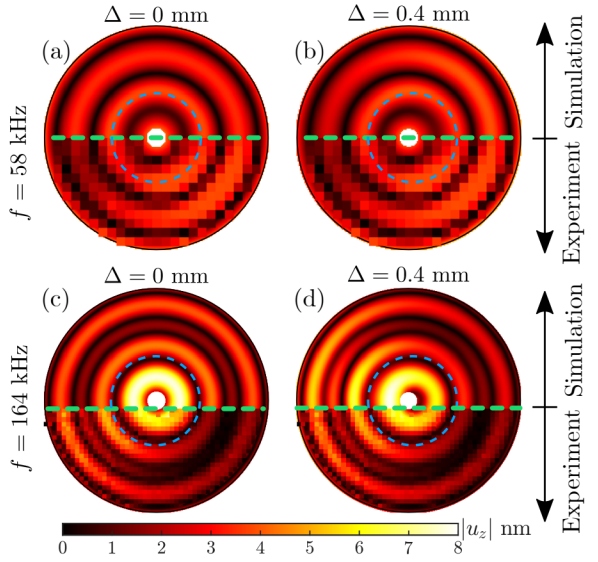

FIG. S8. Simulated and measured normal displacement amplitude $|u_z|$ of a PMMA-1.4-25 ring glued to a Pz27-0.5-10 disk (blue dashed line) driven by a 2-V peak-to-peak AC voltage at the two resonance frequencies $f_{\text{res}} = 58$ and 164 kHz, respectively. The Pz27 disk was measured to be off-centered relative to the PMMA ring by $\Delta = 0.4$ mm. In each panel, the simulation (smooth) is above the green dashed line and the experiment (pixelated) is below. (a) $f_{\text{res}} = 58$ kHz and an axisymmetric simulation with $\Delta = 0$ mm. (b) as (a) but $\Delta = 0.4$ mm in a nonsymmetric simulation. (c) $f_{\text{res}} = 164$ kHz and an axisymmetric simulation with $\Delta = 0$ mm. (d) as (c) but $\Delta = 0.4$ mm in a nonsymmetric simulation.

REFERENCES

[1] N. Pérez, M. A. B. Andrade, F. Buiochi, and J. C. Adamowski, Identification of elastic, dielectric, and piezoelectric constants in piezoceramic disks, IEEE Trans. Ultrason. Ferroelec. Freq. Contr. **57**, 2772 (2010).

[2] W. D. Callister Jr, *Materials Science and Engineering: An Introduction*, seventh ed. (John Wiley & Sons, York, PA, 2007) p. 975.

Chapter 7

Constant-power versus constant-voltage excitation

7.1 Motivation

The development of BAW devices, to a large extent, focuses on the device geometry, the coupling layer, and the choice of the piezoelectric transducer. One aspect that perhaps is given less attention is the electrical domain and the method of electrical excitation. Only a few references explore the impact of the electrical system components, such as amplifier and wiring, on the performance of the acoustofluidic device, and such analysis is more commonly done for SAW devices [110–112]. However, techniques such as electrical impedance matching show how the electrical components can impact and improve the system performance [113, 114]. Therefore, when studying acoustofluidic systems, it can be beneficial to extend the analysis beyond the device itself and consider the acoustofluidic platform as a whole.

Especially when comparing the experimental and numerical results of an acoustofluidic device, it is crucial that the numerical simulation is set up to match the experimental conditions as closely as possible. A critical aspect of numerical simulations is the voltage amplitude φ_0, which is used in the simulation model to excite the piezoelectric transducer. Typically, the voltage amplitude applied to the transducer is assumed to be constant across the different frequencies in our numerical model. Firstly, this assumption is not always valid if the actuation voltage is not directly monitored at the transducer. Secondly, the electrical excitation method of keeping the voltage amplitude constant across frequencies might not be the ideal technique to find the optimal actuation frequency for an acoustofluidic device. In this chapter, we will explore the impact of three different electrical excitation methods in a frequency sweep on the average particle velocity observed in a microfluidic channel.

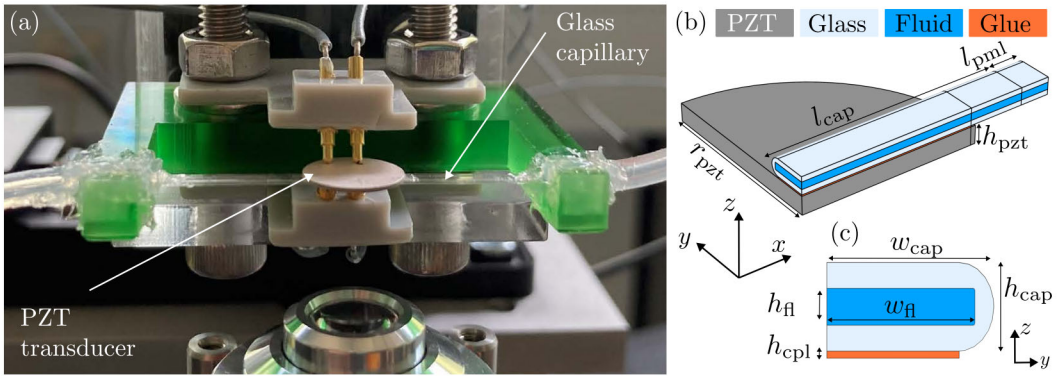

Figure 7.1: (a) Overview of the experimental setup, consisting of a piezoelectric transducer glued to a glass-capillary tube. The voltage signal at the transducer electrodes is applied to and monitored by a four-wire sensing configuration using four spring-loaded pins. (b) Numerical simulations are performed on a quarter of the actual geometry using symmetry arguments. The modeled domains include the piezoelectric transducer (PZT, gray), the glass-capillary tube (light blue), the fluid inside the microchannel (dark blue), and a thin glue layer (orange). (c) A cross-section in the yz-plane visualizes the thin glue layer. The figure has been adapted from [3].

7.2 Summary of the results from Paper III

7.2.1 Overview of the device

In order to study the impact of various electrical excitation methods on the acoustophoretic performance, the experimental setup is based on a glass-capillary tube, which is glued to a disk-shaped piezoelectric transducer. This setup allows us to carry out robust and repeatable measurements. The device and measurement setup, which have been used in this study, are shown in Fig. 7.1(a). A close match to the numerically-modeled system is ensured by using spring-loaded pins for the electrical contact with the transducer. Furthermore, the UEIS method has been employed to characterize the material properties of the piezoelectric transducer. Silicone glue at the interface between the capillary tube and sample holder minimizes any mechanical clamping of the transducer. Simultaneously, the glue mimics the perfectly-matched layer used at both ends of the capillary tube in the numerical simulation. Four spring-loaded pins, two on both sides of the piezoelectric transducer, allow to perform four-wire sensing of the voltage amplitude used for driving the system: Two pins are used to apply the driving signal. The other two pins are required to measure the voltage amplitude over a high-ohmic resistance to minimize the flow of a parasitic electrical current.

Our numerical model consists of a quarter of the actual geometry, shown in Fig. 7.1(b). Symmetry arguments in the x-z-plane at $y = 0$ and in the y-z-plane at $x = 0$ are used to reduce the computational requirements of the simulation. Fig. 7.1(c) shows a cross-section of the modeled geometry, highlighting the thin glue layer used in the simulation.

The dimensions used in the numerical model match the measured dimensions, except for the length of the capillary and the length of the PML layer. Here the PML layer ensures perfect absorption of all outgoing waves, similar to the silicone glue used in the experiment, and helps reduce the computational demands of the model.

7.2.2 Overview of different excitation methods

When driving a piezoelectric transducer in experiments using bulk-acoustic transducers, the voltage amplitude or the electrical power is typically kept at a constant level. However, care needs to be taken where the voltage or power dissipation is kept constant in the system. One common approach is keeping the voltage amplitude constant at the signal generator before the amplification stage. Two alternative approaches are to keep the voltage amplitude directly at the piezoelectric transducer or the power dissipation in the transducer constant over the frequency range. Those approaches, however, require additional measurement probes and a control circuit to keep the values stable. In our work, we consider the following three cases:

(Case 1) Constant voltage amplitude at the signal generator, $\varphi_{\text{gen}} = 1$ V.

(Case 2) Constant voltage amplitude at the transducer, $\varphi_{\text{pzt}} = 0.5$ V.

(Case 3) Constant power dissipation in the transducer, $P_{\text{pzt}} = 50$ mW.

The voltage amplitudes φ_{gen}, φ_{amp}, and φ_{pzt} are measured at different points in the electrical circuit, as shown in Fig. 7.2. The values for φ_{pzt} and P_{pzt} are chosen because, for both cases, nearly the same power dissipation is measured at the resonance frequency of the transducer. In all cases, the gain of the power amplifier is set to 3.

Case 1 might be the most common approach to driving a piezoelectric transducer, as it does not require any voltage or current probes to monitor the amplifier output. However, the results of this excitation method depend strongly on the amplifier's properties, the

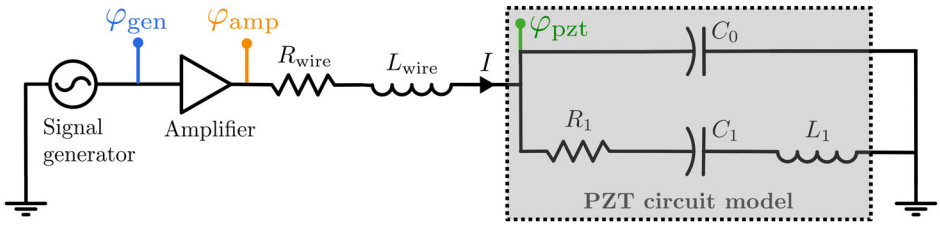

Figure 7.2: Schematic overview, adapted from [3], showing the electrical circuit, consisting of a signal generator, power amplifier, parasitic wire resistance R_{wire} and inductance L_{wire}. The PZT transducer is modeled as an equivalent circuit with the components C_0, R_1, C_1, and L_1. In our experiments the voltage amplitudes φ_{gen}, φ_{amp}, and φ_{pzt} are monitored at the respective locations of the circuit.

wiring between the amplifier and transducer, and the impedance spectrum of the transducer itself. Due to the capacitive behavior and low impedance at resonance, piezoelectric transducers may require high electrical currents, especially in the high-frequency range. Therefore, ensuring a constant gain over a wide frequency range can be challenging, depending on the performance characteristics of the amplifier. A further challenge lies in the resonant circuit formed by the inductance and capacitance of the amplifier, wire, and transducer. Ideally, those parasitic parameters are estimated prior to the acoustophoresis experiment to ensure ideal driving characteristics. A four-wire sensing approach might be crucial to measure the actuation amplitude directly at the transducer to ensure precise control over the voltage amplitude or power dissipation in the transducer. This precise voltage control is especially relevant when parasitic resistance and inductance of the wire connecting the amplifier and transducer cannot be neglected. Therefore the voltage φ_{amp}, measured at the amplifier output, can differ from the transducer voltage φ_{pzt}.

In our experimental setup, we utilized a four-wire sensing approach and implemented a feedback loop that ensures either constant voltage (Case 2) or constant power dissipation in the transducer (Case 3). The results are compared with Case 1, which is not requiring any voltage feedback. In our setup, the power dissipation is calculated based on the transducer's previously measured impedance spectrum and the recorded voltage amplitude. The use of an additional current probe would be ideal, but it could not be used due to the limitations of the experimental setup.

7.2.3 Resulting spectrum of the acoustophoretic particle speed

In our work, we compare the magnitude of the average particle velocity inside the microchannel for the three different electrical excitation cases. The experimentally-observed particle speed v_{exp} is analyzed for the frequency range from 3.3 to 4.3 MHz. The nominal transducer resonance is located close to 4 MHz. Based on a one-dimensional hard-wall estimate, we would expect a vertical standing half-wave at around $f^{(0,1)} = \frac{c_0}{2h_{\mathrm{ch}}} \approx 3.75$ MHz and a horizontal resonance with ten half-waves in the width of the channel at around $f^{(10,0)} = \frac{5c_0}{w_{\mathrm{ch}}} \approx 3.64$ MHz. Our numerical and experimental findings show that those simple estimates are not very accurate, even for a glass-based system. The dimensions and material properties of the transducer, coupling layer, and chip must be considered.

In Fig. 7.3(a), the experimental results for the acoustophoretic particle speed v_{exp} at the three different excitation methods are shown. In contrast, Fig. 7.3(b) visualizes the power dissipation P_{pzt} in the transducer in the three cases. The results can be summarized as follows: Case 1, with constant φ_{gen}, depends on the parasitic properties of the amplifier, the wire, and the transducer itself. Case 2, where φ_{pzt} is constant, leads to the strongest response at the intrinsic resonance of the transducer, $f_{\mathrm{exp}}^{(0,1)\varphi} = 3.98$ MHz, where the impedance is minimal. Case 3 of constant dissipation P_{pzt} is ideal, as it yields the most power-efficient actuation frequency, $f_{\mathrm{exp}}^{(0,1)\mathrm{P}} = 4.03$ MHz, and reveals further interesting features, such as the transverse resonance at $f_{\mathrm{exp}}^{(10,0)P} = 3.51$ MHz.

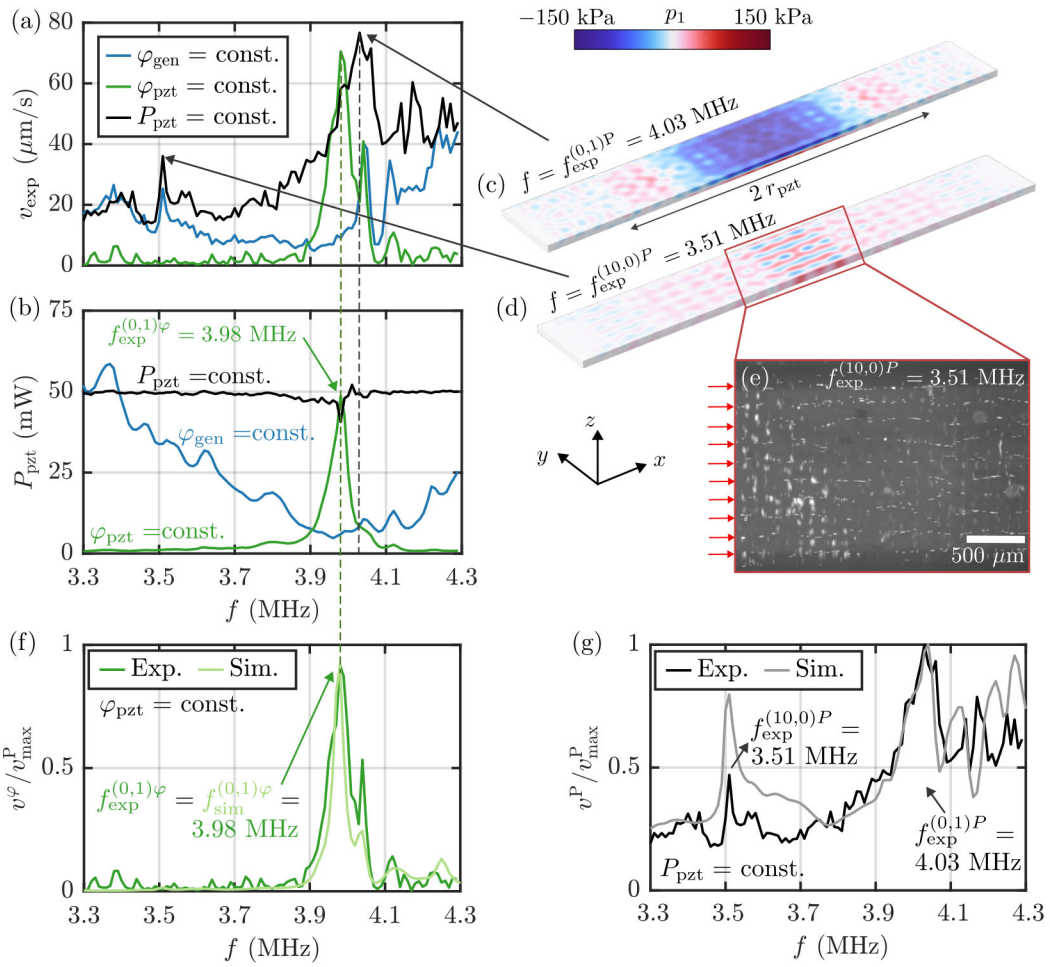

Figure 7.3: (a) The measured average acoustophoretic particle velocity magnitude v_{exp} versus frequency f from 3.3 to 4.3 MHz for the three different cases of constant $\varphi_{\text{gen}} = 1$ V (blue), constant $\varphi_{\text{pzt}} = 0.5$ V (green), and constant power dissipation $P_{\text{pzt}} = 50$ mW (black) is shown. (b) Power dissipation in the piezoelectric transducer for the three different cases. (c,d) Simulated field of the pressure p_1 inside the microfluidic channel at $f = f_{\text{exp}}^{(0,1)\text{P}} = 4.03$ MHz, and $f = f_{\text{exp}}^{(10,0)\text{P}} = 3.51$ MHz respectively. The pressure amplitude ranges from −150 kPa (blue) to 150 kPa (red). (e) Micrograph of the microfluidic channel at $f_{\text{exp}}^{(10,0)\text{P}} = 3.51$ MHz, revealing 10 nodal lines, highlighted by red arrows. (f) Comparison of the experimentally and numerically obtained normalized particle speed $v^{\varphi}/v_{\text{max}}^{\text{P}}$ at constant voltage φ_{pzt} versus frequency. Here the maximum of the particle speed $v_{\text{exp}}^{\text{P}}$ from the constant-power case has been used for normalization. (g) The same as (f), but for the case of constant power dissipation P_{pzt}. The figure has been adapted from [3].

Fig. 7.3(c,d) show the numerically obtained pressure fields in the microchannel for the vertical and the transverse mode. A micrograph of the transverse resonance $f_{\mathrm{exp}}^{(10,0)P} = 3.51$ MHz is shown in Fig. 7.3(e), revealing the ten nodal lines of the five standing waves along the width of the channel. The numerically simulated fields show an excellent agreement with the experimentally observed particle focusing. The use of the UEIS method for determining the material properties of the piezoelectric transducer and the precise monitoring of the voltage amplitudes enabled a very accurate numerical description of the system, as seen in Fig. 7.3(f,g), where a close match between the simulated and the measured spectrum of the particle speed is found.

If we compare the observed resonance frequency of those two modes with analytical 1D estimates, we find that the experimentally- and numerically-obtained frequency of the vertical $\lambda/2$-mode deviates by almost 8% from the analytical 1D estimate. On the other hand, the mode found at $f_{\mathrm{exp}}^{(10,0)P}$ deviates by less than 4% from the estimated value. Deviations for the vertical mode may be partially explained due to the dependency on parameters of all four layers along the z-axis, consisting of the transducer, glue, chip, and fluid channel. The transverse mode, conversely, is mainly governed by the chip and channel width and their respective properties. Nevertheless, the differences between the simplified 1D estimate compared to the closely-matching resonance frequencies found in the experiment and simulation emphasize the need for numerical simulations to perform reliable system behavior predictions.

7.3 Implications for polymer-based acoustofluidic devices

Microfluidic chips made from polymers have much larger acoustic attenuation than their corresponding glass-based counterparts. With quality factors in the order of $Q = \frac{|C'_{ij}|}{|C''_{ij}|} \approx$ 10–100, the damping in polymers is up to two orders of magnitude higher than for glass- or silicon-based devices. While the lower quality factor in polymer systems leads to broader resonance peaks, it also requires higher voltage amplitudes or higher input powers to reveal these peaks in a frequency sweep when studying acoustophoresis experimentally. Suppose the polymer chip's resonance does not closely match the resonance frequency of the transducer. In that case, polymer resonances resulting in good acoustic focusing may be missed in a frequency sweep using constant-voltage excitation. Constant-power excitation, on the other hand, will ensure that also whole-system-resonances are spotted, which are located further away from the transducer resonance.

7.4 Concluding remarks

Special care must be taken in choosing the electrical excitation method for acoustofluidic experiments. Monitoring the voltage amplitude and the power directly at the transducer can help control the system behavior and compare performance across frequencies and devices. In addition, ensuring constant-power excitation can be beneficial to reveal device resonances located further away from the transducer's resonance frequency. Relying on

constant-voltage frequency sweeps, on the contrary, can lead to misleading results regarding the ideal resonance frequency because this method does not always yield the most power-efficient frequency, as shown in Fig. 7.3.

When performing numerical simulations of different acoustophoresis systems, it is crucial to ensure that the voltage amplitude used in the model matches the experimental protocol closely. Furthermore, it can be beneficial to utilize constant-power excitation in numerical simulations, particularly when performing device optimization. This type of excitation enables a better comparison between the performance of different geometries and helps find the system with the strongest acoustophoretic response for a given input power.

For polymer-based devices that rely on whole-system resonances and the underlying eigenmodes of the polymer chip, it might not always be possible to precisely match the resonant mode of the chip to the resonance frequency of the piezoelectric transducer. Suppose frequency sweeps with a constant voltage at the transducer are performed. In that case, suitable whole-system resonances might be overlooked, as the electrical power dissipation and the related displacement amplitude of the transducer is too small to result in high acoustic energy densities in the microchannel. Constant-power excitation could therefore prove helpful, especially when studying polymer-based devices.

7.5 Paper III: Micromachines 13, 1886 1-16 (2022)

Constant-Power versus Constant-Voltage Actuation in Frequency Sweeps for Acoustofluidic Applications

DOI: 10.3390/mi13111886

Authors: F. Lickert, H. Bruus, and M. Rossi.
Journal: Micromachines **13**, 1886 1-16(2022)

micromachines

MDPI

Article

Constant-Power versus Constant-Voltage Actuation in Frequency Sweeps for Acoustofluidic Applications

Fabian Lickert *, Henrik Bruus * and Massimiliano Rossi *

Department of Physics, Technical University of Denmark, DTU Physics Building 309, DK-2800 Kongens Lyngby, Denmark

* Correspondence: fabianl@dtu.dk (F.L.); bruus@fysik.dtu.dk (H.B.); rossi@fysik.dtu.dk (M.R.)

Abstract: Supplying a piezoelectric transducer with constant voltage or constant power during a frequency sweep can lead to different results in the determination of the acoustofluidic resonance frequencies, which are observed when studying the acoustophoretic displacements and velocities of particles suspended in a liquid-filled microchannel. In this work, three cases are considered: (1) Constant input voltage into the power amplifier, (2) constant voltage across the piezoelectric transducer, and (3) constant average power dissipation in the transducer. For each case, the measured and the simulated responses are compared, and good agreement is obtained. It is shown that Case 1, the simplest and most frequently used approach, is largely affected by the impedance of the used amplifier and wiring, so it is therefore not suitable for a reproducible characterization of the intrinsic properties of the acoustofluidic device. Case 2 strongly favors resonances at frequencies yielding the lowest impedance of the piezoelectric transducer, so small details in the acoustic response at frequencies far from the transducer resonance can easily be missed. Case 3 provides the most reliable approach, revealing both the resonant frequency, where the power-efficiency is the highest, as well as other secondary resonances across the spectrum.

Keywords: acoustofluidics; microparticle acoustophoresis; general defocusing particle tracking; particle-velocity spectroscopy

Citation: Lickert, F.; Bruus, H.; Rossi, M. Constant-Power versus Constant-Voltage Actuation in Frequency Sweeps for Acoustofluidic Applications. *Micromachines* **2022**, *13*, 1886. https://doi.org/10.3390/mi13111886

Academic Editor: David J. Collins

Received: 4 October 2022
Accepted: 27 October 2022
Published: 1 November 2022

1. Introduction

In many experimental acoustofluidic platforms, the device is actuated by an attached piezoelectric transducer, driven by a sine-wave generator through a power amplifier. To describe the performance of the acoustofluidic actuation, the operating conditions are typically expressed in terms of the voltage amplitude or the electric power dissipation together with quantities such as the acoustic energy density, the acoustic focusing time, or achievable flow rates [1–3]. Often, it is however left unclear under which conditions and at which point in the electric circuit, the relevant quantities such as voltage amplitude or power dissipation have been measured. Recent studies compare device performance at constant average power for different placements of the transducer [4,5]. Dubay et al. [6] performed thorough power and voltage measurements for the evaluation of their acoustofluidic device, however, they noted that the actual power delivered to the transducer might reduce to only a fraction (as low as 10%) of the reported value. The likely cause of this reduction is that the transducer is acting as a large capacitive load, where electrical impedance matching between source and load impedance is difficult to accomplish [6,7].

Whereas optimization of the driving circuit is customary in other fields, such as ultrasonic transducers for cellular applications [8], non-destructive testing [9], and pulse-echo systems [10], this has not been given much consideration in the field of acoustofluidics, where the focus often lies on optimizing the acoustic impedance matching [11,12], while neglecting the impact of the driving circuit. A recent work, though, considers topics such as electrical impedance matching in the context of developing low-cost and possibly hand-held driving circuits for acoustofluidics [13]. To our knowledge, studies have not yet been

performed, in which the impact of different electrical excitation methods on a transducer in a given acoustofluidic device is compared with respect to the resulting acoustophoretic particle focusing.

In the case of bulk piezoelectric transducers, where the electrical impedance ranges over several orders of magnitude as a function of frequency, the voltage amplitude across the transducer can differ severely from the amplitude expected by simply considering the voltage input at the amplifier. Suitable voltage compensation circuits or voltage correction methods should be used to achieve the desired voltage amplitude directly at the transducer. Furthermore, a standard has not yet been established whether it is more beneficial to run frequency sweeps at a constant voltage or at a constant power. We therefore in this work investigate the impact of three different actuation approaches during a frequency sweep: (1) Constant input voltage into the amplifier, (2) constant voltage at the transducer, and (3) constant power dissipation in the transducer. We compare experimental findings with our numerical model. The aim of this paper is to establish guidelines on which actuation approach is preferable for acoustofluidic applications using bulk piezoelectric transducers to generate acoustophoresis in bulk acoustic waves.

The paper is structured in the following way: In Section 2 a brief summary is given of the governing equations for the pressure field, the displacement field, and the electric potential in our acoustofluidic device. Section 3 gives an overview of our experimental setup, and the procedure used for the measurement of the particle velocities is described step by step. In Section 4 we describe the numerical approach used in our study, and in Section 5 we compare several aspects of the obtained results for the device under study: a comparison between the electrical characteristics of the device, as well as the numerically and experimentally observed acoustophoretic particle velocities are given. Furthermore, some details of the simulated fields are shown. Finally, the paper concludes in Section 6 with a short summary and some guidelines on the actuation of piezoelectric transducers for acoustofluidic applications.

2. Theory

The theoretical approach follows our previous work [3,14–16], in which the computational effort in the simulations is reduced by employing the effective-boundary-layer theory derived by Bach and Bruus [17]. We assume time-harmonic first-order fields with angular frequency $\omega = 2\pi f$ for the acoustic pressure $\tilde{p}_1(\boldsymbol{r},t) = p_1(\boldsymbol{r})\,\mathrm{e}^{-\mathrm{i}\omega t}$, the electric potential $\tilde{\varphi}(\boldsymbol{r},t) = \varphi(\boldsymbol{r})\,\mathrm{e}^{-\mathrm{i}\omega t}$, and the displacement field $\tilde{\boldsymbol{u}}(\boldsymbol{r},t) = \boldsymbol{u}(\boldsymbol{r})\,\mathrm{e}^{-\mathrm{i}\omega t}$. Derived through a perturbation approach, these fields represent tiny perturbations of the unperturbed zero-order fields.

2.1. Governing Equations

For a fluid with speed of sound c_0, density ρ_0, dynamic and bulk viscosity of the fluid η_0 and η_0^{b}, damping coefficient Γ_0, and the isentropic compressibility $\kappa_0 = (\rho_0 c_0^2)^{-1}$, the acoustic pressure p_1 is governed by the Helmholtz equation, and the acoustic velocity $\boldsymbol{v}_1$ is a gradient field,

$$\nabla^2 p_1 = -\frac{\omega^2}{c_0^2}\left(1+\mathrm{i}\Gamma_0\right) p_1, \text{ with } \Gamma_0 = \left(\frac{4}{3}\eta_0 + \eta_0^{\mathrm{b}}\right)\omega\kappa_0, \tag{1a}$$

$$\boldsymbol{v}_1 = -\mathrm{i}\,\frac{1-\mathrm{i}\Gamma_0}{\omega\rho_0}\,\boldsymbol{\nabla} p_1. \tag{1b}$$

For an elastic solid with density ρ_{sl}, the displacement field $\boldsymbol{u}$ is governed by the Cauchy equation

$$-\omega^2\rho_{\mathrm{sl}}\,\boldsymbol{u} = \boldsymbol{\nabla}\cdot\boldsymbol{\sigma}, \tag{2}$$

where $\boldsymbol{\sigma}$ is the stress tensor. In the Voigt notation, the 1×6 stress $\boldsymbol{\sigma}$ and strain $\boldsymbol{s}$ column vectors are given by the 6×1 transposed row vectors $\boldsymbol{\sigma}^{\mathsf{T}} = (\sigma_{xx},\sigma_{yy},\sigma_{zz},\sigma_{yz},\sigma_{xz},\sigma_{xy})$ and

$\boldsymbol{s}^{\mathsf{T}} = (\partial_x u_x, \partial_y u_y, \partial_z u_z, \partial_y u_z + \partial_z u_y, \partial_x u_z + \partial_z u_x, \partial_x u_y + \partial_y u_x)$, respectively, and $\boldsymbol{\sigma}$ is related to $\boldsymbol{s}$ by the 6×6 stiffness tensor $\boldsymbol{C}$ having the elastic moduli C_{ik} as components. For a linear, isotropic, elastic solid of the ∞mm-symmetry class the relation is,

$$\boldsymbol{\sigma} = \boldsymbol{C} \cdot \boldsymbol{s}, \qquad \boldsymbol{C} = \begin{pmatrix} C_{11} & C_{12} & C_{13} & 0 & 0 & 0 \\ C_{12} & C_{11} & C_{13} & 0 & 0 & 0 \\ C_{13} & C_{13} & C_{33} & 0 & 0 & 0 \\ 0 & 0 & 0 & C_{44} & 0 & 0 \\ 0 & 0 & 0 & 0 & C_{44} & 0 \\ 0 & 0 & 0 & 0 & 0 & C_{66} \end{pmatrix}. \tag{3}$$

Here, the components $C_{ik} = C'_{ik} + \mathrm{i}C''_{ik}$ are complex-valued with real and imaginary parts relating to the speed and the attenuation of sound waves in the solid, respectively. In this work, we assume the glass and the glue layer to be isotropic, yielding the following relations $C_{33} = C_{11}$, $C_{66} = C_{44}$ and $C_{13} = C_{12} = C_{11} - 2C_{44}$. This leaves the two independent complex-valued parameters C_{11} and C_{44}, relating to the longitudinal and transverse speed of sound and attenuation in the glass and glue layer. For a lead zirconate titanate (PZT) transducer, $C_{66} = \frac{1}{2}(C_{11} - C_{12})$, which leaves five independent complex-valued elastic moduli, C_{11}, C_{12}, C_{13}, C_{33}, and C_{44}.

The electrical potential φ inside the PZT transducer is governed by Gauss's law for a linear, homogeneous dielectric with a zero density of free charges,

$$\boldsymbol{\nabla} \cdot \boldsymbol{D} = \boldsymbol{\nabla} \cdot (-\boldsymbol{\varepsilon} \cdot \boldsymbol{\nabla} \varphi) = 0, \tag{4}$$

where $\boldsymbol{D}$ is the electric displacement field and $\boldsymbol{\varepsilon}$ the dielectric tensor. Furthermore in PZT, the complete linear electromechanical coupling relating the stress and the electric displacement to the strain and the electric field is given as,

$$\begin{pmatrix} \boldsymbol{\sigma} \\ \boldsymbol{D} \end{pmatrix} = \begin{pmatrix} \boldsymbol{C} & -\boldsymbol{e}^{\mathsf{T}} \\ \boldsymbol{e} & \boldsymbol{\varepsilon} \end{pmatrix} \begin{pmatrix} \boldsymbol{s} \\ \boldsymbol{E} \end{pmatrix}, \tag{5a}$$

$$\text{with } \boldsymbol{e} = \begin{pmatrix} 0 & 0 & 0 & 0 & e_{15} & 0 \\ 0 & 0 & 0 & e_{15} & 0 & 0 \\ e_{31} & e_{31} & e_{33} & 0 & 0 & 0 \end{pmatrix} \text{ and } \boldsymbol{\varepsilon} = \begin{pmatrix} \varepsilon_{11} & 0 & 0 \\ 0 & \varepsilon_{11} & 0 \\ 0 & 0 & \varepsilon_{33} \end{pmatrix}. \tag{5b}$$

2.2. The Acoustic Radiation Force and the Acoustophoretic Particle Velocity

We consider polystyrene particles with density ρ_{ps}, compressibility κ_{ps}, and a radius a, which is much larger than the viscous boundary layer and much smaller than the acoustic wavelength. In this case, the acoustic radiation force $\boldsymbol{F}^{\mathrm{rad}}$ on the particles placed in water is given by the negative gradient of the Gorkov potential U^{rad}, [18]

$$\boldsymbol{F}^{\mathrm{rad}} = -\boldsymbol{\nabla} U^{\mathrm{rad}}, \text{ with} \tag{6a}$$

$$U^{\mathrm{rad}} = \pi a^3 \Big(\frac{1}{3} f_0 \, \kappa_0 |p_1|^2 - \frac{1}{2} f_1 \, \rho_0 |\boldsymbol{v}_1|^2 \Big), \quad f_0 = 1 - \frac{\kappa_{\mathrm{ps}}}{\kappa_0}, \text{ and } f_1 = \frac{2(\rho_{\mathrm{ps}} - \rho_0)}{2\rho_{\mathrm{ps}} + \rho_0}. \tag{6b}$$

If a (polystyrene) microparticle of radius a is placed in a fluid of viscosity η_0 flowing with the local velocity $\boldsymbol{v}_0$, the presence of $\boldsymbol{F}^{\mathrm{rad}}$ imparts a so-called acoustophoretic velocity $\boldsymbol{v}_{\mathrm{ps}}$ to the particle. As inertia is negligible, $\boldsymbol{v}_{\mathrm{ps}}$ is found from a balance between $\boldsymbol{F}^{\mathrm{rad}}$ and the viscous Stokes drag force $\boldsymbol{F}^{\mathrm{drag}}$, [14]

$$\boldsymbol{v}_{\mathrm{ps}} = \frac{1}{6\pi\eta_0 a} \boldsymbol{F}^{\mathrm{rad}} + \boldsymbol{v}_0. \tag{7}$$

2.3. Electrical Impedance and Power Dissipation

For a PZT transducer with an excited top electrode and a grounded bottom electrode set by the respective potentials $\varphi = \varphi_{\mathrm{pzt}}$ and $\varphi = 0$ V, the electrical impedance Z is given by the ratio of $\varphi_{\mathrm{pzt}} - 0$ V and the surface integral of the polarization current density $\boldsymbol{D} + \epsilon_0 \boldsymbol{\nabla} \varphi$ as [15],

$$Z = \frac{\varphi_{\mathrm{pzt}}}{I}, \quad \text{with} \quad I = -\mathrm{i}\omega \int_{\partial\Omega} \boldsymbol{n} \cdot (\boldsymbol{D} + \epsilon_0 \boldsymbol{\nabla} \varphi) \, \mathrm{d}a. \tag{8}$$

The electrical power dissipation P_{pzt} in the PZT transducer is given by the usual expression

$$P_{\mathrm{pzt}} = \frac{1}{2} \operatorname{Re}\left[(\varphi_{\mathrm{pzt}}) I^{\star}\right] = \frac{1}{2} |\varphi_{\mathrm{pzt}}| \, |I| \cos\theta, \quad \text{with} \quad \theta = \arg(Z). \tag{9}$$

2.4. Butterworth-Van Dyke Circuit Model

To describe the electrical response of the transducer around its thickness resonance frequency, we use a single-frequency Butterworth-Van Dyke (BVD) model. We furthermore include the impact of the wiring and the parasitic effects of the circuit leading to the PZT transducer in our model. An equivalent circuit of our model is shown in Figure 1a. It consists of the parasitic wire resistance R_{wire} and inductance L_{wire} in series with a PZT circuit having the transducer capacitance C_0 in parallel with an transducer LCR-circuit R_1-L_1-C_1. The four parameters R_1, L_1, C_1, and C_0 can be obtained from the PZT admittance spectrum $Y(f) = 1/Z(f)$ at the resonance frequency f_{r} and anti-resonance frequency f_{a} [19,20],

$$C_0 = \frac{\operatorname{Im} Y(f_{\mathrm{r}})}{2\pi f_{\mathrm{r}}}, \quad R_1 = \frac{1}{\operatorname{Im} Y(f_{\mathrm{r}})}, \quad C_1 = C_0 \left[\frac{f_{\mathrm{a}}^2}{f_{\mathrm{r}}^2} - 1\right], \quad L_1 = \frac{1}{(2\pi f_{\mathrm{r}})^2 C_1}. \tag{10}$$

We perform simulations of the BVD-circuit using the SPICE-based circuit simulator software LTspice with parameters for the circuit components obtained via Equation (10) and the measured values of the wire resistance R_{wire} and inductance L_{wire}.

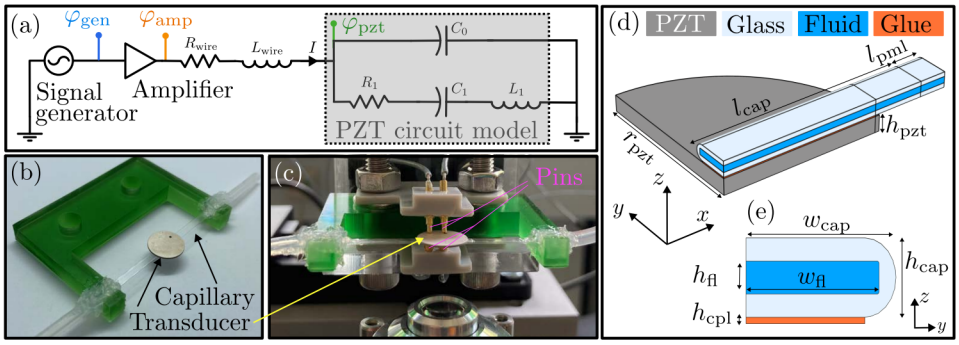

Figure 1. (**a**) A schematic overview of the electrical circuit driving the transducer. The transducer, represented by the BVD-model with a resistor R_1, an inductor L_1, and two capacitors C_0 and C_1, is coupled in series with the parasitic wire resistance and inductance. (**b**) A disk-shaped piezoelectric transducer is glued to a long, straight glass capillary tube. The tube is connected to a 3D-printed sample holder (green), and inlet/outlet tubing is glued to the ends of the tube. (**c**) The acoustofluidic device is mounted above the microscope lens and is electrically connected via two spring-loaded pins on each side of the transducer. (**d**) Using the symmetry planes x-z and y-z, only a quarter of the actual geometry needs to be simulated numerically. The different domains of the model are: PZT (gray), glass (light blue), water (dark-blue), and the thin glue layer (orange). The dimensions are $r_{\mathrm{pzt}} = 5.02$ mm, $h_{\mathrm{pzt}} = 506$ µm, $w_{\mathrm{fl}} = 2060$ µm, $h_{\mathrm{fl}} = 200$ µm, $h_{\mathrm{cpl}} = 39$ µm, $w_{\mathrm{cap}} = 2324$ µm, and $h_{\mathrm{cap}} = 483$ µm. In the simulation the reduced lengths are $l_{\mathrm{cap}} = 6.44$ mm and $l_{\mathrm{pml}} = 839$ µm. (**e**) The cross-section in the y-z-plane is showing the glass tube, the water, and the glue layer.

3. Materials and Methods

3.1. The Experimental Setup

In this work, an acoustofluidic device is used, that consists of a 483-µm-high, 2324-µm-wide, and 50.9-mm-long glass capillary (VitroTubes, VitroCOM, Mountain Lakes, NJ, USA) containing a 200 µm high and 2.06 mm wide microchannel. The device is glued to a cylindrical piezoelectric transducer disk (Pz27, Meggitt A/S, Kvistgaard, Denmark), made from PZT, of thickness 506 µm and diameter 10.045 mm with a nominal resonance frequency at around 4 MHz. The capillary tube is glued to the transducer by a thin (39 µm) layer of UV-curable glue (NOA 86H, Norland Products, Jamesburg, NJ, USA). An overview of the device is shown in Figure 1b. Using silicone glue, the device is mounted on a 3D-printed sample holder, and rubber tubing is glued to the glass capillary tube on both ends. The electrical connection to the piezoelectric transducer is made via four spring-loaded pins, as can be seen in Figure 1c. These pins both minimize the clamping force on the transducer and enable four-probe measurement of the electric voltage across the transducer.

A schematic overview of the electrical circuit, including signal generator and amplifier, is shown in Figure 1a. As signal generator an Analog Discovery 2 (Digilent, Pullman, WA, USA) in connection with the power amplifier TOE 7607 (TOELLNER Electronic Instrumente GmbH, Herdecke, Germany) is used to drive the piezoelectric transducer. The output of the amplifier is connected to the spring-loaded pins via a coaxial cable followed by 30 cm hookup wire. The wire is considered as a short transmission line with negligible capacitance, but with non-negligible parasitic resistance R_{wire} and inductance L_{wire}. In our simplified circuit model, we only consider the thickness resonance at around 4 MHz of the transducer, and model the transducer via the BVD-model of Equation (10).

3.2. Fabrication and Characterization of the Devices

The device is assembled in a step-by-step procedure, and after each fabrication step the electrical impedance spectrum $Z(f)$ of the piezoelectric transducer is recorded with the Vector Network Analyzer Bode 100 (OMICRON electronics GmbH, Klaus, Austria) in the range from 500 Hz to 5 MHz. Device dimensions were measured using an electronic micrometer (RS Pro, RS Components, Corby, UK) with an accuracy of ± 4 µm. The assembly process consisted of the followings seven steps:

1. Measure the dimensions of the capillary tube and the transducer.
2. Measure the initial impedance spectrum $Z_{\text{init}}(f)$ of the Pz27 disk.
3. Fit the Pz27 material parameters using ultrasound electrical impedance spectroscopy (UEIS), following the method described in Ref. [21].
4. Glue the capillary tube onto the transducer and UV-curing using an exposure time of 168 s at a UV-intensity of 15 mW/cm^2 and a wavelength of 365 nm.
5. Measure the total device thickness to obtain the glue layer thickness.
6. Mount the device on a 3D-printed sample holder and connect rubber tubing using silicone glue
7. Measure the impedance spectrum $Z_{\text{sys}}(f)$ of the combined capillary-glue-transducer system, both air- and fluid-filled.

Using the four-probe setup, shown in Figure 1a,c, the voltage amplitudes φ_{gen} at the signal generator, φ_{amp} at the amplifier, and φ_{pzt} directly across at the transducer were recorded during the measurements. The time-averaged dissipated power P_{pzt} for a given frequency f is the standard expression calculated from Equations (8) and (9) as

$$P_{\text{pzt}}(f) = \frac{1}{2}\frac{\varphi_{\text{pzt}}^2 \cos\left[\theta_{\text{sys}}(f)\right]}{|Z_{\text{sys}}(f)|}, \quad \text{with} \quad \theta_{\text{sys}} = \arg(Z_{\text{sys}}). \tag{11}$$

A feedback control system is implemented to actuate the transducer at the desired constant power or constant voltage during the frequency sweeps. In the following analysis, we consider the following three case:

Case 1: Constant voltage at the generator, $\varphi_{\mathrm{gen}} = 1$ V.

Case 2: Constant voltage at the transducer, $\varphi_{\mathrm{pzt}} = 0.5$ V.

Case 3: Constant power dissipation in the transducer, $P_{\mathrm{pzt}} = 50$ mW.

3.3. Determination of Acoustofluidic Resonance Frequencies by Particle Tracking Velocimetry

The acoustofluidic resonance frequencies were determined by measuring the average velocity of particles focusing under acoustofluidic actuation. For the particle focusing experiment, we used a neutrally buoyant solution of 10-µm-diameter fluorescent polystyrene spheres (microparticles GmbH, Berlin, Germany) in a fluid consisting of 83% (*v/v*) ultrapure water (Direct-Q3 System, Merck) and 17% (*v/v*) OptiPrep (Density Gradient Medium, Sigma-Aldrich). The particle concentration was approximately 500 particles/µ L.

The acoustic focusing was studied using single-camera 3D particle tracking performed with the general defocusing particle tracking (GDPT) method [22]. GDPT determines the depth position of defocused particle images from the analysis of the corresponding defocusing patterns, previously mapped with a proper calibration procedure [23]. The particle images were recorded using a high-sensitive sCMOS camera (pco.edge 5.5, Excelitas PCO GmbH, Kelheim, Germany) with an optical system consisting of a 5× microscope objective (EC EPIPlan, Zeiss AG, Oberkochen, Germany) and a cylindrical lens in front of the camera sensor to enhance the defocusing patterns. The images were processed using the open-source software *defocustracker* version 2.0.0 [24].

In each experiment, 200 images were recorded at 25 frames/s, and the signal generator was switched on precisely 1 s after the camera had started to record the first frame using an electrical trigger. The frequency sweeps were performed at frequencies in the range from 3.3 to 4.3 MHz in steps of 10 kHz. After the GDPT evaluation, we obtained a set of N measured three-dimensional particle trajectories $\boldsymbol{s}^{(j)}(t) = \{x(t), y(t), z(t)\}^{(j)}$ for each frequency. We then proceeded to compute the three components $s_i^{\mathrm{exp}}(t)$ of the average cumulative particle displacement vector $\boldsymbol{s}^{\mathrm{exp}}(t)$ as

$$s_i^{\mathrm{exp}}(t) = \frac{1}{N}\sum_{j=1}^{N} |s_i^{(j)}(t) - s_i^{(j)}(t_0)|, \quad \text{for } i = x, y, z, \tag{12}$$

where t_0 is the time when the acoustics was turned on. The average acoustophoretic speed v_{exp} of the particles was then calculated at time $t_{\mathrm{exp}} = 40$ ms after turning on the acoustics,

$$v_{\mathrm{exp}} = \sqrt{\sum_{i=x,y,z} \left(\partial_t s_i^{\mathrm{exp}}|_{t=t_{\mathrm{exp}}}\right)^2}. \tag{13}$$

4. Numerical Model

4.1. Description of the Modeled System

We perform numerical simulations of the device described in Section 3.1 using the software COMSOL Multiphysics 6.0, following the implementation in Refs. [3,14,25]: We use the weak form interface "*Weak Form PDE*" to obtain the potential φ in the PZT, the displacement $\boldsymbol{u}$ in all solids, and the acoustic pressure field p_1 in the fluid channel. By using the x-z and y-z symmetry planes, only a quarter of the actual geometry is modeled. In the model we consider the piezoelectric transducer, a thin coupling layer, and the water-filled glass capillary tube. To further minimize the computational complexity, we apply a perfectly matched layer (PML) at the end of the glass capillary [25]. The PML mimicks perfect absorption of all outgoing waves, and it allows to reduce the length of the capillary tube. In our experimental setup, the damping at the edge of the tube is ensured by the silicone glue connecting the tube to the sample holder. A sketch of the system is shown in Figure 1d,e. The simulations were performed on a workstation with a 12-core, 3.5-GHz central processing unit and 128 GB random access memory. Details on the mesh convergence analysis and the material parameters used for the simulation can be found in the Appendices A and B.

4.2. Numerical Simulation of the Particle Velocity

In the second and final study step of our simulation model, we use the "*Particle Tracing for Fluid Flow*" module [26] to compute the particle trajectories of 1000 randomly distributed particles based on the fields computed in the first study step. The wall condition is set to "*Stick*" to mimic stuck particles, which were also commonly observed in the experimental setup. The force acting on the particles is the simulated radiation force $\boldsymbol{F}^{\mathrm{rad}}$, see Equation (6). Acoustic streaming is neglected as the particles are relatively big [26], and the influence of gravity is neglected due to the use of a neutrally-buoyant solution. Similarly to what is done for the experimental data, we obtain the velocity $\boldsymbol{v}_i$ of each particle i at time t_{sim} and compute the average speed v_{sim} of the particle as

$$v_{\mathrm{sim}} = \frac{1}{N}\sum_{i=1}^{N} \left|\boldsymbol{v}_i(t_{\mathrm{sim}})\right|, \tag{14}$$

at time $t_{\mathrm{sim}} = (40\, t_{\mathrm{sim}}^{\mathrm{foc}}/t_{\mathrm{exp}}^{\mathrm{foc}})$ ms, where $t_{\mathrm{sim}}^{\mathrm{foc}}/t_{\mathrm{exp}}^{\mathrm{foc}}$ is the ratio between the numerical and experimental focusing time at resonance.

4.3. Boundary Conditions at the Fluid-Solid and the PZT-Solid Interfaces

In the simulations, we assume a time-harmonic voltage amplitude of φ_{pzt} at the top surface of the piezoelectric transducer, while the bottom surface is grounded to $\varphi_{\mathrm{gnd}} = 0$. We furthermore assume continuous stress between the different domains, a zero normal component of the dielectric displacement field $\boldsymbol{D}\cdot\boldsymbol{n} = 0$ at the PZT-air interfaces and zero normal stress at the solid-air interfaces [14]. For the fluid-solid interface, we implement the effective boundary conditions derived by Bach and Bruus [17]. Here, the fields inside the very thin boundary layers of thickness $\delta_{\mathrm{fl}} = \sqrt{2\eta_0/(\rho_0\omega)} \approx 0.5$ µm are taken into account analytically. The pressure p_1 at the fluid-air interface is set to zero. The boundary conditions between the different domains and their corresponding boundary are summarized in Table 1.

Table 1. The boundary conditions used in the numerical simulations with the surface normal vector $\boldsymbol{n}$ pointing away from the respective domain. We use the solid velocity $\boldsymbol{v}_{\mathrm{sl}} = -\mathrm{i}\omega\boldsymbol{u}$, and the complex-valued shear-wave number $k_{\mathrm{s}} = (1+\mathrm{i})\,\delta_{\mathrm{fl}}^{-1} = (1+\mathrm{i})\,\sqrt{\rho_0\omega/(2\eta_0)}$.

Domain	←	**Boundary**	**Boundary Condition**
PZT	←	top electrode	$\varphi = \varphi_{\mathrm{pzt}}$
PZT	←	bottom electrode	$\varphi = 0$
PZT	←	air	$\boldsymbol{D}\cdot\boldsymbol{n} = 0$
Solid	←	air	$\boldsymbol{\sigma}\cdot\boldsymbol{n} = \boldsymbol{0}$
Solid	←	fluid	$\boldsymbol{\sigma}\cdot\boldsymbol{n} = -p_1\,\boldsymbol{n} + \mathrm{i}k_{\mathrm{s}}\eta_0(\boldsymbol{v}_{\mathrm{sl}} - \boldsymbol{v}_1)$
Fluid	←	solid	$\boldsymbol{v}_1\cdot\boldsymbol{n} = \boldsymbol{v}_{\mathrm{sl}}\cdot\boldsymbol{n} + \frac{\mathrm{i}}{k_{\mathrm{s}}}\boldsymbol{\nabla}_{\parallel}\cdot(\boldsymbol{v}_{\mathrm{sl}} - \boldsymbol{v}_1)_{\parallel}$
Fluid	←	air	$p_1 = 0$

We assume symmetry of all simulated fields at the yz-plane at $x = 0$ and at the xz-plane at $y = 0$. The symmetry boundary conditions therefore are implemented as follows:

$$\text{Symmetry at } x = 0: \qquad u_x = 0, \quad \sigma_{yx} = \sigma_{zx} = 0, \quad \partial_x p_1 = 0, \quad \partial_x \varphi = 0. \tag{15a}$$

$$\text{Symmetry at } y = 0: \qquad u_y = 0, \quad \sigma_{xy} = \sigma_{zy} = 0, \quad \partial_y p_1 = 0, \quad \partial_y \varphi = 0. \tag{15b}$$

5. Results and Discussion

5.1. Electrical Impedance Measurements

The electrical impedance spectrum $Z(f)$ of the unloaded and loaded Pz27 transducer was measured after each step in the fabrication procedure. The material parameters of

the specific Pz27 transducer used in this study, were obtained by electrical impedance spectroscopy (UEIS), following the procedure described in Ref. [21], based on the measured $Z(f)$ of the unloaded transducer. The result is shown in Figure 2a, were it is seen that the fitted spectrum $|Z(f)|$ agrees well with the measured one. The piezoelectric parameters obtained from this UEIS fitting, were then subsequently used together with the remaining material parameters listed in Appendix B to simulate numerically the pressure field p_1, the displacement field $\boldsymbol{u}$, and the electric potential φ of the transducer-glue-capillary-tube system. The measured and the simulated impedance spectrum of the full system in the frequency range 3.3 to 4.3 MHz are shown in Figure 2b, and good agreement is found. Numerical simulations were performed using both the fitted values, and the values for Pz27 given in Ref. [21]. The discrepancy between the two resulting spectra emphasizes the need of obtaining fitted material parameters for the specific transducer used in the study. The remaining deviations from the measured impedance spectrum stem from uncertainties in the glass material parameters, which where taken from the literature and not fitted by UEIS.

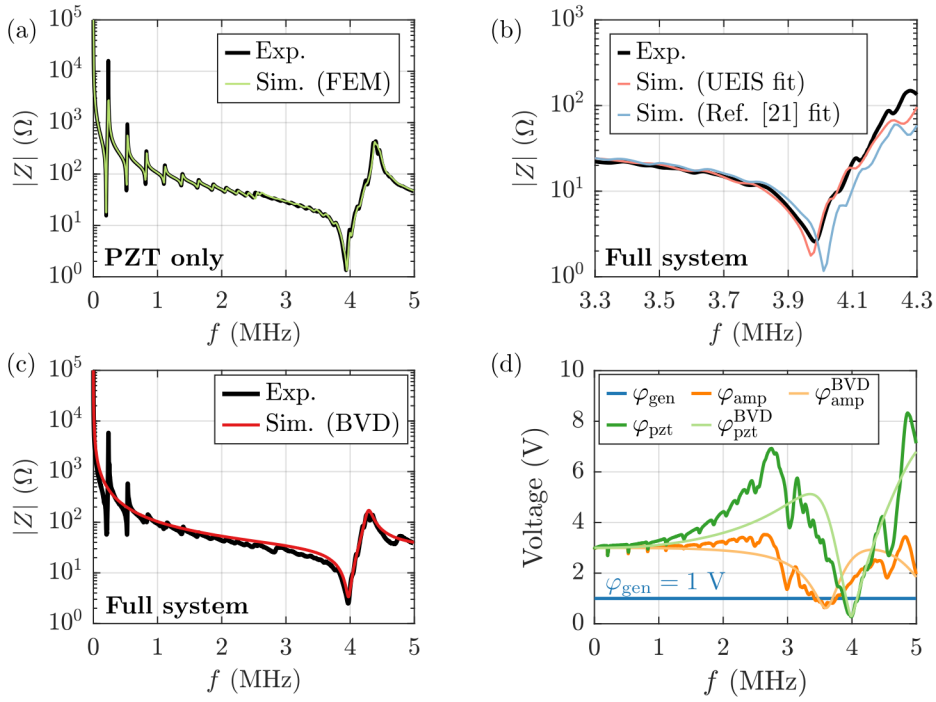

Figure 2. (**a**) Measured (black) and simulated (green) electrical impedance spectrum $|Z(f)|$ in the frequency range 0.5–5000 kHz of the unloaded Pz27 disk. (**b**) Measured (black) and simulated $|Z(f)|$ for 3.3–4.3 MHz, using either UEIS fitted parameters (red) or the parameters from Ref. [21] (blue) of the full system consisting of Pz27 disk, glue layer and liquid-filled glass capillary tube. (**c**) The measured $|Z(f)|$ (black) for 0.5–5000 kHz of the full system (Pz27 disk, glue layer, and liquid-filled glass capillary tube), and the computed $|Z(f)|$ (red) based on the single-frequency BVD-model of Section 2.4. (**d**) The three measured voltage amplitudes versus frequency f at different points in the circuit: φ_{pzt} (dark-green) obtained by four-probe measurements directly across the piezoelectric transducer, φ_{amp} (dark-orange) measured at the output of the amplifier, φ_{gen} (dark-blue) measured at the signal generator. Shown also are the two *LTspice*-simulated voltage amplitudes: $\varphi_{\text{pzt}}^{\text{BVD}}$ (light green) and $\varphi_{\text{amp}}^{\text{BVD}}$ (light orange) computed from the BVD-model.

5.2. Impact of the Cable and the Circuit Resonances on Measured Voltage Amplitude

Using the measured impedance spectrum $Z(f)$ of the full system around the 4-MHz resonance, we obtain the required parameters to describe the transducer through the BVD model of Section 2.4, and we find $C_0 = 1.28$ nF, $C_1 = 207$ pF, $L_1 = 7.69$ µH, and $R_1 = 2.59$ Ω.

We estimate for each of the two wires connecting the amplifier and the transducer that $R_{\text{wire}} = 1\ \Omega$ and $L_{\text{wire}} = 411$ nH. In Figure 2c, we compare $Z(f)$ computed from the BVD model with the measured $Z(f)$. It is seen that the BVD model captures well the characteristics around the 4-MHz resonance of the transducer, and it can therefore aid the understanding of the circuit characteristics.

When comparing the voltage amplitudes at various points in the circuit using a constant generator voltage amplitude $\varphi_{\text{gen}} = 1$ V, we find as shown in Figure 2d that for most of the frequencies in the range 0.5–5000 kHz, the voltage amplitude φ_{pzt} across the transducer is larger than the voltage amplitude φ_{amp} right after the amplifier. This may seem counter-intuitive, but given the resonant nature of the circuit, charge may build up on the capacitive circuit elements. We furthermore find two frequencies were the voltage amplitude is minimal: At $f_{\text{amp}} = 3.56$ MHz, the impedance of the full circuit has an impedance minimum, and at $f_{\text{pzt}} = 3.98$ MHz, the impedance of the transducer has a minimum. The down-shift of f_{amp} by 0.42 MHz from f_{pzt} is due to the parasitic inductance of the wire connecting the amplifier and the transducer. We note that if the voltage amplitude is recorded right after the amplifier, and not directly across the transducer, a wrong estimate of the voltage amplitude and power dissipation of the transducer may result. Furthermore, the parasitic inductance minimizes the power transfer from the amplifier to the transducer, and therefore it is in general beneficial to minimize this inductance by use of shortened and shielded cables. To minimize the ratio $r = f_{\text{amp}}/f_{\text{pzt}}$, the inductance of the wire L_{wire} should be minimized according to

$$L_{\text{wire}} < \frac{(1-r^2)}{2r^2} \frac{C_1 L_1}{C_1 + C_0(1-r^2)}. \tag{16}$$

In our circuit, it is required that $L_{\text{wire}} < 70$ nH to keep the mismatch of f_{circuit} and f_{pzt} below 1%. This is typically hard to achieve, as it requires very thin and short wires. Alternatively, a capacitor $C_{\text{comp}} = (2\pi f_{\text{comp}})^{-2} L_{\text{wire}}^{-1}$ in series with the wire could be used to counteract the impact of L_{wire} at the frequency f_{comp}. Further improvements of the circuit could be obtained by impedance-matching the load impedance Z_{load} to the source impedance Z_{source}, by adding circuit components to the load such that $Z_{\text{source}} = Z_{\text{load}}^*$ [19].

5.3. Voltage Amplitude and Power Dissipation

The voltage amplitudes and power dissipation in a frequency sweep are depending significantly on the chosen electrical excitation method in the actuation process. In Figure 3a–c are shown frequency sweeps of the the voltage amplitudes φ_{gen} and φ_{pzt}, and the average dissipated power P_{pzt} for the three considered cases of constant φ_{gen}, constant φ_{pzt}, and constant P_{pzt}.

The first case with constant $\varphi_{\text{gen}} = 1$ V is shown in Figure 3a. It is seen that φ_{pzt} and P_{pzt} are minimal at or close to the transducer impedance minimum at $f_{\text{pzt}} = 3.98$ MHz. This is not an ideal situation, because many systems are designed with a resonance close to the nominal transducer resonance in mind. Instead, it is beneficial to stabilize either φ_{pzt} or P_{pzt}.

The second case with constant $\varphi_{\text{pzt}} = 0.5$ V is shown in Figure 3b. Both φ_{gen} and P_{pzt} have a narrow peak near $f_{\text{pzt}} = 3.98$ MHz. As will be discussed in Sections 5.4 and 5.5, this might not be ideal for particle focusing experiments when comparing device performances over wider frequency ranges.

The third case with constant $P_{\text{pzt}} = 50$ mW is shown in Figure 3c. To stabilize P_{pzt}, the voltage φ_{gen} needs to be adjusted according to the electrical impedance spectrum of the transducer. The voltage φ_{gen} needs to be higher when running the transducer on-resonance, compared to off-resonance. As in the first case, the voltage amplitude φ_{pzt} is minimal at the resonance $f_{\text{pzt}} = 3.98$ MHz. Other effects, such as the non-linear gain of the amplifier and non-linearity of the piezoelectric transducer, may lead to increased discrepancies between φ_{gen} and φ_{pzt}, which furthermore emphasizes the need to monitor φ_{pzt} and P_{pzt}, and to specify which of them, if any, is kept constant.

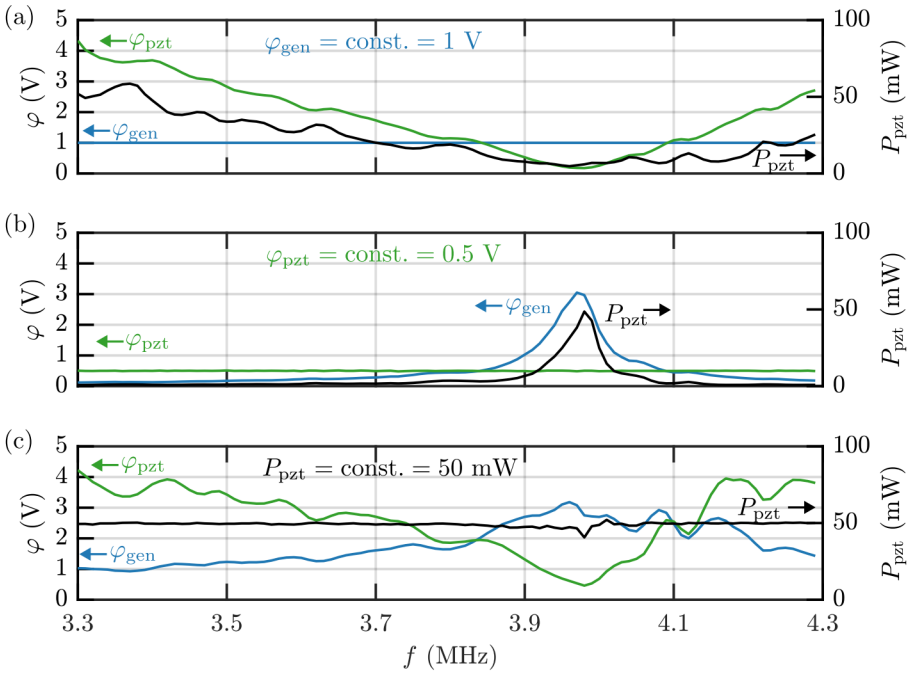

Figure 3. The measured voltage amplitudes φ_{pzt} (green, left axis) and φ_{gen} (blue, left axis) as well as the measured average power dissipation P_{pzt} (black, right axis) plotted versus frequency for 3.3–4.3 MHz for the three cases (**a**) constant voltage φ_{gen} at the signal generator, (**b**) constant voltage φ_{pzt} across the piezoelectric transducer, and (**c**) P_{pzt} constant average power dissipation.

5.4. Average Acoustophoretic Particle Speed

When the acoustic pressure field p_1 is switched on via the Pz27 transducer in our setup shown in Figure 1, polystyrene microparticles inside the water-filled capillary tube acquire an acoustophoretic velocity $\boldsymbol{v}_{\mathrm{ps}}$, see Equations (7), (13) and (14), proportional to the acoustic radiation force $\boldsymbol{F}^{\mathrm{rad}}$, see Equation (6). For the above three cases, the experimental results for the average particle speed v_{exp} are shown in Figure 4a, and the corresponding results for P_{pzt} are shown in Figure 4b. In the case of constant $\varphi_{\mathrm{gen}} = 1$ V, we measure the highest particle speed at the resonance frequency $f = f_{\mathrm{exp}}^{\mathrm{res,g}} = 4.24$ MHz with $v_{\mathrm{exp}} \approx 46\ \mu\mathrm{m\,s^{-1}}$. In the following discussion, we refer to experimental $f_{\mathrm{exp}}^{(ny,nz)\mathrm{B}}$ and simulated $f_{\mathrm{sim}}^{(ny,nz)\mathrm{B}}$ resonance frequencies with well-identified numbers n_y and n_z of standing half-waves in the width (y) and height (z) directions of the microchannel in the respective cases of constant φ_{gen}, φ_{pzt}, and P_{pzt} indicated by the superscript "B" = "g", "φ", and "P". For constant $\varphi_{\mathrm{pzt}} = 0.5$ V, we find the highest particle speed at $f = f_{\mathrm{exp}}^{(0,1)\varphi} = 3.98$ MHz with $v_{\mathrm{exp}} \approx 71\ \mu\mathrm{m\,s^{-1}}$. Finally, for constant $P_{\mathrm{pzt}} = 50$ mW, a resonance appears at $f = f_{\mathrm{exp}}^{(0,1)P} = 4.03$ MHz with $v_{\mathrm{exp}} \approx 77\ \mu\mathrm{m\,s^{-1}}$. Furthermore, for $\varphi_{\mathrm{pzt}} = 0.5$ V and $P_{\mathrm{pzt}} = 50$ mW, we observe a local resonance at $f = f_{\mathrm{exp}}^{(10,0)P} = 3.51$ MHz. This frequency $f_{\mathrm{exp}}^{(10,0)P}$, corresponding to $n_y = 10$ half-wavelengths across the channel width, relates to an acoustic mode leading to particle focusing in 10 nodal lines parallel to the length and evenly distributed across the width of the microchannel, as discussed further in Section 5.5.

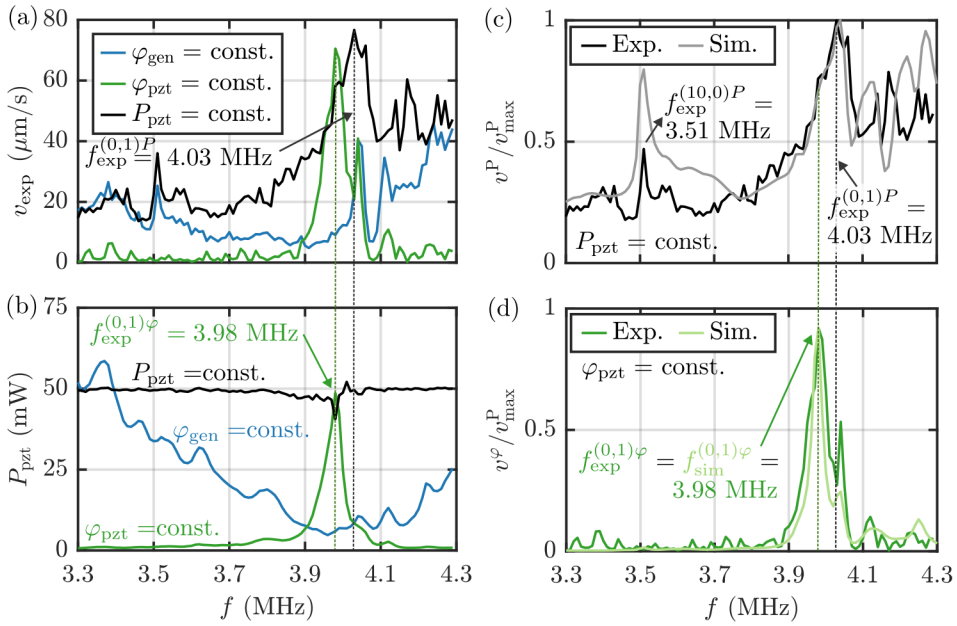

Figure 4. (**a**) Plot of the measured average acoustophoretic particle speed $v_{\rm exp}$ versus frequency f in the range 3.3–4.3 MHz. (**b**) The measured power dissipation $P_{\rm pzt}$ in the transducer versus f for 3.3–4.3 MHz for the three cases of constant voltage $\varphi_{\rm gen}$ at the signal generator, constant voltage $\varphi_{\rm pzt}$ across the piezoelectric transducer, and constant average power dissipation $P_{\rm pzt}$. (**c**) The experimental (black) and simulated (gray) normalized average particle speed $v^{\rm P}/v^{\rm P}_{\rm max}$ versus frequency f at constant-power dissipation $P_{\rm pzt} = 50$ mW. (**d**) The experimental (dark-green) and simulated (light-green) normalized average particle speed $v^{\varphi}/v^{\rm P}_{\rm max}$ versus frequency f at constant transducer voltage $\varphi_{\rm pzt} = 0.5$ V.

When analyzing the measurements in Figure 4b of the power dissipation in the three cases, we find that, when driving the transducer at constant $\varphi_{\rm pzt}$, a clear maximum in $P_{\rm pzt}$ appears at $f_{\rm exp}^{(0,1)\varphi} = 3.98$ MHz, but conversely, $P_{\rm pzt}$ has a minimum at the same frequency for constant $\varphi_{\rm gen}$. The reason is that at this frequency, the transducer has an intrinsic resonance and thus a minimum in its impedance. Lastly, we note that experimentally it is difficult to perfectly stabilize $P_{\rm pzt}$ near the transducer resonance $f_{\rm exp}^{(0,1)\varphi} = 3.98$ MHz. This difficulty is likely due to on-resonance heating effects of the transducer.

5.5. Comparing Numerical Simulations with Experiments

In Figure 4c using constant $P_{\rm pzt} = 50$ mW, the measured $v^{\rm P}_{\rm exp}/v^{\rm P}_{\rm max}$ and the simulated $v^{\rm P}_{\rm sim}/v^{\rm P}_{\rm max}$ average acoustophoretic speed, normalized by the measured maximum speed $v^{\rm P}_{\rm max} = \max|v^{\rm P}_{\rm exp}|$, are plotted versus frequency for 3.3–4.3 MHz. The agreement between the two curves is good, and they both show a resonance at nearly the same frequency $f = f_{\rm exp}^{(0,1)P} = 4.03$ MHz and $f = f_{\rm sim}^{(0,1)P} = 4.04$ MHz, respectively. A similar plot is shown in Figure 4d, but now for the case of constant $\varphi_{\rm pzt} = 0.5$ V, namely the measured $v^{\varphi}_{\rm exp}/v^{\rm P}_{\rm max}$ and the simulated $v^{\varphi}_{\rm sim}/v^{\rm P}_{\rm max}$ versus frequency with the same normalization $v^{\rm P}_{\rm max}$ as before. Again, the agreement between simulation and experiment is good, and both curves have a maximum at $f = f_{\rm exp}^{(0,1)\varphi} = f_{\rm sim}^{(0,1)\varphi} = 3.98$ MHz, about 50 kHz lower than the constant-power resonance frequency $f_{\rm exp}^{(0,1)P} = 4.03$ MHz.

Some interesting features are seen in the measured and simulated spectrum of the constant-voltage acoustophoretic velocity spectrum $v^{\varphi}_{\rm exp}(f)$ in Figure 4d. Its maximum, obtained at $f_{\rm exp}^{(0,1)\varphi} = 3.98$ MHz, is 8% less then the one obtained in the constant-power velocity spectrum $v^{\rm P}(f)$ in Figure 4c, $v^{\varphi}_{\rm max} = 0.92\, v^{\rm P}_{\rm max}$. Moreover, far from being at

the maximum, $v^{\varphi}(f_{\mathrm{exp}}^{\mathrm{P}}) = 0.27\, v_{\mathrm{max}}^{\mathrm{P}}$ is a local minimum. Clearly, the optimal operating condition for acoustophoresis is to run the system at $f_{\mathrm{exp}}^{(0,1)P}$ with constant-power actuation. Operating directly at the transducer resonance at $f_{\mathrm{exp}}^{(0,1)\varphi} = 3.98$ MHz, is not equally efficient due to the low impedance of the transducer and the resulting high power dissipation at this frequency. Constant-voltage frequency sweeps can be misleading in that regard.

In the simulation and experiment with constant P_{pzt}, see Figure 4a,c, a local maximum in the average particle speed v is observed at $f = f_{\mathrm{exp}}^{(10,0)P} = 3.51$ MHz. In Figure 5a,b we compare the simulated pressure field at this frequency with the simulation results at $f = f_{\mathrm{exp}}^{(0,1)P} = 4.03$ MHz. Images of the particles after 4 s at the two corresponding frequencies are shown in Figure 5c,d. Both in the numerically simulated pressure field, as well as in the measured particle positions, we observe in the x-y plane at $f = f_{\mathrm{exp}}^{(10,0)P} = 3.51$ MHz, the formation of 10 nodal lines parallel to the tube axis along the x direction, and with an equidistant distribution across the width, see Figure 5c. In contrast, at the main resonance at $f_{\mathrm{exp}}^{(0,1)P} = 4.03$ MHz shown in Figure 5d, we observe particle focusing in the x-y center plane of the glass capillary tube, above the center region of the Pz27 transducer, caused by the standing half-wave in the vertical z-direction. No transverse nodal lines are observed here.

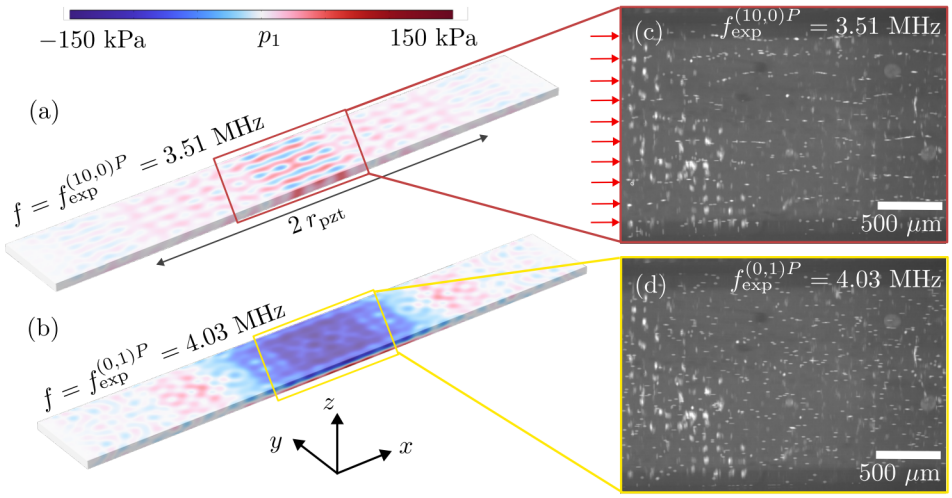

Figure 5. Color plot from −150 kPa (blue) to 150 kPa (red) of the simulated acoustic pressure field p_1 inside the fluid channel at (**a**) $f = f_{\mathrm{exp}}^{(10,0)P} = 3.51$ MHz with a standing-5-wavelength resonance mode in the y-direction (10 nodal lines above the center region of the transducer), and (**b**) at $f = f_{\mathrm{exp}}^{(0,1)P} = 4.03$ MHz with a standing-$\frac{1}{2}$-wavelength resonance mode in z-direction. (**c**) Micrograph of the particles focused in 10 nodal lines (marked by red arrows) inside the microfluidic channel after 4 s at the resonance frequency $f_{\mathrm{exp}}^{(10,0)P} = 3.51$ MHz. (**d**) Micrograph of the particles focused in 1 nodal plane (the xy-plane) inside the microfluidic channel after 4 s at the resonance frequency $f_{\mathrm{exp}}^{(0,1)P} = 4.03$ MHz.

6. Conclusions

Monitoring power dissipation in and voltage across the piezoelectric transducer is important and helpful for understanding and optimizing the performance of acoustofluidic systems. As shown by our measurements on the setup shown in Figure 1, the voltage can differ significantly between amplifier output and transducer, due to the varying impedance of the transducer at different frequencies. In this work, we compared the performance of an acoustofluidic device using three types of actuation: (Case 1) Supplying a constant voltage amplitude φ_{gen} to the amplifier input from the signal generator, (Case 2) driving the piezoelectric transducer using constant-voltage actuation φ_{pzt}, and (Case 3) keeping

the power dissipation P_{pzt} in the transducer constant. The acoustofluidic performance was evaluated in terms of the average acoustophoretic particle speed v in the microfluidic channel measured with 3D particle tracking velocimetry and computed numerically, see Figure 4.

Case 1, performing frequency sweeps with constant φ_{gen}, which is typically used for acoustofluidic devices, may result in a misleading identification of the ideal actuation frequency. The reason is that the power dissipation in the transducer is dependent of the impedance of the transducer as well as the resonant behavior of the cables connecting amplifier and transducer. Instead, keeping a constant power P_{pzt} is a better choice for obtaining a reproducible characterization of the intrinsic properties of acoustofluidic devices.

Case 2, frequency sweeps with constant φ_{pzt} often result in high power dissipation at the transducer resonance frequency $f_{\mathrm{exp}}^{(0,1)\varphi}$, where the impedance of the transducer is at a minimum. Therefore, the strongest acoustofluidic response will be observed closest to this frequency, but it is likely not the most power-efficient frequency, as it results in increased heating and comes at the cost of high input powers. Acoustofluidic applications, however, are often constrained by power-limitations of the frequency generator or the amplifier, as well as the requirement of maintaining a defined temperature to enable the processing of biological samples.

Case 3, frequency sweeps with constant P_{pzt} appear to be a better measure to compare device performance across frequencies, as this compensates for the decrease in impedance at the transducer resonance. As a consequence, also finer details in the acoustic fields that occur at frequencies further away from the transducer resonance frequency can be observed. This is exemplified by the transverse resonance in the width direction at $f = f_{\mathrm{sim}}^{(10,0)P} = 3.51$ MHz, see Figure 5a,c; a resonance clearly visible as a strong peak in the constant-power spectrum in Figure 4c, but not visible in the constant-voltage spectrum in Figure 4d. Keeping P_{pzt} constant, enhances the intrinsic properties of the device performance, as it does not depend on the wiring. In conclusion, frequency sweeps with constant power are the recommended procedure for the characterization of acoustofluidic resonances across the frequency spectrum, both experimentally and numerically. If it is not possible to control the power, and if the frequency sweeps are performed with constant input voltage at the generator or at the transducer, special care must be taken in analyzing the results to avoid misinterpretation of the data.

Lastly, the external circuitry, see Figure 1, may have an impact on the resonance behavior of the setup. In this work, the parasitic impact of the wire inductance, connecting the amplifier and the transducer, was observed. We note that by fine-tuning the impedance of the external circuitry to match the impedance of the transducer at resonance, the power transfer to the transducer can be increased. Such an impedance matching is common in many other fields. Considering the whole circuit, rather than just the piezoelectric transducer in an acoustofluidic setup, therefore can be beneficial to further improve system performance in various acoustofluidic applications.

Author Contributions: Conceptualization, F.L., H.B. and M.R.; methodology, F.L., H.B. and M.R.; software, F.L. and M.R.; validation, F.L., H.B. and M.R.; formal analysis, F.L., H.B. and M.R.; investigation, F.L., H.B. and M.R.; resources, F.L. and M.R.; data curation, F.L.; concluding discussions, F.L., H.B. and M.R.; writing—original draft preparation, F.L.; writing—review and editing, F.L., H.B. and M.R.; visualization, F.L., H.B. and M.R.; supervision: H.B. on theory and simulation, M.R. on experiment; project administration, H.B. and M.R.; funding acquisition, H.B. and M.R. All authors have read and agreed to the published version of the manuscript.

Funding: This work is part of the Eureka Eurostars-2 joint programme E!113461 AcouPlast project funded by Innovation Fund Denmark, grant no. 9046-00127B, and Vinnova, Sweden's Innovation Agency, grant no. 2019-04500, with co-funding from the European Union Horizon 2020 Research and Innovation Programme. MR acknowledges the financial support by the VILLUM foundation, grant no. 00036098.

Institutional Review Board Statement: Not applicable.

Informed Consent Statement: Not applicable.

Data Availability Statement: The data presented in this study are available on request from the corresponding author.

Conflicts of Interest: The authors declare no conflict of interest.

Abbreviations

The following abbreviations are used in this manuscript:

BVD	Butterworth–Van Dyke
GDPT	General Defocusing Particle Tracking
PML	Perfectly Matched Layer
UEIS	Ultrasound Electrical Impedance Spectroscopy

Appendix A. Convergence Analysis for the Mesh and Perfectly Matched Layer

To confirm that the meshing of our finite element model is sufficient we perform mesh convergence testing, following Ref. [26]. We compute the convergence of a given field f compared to a reference solution f_{ref} which is obtained at a high mesh resolution, by gradually increasing the mesh resolution with scale s and computing the L_2-norm,

$$C[f(s)] = \sqrt{\frac{\int_\Omega |f(s) - f_{\text{ref}}|^2 \mathrm{d}V}{\int_\Omega |f_{\text{ref}}|^2 \mathrm{d}V}}. \tag{A1}$$

The results are shown in Figure A1. For our final mesh we use a mesh scale of $s = 8$ and find a convergence of 3.8% for the displacement u_x, 2.7% for the displacement u_y, 1.9% for the displacement u_z, 1.5% for the pressure field p_1, and 0.8% for the electric potential φ. The length of the perfectly matched layer (PML) region is chosen relative to the longitudinal wavelength in glass $\lambda_{\text{lo}}^{\text{glass}}$. In our convergence study it was gradually increased from $0.1\lambda_{\text{lo}}^{\text{glass}}$ to $2\lambda_{\text{lo}}^{\text{glass}}$. We find good convergence starting from $L_{\text{pml}} = 0.7\lambda_{\text{lo}}^{\text{glass}} \approx 921$ µm with convergence below 1% compared to the longest simulated PML layer.

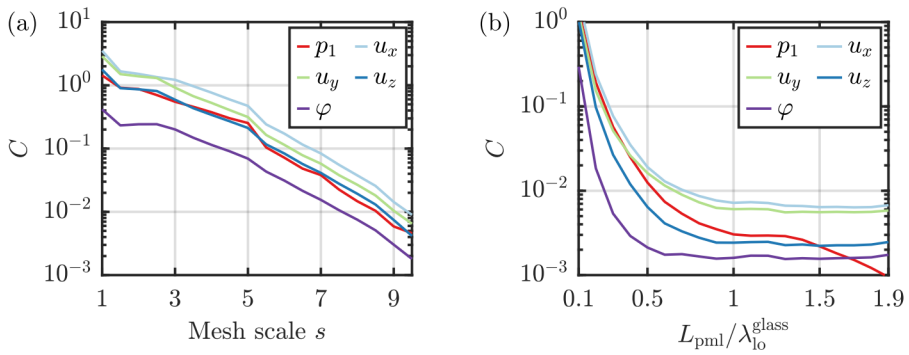

Figure A1. (**a**) Convergence of the pressure field p_1, displacement field components u_x, u_y, u_z and the electric potential φ with increasing mesh scale s. (**b**) Convergence of the pressure field p_1, displacement field components u_x, u_y, u_z with increasing length of the PML layer L_{pml}, expressed relative to the wavelength in glass $\lambda_{\text{lo}}^{\text{glass}}$.

Appendix B. Material Parameters

We study 10 µm-diameter polystyrene particles suspended in a liquid at a temperature of $T = 24$ ℃ to match the laboratory conditions. To obtain neutral buoyancy of the particles, distilled water is mixed with the chemical OptiPrep, resulting in a volume fraction of 17% (*v*/*v*) OptiPrep in water. The glass capillary tube is made from borosilicate glass, the transducer is PZT, and the glue layer is the urethane-related resin NOA86H. The values of the material parameters for the liquid, polystrene particles and glass capillary tube are

taken from the literature. The material parameters for the glue layer and the piezoelectric transducer were obtained via ultrasound electrical impedance spectroscopy, as described in [21]. The material parameters used in the numerical simulations are summarized in Table A1.

Table A1. List of parameters at 24 ℃ used in the numerical simulation: the aqueous OptiPrep solution, 10 µm-diameter polystyrene particles, borosilicate glass, glue, and PZT. For PMMA $C_{12} = C_{11} - 2C_{44}$. For PZT $C_{12} = C_{11} - 2C_{66}$.

Parameter	Symbol	Value	Unit
0.83/0.17 (v/v) water-OptiPrep solution [27,28]			
Mass density	ρ_0	1054	$\mathrm{kg\,m^{-3}}$
Speed of sound	c_0	1501	$\mathrm{m\,s^{-1}}$
Compressibility	κ_0	421	$\mathrm{TPa^{-1}}$
Dynamic viscosity	η_0	0.911	mPa s
Bulk viscosity	η_0^{b}	2.551	mPa s
Polystyrene [29]			
Mass density	ρ_{ps}	1052	$\mathrm{kg\,m^{-3}}$
Compressibility	κ_{ps}	238	$\mathrm{TPa^{-1}}$
Monopole coefficient	f_0	0.434	
Dipole coefficient	f_1	0	
Borosilicate glass [30,31]			
Mass density	ρ_{sl}	2230	$\mathrm{kg\,m^{-3}}$
Elastic modulus	C_{11}	$64.84 - \mathrm{i}0.03$	GPa
Elastic modulus	C_{44}	$24.32 - \mathrm{i}0.01$	GPa
Glue (NOA86H) (measured using UEIS-method [21])			
Mass density	ρ_{sl}	1250	$\mathrm{kg\,m^{-3}}$
Elastic modulus	C_{11}	$4.65 - \mathrm{i}0.51$	GPa
Elastic modulus	C_{44}	$1.21 - \mathrm{i}0.12$	GPa
PZT (Pz27) (measured using UEIS-method [21])			
Mass density	ρ_{sl}	7707	$\mathrm{kg\,m^{-3}}$
Elastic modulus	C_{11}	$121 - \mathrm{i}0.67$	GPa
Elastic modulus	C_{12}	$72.4 + \mathrm{i}0.61$	GPa
Elastic modulus	C_{13}	$75.6 + \mathrm{i}0.12$	GPa
Elastic modulus	C_{33}	$116 - \mathrm{i}0.54$	GPa
Elastic modulus	C_{44}	$21.4 - \mathrm{i}0.83$	GPa
Coupling constant	e_{15}	13.4	$\mathrm{C\,m^{-2}}$
Coupling constant	e_{31}	-5.2	$\mathrm{C\,m^{-2}}$
Coupling constant	e_{33}	16.1	$\mathrm{C\,m^{-2}}$
Electric permittivity	ε_{11}	$925\epsilon_0$	
Electric permittivity	ε_{33}	$791\epsilon_0$	

References

1. Barnkob, R.; Augustsson, P.; Laurell, T.; Bruus, H. Measuring the local pressure amplitude in microchannel acoustophoresis. *Lab Chip* **2010**, *10*, 563–570. [CrossRef]
2. Barnkob, R.; Iranmanesh, I.; Wiklund, M.; Bruus, H. Measuring acoustic energy density in microchannel acoustophoresis using a simple and rapid light-intensity method. *Lab Chip* **2012**, *12*, 2337–2344. [CrossRef] [PubMed]
3. Lickert, F.; Ohlin, M.; Bruus, H.; Ohlsson, P. Acoustophoresis in polymer-based microfluidic devices: Modeling and experimental validation. *J. Acoust. Soc. Am.* **2021**, *149*, 4281–4291. [CrossRef] [PubMed]
4. Barani, A.; Mosaddegh, P.; Haghjooy Javanmard, S.; Sepehrirahnama, S.; Sanati-Nezhad, A. Numerical and experimental analysis of a hybrid material acoustophoretic device for manipulation of microparticles. *Sci. Rep.* **2021**, *11*, 1–17. [CrossRef]
5. Qiu, W.; Baasch, T.; Laurell, T. Enhancement of Acoustic Energy Density in Bulk-Wave-Acoustophoresis Devices Using Side Actuation. *Phys. Rev. Appl.* **2022**, *17*, 044043. [CrossRef]
6. Dubay, R.; Lissandrello, C.; Swierk, P.; Moore, N.; Doty, D.; Fiering, J. Scalable high-throughput acoustophoresis in arrayed plastic microchannels. *Biomicrofluidics* **2019**, *13*, 034105. [CrossRef]
7. Lissandrello, C.; Dubay, R.; Kotz, K.T.; Fiering, J. Purification of Lymphocytes by Acoustic Separation in Plastic Microchannels. *SLAS Technol.* **2018**, *23*, 352–363. [CrossRef] [PubMed]

8. Kim, M.G.; Yoon, S.; Kim, H.H.; Shung, K.K. Impedance matching network for high frequency ultrasonic transducer for cellular applications. *Ultrasonics* **2016**, *65*, 258–267. [CrossRef] [PubMed]
9. Garcia-Rodriguez, M.; Garcia-Alvarez, J.; Yañez, Y.; Garcia-Hernandez, M.; Salazar, J.; Turo, A.; Chavez, J. Low cost matching network for ultrasonic transducers. *Phys. Procedia* **2010**, *3*, 1025–1031. [CrossRef]
10. Emeterio, J.S.; Ramos, A.; Sanz, P.; Ruiz, A. Evaluation of impedance matching schemes for pulse-echo ultrasonic piezoelectric transducers. *Ferroelectrics* **2002**, *273*, 297–302. [CrossRef]
11. Leibacher, I.; Schatzer, S.; Dual, J. Impedance matched channel walls in acoustofluidic systems. *Lab Chip* **2014**, *14*, 463–470. [CrossRef] [PubMed]
12. Ohlsson, P.; Petersson, K.; Augustsson, P.; Laurell, T. Acoustic impedance matched buffers enable separation of bacteria from blood cells at high cell concentrations. *Sci. Rep.* **2018**, *8*, 2045–2322. [CrossRef] [PubMed]
13. Huang, A.; Connacher, W.; Stambaugh, M.; Zhang, N.; Zhang, S.; Mei, J.; Jain, A.; Alluri, S.; Leung, V.; Rajapaksa, A.E.; et al. Practical microcircuits for handheld acoustofluidics. *Lab Chip* **2021**, *21*, 1352–1363. [CrossRef]
14. Skov, N.R.; Bach, J.S.; Winckelmann, B.G.; Bruus, H. 3D modeling of acoustofluidics in a liquid-filled cavity including streaming, viscous boundary layers, surrounding solids, and a piezoelectric transducer. *AIMS Math.* **2019**, *4*, 99–111. [CrossRef]
15. Skov, N.R.; Sehgal, P.; Kirby, B.J.; Bruus, H. Three-Dimensional Numerical Modeling of Surface-Acoustic-Wave Devices: Acoustophoresis of Micro- and Nanoparticles Including Streaming. *Phys. Rev. Appl.* **2019**, *12*, 044028. [CrossRef]
16. Steckel, A.G.; Bruus, H. Numerical study of bulk acoustofluidic devices driven by thin-film transducers and whole-system resonance modes. *J. Acoust. Soc. Am.* **2021**, *150*, 634–645. [CrossRef]
17. Bach, J.S.; Bruus, H. Theory of pressure acoustics with viscous boundary layers and streaming in curved elastic cavities. *J. Acoust. Soc. Am.* **2018**, *144*, 766–784. [CrossRef]
18. Settnes, M.; Bruus, H. Forces acting on a small particle in an acoustical field in a viscous fluid. *Phys. Rev. E* **2012**, *85*, 016327. [CrossRef]
19. Rathod, V.T. A review of electric impedance matching techniques for piezoelectric sensors, actuators and transducers. *Electronics* **2019**, *8*, 169. [CrossRef]
20. Huang, H.; Paramo, D. Broadband electrical impedance matching for piezoelectric ultrasound transducers. *IEEE Trans. Ultrason. Ferroelectr. Freq. Control* **2011**, *58*, 2699–2707. [CrossRef]
21. Bodé, W.N.; Lickert, F.; Augustsson, P.; Bruus, H. Determination of the complex-valued elastic moduli of polymers by electrical impedance spectroscopy for ultrasound applications. *Phys. Rev. Appl.* 2022, 10p, *submitted*. [CrossRef]
22. Barnkob, R.; Kähler, C.J.; Rossi, M. General defocusing particle tracking. *Lab Chip* **2015**, *15*, 3556–3560. [CrossRef] [PubMed]
23. Rossi, M.; Barnkob, R. A fast and robust algorithm for general defocusing particle tracking. *Meas. Sci. Technol.* **2020**, *32*, 014001. [CrossRef]
24. Barnkob, R.; Rossi, M. DefocusTracker: A modular toolbox for defocusing-based, single-camera, 3D particle tracking. *J. Open Res. Softw.* **2021**, *9*, 22. [CrossRef]
25. Bodé, W.N.; Bruus, H. Numerical study of the coupling layer between transducer and chip in acoustofluidic devices. *J. Acoust. Soc. Am.* **2021**, *149*, 3096–3105. [CrossRef]
26. Muller, P.B.; Barnkob, R.; Jensen, M.J.H.; Bruus, H. A numerical study of microparticle acoustophoresis driven by acoustic radiation forces and streaming-induced drag forces. *Lab Chip* **2012**, *12*, 4617–4627. [CrossRef]
27. Muller, P.B.; Bruus, H. Numerical study of thermoviscous effects in ultrasound-induced acoustic streaming in microchannels. *Phys. Rev. E* **2014**, *90*, 043016. [CrossRef]
28. Karlsen, J.T.; Augustsson, P.; Bruus, H. Acoustic Force Density Acting on Inhomogeneous Fluids in Acoustic Fields. *Phys. Rev. Lett.* **2016**, *117*, 114504. [CrossRef]
29. Karlsen, J.T.; Bruus, H. Forces acting on a small particle in an acoustical field in a thermoviscous fluid. *Phys. Rev. E* **2015**, *92*, 043010. [CrossRef]
30. SCHOTT, SCHOTT Suisse SA, 2 Rue Galilée, Yverdon, Switzerland. Borosilicate Glass Substrates Available online: https://www.epfl.ch/research/facilities/cmi/wp-content/uploads/2020/05/D263T_d.pdf (accessed on 18 August 2022).
31. Steckel, A.G.; Bruus, H.; Muralt, P.; Matloub, R. Fabrication, Characterization, and Simulation of Glass Devices with AlN Thin-Film Transducers for Excitation of Ultrasound Resonances. *Phys. Rev. Appl.* **2021**, *16*, 014014. [CrossRef]

Chapter 8

Numerical optimization of polymer-based devices

8.1 Towards improved acoustophoresis in polymer chips

Paper I [1] concludes with the following words on the presented numerical model and the potential of polymer-based acoustofluidic devices:

> "The existing model can be used for further optimizations of the design, to yield higher acoustic energy densities and therefore in turn enable flow rates higher than the reported $Q_{\text{flow}} = 10$ µL/min. Scaling up the flow rate by 1 or 2 orders of magnitude seems possible and would make polymer-based acoustofluidic devices competitive with other particle focusing and separation solutions." [1]

In this chapter, the numerical optimization of a polymer device will be presented based on the various lessons learned from the previous chapters. For the optimization, UEIS-obtained parameters for the polymers PMMA and COC and the piezoelectric material Pz27 are used. Furthermore, the optimization procedure follows a constant voltage and a constant power approach.

Numerical design optimization requires the precise control of a large number of design parameters and – given the computational complexity of the problem – an optimization procedure that works in several steps to be time-efficient. All the required steps of the optimization procedure are presented in the following.

8.2 Design parameters

As shown in Section 3.3.2, the simulated resonance frequencies in an anti-symmetrically-actuated system show good agreement between 2D and 3D simulations. Therefore, the length dimensions of the transducer, microfluidic chip, and channel shall be chosen based on experimental requirements and are not subject to optimization. A 3D simulation is only used for final design verification, while 2D simulations are used to perform the

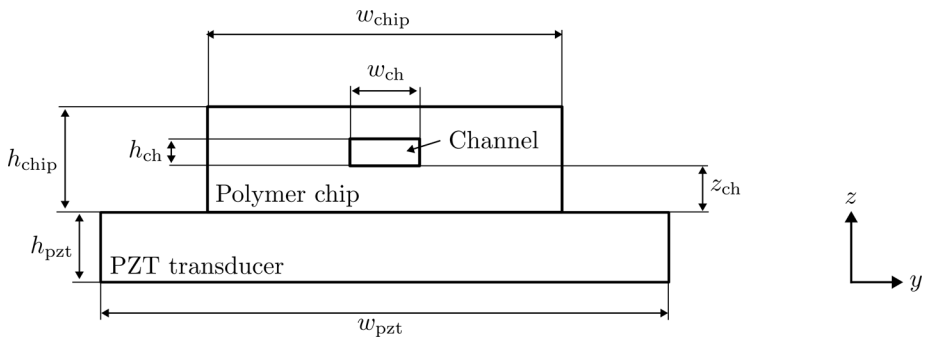

Figure 8.1: A 2D sketch of the device is shown with the chip dimensions w_{chip} and h_{chip}, channel dimensions w_{ch}, h_{ch}, z_{ch} and piezoelectric transducer dimensions w_{pzt} and h_{pzt} indicated by arrows.

optimization. In a 2D system, the following parameters shall be optimized in order to obtain ideal device performance: the channel width w_{ch} and channel height h_{ch}, the vertical position of the channel z_{ch}, the chip width w_{chip} and chip height h_{chip}, the transducer width w_{pzt}, and lastly the transducer height h_{pzt}. An overview of those dimensions is shown in Fig. 8.1. The horizontal position of the channel is, by symmetry requirements, confined to the center of the polymer chip. The thickness of the piezoelectric transducer h_{pzt} defines the resonance frequency of the thickness mode and, therefore, shall be determined initially.

8.3 Finding suitable resonance modes

8.3.1 Resonance modes of the piezoelectric transducer

Piezoelectric transducers are typically used at a resonance frequency corresponding to their thickness mode, where the displacement amplitude is the largest in the direction of the electric field. When studying the displacement field of a rectangular piezoelectric transducer at such a thickness resonance, we observe a very nonuniform displacement along the surface. Such fields result from the superposition of higher-order modes along the width and length of the transducer. The resonance frequency of a piezoelectric transducer can be estimated using the piezoelectric frequency constant N_{t} for the thickness mode and N_{l} for the lateral mode,

$$f_{\mathrm{t}} = \frac{N_{\mathrm{t}}}{h_{\mathrm{pzt}}}, \tag{8.1}$$

$$f_{\mathrm{l}} = \frac{N_{\mathrm{l}}}{l_{\mathrm{pzt}}}. \tag{8.2}$$

For Pz26 and Pz27, the values $N_{\mathrm{t}} \approx 2000\ \mathrm{m\,s^{-1}}$ and $N_{\mathrm{l}} \approx 1500\ \mathrm{m\,s^{-1}}$ [88] can give a first estimate of the resonance frequency. In Fig. 8.2, the resonance modes of a 3-mm-wide, 0.5-mm-thick Pz27 transducer in the frequency range from 500 Hz to 5 MHz for symmetric

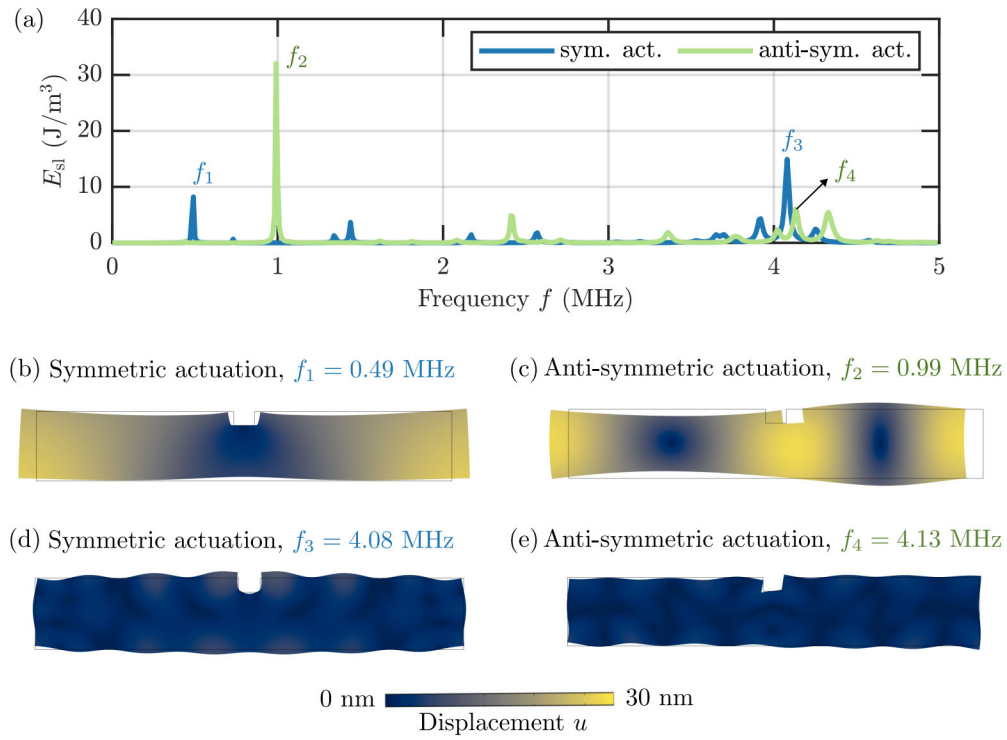

Figure 8.2: (a) Simulated solid energy density E_{sl} versus frequency f in a 3-mm-wide, 0.5-mm-thick Pz27 transduce with a split top electrode. The simulation results for actuation with an anti-symmetric driving voltage (green) and in a transducer with a symmetric driving voltage (blue) are shown. A constant voltage amplitude of $\varphi_0 = 1$ V across the frequency range has been used in the simulation. (b)-(e) Displacement magnitude u from 0 nm (dark blue) to 30 nm (yellow) at different resonance frequencies for symmetric and anti-symmetric actuation.

and anti-symmetric actuation can be seen. We expect a thickness resonance at around 4 MHz for such a transducer in both cases. A lateral mode is expected at 500 kHz for symmetric actuation and around 1 MHz for anti-symmetric actuation since the transducer length is effectively halved. In the energy density spectrum in Fig. 8.2(a), we can see that the simulated resonances are close to the predicted values. The simulated fields of the displacement magnitude u in Fig. 8.2(b) and (c) show substantial displacement of the lateral mode. The anti-symmetric lateral mode shown in Fig. 8.2(c) resembles almost a sine-wave. The thickness mode shown in Fig. 8.2(d) and (e), on the contrary, shows a less uniform displacement field with small displacement ripples along the surface of the transducer. Given the sine-wave-like displacement field of the anti-symmetric lateral mode, as seen in Fig. 8.2(c), such modes seem promising for the anti-symmetric actuation of acoustofluidic devices. Therefore, these anti-symmetric lateral modes of Pz27 shall be utilized in the following optimization procedure.

8.3.2 Resonance modes of the polymer chip

In order to design an optimized acoustophoresis device from polymers, it can be helpful to understand the eigenmodes of a polymer chip without a microfluidic channel first. The wider and higher the geometry at a given frequency, the more standing waves will fit in the width and height direction. This geometry leads to very complex displacement patterns, even without a microchannel. Reducing the size of the geometry or the driving frequency leads to lower-order vibrational modes of the polymer chip. These lower-order modes are helpful in the design process as it makes the behavior more predictable. As was briefly discussed in Chapter 5, the formation of transverse modes, consisting of a full standing wave in the width of the polymer chip, is highly beneficial.

In Fig. 8.3, the normalized solid energy density $E_{\mathrm{sl}}/E_{\mathrm{sl}}^{\mathrm{max}}$ for an anti-symmetrically driven polymer chip is shown for various aspect ratios $\mathrm{AR} = h_{\mathrm{chip}}/w_{\mathrm{chip}}$ and different frequencies f. Assuming n longitudinal half-waves $\lambda_{\mathrm{lo}}/2$ in the width of the chip, which

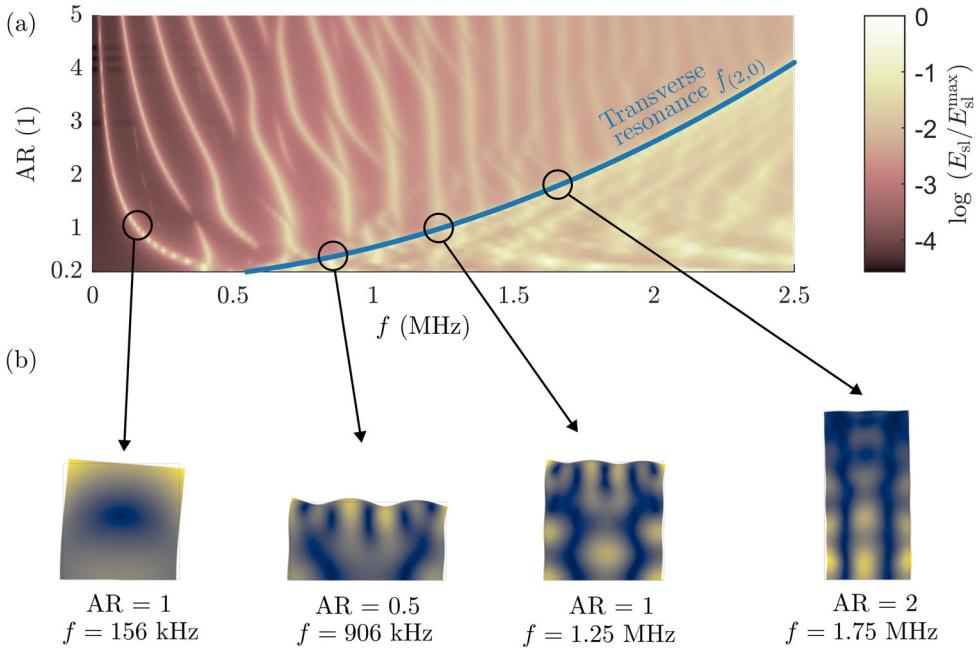

Figure 8.3: (a) Normalized solid energy density $E_{\mathrm{sl}}/E_{\mathrm{sl}}^{\mathrm{max}}$ in the polymer chip at different aspect ratios $\mathrm{AR} = h_{\mathrm{chip}}/w_{\mathrm{chip}}$ for frequencies f ranging from 500 Hz to 2.5 MHz. In this 2D simulation, the cross-section area of the chip is kept constant at $A_{\mathrm{chip}} = 4\ \mathrm{mm}^2$, while the aspect ratio is changed from 0.2 (a very wide chip) to 5 (a very tall but narrow chip). The blue line indicates the resonance frequency $f_{(2,0)}$ of the transverse mode in the chip width. (b) Normalized displacement field u from 0 (dark blue) to maximum displacement (yellow) for different eigenmodes of the polymer chip.

are decoupled from the shear wave, a resonance frequency for this transverse resonance $f_{(n,0)}$ can be obtained,

$$f_{(n,0)} = \frac{nc_{\mathrm{lo}}}{2w_{\mathrm{chip}}} = \frac{nc_{\mathrm{lo}}}{2}\sqrt{\frac{\mathrm{AR}}{A_{\mathrm{chip}}}}. \tag{8.3}$$

In Fig. 8.3(a), the resonance frequency $f_{(2,0)}$ is plotted as a blue line for the different aspect ratios. At this frequency, a full standing wave ($n = 2$) in the width of the polymer chip is observed. Given the anti-symmetric displacement boundary condition at the bottom of this chip, a standing-half-wave mode ($n = 1$) is not possible. Therefore $f_{(2,0)}$ is the lowest mode in the width direction. These modes, indicated by the blue curve in Fig. 8.3(a), act as a "barrier" to the higher-order mixed modes, where both shear and longitudinal modes exist. Below the frequency $f_{(2,0)}$ only shear modes exist. A few eigenmodes for the three different aspect ratios AR $= 0.5, 1, 2$ are shown in Fig. 8.3(b).

8.4 Overview of the optimization procedure

8.4.1 Initial design parameters

To perform numerical optimization, a set of initial parameters p_0 needs to be defined, acting as the starting point of the optimization procedure. Studying the eigenmodes of a polymer chip and a PZT transducer, as done above, can be helpful for the choice of design parameters. Based on the target resonance frequency, an initial chip width is therefore selected as $w_{\mathrm{chip}} = \lambda_{\mathrm{lo}}$ to achieve a standing wave along the width of the chip as shown above. Due to fabrication constraints, we limit the optimization procedure to aspect ratios from 0.5 to 2 and choose $AR = 1$ or equivalently $h_{\mathrm{chip}} = \lambda_{\mathrm{lo}}$ as an initial parameter for the chip height. In polymer devices, we typically observe standing waves in the microfluidic channel, where the wavelength ranges from 0.2 to 0.5 times the acoustic wavelength λ_0 in the fluid, as was discussed in Chapter 5. Therefore, the value $\frac{\lambda_0}{3}$ shall be used as an initial channel width. The vertical position z_{ch} is constrained by the thickness t_{foil} of the polymer foil used to seal the channel, and we are therefore constrained to $z_{\mathrm{ch}} = t_{\mathrm{foil}}$. The width w_{pzt} and height h_{pzt} of the piezoelectric transducer govern the thickness and width resonance frequencies and, therefore, should be chosen based on the target frequency, as explained previously in Section 8.3.1. The initial parameters and the lower and upper boundary of each design parameter are summarized in Table 8.1.

Table 8.1: Initial parameters p_0 of the device geometry and lower and upper boundaries used for the optimization procedure. λ_0 denotes the acoustic wavelength in water and λ_{lo} denotes the longitudinal wavelength in the polymer chip. N_{t} and N_{l} are the piezoelectric frequency constants for the thickness and lateral resonance frequencies f_{t} and f_{l} of the transducer. t_{foil} is the thickness of the polymer foil used to seal the microfluidic channel.

	w_{ch}	h_{ch}	z_{ch}	w_{chip}	h_{chip}	w_{pzt}	h_{pzt}
Initial parameter	$\lambda_0/3$	$\lambda_0/3$	t_{foil}	λ_{lo}	λ_{lo}	$N_{\mathrm{l}}/(2f_{\mathrm{l}})$	$N_{\mathrm{t}}/f_{\mathrm{t}}$
Lower boundary	$\lambda_0/5$	$\lambda_0/5$	–	$0.5\lambda_{\mathrm{lo}}$	$0.5\lambda_{\mathrm{lo}}$	$0.9\, w^0_{\mathrm{pzt}}$	–
Upper boundary	$\lambda_0/2$	$\lambda_0/2$	–	$2\lambda_{\mathrm{lo}}$	$2\lambda_{\mathrm{lo}}$	$1.1\, w^0_{\mathrm{pzt}}$	–

8.4.2 Optimization parameter

The optimization procedure aims to improve the acoustophoresis performance of polymer-based devices. It is, therefore, essential to quantify this performance using a suitable optimization parameter that can be maximized. Gustav Kildevang Modler, a master's student in the TMF group, shall be mentioned in this context, who aided the development of the optimization procedure with helpful thoughts and discussions on the optimization parameter presented in the following. The main goal related to this thesis project is to perform particle separation at high flow rates. We, therefore, aim to optimize the throughput of the system or, equivalently, the maximum achievable flow rate $Q_{\text{flow}}^{\max}$ while maintaining particle focusing. The flow rate $Q_{\text{flow}}^{\max}$ thereby relates to the focusing time t_{foc} and the active volume $V_{\text{fl}} = w_{\text{ch}} h_{\text{ch}} l_{\text{pzt}}$ of the microfluidic channel, which is located above the piezoelectric transducer of length l_{pzt}, so that

$$Q_{\text{flow}}^{\max} = \frac{V_{\text{fl}}}{t_{\text{foc}}}. \tag{8.4}$$

With the definition of the focusing time $t_{\text{foc}} \propto \frac{w_{\text{ch}}^2}{E_{\text{ac}}}$, given in Eq. (2.18), and neglecting the transducer length l_{pzt} in this 2D analysis, we obtain an expression for the optimization parameter $\mathcal{Q}$ with the microfluidic channel centered at $y = 0$,

$$\mathcal{Q} = \mathcal{R} E_{\text{ac}} \frac{h_{\text{fl}}}{w_{\text{fl}}}, \quad \text{with } \mathcal{R} = \frac{\int_\Omega -\text{sign}(y) F_y^{\text{rad}} \text{d}V}{\int_\Omega |F_z^{\text{rad}}| \text{d}V}. \tag{8.5}$$

In this expression, the ratio $\mathcal{R}$ between the horizontal radiation force F_y^{rad} in y-direction, and the vertical radiation force F_z^{rad} in z-direction is taken into account. For focusing in the horizontal y-direction, we want to obtain a radiation force F_y^{rad} that is much greater than the radiation force in the vertical z-direction, F_z^{rad}. Maximizing the optimization parameter $\mathcal{Q}$ ensures that high flow rates $Q_{\text{flow}}^{\max}$ can be achieved while also ensuring strong focusing in the horizontal y-direction.

8.4.3 Steps in the optimization procedure

The optimization procedure consists of several steps. Initially, the transducer's resonance frequency f_{pzt} needs to be selected. Based on this frequency, the optimal dimensions of the polymer chip can be determined. In the second step, initial parameters and lower and upper boundaries are defined for each parameter that needs to be determined. Those parameters have been outlined above in Table 8.1. The third step consists of optimizing the 2D geometry using the MATLAB-package *fminsearchbnd* [86] and excluding the piezoelectric transducer. In this step, an anti-symmetric displacement boundary condition is used to drive the system, and a narrow frequency range around the previously selected frequency f_{pzt} is chosen. The optimization algorithm minimizes the cost function $\mathcal{C} = \mathcal{Q}^{-1}$ in several steps until convergences of $\mathcal{C}$ with changes below 0.01% are observed. In the fourth step of the procedure, the piezoelectric transducer is included in the optimization. Optimizing the polymer dimensions in an individual step helps the optimization procedure to

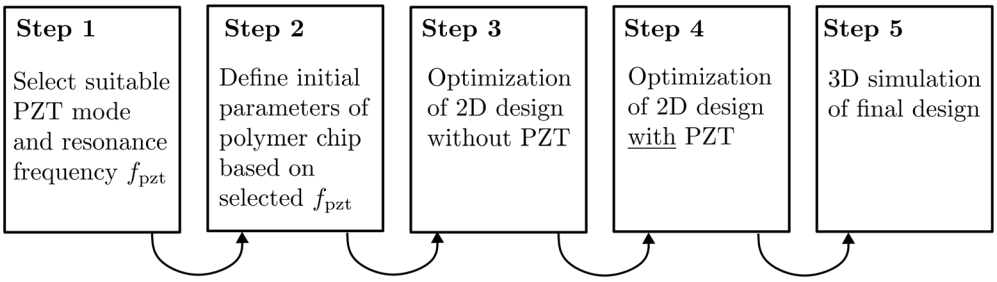

Figure 8.4: Overview of the optimization procedure consisting of five steps.

match the transducer resonance to a suitable polymer mode by providing improved initial values for the final optimization step. In the last step, a 3D simulation of the optimized geometry is performed to verify the performance in terms of the acoustic energy density E_{ac} and achievable flow rates $Q_{\mathrm{flow}}^{\mathrm{max}}$. A flow chart of the procedure is shown in Fig. 8.4.

8.5 Results of the optimization procedure

Device optimization was performed for a polymer chip and piezoelectric transducer with a split top-electrode, utilizing anti-symmetric actuation of a 0.5 mm thick and approximately 3-mm-wide Pz27 transducer. Such a transducer shows an anti-symmetric lateral mode at $f \approx 1$ MHz, closely resembling a sinusoidal actuation pattern, as shown in Fig. 8.2(c). Here, the two cases of constant voltage amplitude and constant power dissipation in the transducer were studied in a frequency range from 0.5 MHz to 2.5 MHz. The two optimized systems, labeled "Optim. A" and "Optim. B" in the following, are then compared to a reference system, and their performance is quantified. In our optimization procedure, the vertical channel position is fixed at a value of $z_{\mathrm{ch}} = 0.13$ mm due to fabrication constraints since the device fabrication requires the bonding of an approximately 0.13 mm thick polymer foil to seal the channel.

8.5.1 Overview of the optimized and the reference system

Device optimization has been performed using the material COC for the polymer chip and Pz27 for the transducer. Both materials have been thoroughly characterized using the UEIS technique presented in Chapter 6, and their corresponding material parameters are listed in the appendix in Table A.3. Furthermore, COC yields lower acoustic attenuation than PMMA and is therefore preferable to achieve good focusing performance. The device presented and characterized in Paper I [1] was chosen as the reference system. This reference device was re-simulated using UEIS-obtained elastic moduli for PMMA and the material parameters for Pz26 from the literature. In a second simulation of the reference system, the UEIS values for Pz27 and COC were used while keeping the same device dimensions. These simulations allow us to obtain a reasonable estimate of how the numerical performance compares with the experimental performance presented in Paper I [1].

Table 8.2: Dimensions of the reference systems and dimensions for optimized polymer chip systems: The device presented in Chapter 5 is used as the reference system. The system "Ref. PMMA" uses UEIS-obtained PMMA material parameters and literature values for Pz26, while system "Ref. COC" uses the UEIS-values for Pz27 and COC, which are listed in Chapter A. "Init. COC" are the initial parameters used for the optimization procedure. System "Optim. A" results from an optimization using a constant-voltage approach. System "Optim. B" was obtained using a constant-power optimization.

	PZT	Polymer	w_{ch} (µm)	h_{ch} (µm)	z_{ch} (mm)	w_{chip} (mm)	h_{chip} (mm)	w_{pzt} (mm)	h_{pzt} (mm)
Ref. PMMA	Pz26	PMMA	375	150	0.85	5.0	1.18	8.0	2.0
Ref. COC	Pz27	COC	375	150	0.85	5.0	1.18	8.0	2.0
Init. COC	Pz27	COC	494	494	0.13	2.40	2.40	3.00	0.5
Optim. A	Pz27	COC	392	351	0.13	2.39	2.32	3.00	0.5
Optim. B	Pz27	COC	480	454	0.13	2.74	2.59	2.89	0.5

Table 8.2 lists the two reference systems, "Ref. PMMA" and "Ref. COC", as well as the two optimized designs, labeled "Optim. A" and "Optim. B". The initial conditions for the optimization procedure of the COC chip are listed as "Init. COC".

Initially, in this work, only optimization using the conventional constant-voltage excitation approach was performed. The final dimensions resulting from this optimization are listed in Table 8.2 and are labeled "Optim. A". However, as later discovered and explained in Chapter 7, it can be beneficial to electrically excite acoustofluidic devices while ensuring constant power dissipation in the transducer when performing frequency sweeps. This type of excitation helps to identify the most power-efficient actuation frequencies and, especially in the case of polymer devices, ensures that whole-system resonances that are not perfectly matched to the transducer resonance can be observed experimentally and numerically. Therefore a further optimization was performed, where the power dissipation was kept at a constant value. The obtained device dimensions for this constant-power excitation are listed as "Optim. B".

8.5.2 Numerical results of the optimized system

The performance of the four different systems is quantified in terms of the optimization parameter $\mathcal{Q}$ at the resonance frequency f_{res}, as well as the acoustic energy density E_{ac}, and the ratio of the vertical and horizontal radiation force $\mathcal{R}$ at this frequency. In Table 8.3, we compare the performance of a constant-voltage actuation with a constant voltage amplitude of $\varphi_0 = 1$ V, and the case of constant power dissipation in the transducer with $P_{\mathrm{pzt}} = 68$ mW. The power dissipation of 68 mW corresponds to the peak power dissipation in the transducer, which was observed for constant-voltage excitation of the four different devices in the frequency range from 0.5 MHz to 2.5 MHz.

Table 8.3: The performance metrics for the different optimized systems are listed together with the results of the reference system of Chapter 5. The optimized system "Optim. A" was obtained using a constant-voltage optimization approach. System "Optim. B" is the result of a constant-power optimization. The left half of the table lists the performance metrics at a constant voltage. The right half of the table shows the corresponding performance metrics for a constant power of $P_{\mathrm{pzt}} = 68$ mW.

	$\varphi_0 = 1$ V = const.				$P_{\mathrm{pzt}} = 68$ mW = const.			
	f_{res} (MHz)	$\mathcal{Q}$ (J/m^3)	E_{ac} (J/m^3)	$\mathcal{R}$ (—)	f_{res} (MHz)	$\mathcal{Q}$ (J/m^3)	E_{ac} (J/m^3)	$\mathcal{R}$ (—)
Ref. PMMA	1.15	0.04	0.05	2.1	1.04	6.2	4.2	3.7
Ref. COC	1.07	2.2	1.7	3.2	0.79	13.9	3.9	8.9
Optim. A	0.99	48.4	3.2	16.9	1.02	175.8	9.9	19.7
Optim. B	0.91	10.2	0.4	29.1	0.91	271.6	9.9	29.1

The left half of Table 8.3 shows the results for the constant-voltage optimization. Device "Optim. A", which was optimized for constant-voltage excitation, shows the best performance in terms of the optimization parameter $\mathcal{Q}$. The optimized device shows excellent performance with $\mathcal{Q}$ being 20 times larger than for the reference system "Ref. COC". The acoustic energy density in the microfluidic channel is most notably increased when using the material COC, instead of the polymer PMMA, due to the lower acoustic attenuation of COC. On the other hand, device "Optim. B", which was optimized for a constant-power excitation, performs very poorly in the constant voltage case with a very low acoustic energy of only 0.4 J m^{-3}. Looking at the performance metrics in the case of constant-power excitation, ensuring a constant $P_{\mathrm{pzt}} = 68$ mW across the whole frequency range, we now find that device "Optim. B" shows the strongest overall performance in terms of the optimization parameter $\mathcal{Q}$. While device "Optim. A" yields an equally high acoustic energy density E_{ac}, "Optim. B" still performs better due to the higher ratio $\mathcal{R}$, therefore allowing higher achievable flow rates with device "Optim. B".

In Fig. 8.5, the power dissipation and optimization parameter $\mathcal{Q}$ are shown for the two optimized devices and contrasted to the reference system "Ref. COC". System "Optim. A" shows a peak power dissipation of 68 mW at a frequency of $f_{\mathrm{A}}^{\varphi} = 0.99$ MHz. This value was consequentially used for the constant-power excitation comparison. Studying the case of constant voltage in Fig. 8.5(b), the system "Optim. A" performs an order of magnitude better than the unoptimized reference system "Ref. COC" in terms of the parameter $\mathcal{Q}$. Since system "Optim. A" has been optimized for constant-voltage excitation, it shows a resonance at the frequency of highest power dissipation f_{A}^{φ}. System "Optim. B," on the contrary, is optimized for power efficiency and yields a high value of $\mathcal{Q}$ at the same frequency $f_{\mathrm{B}} = 0.91$ MHz both in Fig. 8.5(b) and (c). In Fig. 8.5(c), for constant power dissipation across all frequencies, the device "Optim. B" outperforms geometry "Optim. A" and yields a 20 times better performance than the reference system "Ref. COC".

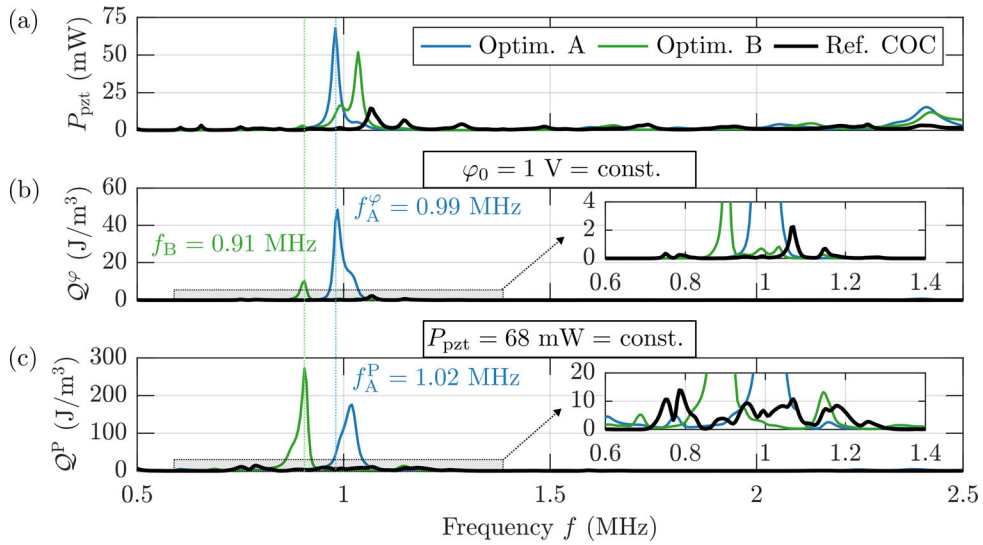

Figure 8.5: (a) Power dissipation of the optimized systems "Optim. A" (blue) and "Optim. B" (green), and the reference system "Ref. COC" (black). (b) The optimization parameter $\mathcal{Q}$ versus frequency f in the range from 0.5 to 2.5 MHz is shown for constant-voltage excitation. (c) Same as (b), but here $\mathcal{Q}$ is shown for a constant power dissipation $P_{\mathrm{pzt}} = 68$ mW in the transducer.

8.5.3 Parameter sensitivity of the optimized system

In order to get an estimate for fabrication tolerances when producing one of the optimized systems, the sensitivity of the optimization parameter $\mathcal{Q}$ towards changes in the dimensions of the polymer chip was analyzed. The results for relative dimensions changes for the optimized system "Optim. B" at constant power are shown in Fig. 8.6. It is found that the channel width w_{ch} and height h_{ch} can be increased or decreased by around 15% before the optimization parameter decreases to half of its maximum value 0.5 max($\mathcal{Q}$). A green contour line indicates this value in Fig. 8.6. $\mathcal{Q}$ shows a higher sensitivity to relative changes in the chip width w_{chip} and height h_{chip}. A change of about 10% for w_{chip} and h_{chip} is required to decrease $\mathcal{Q}/\max(\mathcal{Q})$ to 0.5. In terms of absolute changes, this translates to approximately a 260 µm change of the corresponding outer dimensions of the chip. In contrast, the channel dimensions need to be changed by only 70 µm to observe the same relative decrease of $\mathcal{Q}/\max(\mathcal{Q})$.

The red cross in Fig. 8.6(a-d) visualizes the global maximum of the normalized optimization parameter. A blue circle indicates the value reached by the optimization algorithm. In a fully optimized system, we expect to find the global optimum at the dimension $p/p^{\mathrm{optim}} = 1$, which requires very fine stepping and low tolerances on the termination criterion. Such fine stepping comes at the cost of a higher run time of the optimization procedure, and it is typically sufficient to terminate the optimization close to the global

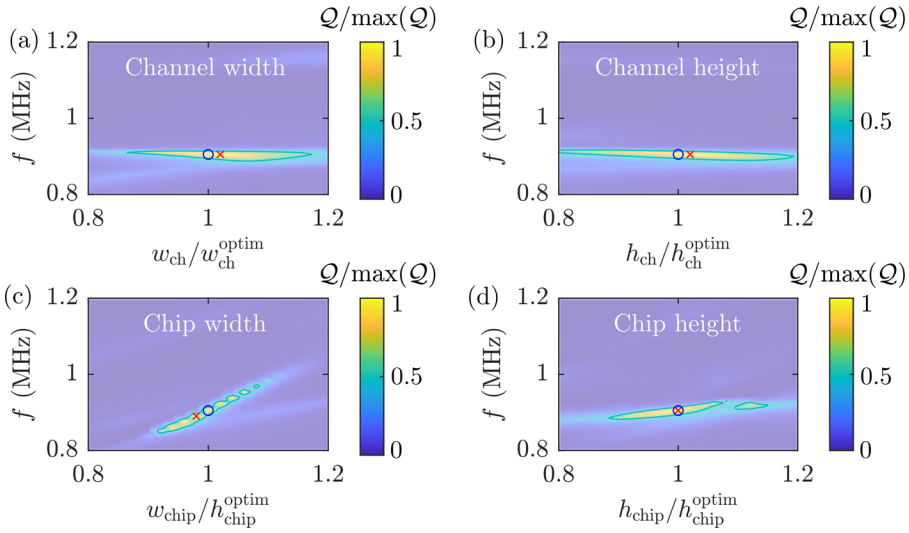

Figure 8.6: The normalized optimization parameter $\mathcal{Q}/\max(\mathcal{Q})$ is shown versus frequency f in the range from 0.8 to 1.2 MHz, and versus changes in dimensions of the polymer chip for system "Optim. B". A green contour line indicates the 50% level, where $\mathcal{Q} = 0.5\ \max(\mathcal{Q})$. A red cross visualizes the global maximum in the simulated region, and a blue circle indicates the value found by the optimization procedure. The sensitivity of $\mathcal{Q}$ towards changes in the different dimensions is shown for (a) the channel width w_{ch}, (b) the channel height h_{ch}, (c) the chip width w_{chip}, and (d) the chip height h_{chip}.

optimum. Nevertheless, the optimization algorithm still can be improved, and performing several iterations, similar to as done for the UEIS method, might be beneficial to ensure that the global optimum is found.

8.5.4 3D simulation of the optimized system

Initially, only optimization using constant-voltage excitation was performed. However, the benefits of maintaining a constant power dissipation across frequencies were only discovered later in the project, with the results summarized in Chapter 7. Therefore it is device "Optim. A", which is currently being manufactured by the project collaborators at DTU Construct. While device "Optim. B" promises better performance at the same electrical input power, it requires higher actuation voltages which are not always easy to accomplish experimentally. The following analysis, therefore, is based on the device "Optim. A".

Simulations of a quarter of the whole geometry of device "Optim. A" have been performed in 3D. For this simulation symmetry boundary conditions in the yz-plane and anti-symmetry boundary conditions in the xz-plane have been used, similar to the work described in Paper I [1]. For this simulation, a length $l_{\mathrm{pzt}} = 20$ mm for the piezoelectric transducer, a chip length $l_{\mathrm{chip}} = 40$ mm, and a channel length $l_{\mathrm{ch}} = 35$ mm have been selected. The width and height dimensions are the same as listed in Table 8.2.

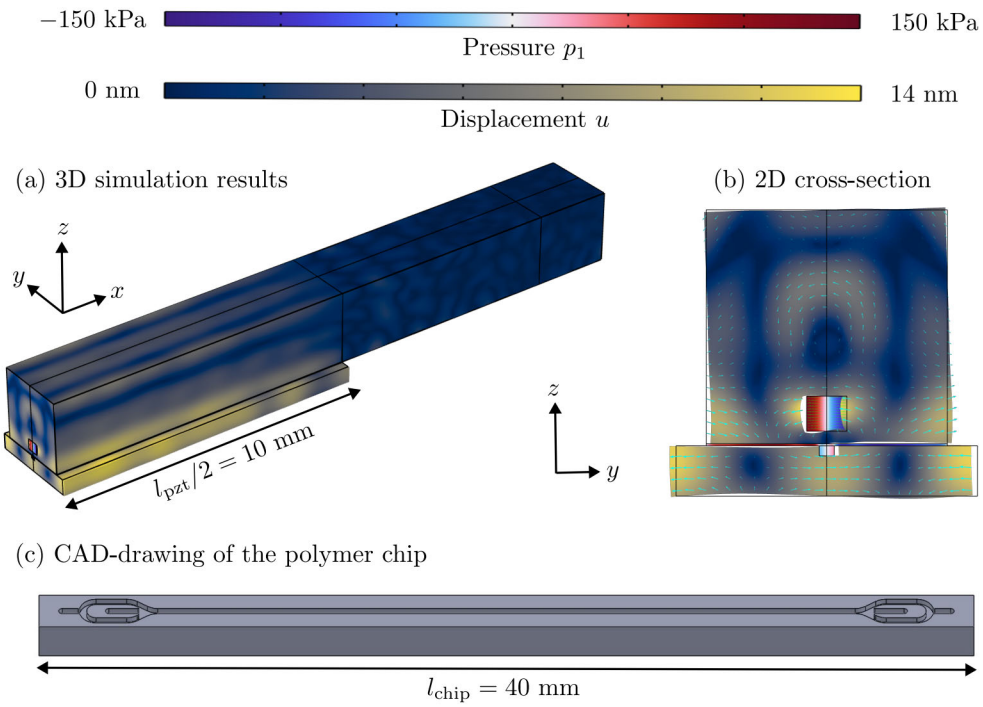

Figure 8.7: (a) 3D simulation results of the optimized geometry "Optim. A" at the resonance frequency $f = 0.99$ MHz. The pressure p_1 in the fluid channel and the coupling layer ranges from −150 kPa (blue) to 150 kPa (red). The displacement u ranges from 0 nm (dark blue) to 14 nm (yellow). (b) The 2D cross-section of the device shows a transverse mode along the y-direction leading to good particle focusing in the pressure node in the center of the channel. The displacement has been scaled by a factor of 5000 to make the nm-deformation more visible. (c) CAD-model of the optimized polymer chip, which the project collaborators from DTU Construct will fabricate.

The results of the simulated fields in 3D for the optimized device (Optim. A) are shown in Fig. 8.7(a,b). As the driving mechanism of the standing wave in the microfluidic channel, the displacement of the left and right channel walls in y-direction is identified. The obtained resonance frequency of the 3D system is 0.99 MHz and therefore matches the results of the optimized 2D system. The acoustic energy density at this frequency is $E_{ac} = 2.7\ \mathrm{J\,m^{-3}}$ for an excitation voltage amplitude of $\varphi_0 = 1$ V and at an input power of $P_{input} = 21$ mW. For 4.8 µm-diameter polystyrene particles in water, this energy density relates to a focusing time of approximately 14 s. The achievable flow rate at this input power corresponds to 12 µL/min or about 0.6 mL/min per 1 W input power.

If we compare this performance to the reference PMMA device studied in Paper I [1], the acoustic energy density at a voltage amplitude of $\varphi_0 = 1$ V has been increased from $E_{ac} = 0.05\ \mathrm{J\,m^{-3}}$ to $E_{ac} = 2.7\ \mathrm{J\,m^{-3}}$, which is an improvement by more than a factor of 50. Furthermore, the reported flow rate in Paper I [1] was 10 µL/min at an estimated input power of 200 mW. We expect to reach the same flow rate at a much lower input

power of 21 mW in the optimized system. Compared to the polystyrene-based devices presented by Mueller *et al.* in Ref. [18], this is an improvement by a factor of five at the same input power of 1 W.

Fig. 8.7(c) shows a CAD drawing of the optimized geometry, including flow splitters which were not included in the numerical simulation. Such a device is currently being manufactured by the project collaborators at DTU Construct, using the material COC (Topas 5013). However, the experimental characterization of this device is ongoing work that has not been completed due to time constraints.

8.6 Concluding remarks

Numerical optimization of acoustofluidic devices is a challenging task, as the device's performance depends on multiple design parameters, as well as on the material parameters of the system. This chapter presented an approach to perform device optimization based on a multiple-step procedure. A critical aspect of the optimized design is using an anti-symmetric lateral mode of a piezoelectric transducer much below the frequency of its thickness resonance. This mode yields a clean displacement field free of higher-order modes and closely resembling a sine-wave-like actuation of the polymer chip. Furthermore, a transverse mode of the polymer chip, where the chip width approximately matches the longitudinal wavelength λ_{lo}, can be used as the mechanism driving acoustophoresis in a microfluidic channel.

When designing an acoustofluidic device, the experimental requirements and fabrication constraints need to be considered, as well as the limitations of the numerical simulation. Performing numerical optimization in 3D is hardly feasible due to the high complexity of the mesh and the long computation time requiring several days, if not weeks, of computation. Furthermore, the question under which aspect the optimization shall be performed is essential and needs to be derived from an experimental perspective. In this chapter, an optimization parameter $\mathcal{Q}$ was introduced that is related to a maximum achievable flow rate $Q_{\mathrm{flow}}^{\mathrm{max}}$ of the system. Furthermore, the ratio $\mathcal{R}$ between the vertical and horizontal radiation force was taken into account in the optimization. Two improved designs for an acoustophoresis device made from the polymer COC have been proposed. The importance of the experimental circumstances, meaning which type of electrical excitation technique is being used, also needs to be considered in the design process. Therefore, the two designs, "Optim. A" and "Optim. B," have been introduced. The former has been developed for a constant-voltage frequency sweep and is currently in the fabrication process.

Three-dimensional simulations of the optimized geometry promise a performance increase by more than an order of magnitude compared to the reference device studied in Paper I [1], therefore fulfilling the goal mentioned in the introduction to this chapter. This performance increase translates to flow rates of up to 0.6 mL/min at an input power of 1 W. Ongoing experimental validation measurements will show whether the device will yield this predicted order of magnitude increase in acoustic energy density compared to the reference design introduced in Chapter 5.

Chapter 9

Conclusion & Outlook

In this chapter, we briefly examine the work presented in this thesis. Then, the identified challenges and the proposed solutions in polymer-based acoustofluidics are summarized before looking toward the future role of polymer devices and possible follow-up studies.

9.1 Conclusion

This thesis aimed to identify and solve some of the challenges of using polymer devices for acoustofluidic applications. Ensuring the validity of numerical simulations is one of the most important aspects when using simulations as a predictive tool. In that regard, a feedback loop has been established to bridge theory, simulation, and experiment for reliable system optimization. The quality of the simulation results strongly relies on sufficiently-accurate material parameters, and the lack thereof was identified as another challenge addressed in this thesis. While focusing on some experimental aspects of acoustofluidic device characterization, broad differences in the means of electrical excitation methods have been observed in the acoustofluidic community. When comparing device performance, the details of this excitation technique become essential, as was addressed by a comparative study of constant-voltage and constant-power excitation methods. Combining all these crucial lessons enabled the numerical optimization of a polymer device with a predicted performance increase by more than an order of magnitude compared to the reference design. A few key points that were presented in this thesis are summarized below.

(1) **Experimental validation of the numerical model** (Paper I [1], Chapter 5)
In order to rely on numerical simulations as a predictive tool for device design, the model's validity needs to be ensured. This has been done by comparing the experimental results of a polymer-based acoustofluidic device to numerical results over a wide frequency range from 0.5 MHz to 2.5 MHz. In that scope, the focusability $\mathcal{F}$ has been introduced to compare the focusing efficiency between simulation and experiment. The numerically predicted resonance of the focusability $\mathcal{F}$ differs by only 2.6% in that study. The simulated pressure- and displacement-fields aid the understanding of the driving mechanism of resonances in polymer devices. The findings indicate that the eigenmode of the polymer chip and the associated motion of

the fluid channel walls are driving the acoustophoresis. This finding also explains why resonances in polymer devices are typically not observed at the conventional half-wave frequency resulting from the channel width. To further improve the accuracy of the numerical model, missing or inaccurate material parameters for polymers have been identified as one of the core challenges.

(2) **Ultrasound electrical impedance spectroscopy to determine elastic moduli of polymers** (Paper II [2], Chapter 6)
The method "Ultrasound electrical impedance spectroscopy" (UEIS) has been developed to determine accurate and precise material parameters. The UEIS method enables a complete set of material parameters for the polymer chip, the piezoelectric transducer, and polymer-based coupling layers based on a simple measurement of the electrical impedance spectrum. Compared to conventional measurement techniques, UEIS takes a full frequency spectrum from 500 Hz to 5 MHz into account, and measurements, therefore, occur at frequency ranges that are relevant for acoustofluidic applications. The UEIS method enables a nearly *in-situ* characterization of the material parameters.

(3) **Comparison of electrical excitation methods** (Paper III [3], Chapter 7)
In many acoustofluidic simulations and experiments, the voltage amplitude at the piezoelectric transducer is kept or assumed to be constant. However, this approach is not always ideal, and more care must be given to the electrical setup to maximize the acoustophoretic performance. Furthermore, it has been shown in Paper III [3] that driving the piezoelectric transducer at a constant power dissipation may be more advantageous. Especially if the resonant mode of the polymer chip is not perfectly matched to the resonance frequency of the piezoelectric transducer, constant-power excitation ensures that such modes can be observed experimentally. Paper III [3] furthermore made use of the UEIS method to characterize the piezoelectric transducer used in the experiments and the numerical study to obtain a good match between the two.

(4) **Numerical optimization of a polymer-based device** (Chapter 8)
A polymer-based acoustofluidic device has been optimized by employing UEIS-characterized polymer material parameters. This optimization also took the constant-power excitation into account to obtain improved dimensions of a polymer chip, enabling high flow rates for particle separation experiments. Furthermore, this geometry utilizes an anti-symmetric lateral mode of the piezoelectric transducer and a transverse mode of the polymer chip for high performance. 3D simulations of the optimized device promise an increase in the achievable flow rate by an order of magnitude compared to the PMMA device studied in Paper I [1].

The development of polymer-based devices remains challenging because a good understanding of all components of the whole system is required. For example, the low acoustic impedance of polymers gives rise to whole-system resonances, as demonstrated

in Paper I [1]. In such a WSUR, the properties of the fluid, the coupling layer, the polymer, and the piezoelectric transducer must be known with sufficient accuracy to perform predictions of the expected resonant modes. While Paper II [2] with the presented UEIS method provides a tool to obtain those material parameters, it is nevertheless essential to measure these properties before designing a new device. Batch-to-batch variations in piezoelectric transducers and differences in the properties of various polymers almost rule out the use of literature values when aiming for a perfect match between simulation and experiment.

Design rules, often employed for glass-capillary-based microfluidic chips, are based on half-wave modes in the channel width or height and require the hard-wall boundary condition $\boldsymbol{n} \cdot \nabla p_1 = 0$ at the channel walls to be fulfilled. This condition is typically not fulfilled for the mechanically soft polymers with acoustic impedance in the range of $Z = 1$–3 MRayl, much lower than found for, e.g., glass or silicon. However, the numerical study of polymer devices has shown that some of the classical design rules for hard-wall devices can be modified for polymer-based devices. For example, for a width of the polymer chip that matches approximately the longitudinal wavelength of the polymer, a simple transverse mode occurs in the polymer leading to lateral motion of the channel walls. In such a case, channel dimensions close to $\lambda_0/4$ in terms of the wavelength λ_0 of the fluid are found to be ideal. However, such design rules need to be taken with a grain of salt, as it is still a whole-system resonance at play for polymer-based devices. Generally, simulations of the whole system are required, and design rules should act as a starting point for numerical device optimization. At larger device dimensions, especially in terms of the width and height of the polymer chip, a more complex wave motion in the polymer chip is found, causing compression or squeezing motion from the channel wall as seen in Paper I [1]. Furthermore, the vertical placement of the channel has a substantial impact on which driving mechanism is at play for the observed resonance.

Fabrication requirements in the injection-molding process significantly constrain the design of polymer-based devices for acoustofluidics. Especially the required bonding of a thin polymer foil imposes limitations on the vertical channel position. However, the techniques and solutions proposed in this thesis are not limited to injection-molded devices, and alternative fabrication methods with more design freedom present an exciting opportunity to explore the topic of polymer-based acoustofluidics further.

9.2 Outlook

Many interesting studies are still to be done outside this thesis's scope. One crucial step is the experimental characterization of the optimized geometry presented in Chapter 8, which could not be completed due to time constraints. The collaborators are currently fabricating the proposed device within the *AcouPlast* project at DTU Construct. The device's capability to perform high-throughput particle separation is of vital interest and, therefore, shall be determined in a subsequent study by AcouSort. The robustness of polymer devices and performance differences across different polymer materials is another important study.

The optimization procedure presented in Chapter 8 can be seen as the starting point for a more elaborate optimization scheme. Adjustments to the cost function and the termination criterion of the optimization routine are suggested in order to ensure that the dimensionless ratio $\mathcal{R}$ of the radiation forces does not outweigh improvements of the acoustic energy density E_{ac}. This work utilized the MATLAB-toolbox `fminsearchbnd` for device optimization to minimize the cost function. A comparative study on the performance of different optimization algorithms would present an helpful overview and could lead to further device improvements. The optimization performed in this thesis has been subject to several constraints regarding the thickness of the polymer chip and the vertical channel placement. Alternative fabrication techniques might offer the advantage of nearly unconstrained optimization.

3D printing for polymer-based acoustofluidics is a fascinating and rapidly evolving topic. My colleague William Naundrup Bodé performed a numerical study of a 3D-printable acoustofluidic device in the scope of his Ph.D. thesis with encouraging results. Unlike injection molding, 3D printing enables rapid prototyping and allows the flexibility to analyze several different device geometries quickly and experimentally. 3D printing also allows more complex channel geometries than the conventional rectangular microfluidic channel, resulting from lithography requirements. It furthermore opens up the possibility of low-cost device fabrication, even for low-quantity batches. The UEIS technique can be utilized for 3D-printing materials in the same manner as injection-molded materials and can assist the device design.

UEIS is not limited to its use in the field of acoustofluidics. This technique's extension towards other applications utilizing ultrasound acoustics is imaginable. Research and development concerning medical ultrasound, including piezoelectric or capacitive micromachined ultrasonic transducers (PMUT/CMUT), likely can profit from reliable material parameters that have been characterized at frequencies close to transducer frequencies.

So far, the optimization of acoustofluidic devices has mainly focused on improving the device. Another aspect that briefly was mentioned in the context of Paper III [3] is optimizations to the electrical circuit driving the piezoelectric transducer. Similarly, as acoustic impedance matching between the transducer and acoustofluidic device is used, electrical impedance matching can increase the device's performance at the same input power.

Another interesting study focusing on the electrical characteristics of an acoustofluidic system would be to measure the transducer temperature across a wide frequency range while using different methods of electrical excitation. The temperature of an acoustofluidic device is highly important for many biomedical applications and has been primarily neglected throughout this thesis. While Peltier-cooling can bypass some heating-related problems, temperature effects can lead to essential phenomena in acoustofluidics.

Another aspect that this thesis did not explore is the occurrence of acoustic streaming and the resulting acoustic drag force acting on small particles. Streaming has been neglected in this work due to the intended use of polymer devices for particle separation applications focusing on larger particle sizes, such as red blood cells. When the study and the manipulation of smaller particles below 1 µm are of interest, the drag force becomes dominating, making particle focusing difficult. Shape-optimization of the fluid channel

presents the unique opportunity to minimize acoustic streaming as numerically predicted by Bach *et al.* [123]. Polymer devices are a promising candidate to facilitate such shape-optimized channels.

The future presents a promising outlook for polymer-based acoustofluidic devices fabricated using injection molding or rapidly evolving 3D-printing tools. With the methods and techniques presented in this work, the characterization of different polymer materials enables numerical optimization of such devices, decreasing the performance gap compared to glass and silicon devices. The findings of this thesis hopefully will assist the development of low-cost polymer-based devices for use in point-of-care applications, bringing acoustofluidics one step closer to mainstream applications outside the research environment.

Appendix A

Material parameters

A.1 Material parameters obtained from literature

Table A.1: List of fluid parameters at 20 °C obtained from the literature. Values for pure water, 16% v/v iodixanol in water, and 99% glycerol solution are listed.

Parameter	Symbol	Value	Unit
Water [69]			
Mass density	ρ_0	998	$\mathrm{kg\,m^{-3}}$
Speed of sound	c_0	1482	$\mathrm{m\,s^{-1}}$
Compressibility	κ_0	455	$\mathrm{TPa^{-1}}$
Dynamic viscosity	η_0	1.002	mPa s
Bulk viscosity	η_0^{b}	2.860	mPa s
Water-iodixanol mixture [69, 70]			
Mass density	ρ_0	1050	$\mathrm{kg\,m^{-3}}$
Speed of sound	c_0	1482	$\mathrm{m\,s^{-1}}$
Compressibility	κ_0	433	$\mathrm{TPa^{-1}}$
Dynamic viscosity	η_0	1.474	mPa s
Bulk viscosity	η_0^{b}	1.966	mPa s
Glycerol [71–73]			
Mass density	ρ_0	1260	$\mathrm{kg\,m^{-3}}$
Speed of sound	c_0	1923	$\mathrm{m\,s^{-1}}$
Compressibility	κ_0	215	$\mathrm{TPa^{-1}}$
Dynamic viscosity	η_0	1.137	Pa s
Bulk viscosity	η_0^{b}	0.790	Pa s

Table A.2: List of parameters at 20 °C obtained from the literature. Values for polystyrene particles, borosilicate glass, silver, PMMA, and PZT Pz26 are listed. For PMMA $C_{12} = C_{11} - 2C_{44}$. For PZT $C_{12} = C_{11} - 2C_{66}$.

Parameter	Symbol	Value	Unit
Polystyrene [36]			
Mass density	ρ_p	1050	$\mathrm{kg\,m^{-3}}$
Compressibility	κ_p	238	$\mathrm{TPa^{-1}}$
Monopole coefficient	f_0	0.479	
Dipole coefficient	f_1	0	
Borosilicate glass [31, 122]			
Mass density	ρ_sl	2230	$\mathrm{kg\,m^{-3}}$
Elastic modulus	C_{11}	$64.84 - \mathrm{i}0.03$	GPa
Elastic modulus	C_{44}	$24.32 - \mathrm{i}0.01$	GPa
Silver [124]			
Mass density	ρ_sl	10485	$\mathrm{kg\,m^{-3}}$
Elastic modulus	C_{11}	$134 - \mathrm{i}0.05$	GPa
Elastic modulus	C_{44}	$25.9 - \mathrm{i}0.01$	GPa
PMMA [74–80]			
Mass density	ρ_sl	1186	$\mathrm{kg\,m^{-3}}$
Elastic modulus	C_{11}	$8.93 - \mathrm{i}0.10$	GPa
Elastic modulus	C_{44}	$2.32 - \mathrm{i}0.03$	GPa
PZT (Pz26) [16, 32, 81]			
Mass density	ρ_sl	7700	$\mathrm{kg\,m^{-3}}$
Elastic modulus	C_{11}	$168 - \mathrm{i}3.36$	GPa
Elastic modulus	C_{12}	$110 - \mathrm{i}2.20$	GPa
Elastic modulus	C_{13}	$99.9 - \mathrm{i}2.00$	GPa
Elastic modulus	C_{33}	$123 - \mathrm{i}2.46$	GPa
Elastic modulus	C_{44}	$30.1 - \mathrm{i}0.60$	GPa
Coupling constant	e_{15}	9.86	$\mathrm{C\,m^{-2}}$
Coupling constant	e_{31}	-2.8	$\mathrm{C\,m^{-2}}$
Coupling constant	e_{33}	14.7	$\mathrm{C\,m^{-2}}$
Electric permittivity	ε_{11}	$828 - \mathrm{i}17$	ϵ_0
Electric permittivity	ε_{33}	$700 - \mathrm{i}14$	ϵ_0

A.2 Material parameters obtained via UEIS

Table A.3: UEIS-obtained material properties for the polymers PMMA (Diakon TD525), PMMA (LG IG 840) at an injection speed of 16 mm/s, COC (Topas 5013), and NOA 86H. Values in parentheses denote the standard error of the mean based on N samples.

Parameter	Symbol	Value	Unit
PMMA (Diakon TD525), $N = 4$			
Mass density	ρ_{sl}	1162(4)	$\mathrm{kg\,m^{-3}}$
Elastic modulus	C_{11}	$7.18(4) - \mathrm{i}0.183(5)$	GPa
Elastic modulus	C_{44}	$1.553(8) - \mathrm{i}0.111(7)$	GPa
PMMA (LG IG 840), $N = 3$			
Mass density	ρ_{sl}	1174(3)	$\mathrm{kg\,m^{-3}}$
Elastic modulus	C_{11}	$8.69(6) - \mathrm{i}0.138(8)$	GPa
Elastic modulus	C_{44}	$2.089(1) - \mathrm{i}0.087(5)$	GPa
COC (Topas 5013), $N = 1$			
Mass density	ρ_{sl}	1011	$\mathrm{kg\,m^{-3}}$
Elastic modulus	C_{11}	$6.12 - \mathrm{i}0.08$	GPa
Elastic modulus	C_{44}	$1.33 - \mathrm{i}0.04$	GPa
NOA 86H, $N = 1$			
Mass density	ρ_{sl}	1300	$\mathrm{kg\,m^{-3}}$
Elastic modulus	C_{11}	$4.65 - \mathrm{i}0.51$	GPa
Elastic modulus	C_{44}	$1.21 - \mathrm{i}0.12$	GPa

Table A.4: The average of the UEIS-obtained material parameters for the piezoelectric material Pz27 resulted from measurements of 32 different Pz27 samples. The values in parentheses denote the standard error of the mean for $N = 32$.

Parameter	Symbol	Value	Unit
PZT (Pz27)			
Mass density	ρ_{sl}	7700	$\mathrm{kg\,m^{-3}}$
Elastic modulus	C_{11}	$122.3(6) - \mathrm{i}0.58(5)$	GPa
Elastic modulus	C_{12}	$75.1(4) + \mathrm{i}0.1(3)$	GPa
Elastic modulus	C_{13}	$76.1(6) + \mathrm{i}0.11(3)$	GPa
Elastic modulus	C_{33}	$117.8(3) - \mathrm{i}0.48(4)$	GPa
Elastic modulus	C_{44}	$21.4(1) - \mathrm{i}0.66(7)$	GPa
Coupling constant	e_{15}	11.6(3)	$\mathrm{C\,m^{-2}}$
Coupling constant	e_{31}	−4.88(5)	$\mathrm{C\,m^{-2}}$
Coupling constant	e_{33}	16.11(5)	$\mathrm{C\,m^{-2}}$
Electric permittivity	ε_{11}	973(12)	ϵ_0
Electric permittivity	ε_{33}	$812(5) + \mathrm{i}2.88(8)$	ϵ_0

Bibliography

[1] F. Lickert, M. Ohlin, H. Bruus, and P. Ohlsson, *Acoustophoresis in polymer-based microfluidic devices: Modeling and experimental validation*. J. Acoust. Soc. Am. **149**(6), 4281–4291 (2021).

[2] W. N. Bodé, F. Lickert, P. Augustsson, and H. Bruus, *Determination of the complex-valued elastic moduli of polymers by electrical impedance spectroscopy for ultrasound applications*. Phys. Rev. Applied **resubmitted**, 11 pages (2022), https://arxiv.org/abs/2204.06464.

[3] F. Lickert, H. Bruus, and M. Rossi, *Constant-power versus constant-voltage actuation in frequency sweeps for acoustofluidic applications*. Micromachines **13**(11), 1886 (2022).

[4] A. Marzo, A. Barnes, and B. W. Drinkwater, *Tinylev: A multi-emitter single-axis acoustic levitator*. Rev. Sci. Instrum. **88**(8), 085105 (2017).

[5] W. Cui, L. Mu, X. Duan, W. Pang, and M. A. Reed, *Trapping of sub-100 nm nanoparticles using gigahertz acoustofluidic tweezers for biosensing applications*. Nanoscale **11**(31), 14625–14634 (2019).

[6] T. Frommelt, M. Kostur, M. Wenzel-Schaefer, P. Talkner, P. Haenggi, and A. Wixforth, *Microfluidic mixing via acoustically driven chaotic advection*. Phys. Rev. Lett. **100**(3), 034502 (2008).

[7] C. Zhang, P. Brunet, L. Royon, and X. Guo, *Mixing intensification using sound-driven micromixer with sharp edges*. Chem. Eng. J. **410**, 128252 (2021).

[8] K. Lee, H. Shao, R. Weissleder, and H. Lee, *Acoustic purification of extracellular microvesicles*. ACS Nano **9**(3), 2321–2327 (2015).

[9] M. Evander, L. Johansson, T. Lilliehorn, J. Piskur, M. Lindvall, S. Johansson, M. Almqvist, T. Laurell, and J. Nilsson, *Noninvasive acoustic cell trapping in a microfluidic perfusion system for online bioassays*. Anal. Chem. **79**(7), 2984–2991 (2007).

[10] B. Hammarström, M. Evander, H. Barbeau, M. Bruzelius, J. Larsson, T. Laurell, and J. Nillsson, *Non-contact acoustic cell trapping in disposable glass capillaries*. Lab Chip **10**(17), 2251–2257 (2010).

[11] P. Dow, K. Kotz, S. Gruszka, J. Holder, and J. Fiering, *Acoustic separation in plastic microfluidics for rapid detection of bacteria in blood using engineered bacteriophage.* Lab Chip **18**(6), 923–932 (2018).

[12] Y. Gu, C. Chen, Z. Wang, P.-H. Huang, H. Fu, L. Wang, M. Wu, Y. Chen, T. Gao, J. Gong, J. Kwun, G. M. Arepally, and T. J. Huang, *Plastic-based acoustofluidic devices for high-throughput, biocompatible platelet separation.* Lab Chip **19**, 394–402 (2019).

[13] K. Olofsson, B. Hammarstrom, and M. Wiklund, *Acoustic separation of living and dead cells using high density medium.* Lab Chip **20**(11), 1981–1990 (2020).

[14] J. Rufo, F. Cai, J. Friend, M. Wiklund, and T. J. Huang, *Acoustofluidics for biomedical applications.* Nat Rev Methods Primers **2**(1), 1–21 (2022).

[15] P. Hahn, O. Schwab, and J. Dual, *Modeling and optimization of acoustofluidic microdevices.* Lab Chip **14**, 3937–3948 (2014).

[16] W. N. Bodé, L. Jiang, T. Laurell, and H. Bruus, *Microparticle acoustophoresis in aluminum-based acoustofluidic devices with PDMS covers.* Micromachines **11**(3), 292 (2020).

[17] N. Bhattacharjee, A. Urrios, S. Kang, and A. Folch, *The upcoming 3D-printing revolution in microfluidics.* Lab on a Chip **16**(10), 1720–1742 (2016).

[18] A. Mueller, A. Lever, T. V. Nguyen, J. Comolli, and J. Fiering, *Continuous acoustic separation in a thermoplastic microchannel.* J Micromech Microeng **23**(12), 125006 (2013).

[19] R. Silva, P. Dow, R. Dubay, C. Lissandrello, J. Holder, D. Densmore, and J. Fiering, *Rapid prototyping and parametric optimization of plastic acoustofluidic devices for blood-bacteria separation.* Biomedical Microdevices **19**(3), 70 (2017).

[20] C. Lissandrello, R. Dubay, K. T. Kotz, and J. Fiering, *Purification of lymphocytes by acoustic separation in plastic microchannels.* SLAS Technology **23**(4), 352–363 (2018).

[21] R. Dubay, C. Lissandrello, P. Swierk, N. Moore, D. Doty, and J. Fiering, *Scalable high-throughput acoustophoresis in arrayed plastic microchannels.* Biomicrofluidics **13**(3), 034105 (2019).

[22] H. D. Santos, A. E. Silva, G. C. Silva, E. B. Lima, A. S. Marques, M. S. Alexandre-Moreira, A. C. Queiroz, C. Jacinto, J. Henrique Lopes, U. Rocha, *et al.*, *3D-Printed Acoustofluidic Devices for Raman Spectroscopy of Cells.* Adv. Eng. Mater. **23**(10), 2100552 (2021).

[23] E. Cesewski, A. P. Haring, Y. Tong, M. Singh, R. Thakur, S. Laheri, K. A. Read, M. D. Powell, K. J. Oestreich, and B. N. Johnson, *Additive manufacturing of three-dimensional (3D) microfluidic-based microelectromechanical systems (MEMS) for acoustofluidic applications*. Lab Chip **18**(14), 2087–2098 (2018).

[24] Y. Lin, C. Gao, Y. Gao, M. Wu, A. A. Yazdi, and J. Xu, *Acoustofluidic micromixer on lab-on-a-foil devices*. Sens. Actuators B: Chem. **287**, 312–319 (2019).

[25] Y. Lin, Y. Gao, M. Wu, R. Zhou, D. Chung, G. Caraveo, and J. Xu, *Acoustofluidic stick-and-play micropump built on foil for single-cell trapping*. Lab Chip **19**(18), 3045–3053 (2019).

[26] R. P. Moiseyenko and H. Bruus, *Whole-system ultrasound resonances as the basis for acoustophoresis in all-polymer microfluidic devices*. Phys. Rev. Applied **11**, 014014 (2019).

[27] N. Pérez, M. A. B. Andrade, F. Buiochi, and J. C. Adamowski, *Identification of elastic, dielectric, and piezoelectric constants in piezoceramic disks*. IEEE Trans. Ultrason. Ferroelec. Freq. Contr. **57**(12), 2772–2783 (2010).

[28] J. Ilg, S. J. Rupitsch, A. Sutor, and R. Lerch, *Determination of Dynamic Material Properties of Silicone Rubber Using One-Point Measurements and Finite Element Simulations*. IEEE T. Instrum. Meas. **61**(11), 3031–3038 (2012).

[29] N. Pérez, R. Carbonari, M. Andrade, F. Buiochi, and J. Adamowski, *A FEM-based method to determine the complex material properties of piezoelectric disks*. Ultrasonics **54**(6), 1631–1641 (2014).

[30] C. Y. Kiyono, N. Perez, and E. C. N. Silva, *Determination of full piezoelectric complex parameters using gradient-based optimization algorithm*. Smart Mater. Struct. **25**(2), 025019 (2016).

[31] A. G. Steckel, H. Bruus, P. Muralt, and R. Matloub, *Fabrication, characterization, and simulation of glass devices with* AlN *thin-film transducers for excitation of ultrasound resonances*. Phys. Rev. Applied **16**, 014014, 1–10 (2021).

[32] N. R. Skov, J. S. Bach, B. G. Winckelmann, and H. Bruus, *3D modeling of acoustofluidics in a liquid-filled cavity including streaming, viscous boundary layers, surrounding solids, and a piezoelectric transducer*. AIMS Mathematics **4**, 99–111 (2019).

[33] N. R. Skov, P. Sehgal, B. J. Kirby, and H. Bruus, *Three-dimensional numerical modeling of surface-acoustic-wave devices: Acoustophoresis of micro- and nanoparticles including streaming*. Phys. Rev. Applied **12**, 044028 (2019).

[34] A. G. Steckel and H. Bruus, *Numerical study of bulk acoustofluidic devices driven by thin-film transducers and whole-system resonance modes*. J. Acoust. Soc. Am. **150**(1), 634–645 (2021).

[35] J. S. Bach and H. Bruus, *Theory of pressure acoustics with viscous boundary layers and streaming in curved elastic cavities*. J. Acoust. Soc. Am. **144**, 766–784 (2018).

[36] J. T. Karlsen and H. Bruus, *Forces acting on a small particle in an acoustical field in a thermoviscous fluid*. Phys. Rev. E **92**, 043010 (2015).

[37] J. H. Joergensen and H. Bruus, *Theory of pressure acoustics with thermoviscous boundary layers and streaming in elastic cavities*. J. Acoust. Soc. Am. **149**(5), 3599–3610 (2021).

[38] J. H. Joergensen and H. Bruus, *Theory and modeling of nonperturbative effects at high acoustic energy densities in thermoviscous acoustofluidics*. Phys. Rev. E **submitted**, 15 pages (2021), https://arxiv.org/abs/2112.10737.

[39] J. H. Joergensen, W. Qiu, and H. Bruus, *A transition from boundary- to bulk-driven acoustic streaming due to nonlinear thermoviscous effects at high acoustic energy densities*. Phys. Rev. Lett. **submitted**, 5 pages (2022), https://arxiv.org/abs/2112.11410.

[40] J. S. Bach, *Theory of acoustic fields and streaming with viscous boundary layers in microsystems*. Ph.D. thesis, Technical University of Denmark, DTU Physics Building 309, DK-2800 Kongens Lyngby, Denmark (2020), https://bruus-lab.dk/TMF/publications/PhD/PhD_2020_JSB.pdf, accessed 10 Nov 2022.

[41] M. Settnes and H. Bruus, *Forces acting on a small particle in an acoustical field in a viscous fluid*. Phys. Rev. E **85**, 016327 (2012).

[42] L. P. Gorkov, *On the forces acting on a small particle in an acoustical field in an ideal fluid*. Sov. Phys.–Dokl. **6**(9), 773–775 (1962), [Doklady Akademii Nauk SSSR **140**, 88 (1961)].

[43] M. R. Maxey and J. J. Riley, *Equation of motion for a small rigid sphere in a nonuniform flow*. The Physics of Fluids **26**(4), 883–889 (1983).

[44] R. Barnkob, I. Iranmanesh, M. Wiklund, and H. Bruus, *Measuring acoustic energy density in microchannel acoustophoresis using a simple and rapid light-intensity method*. Lab Chip **12**, 2337–2344 (2012).

[45] T. Ikeda, *Fundamentals of Piezoelectricity* (Oxford University Press, London, UK) (1996).

[46] R. Holland, *Representation of Dielectric, Elastic, and Piezoelectric Losses by Complex Coefficients*. IEEE Transactions on Sonics and Ultrasonics **14**(1), 18–20 (1967).

[47] H. Bruus, *Lecture notes for DTU course 10350 Numerical studies in physics* (2020), available on request by bruus@fysik.dtu.dk.

[48] C. Liu, *Implementing the Weak Form in COMSOL Multiphysics*. COMSOL Multiphysics, https://www.comsol.com/blogs/implementing-the-weak-form-in-comsol-multiphysics/, accessed 10 Nov 2022.

[49] COMSOL Multiphysics 6.0, (2022), http://www.comsol.com.

[50] K. Saeedabadi, G. Tosello, and M. Calaon, *Optimization of injection molded polymer lab-on-a-chip for acoustic blood plasma separation using virtual design of experiment*. Procedia CIRP **107**, 40–45 (2022).

[51] C. Tsao, L. Hromada, J. Liu, P. Kumar, and D. DeVoe, *Low temperature bonding of pmma and coc microfluidic substrates using uv/ozone surface treatment*. Lab Chip **7**(4), 499–505 (2007).

[52] R. Günther, W. R. Caseri, and C. Brändli, *Direct bonding and de-bonding on demand of polystyrene and polyamide surfaces, treated with oxygen plasma*. Journal of Applied Polymer Science **139**(10), 51753 (2022).

[53] P. S. Nunes, P. D. Ohlsson, O. Ordeig, and J. P. Kutter, *Cyclic olefin polymers: emerging materials for lab-on-a-chip applications*. Microfluid. Nanofluid. **9**(2-3), 145–161 (2010).

[54] W. N. Bodé and H. Bruus, *Numerical study of the coupling layer between transducer and chip in acoustofluidic devices*. J. Acoust. Soc. Am. **149**(5), 3096–3105 (2021).

[55] A. Lenshof, M. Evander, T. Laurell, and J. Nilsson, *Acoustofluidics 5: Building microfluidic acoustic resonators*. Lab Chip **12**, 684–695 (2012).

[56] V. Vitali, G. Core, F. Garofalo, T. Laurell, and A. Lenshof, *Differential impedance spectra analysis reveals optimal actuation frequency in bulk mode acoustophoresis*. Scientific reports **9**(1), 1–10 (2019).

[57] R. Barnkob, C. J. Kähler, and M. Rossi, *General defocusing particle tracking*. Lab Chip **15**, 3556–3560 (2015).

[58] M. Rossi and R. Barnkob, *A fast and robust algorithm for general defocusing particle tracking*. Meas. Sci. Technol. **32**(1), 014001 (2020).

[59] A. Tahmasebipour, L. Friedrich, M. Begley, H. Bruus, and C. Meinhart, *Toward optimal acoustophoretic microparticle manipulation by exploiting asymmetry*. J. Acoust. Soc. Am. **148**(1), 359–373 (2020).

[60] P. Augustsson, R. Barnkob, S. T. Wereley, H. Bruus, and T. Laurell, *Automated and temperature-controlled micro-PIV measurements enabling long-term-stable microchannel acoustophoresis characterization*. Lab Chip **11**(24), 4152–4164 (2011).

[61] W. Qiu, T. Baasch, and T. Laurell, *Enhancement of acoustic energy density in bulk-wave-acoustophoresis devices using side actuation*. Phys. Rev. Appl. **17**(4), 044043 (2022).

[62] S. O. Ural, S. Tuncdemir, Y. Zhuang, and K. Uchino, *Development of a high power piezoelectric characterization system and its application for resonance/antiresonance mode characterization*. Jpn. J. Appl. Phys. **48**(5R), 056509 (2009).

[63] Y. Liu, R. Ozaki, and T. Morita, *Investigation of nonlinearity in piezoelectric transducers*. Sens. Actuator A Phys. **227**, 31–38 (2015).

[64] E. K. Sackmann, A. L. Fulton, and D. J. Beebe, *The present and future role of microfluidics in biomedical research*. Nature **507**(7491), 181–189 (2014).

[65] I. Gonzalez, M. Tijero, A. Martin, V. Acosta, J. Berganzo, A. Castillejo, M. M. Bouali, and J. Luis Soto, *Optimizing polymer lab-on-chip platforms for ultrasonic manipulation: Influence of the substrate*. Micromachines **6**(5), 574–591 (2015).

[66] C. Yang, Z. Li, P. Li, W. Shao, P. Bai, and Y. Cui, *Acoustic particle sorting by integrated micromachined ultrasound transducers on polymerbased microchips*. IEEE International Ultrasonics Symposium (IUS) 1–4 (2017).

[67] R. Barnkob, P. Augustsson, T. Laurell, and H. Bruus, *Measuring the local pressure amplitude in microchannel acoustophoresis*. Lab Chip **10**(5), 563–570 (2010).

[68] P. B. Muller, M. Rossi, A. G. Marin, R. Barnkob, P. Augustsson, T. Laurell, C. J. Kähler, and H. Bruus, *Ultrasound-induced acoustophoretic motion of microparticles in three dimensions*. Phys. Rev. E **88**(2), 023006 (2013).

[69] P. B. Muller and H. Bruus, *Numerical study of thermoviscous effects in ultrasound-induced acoustic streaming in microchannels*. Phys. Rev. E **90**(4), 043016 (2014).

[70] J. T. Karlsen, P. Augustsson, and H. Bruus, *Acoustic force density acting on inhomogeneous fluids in acoustic fields*. Phys. Rev. Lett. **117**, 114504 (2016).

[71] W. Slie, A. Donfor Jr, and T. Litovitz, *Ultrasonic shear and longitudinal measurements in aqueous glycerol*. The Journal of Chemical Physics **44**(10), 3712–3718 (1966).

[72] L. Negadi, B. Feddal-Benabed, I. Bahadur, J. Saab, M. Zaoui-Djelloul-Daouadji, D. Ramjugernath, and A. Negadi, *Effect of temperature on density, sound velocity, and their derived properties for the binary systems glycerol with water or alcohols*. The Journal of Chemical Thermodynamics **109**, 124–136 (2017).

[73] N.-S. Cheng, *Formula for the viscosity of a glycerol-water mixture*. Ind. Eng. Chem. Res. **47**(9), 3285–3288 (2008).

[74] B. Hartmann and J. Jarzynski, *Polymer sound speeds and elastic constants*. Naval Ordnance Laboratory **Report NOLTR 72-269**, 1–10 (1972), https://apps.dtic.mil/sti/pdfs/AD0755695.pdf, accessed 10 Nov 2022.

[75] D. Christman, *Dynamic properties of poly (methylmethacrylate) (PMMA) (plexiglas)*. Report No. DNA 2810F, MSL-71-24 **1**(1) (1972), https://apps.dtic.mil/sti/pdfs/AD0743547.pdf, accessed 10 Nov 2022.

[76] H. Sutherland and R. Lingle, *Acoustic characterization of polymethyl methacrylate and 3 epoxy formulations*. J. Appl. Phys. **43**(10), 4022–4026 (1972).

[77] H. Sutherland, *Acoustical determination of shear relaxation functions for polymethyl methacrylate and Epon 828-Z*. J. Appl. Phys. **49**(7), 3941–3945 (1978).

[78] J. E. Carlson, J. van Deventer, and A. S. C. Carlander, *Frequency and temperature dependence of acoustic properties of polymers used in pulse-echo systems*. IEEE Ultrasonics Symposium 885–888 (2003).

[79] A. Simon, G. Lefebvre, T. Valier-Brasier, and R. Wunenburger, *Viscoelastic shear modulus measurement of thin materials by interferometry at ultrasonic frequencies*. J. Acoust. Soc. Am. **146**(5), 3131–3140 (2019).

[80] H. T. Tran, T. Manh, T. F. Johansen, and L. Hoff, *Temperature effects on ultrasonic phase velocity and attenuation in Eccosorb and PMMA*. In *2016 IEEE International Ultrasonics Symposium (IUS)*, 1–4 (2016).

[81] P. Hahn and J. Dual, *A numerically efficient damping model for acoustic resonances in microfluidic cavities*. Physics of Fluids **27**, 062005 (2015).

[82] COMSOL Multiphysics 5.5, (2019), http://www.comsol.com.

[83] P. B. Muller, R. Barnkob, M. J. H. Jensen, and H. Bruus, *A numerical study of microparticle acoustophoresis driven by acoustic radiation forces and streaming-induced drag forces*. Lab Chip **12**, 4617–4627 (2012).

[84] M. Bora and M. Shusteff, *Efficient coupling of acoustic modes in microfluidic channel devices*. Lab Chip **15**(15), 3192–3202 (2015).

[85] S. J. Rupitsch and R. Lerch, *Inverse Method to estimate material parameters for piezoceramic disc actuators*. Appl. Phys. A **97**(4), 735–740 (2009).

[86] John D'Errico, *fminsearchbnd algorithm*. Matlab file exchange (2012), https://www.mathworks.com/matlabcentral/fileexchange/8277-fminsearchbnd-fminsearchcon, accessed 10 Nov 2022.

[87] J. C. Lagarias, J. A. Reeds, M. H. Wright, and P. E. Wright, *Convergence properties of the nelder–mead simplex method in low dimensions*. SIAM Journal on optimization **9**(1), 112–147 (1998).

[88] Meggitt A/S, Porthusvej 4, DK-3490 Kvistgaard, Denmark, *Ferroperm matrix data*. https://www.meggittferroperm.com/materials/, accessed 10 Nov 2022.

[89] J. Lord and R. Morrell, *Measurement good practice guide no. 98: elastic modulus measurement*. National Physical Lab. Report 1–100 (2007), https://eprintspublications.npl.co.uk/3782/1/MGPG98.pdf, accessed 10 Nov 2022.

[90] N. M. Mehat and S. Kamaruddin, *Investigating the effects of injection molding parameters on the mechanical properties of recycled plastic parts using the taguchi method*. Mater. Manuf. Process. **26**(2), 202–209 (2011).

[91] B. Ozcelik, A. Ozbay, and E. Demirbas, *Influence of injection parameters and mold materials on mechanical properties of abs in plastic injection molding*. Int. Commun. Heat Mass Transf. **37**(9), 1359–1365 (2010).

[92] N. Bretz, J. Strobel, M. Kaltenbacher, and R. Lerch, *Numerical simulation of ultrasonic waves in cavitating fluids with special consideration of ultrasonic cleaning*. In *IEEE Int. Ultrason. Symp.*, 703–706 (2005).

[93] M. T. Todaro, F. Guido, V. Mastronardi, D. Desmaele, G. Epifani, L. Algieri, and M. De Vittorio, *Piezoelectric MEMS vibrational energy harvesters: Advances and outlook*. Microelectron. Eng. **183**, 23–36 (2017).

[94] M. Singh, H. M. Haverinen, P. Dhagat, and G. E. Jabbour, *Inkjet printing-process and its applications*. Adv. Mater. **22**(6), 673–685 (2010).

[95] MatWeb, LLC, *Online Materials Information Resource*. http://www.matweb.com/ (2022).

[96] A. Migliori, J. Sarrao, W. M. Visscher, T. Bell, M. Lei, Z. Fisk, and R. Leisure, *Resonant ultrasound spectroscopic techniques for measurement of the elastic moduli of solids*. Physica B **183**(1), 1–24 (1993).

[97] H. Wang, W. Jiang, and W. Cao, *Characterization of lead zirconate titanate piezoceramic using high frequency ultrasonic spectroscopy*. J. Appl. Phys. **85**(12), 8083–8091 (1999).

[98] G. Xu, Z. Ni, X. Chen, J. Tu, X. Guo, H. Bruus, and D. Zhang, *Acoustic Characterization of Polydimethylsiloxane for Microscale Acoustofluidics*. Physical Review Applied **13**(5), 054069 (2020).

[99] G. Roebben, B. Bollen, A. Brebels, J. Van Humbeeck, and O. Van der Biest, *Impulse excitation apparatus to measure resonant frequencies, elastic moduli, and internal friction at room and high temperature*. Rev. Sci. Instrum. **68**(12), 4511–4515 (1997).

[100] R. Willis, L. Wu, and Y. Berthelot, *Determination of the complex young and shear dynamic moduli of viscoelastic materials*. J. Acoust. Soc. Am. **109**(2), 611–621 (2001).

[101] M. Radovic, E. Lara-Curzio, and L. Riester, *Comparison of different experimental techniques for determination of elastic properties of solids*. Mat Sci Eng A-Struct **368**(1-2), 56–70 (2004).

[102] J. Plesek, R. Kolman, and M. Landa, *Using finite element method for the determination of elastic moduli by resonant ultrasound spectroscopy*. J. Acoust. Soc. Am. **116**(1), 282–287 (2004).

[103] J. Maynard, *Resonant Ultrasound Spectroscopy*. Physics Today **49**, 26–31 (1996).

[104] G. H. Michler and W. Lebek, *Electron microscopy of polymers* (Wiley, Hoboken (NJ)) (2016).

[105] A. G. Steckel and H. Bruus, *Numerical study of acoustic cell trapping above elastic membrane disks driven in higher-harmonic modes by thin-film transducers with patterned electrodes*. Phys. Rev. E **submitted**, 14 pages (2021), https://arxiv.org/abs/2112.12567.

[106] W. D. Callister Jr, *Materials Science and Engineering: An Introduction* (John Wiley & Sons, York, PA), seventh edn. (2007).

[107] Norland Products Inc., Jamesburg, NJ 08831, USA, *Norland Optical Adhesive 86H*. https://www.norlandprod.com/adhesives/NOA86H.html, accessed 10 Nov 2022.

[108] Meggitt A/S, Porthusvej 4, DK-3490 Kvistgaard, Denmark, *Ferroperm matrix data*. https://www.meggittferroperm.com/materials/, accessed 10 Nov 2022.

[109] T. Pritz, *Frequency dependences of complex moduli and complex poisson's ratio of real solid materials*. J. Sound Vib. **214**(1), 83–104 (1998).

[110] Z. Pei, Y. Ma, C. Wang, Y. Wu, F. Song, and X. Wu, *Optimal design of a driver of interdigital transducers used to generate standing surface acoustic waves for cell sorting*. Rev. Sci. Instrum. **92**(3), 034705 (2021).

[111] A. Huang, W. Connacher, M. Stambaugh, N. Zhang, S. Zhang, J. Mei, A. Jain, S. Alluri, V. Leung, A. E. Rajapaksa, *et al.*, *Practical microcircuits for handheld acoustofluidics*. Lab Chip **21**(7), 1352–1363 (2021).

[112] J. Han, F. Yang, H. Hu, Q. Huang, Y. Lei, and M. Li, *Thermal control design and packaging for surface acoustic wave devices in acoustofluidics*. IEEE Trans. Ultrason. Ferroelectr. Freq. Control **69**(1), 386–398 (2021).

[113] V. T. Rathod, *A review of electric impedance matching techniques for piezoelectric sensors, actuators and transducers*. Electronics **8**(2), 169 (2019).

[114] H. Huang and D. Paramo, *Broadband electrical impedance matching for piezoelectric ultrasound transducers*. IEEE Trans. Ultrason. Ferroelectr. Freq. Control **58**(12), 2699–2707 (2011).

[115] A. Barani, P. Mosaddegh, S. Haghjooy Javanmard, S. Sepehrirahnama, and A. Sanati-Nezhad, *Numerical and experimental analysis of a hybrid material acoustophoretic device for manipulation of microparticles*. Sci. Rep. **11**(1), 1–17 (2021).

[116] M. G. Kim, S. Yoon, H. H. Kim, and K. K. Shung, *Impedance matching network for high frequency ultrasonic transducer for cellular applications*. Ultrasonics **65**, 258–267 (2016).

[117] M. Garcia-Rodriguez, J. Garcia-Alvarez, Y. Yañez, M. Garcia-Hernandez, J. Salazar, A. Turo, and J. Chavez, *Low cost matching network for ultrasonic transducers*. Phys. Procedia **3**(1), 1025–1031 (2010).

[118] J. S. Emeterio, A. Ramos, P. Sanz, and A. Ruiz, *Evaluation of impedance matching schemes for pulse-echo ultrasonic piezoelectric transducers*. Ferroelectrics **273**(1), 297–302 (2002).

[119] I. Leibacher, S. Schatzer, and J. Dual, *Impedance matched channel walls in acoustofluidic systems*. Lab Chip **14**(3), 463–470 (2014).

[120] P. Ohlsson, K. Petersson, P. Augustsson, and T. Laurell, *Acoustic impedance matched buffers enable separation of bacteria from blood cells at high cell concentrations*. Sci. Rep. **8**, 2045–2322 (2018).

[121] R. Barnkob and M. Rossi, *Defocustracker: A modular toolbox for defocusing-based, single-camera, 3d particle tracking*. Journal of Open Research Software **9**(1), 22 (2021).

[122] SCHOTT, SCHOTT Suisse SA, 2 Rue Galilée, Yverdon, Switzerland, *Borosilicate glass substrates*. https://www.epfl.ch/research/facilities/cmi/wp-content/uploads/2020/05/D263T_d.pdf, accessed 10 Nov 2022.

[123] J. S. Bach and H. Bruus, *Suppression of acoustic streaming in shape-optimized channels*. Phys. Rev. Lett. **124**, 214501 (2020).

[124] AZoMaterials, Charlotte Street, Manchester, UK, *Silver - Applications and Properties of Silver*. https://www.azom.com/properties.aspx?ArticleID=600, accessed 27 November 2021.